University of Massachusetts UMASS Lowell

TIDC
Transportation Infrastructure Durability Center
AT THE UNIVERSITY OF MAINE

Department of Civil and Environmental Engineering UMass Lowell

Technical Report

December 2025

Development of general guidelines related to the effects of factors such as the bridge span range, range of pile length, roadway profile grade, and skew angle range on integral abutment bridges (IABs)

By Susan Faraji-Hennessey Ph.D. Prof. of Structural Engineering

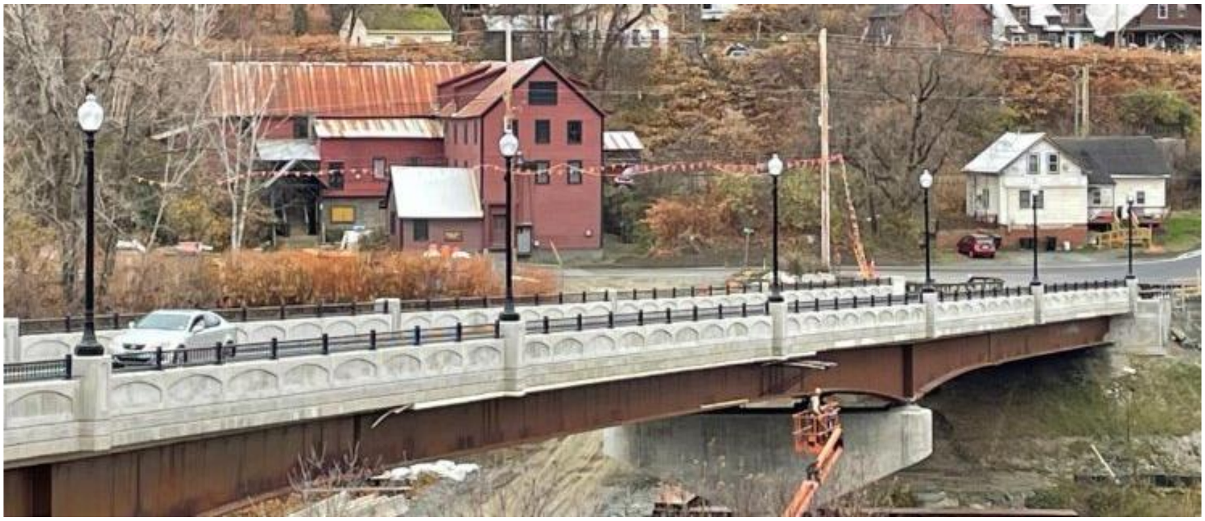

Development of general guidelines related to the effects of factors such as the bridge span range, range of pile length, roadway profile grade, and skew angle range on integral abutment bridges (IABs)

By Susan Faraji-Hennessey Ph.D., Prof. of Structural Engineering
Susan_Farajihennessey@uml.edu

Dept. of Civil and Environmental Engineering
University of Massachusetts Lowell
Lowell Massachusetts 01854

PI: Susan Faraji-Hennessey, Ph.D., Prof. of Structural Engineering

Project Champion: Mr. James Lacroix, PE, State Bridge Design Engineer, VTrans

Research Assistant: Mr. Harsh Gandhi, Ph.D. candidate, UMass Lowell

The Report is conducted for:

Federal Highway Administration through University Transportation Center Program (UTC) University of Maine Transportation Center, Orono Maine 04469

December 2025

Acknowledgment

This work was funded by the Transportation Infrastructure Durability Center at the University of Maine under grant 69A3551847101 from the U.S. Department of Transportation's University Transportation Centers Program. The U.S. Government assumes no liability for the contents or use thereof.
The contents of this reflect the view of the author, who is responsible for the facts and the accuracy of the data presented herein. The contents do not necessarily reflect the official views or policies of the Federal Highway Administration. This report does not constitute a standard, specification or regulation.

Special thanks to the Hexagon PPM/Intergraph Corporation and especially Dr. Michael Swanger for their very generous technical support on the use of GTSTRUDL software.

I would also like to thank the UMass Lowell students who participated in this research.

EXECUTIVE SUMMARY

The overall objective of this research was to improve the guidelines for the modeling, design, and construction of integral abutment bridges (IABs). Based on input from the DOTs the following topics were considered for the study:

(i) In-plane rotation of skewed integral abutment bridges: An analytical study

(ii) Preliminary design of piles in integral abutment bridges

(iii) Impact of the abutment wall height, unsymmetrical backfill stiffness, and the span length on the behavior of integral abutment bridges

(iv) The impact of the use of expanded polystyrene (EPS) geofoam on thermally induced stresses on the superstructure and substructure of integral abutment bridges: A parametric study

For the topics under study, many plots and Tables were created to be used by practicing bridge engineers to optimize the design of integral abutment brides.

Table of Contents

Chapter 1

In-plane Rotation of Skewed Integral Abutment Bridges: An analytical study

---

ABSTRACT

When integral abutments are located on skew the behavior is more complicated. Non-skew integral abutment bridges experience uniformity when the temperature is increased and the lateral soil pressure behind the abutment wall near the deck level tends toward the passive pressure limit state. Study of skewed integral abutment bridges (IABs) has shown that skewed IABs experience rotation in the horizontal plane under thermal loading, which causes a redistribution of the soil pressure acting on the abutment walls and so a non-uniform soil pressure behind the wall. Rotation tends to decrease the translation at the acute corners and increase the translation at the obtuse corners of the of the abutment wall. Therefore, the deformation pattern for skewed IAB may differ substantially from the non-skew state and may produce unanticipated local cracking.

The specific objective of this study was to identify parameters that will control the in-plane rotation and its effect on displaced configuration of skewed IABs that is caused by thermal expansion to be able to design the abutment wall-pile system of skewed IABs more accurately.

To accomplish this objective, a closed form analytical solution was generated for a skewed rigid plate supported by normal and tangential restraining springs on the skew sides of the plate and subjected it to a uniform temperature loading. This model provides a reasonable approximation for the response of a single span skewed IAB subjected to temperature loading. Where plate is the representative of the response of the superstructure and normal and tangential springs on the boundaries of the plate are representative of response of the substructure.

The analytical study reveals that the in-plane rotation and displaced configuration of the plate will be impacted by changes in: the skew angle, the width to length ratio of the plate, the ratio of stiffness of tangential to normal restraining springs on the boundaries, and unsymmetrical restraining springs stiffnesses on the boundaries. The parametric study findings were verified by finite element modeling.

INTRODUCTION

Integral abutment bridges (IABs) are indeterminate single story framed structures with soil interaction. As in any indeterminate frame, the distribution of the forces between the frame members depends on the relative stiffness of the frame members. The biggest uncertainty in the analysis and design of IABs is the reaction of the soil behind the abutment walls and next to the foundation piles. The magnitude of these forces can become substantial during the thermal expansion of the bridge and can greatly affect the overall structural design of the abutment wall-pile system in skewed IABs.

In the past few decades many researchers have studied IABs by means of finite element modeling, parametric and analytical studies (Alqarawi 2020, Dicleli 2004, Dicleli 2005, Faraji 2001, Khard 2014, Peric 2016, Zordan 2011, Xu 2018), experimental and field testing and data collecting (Alqarawi 2020 , Davids 2010, Deng 2015, Khodair 2013) taking into account the impacts of parameters such as span length, stiffness of the soil behind the abutment walls, stiffness of the soil around piles, orientation of piles and so on. Many design and modeling recommendations have been made. This in turn has lent itself to an increase in the construction of more IABs.

On the other hand when it comes to skewed IABs there has been very limited studies have been done and these studies have been case specific (Sanders, 1993Wright, 2015, Zhao, 2021). There are more studies needed to be done. Skewed IABs are generally limited to prescriptive span lengths and skew angles set by local agencies, without substantial research to support these limitations. Therefore, there is a need for a unified set of design guidelines for IABs with longer spans and larger skews. However, the need remains for a unified set of design guidelines for skewed IABs that could be implemented by AASHTO bridge design specifications.

METHETOLOGY

The specific objective of this study was to identify the parameters that will control the in-plane motion of skewed IABs caused by thermal expansion. To accomplish this objective, a closed form analytical solution was generated for a skewed rigid plate supported by normal and tangential restraining springs on the skew sides of the plate and subjected it to a uniform thermal loading. This model provides a reasonable approximation for the response of a single span skewed IAB subjected to temperature loading. Where the skewed plate is the representative of the superstructure and normal and tangential springs on the boundaries of the plate are representative of substructure of skewed single span IAB.

ANALYTICAL FORMULATION

Consider the skew plate shown in Figure 1. The plate is restrained by springs acting on two sides of the plate, lines 1-4 and 2-3 in the normal and tangential directions (see Figure 2). The plate is considerd to be rigid and to be subjected to a uniform temperature increase, ΔT .

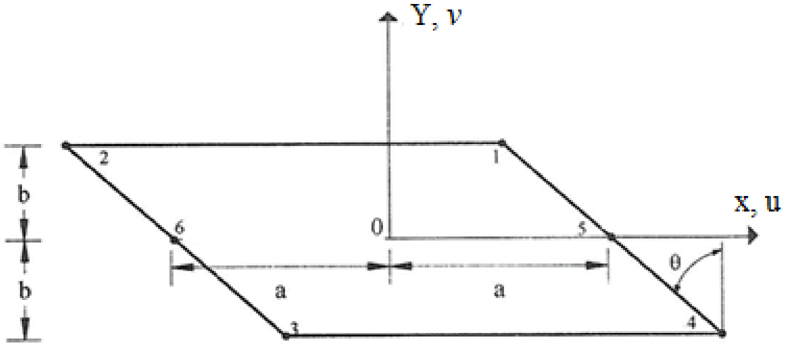

Fig. 1 Geometry of skew plate

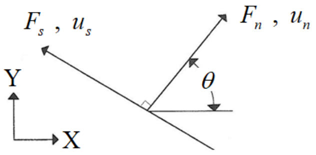

Fig. 2 Orientation of normal and tangential axes

Displacement Field

The strains due to thermal loading, ΔT, on an isotropic plate are:

$$\varepsilon_{\mathrm{x}} = \frac{\partial u}{\partial x} = \alpha_t \, \Delta T \qquad (1)$$

$$\varepsilon_{\mathrm{y}} = \frac{\partial v}{\partial y} = \alpha_t \, \Delta T \qquad (2)$$

$$\gamma_{\mathrm{xy}} = \frac{\partial u}{\partial y} + \frac{\partial v}{\partial x} = 0 \qquad (3)$$

Integrating Equations (1) and (2) and then substituting for u and v in Equation (3) will lead to following expressions for u and v:

$$\begin{aligned} u &= C_1 + C_2 \, y + \left(\alpha_t \, \Delta T\right) x \\ v &= C_3 + C_2 \, x + \left(\alpha_t \, \Delta T\right) y \end{aligned} \qquad (4)$$

Spring Forces

The spring forces for a point on the boundaries (lines 1-4 and 2-3), see Figure 2, are determined with

$$\begin{aligned} F_n &= -k_n \, u_n \\ F_s &= -k_s \, u_s \end{aligned} \qquad (5)$$

where

$$\begin{aligned} u_n &= u \cos\theta + v \sin\theta \\ u_s &= -u \sin\theta + v \cos\theta \end{aligned} \qquad (6)$$

Transforming the normal and tangential spring forces F_n and F_s to Cartesian spring forces F_x, F_y will result in

$$\begin{aligned} F_x &= -k_x \, u - k_{xy} \, v \\ F_y &= -k_{xy} \, u - k_y \, v \end{aligned} \qquad (7)$$

where

$$\begin{aligned} k_x &= k_n\left(\cos\theta\right)^2 + k_s\left(\sin\theta\right)^2 \\ k_y &= k_n\left(\sin\theta\right)^2 + k_s\left(\cos\theta\right)^2 \\ k_{xy} &= \left(k_n - k_s\right)\sin\theta\cos\theta \end{aligned} \qquad (8)$$

For thermal loading, the u and v defined by equation (4) are used in equation (7).

Equilibrium Equations

The global equilibrium equations for the plate are

$$\sum F_{\mathrm{x}} = 0 \qquad (9)$$

$$\sum F_{\mathrm{y}} = 0 \qquad (10)$$

$$\sum M_{\mathrm{o}} = \sum\left(y\ F_{\mathrm{x}} - x\ F_{\mathrm{y}}\right) = 0 \qquad (11)$$

Where the summation extends over the number of boundary springs.

Substituting for the force components in terms of the displacement parameters defined by equation 4, the equations (9), (10) and (11) expand to

$$\begin{aligned} &C_1\ \left(\sum k_x\right) + C_2\ \left\{\left(\sum y\ k_x\right) - \left(\sum x\ k_{xy}\right)\right\} + \ C_3\left(\sum k_{xy}\right) \\ &+\ \left(\alpha_t\ \Delta T\right)\left\{\left(\sum x\ k_x\right) + \left(\sum y\ k_{xy}\right)\right\} = 0 \end{aligned} \qquad (12)$$

$$\begin{aligned} &C_1\ \left(\sum k_{xy}\right) + C_2\ \left\{\left(\sum y\ k_{xy}\right) - \left(\sum x\ k_y\right)\right\} + \ C_3\left(\sum k_y\right) \\ &+\ \left(\alpha_t\ \Delta T\right)\left\{\left(\sum x\ k_{xy}\right) + \left(\sum y\ k_y\right)\right\} = 0 \end{aligned} \qquad (13)$$

$$\begin{aligned} &C_1\ \left\{\left(\sum y\ k_x\right) - \left(\sum x\ k_{xy}\right)\right\} + C_2\ \left\{\left(\sum y^2\ k_x\right) + \left(\sum x^2\ k_y\right) - 2\sum xy\ k_{xy}\right\} \\ &+\ C_3\left\{\left(\sum y\ k_{xy}\right) - \left(\sum x\ k_y\right)\right\} + \ \left(\alpha_t\ \Delta T\right)\left\{\left(\sum\left(k_x - k_y\right)xy\right) + \left(\sum k_{xy}\left(y^2 - x^2\right)\right)\right\} = 0 \end{aligned} \qquad (14)$$

Solving equations (12), (13), and (14) lead to values for C_1 ,C_2 and C_3. With these values known, the displacements and spring forces can be evaluated. The application of these equations to a "skew-symmetric" system is considered next.

Evaluation of constants C_1 ,C_2 , and C_3 for plate with skew-symmetry

In order to continue the analytical computations further, it is necessary to specify the actual locations of the restraining springs on the boundaries of the plate, BDY1 (line 1-4) and BDY2 (line2-3). The geometry of the plate with a symmetrical skew angle, θ and the selected restraining springs locations and their stiffnesses are defined in Figure 3.

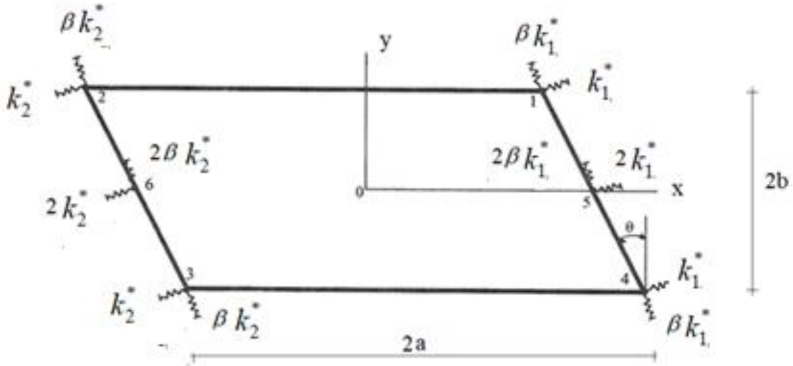

Fig. 3 Plate geometry and location of springs

Table 1 summarizes the coordinates and restraining springs stiffness coefficients for various points on the boundaries of the plate.

The skew symmetry of plate's boundaries will results in:

$$\sum x_i = \sum y_j = 0$$

Table 1 Coordinates and stiffness coefficients

Point i	x_i	y_i	$k_{n,i}$	$k_{s,i}$	$k_{x,i}$	$k_{y,i}$	$k_{xy,i}$
1	$a-b\tan\theta$	b	k_1^*	βk_1^*	$k_{1,x}^*$	$k_{1,y}^*$	$k_{1,xy}^*$
2	$-a\ -b\tan\theta$	b	k_2^*	βk_2^*	$k_{2,x}^*$	$k_{2,y}^*$	$k_{2,xy}^*$
3	$-a\ +b\tan\theta$	$-b$	k_2^*	βk_2^*	$k_{2,x}^*$	$k_{2,y}^*$	$k_{2,xy}^*$
4	$a\ +b\tan\theta$	$-b$	k_1^*	βk_1^*	$k_{1,x}^*$	$k_{2,y}^*$	$k_{1,xy}^*$

5	a	0	$2k_1^*$	$2\beta k_1^*$	$2k_{1,x}^*$	$2k_{1,y}^*$	$2k_{1,xy}^*$
6	$-a$	0	$2k_2^*$	$2\beta k_2^*$	$2k_{2,x}^*$	$2k_{2,y}^*$	$2k_{2,xy}^*$

where $k_1{}^*$ and $k_2{}^*$ are normal spring stiffnesses on the corners of the plate and β is relative stiffness parameter (see Figure 3). Which will lead to the following expressions

$$\begin{aligned} k_{x,i} &= k_{n,i}\left(\cos\theta\right)^2 + \beta k_{n,i}\left(\sin\theta\right)^2 \\ k_{y,i} &= k_{n,i}\left(\sin\theta\right)^2 + \beta k_{n,i}\left(\cos\theta\right)^2 \qquad (15) \\ k_{xy,i} &= \left(1-\beta\right)k_{n,i}\ \left(\sin\theta\cos\theta\right) \end{aligned}$$

or

$$\begin{aligned} \bar{k}_x^* &= \frac{k_{x,i}}{k_{n,i}} = \left(\cos\theta\right)^2 + \beta\left(\sin\theta\right)^2 \\ \bar{k}_y^* &= \frac{k_{y,i}}{k_{n,i}} = \left(\sin\theta\right)^2 + \beta\left(\cos\theta\right)^2 \qquad (16) \\ \bar{k}_{xy}^* &= \frac{k_{xy,i}}{k_{n,i}} = \left(1-\beta\right)\sin\theta\cos\theta \end{aligned}$$

Then the global stiffness factors and the thermal loading terms will expand to

Global stiffness factors:

$$
\begin{gathered}
\sum_i k_{x,i} = 4(k^*_{1,x}+k^*_{2,x}) \qquad \sum_i k_{y,i} = 4(k^*_{1,y}+k^*_{2,y}) \qquad \sum_i k_{xy,i} = 4(k^*_{1,xy}+k^*_{2,xy}) \\
\left\{\sum_i y_i\ k_{x,i} - \sum_i x_i k_{xy,i}\right\} = -4a\ b\ \ (k^*_{1,xy}+k^*_{2,xy}) \\
\left\{\sum_i y_i k_{xy,i} - \sum_i x_i k_{y,i}\right\} = -4a\ b\ \ (k^*_{1,y}+k^*_{2,y}) \\
\left\{\sum_i y_i k_{x,i} - \sum_i x_i k_{xy,i}\right\} = -4a\ b(k^*_{1,xy}+k^*_{2,xy}) \\
\left\{\sum_i {y_i}^2 k_{x,i} + \sum_i {x_i}^2 k_{y,i} - 2\sum_i x_i y_i k_{xy,i}\right\} \\
= 2b^2(k^*_{1,x}+k^*_{2,x}) + \left(4a^{\ 2} + 2b^2\left(\tan\theta\right)^2\right)(k^*_{1,y}+k^*_{2,y}) + 4b^2\tan\theta\left(k^*_{1,xy}+k^*_{2,xy}\right) \\
\left\{\sum_i y_i k_{xy,i} - \sum_i x_i k_{y,i}\right\} = -4a\ b(k^*_{1,y}-k^*_{2,y})
\end{gathered}
\tag{17}
$$

Thermal loading terms:

$$
\begin{gathered}
\alpha_t\ \Delta T\left\{\sum_i x_i k_{x,i} + \sum_i y_i k_{xy,i}\right\} = \alpha_t\ \Delta T\left(4a\ b\right)(k^*_{1,x}-k^*_{2,x}) \\
\alpha_t\ \Delta T\left\{\sum_i x_i k_{xy,i} + \sum_i y_i k_{y,i}\right\} = \alpha_t\ \Delta T\left(4a\ b\right)(k^*_{1,xy}-k^*_{2,xy}) \\
\alpha_t\ \Delta T\left\{\sum_i\left(k_{x,i}-k_{y,i}\right)x_i y_i + \sum_i k_{xy,i}\left({y_i}^2-{x_i}^2\right)\right\} = \\
-2\alpha_t\ \Delta T\left\{b^2\tan\theta\left[-\left(k^*_{1,x}+k^*_{2,x}\right)+\left(k^*_{1,y}+k^*_{2,y}\right)\right]+\left(b^2-2a^{\ 2}-b^2\left(\tan\theta\right)^2\right)\left(k^*_{1,xy}+k^*_{2,xy}\right)\right\}
\end{gathered}
\tag{18}
$$

And the plates normal and tangential displacements, u_n and u_s will expand to

$$\frac{u_n}{a\ \alpha_t\ \Delta T} = \frac{x}{a}\cos\theta + \left(\frac{b}{a}\right)\left(\frac{y}{b}\right)\sin\theta + \frac{C_2}{\alpha_t\ \Delta T}\left[-\frac{x}{a}\sin\theta + \left(\frac{b}{a}\right)\left(\frac{y}{b}\right)\cos\theta\right] + \frac{C_1}{a\ \alpha_t\ \Delta T}\cos\theta + \frac{C_3}{a\ \alpha_t\ \Delta T}\sin\theta$$

$$\frac{u_s}{a\ \alpha_t\ \Delta T} = -\frac{x}{a}\sin\theta + \left(\frac{b}{a}\right)\left(\frac{y}{b}\right)\cos\theta - \frac{C_2}{\alpha_t\ \Delta T}\left[\frac{x}{a}\cos\theta + \left(\frac{b}{a}\right)\left(\frac{y}{b}\right)\sin\theta\right] - \frac{C_1}{a\ \alpha_t\ \Delta T}\sin\theta + \frac{C_3}{a\ \alpha_t\ \Delta T}\cos\theta \tag{19}$$

ANALYTICAL STUDY RESULTS

The analytical study results reveal that the in-plane rotation of the plate due to thermal loading depends on:

i. The skew angle, θ
ii. The plate length to width ratio, a / b
iii. The tangential stiffness coefficient, β
iv. Unsymmetrical restraining springs, $k_2^* > k_1^*$

ANALYTICAL STUDY DISCUTIONS

In the following section the impact of $\theta, a / b, \beta$ on behavior of the plate when restraining springs are symmetrical is discussed first followed by in addition taking into account the impact of unsymmetrical restraining springs of the plate behavior.

Plate with symmetrical restraining springs

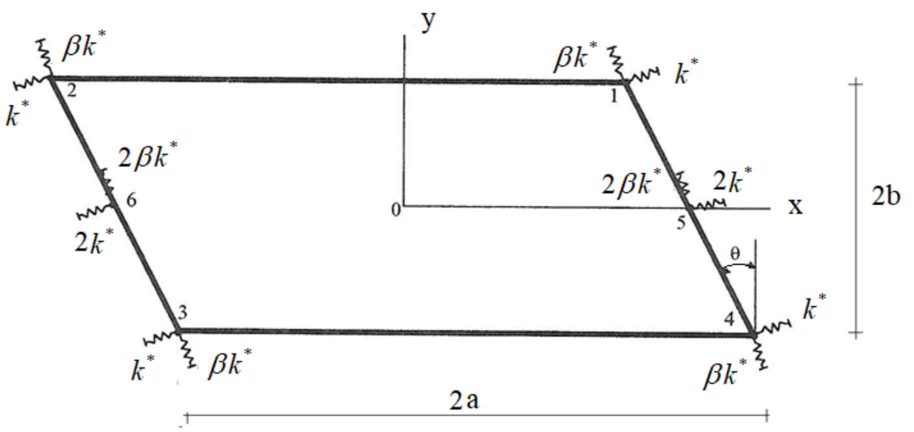

Fig.4 Plate with symmetrical restraining spring on the boundaries,

When the reference restraining springs on the boundaries (lines 1-4 and 2-3) of the plate are identical, that is $k_1^* = k_2^* = k^*$ (see Figure 4), solving equations (12),(13), and (14) will lead to $C_1 = C_3 = 0$ and the expression for C_2 will simplify to

$$\frac{C_2}{\alpha_t\,\Delta T} = \frac{\left(\bar{k}_x^* - \bar{k}_y^*\right)\tan\theta + \left(2\frac{a^2}{b^2} + \left(\tan\theta\right)^2 - 1\right)\bar{k}_{xy}^*}{\bar{k}_x^* + \left(2\frac{a^2}{b^2} + \left(\tan\theta\right)^2\right)\bar{k}_y^* + 2\tan\theta\,\bar{k}_{xy}^*} \tag{20}$$

where

$$\bar{k}_x^* = \left(\cos\theta\right)^2 + \beta\left(\sin\theta\right)^2$$
$$\bar{k}_y^* = \left(\sin\theta\right)^2 + \beta\left(\cos\theta\right)^2$$
$$\bar{k}_{xy}^* = \left(1-\beta\right)\sin\theta\cos\theta$$

Note that positive C_2 is a clockwise rotation of the plate about its origin defined in Fig 1.

Then the normal and tangential displacements of the plate will be simplified to (see Equation (19))

$$\begin{aligned} \frac{u_n}{a\,\alpha_t\,\Delta T} &= \frac{x}{a}\cos\theta + \left(\frac{b}{a}\right)\left(\frac{y}{b}\right)\sin\theta + \frac{C_2}{\alpha_t\,\Delta T}\left[-\frac{x}{a}\sin\theta + \left(\frac{b}{a}\right)\left(\frac{y}{b}\right)\cos\theta\right] \\ \frac{u_s}{a\,\alpha_t\,\Delta T} &= -\frac{x}{a}\sin\theta + \left(\frac{b}{a}\right)\left(\frac{y}{b}\right)\cos\theta - \frac{C_2}{\alpha_t\,\Delta T}\left[\frac{x}{a}\cos\theta + \left(\frac{b}{a}\right)\left(\frac{y}{b}\right)\sin\theta\right] \end{aligned} \tag{21}$$

To gain insight on relative importance of $a/b, \theta,$ and β the following limiting cases are considered. Case 1: For $\beta = 1$, the stiffness terms in Eq.(20) will reduce to $\bar{k}_x^* = \bar{k}_y^* = 1$ and $\bar{k}_{xy}^* = 0$. This will result in $C_2 = 0$ for all for all θ's. Case II: for $\beta = 0$ and $\theta = 45^0$, the upper limit for the skew angle, the expressions for C_2 and the normal and the tangential displacements at node1(obtuse corner) and node 4 (acute corner) will reduce to

$$\frac{C_2}{\alpha_t \, \Delta T} = \frac{(a/b)^2}{2+(a/b)^2} \qquad \text{(22-a)}$$

$$\frac{\sqrt{2}\, u_{n|obtuse}}{a\,\alpha_t\,\Delta T} = \frac{2(1+a/b)}{2+(a/b)^2} \qquad \frac{\sqrt{2}\, u_{n|acute}}{a\,\alpha_t\,\Delta T} = \frac{2(1-a/b)}{2+(a/b)^2} \qquad \text{(22-b)}$$

$$\frac{\sqrt{2}\, u_{s|0btuse}}{a\,\alpha_t\,\Delta T} = -\frac{1+(a/b)^2}{2+(a/b)^2} \qquad \frac{\sqrt{2}\, u_{s|acute}}{a\,\alpha_t\,\Delta T} = \frac{1+(a/b)^2}{2+(a/b)^2} \qquad \text{(22-c)}$$

As Equation (22-b) shows for $\beta = 0$ and $\theta = 45^0$, when $a/b > 1$, the normal displacement at the acute corner of the plate, $u_{n|acute}$ is opposite in sign to normal displacement at the obtuse corner, $u_{n|obtuse}$. Thus, for a small β and a large θ, a combination of active and passive pressures expected when the plate is subjected to a thermal expansion.

The plots in Figures 5, 6, and 7 show the variation of the in-plane rotation of the plate, C_2 with the skew angle, θ caused by the thermal expansion , ΔT for ranges of β and a/b when the restraining spring on the boundaries are symmetrical, $k_1^* = k_2^* = k^*$. (see Eq. (20))

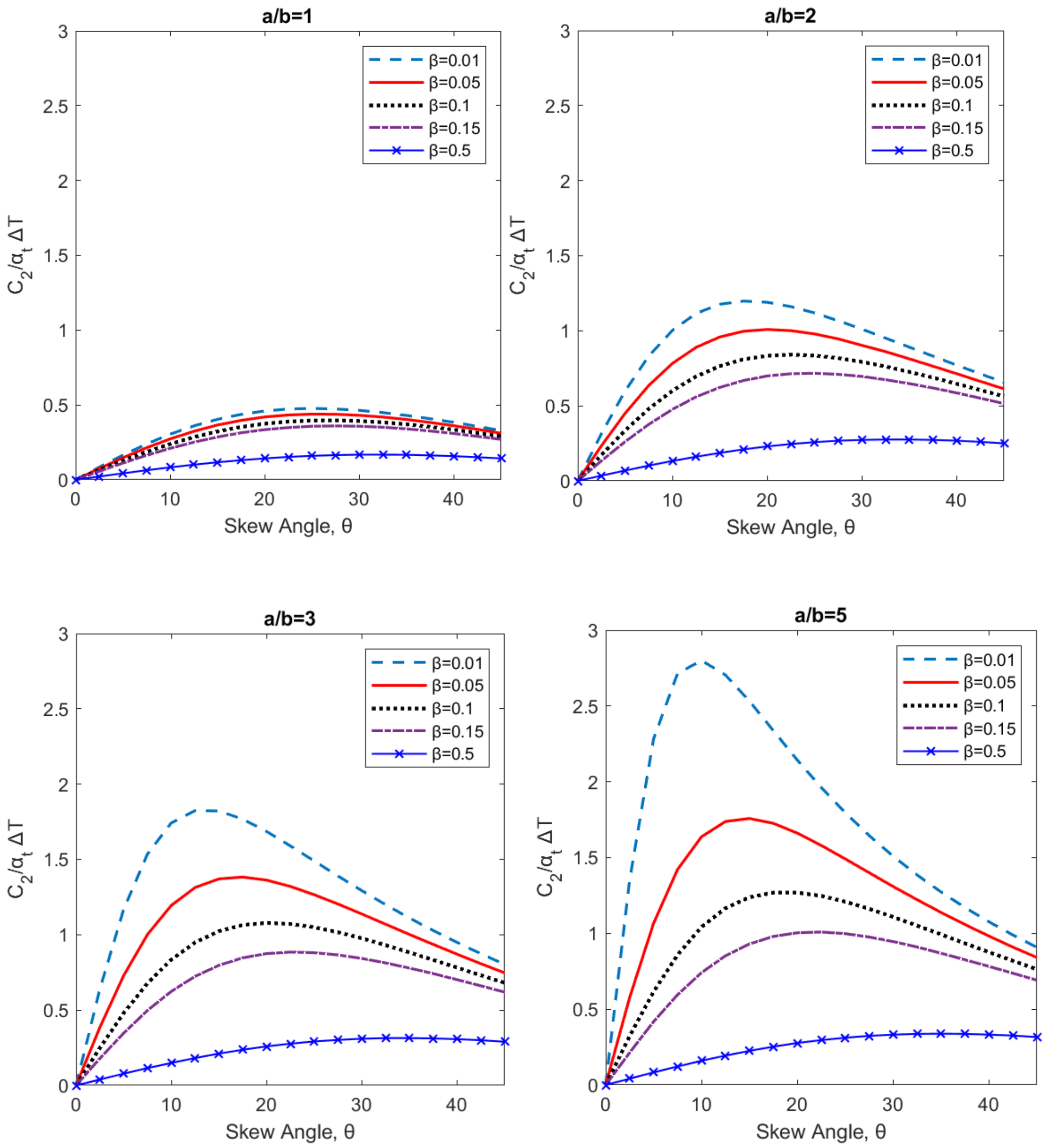

Fig. 5 Variation of C_2 with θ for $k_1^* = k_2^* = k^*$ and ranges of β and a/b

As Figure 5 shows when skew angle increases, the plate rotation increases from zero passing through a maximum, then decreases more gradually. This peak behavior is less pronounced for a smaller a / b and /or a larger β.

Now the question will be how the in plane rotation of the plate caused by thermal loading will impact the plate movement. To show the impact in the following figures $u_{n|obtuse}$ and

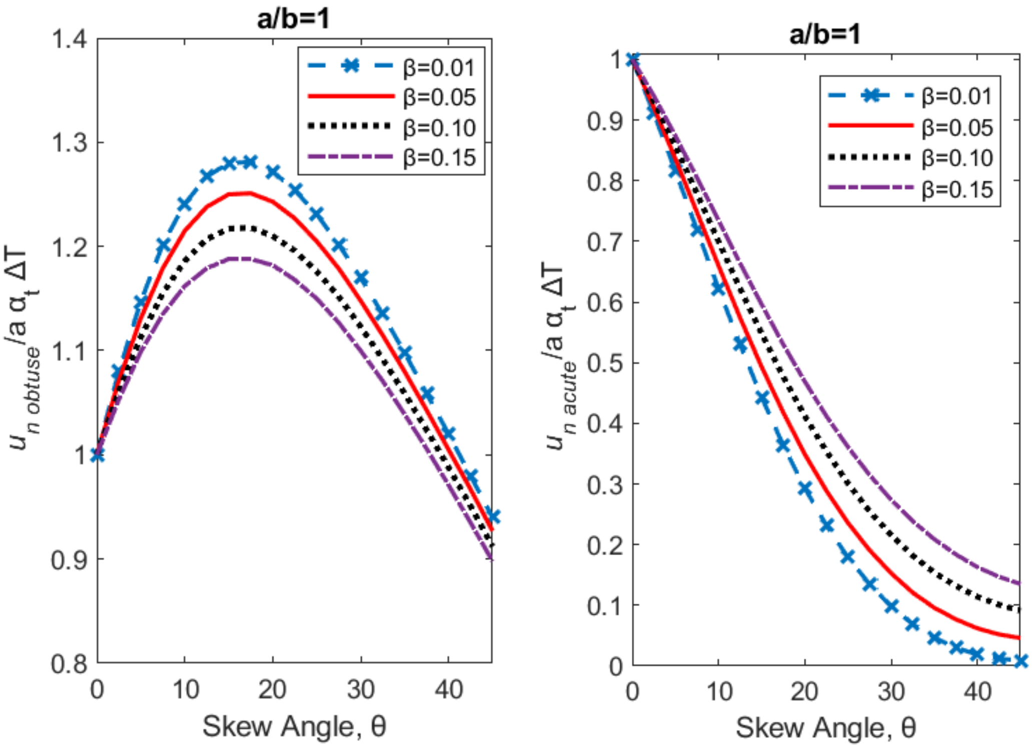

Fig.6 Variation of $u_{n|obtuse}$ and $u_{n|acute}$ with θ for ranges of β, a/b=1, and $k_1^* = k_2^* = k^*$

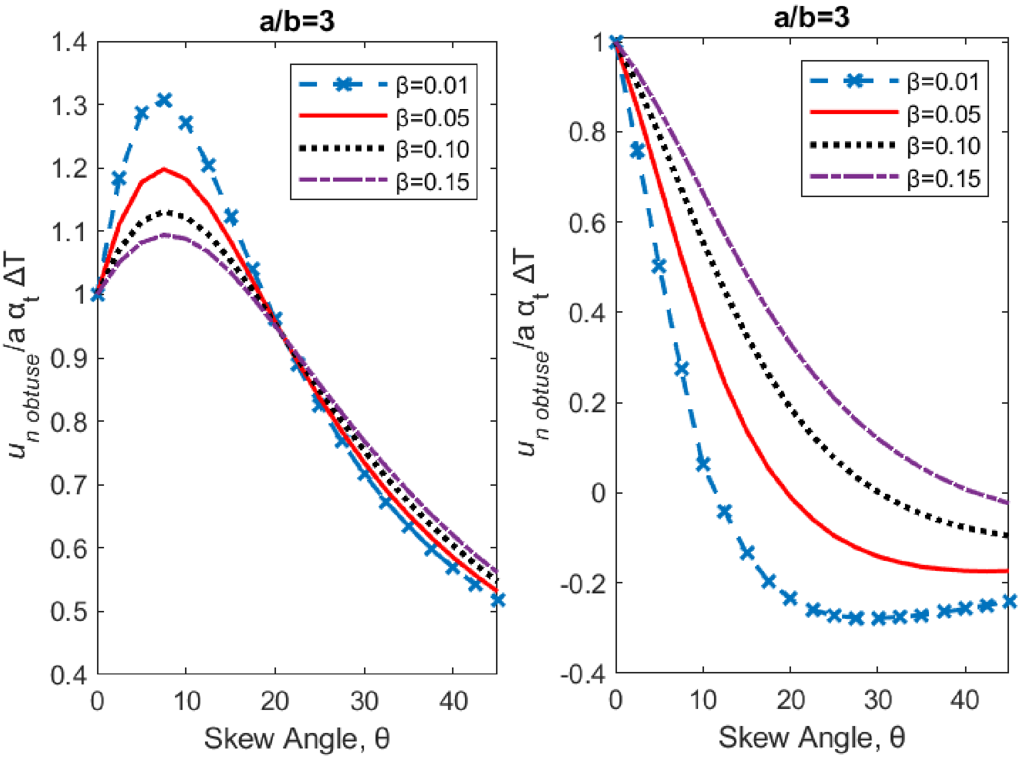

Fig.7 Variation of $u_{n|obtuse}$ and $u_{n|acute}$ with θ for ranges of β, a/b=3, and $k_1^* = k_2^* = k^*$

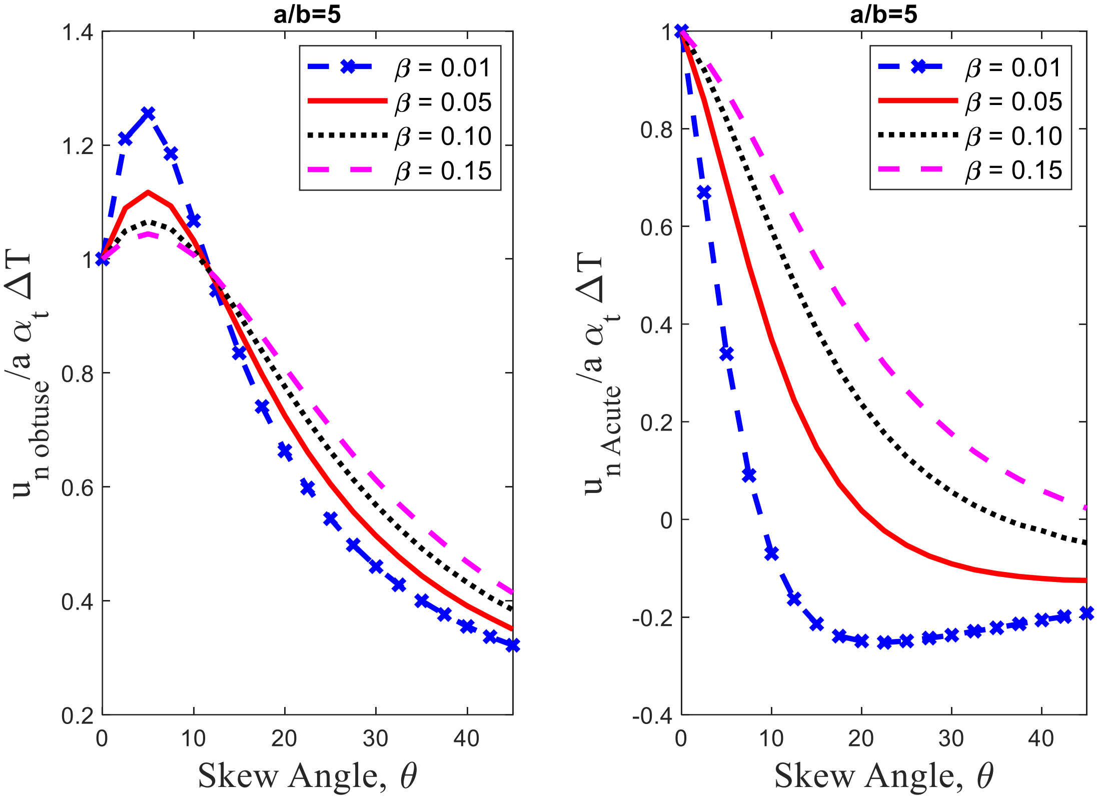

Fig.8 Variation of $u_{n|obtuse}$ and $u_{n|acute}$ with θ for ranges of β, a/b=5, and $k_1^* = k_2^* = k^*$

As figures 6-8 show that there is a contrast in the behavior of the acute and obtuse corners of the plate. At the obtuse corners, as θ increases, the normal displacement increases, passes through a maximum and then decreases gradually. On the other hand at the acute corners, as θ increases, the normal displacement decreases and by increasing a/b the normal displacement will move be negative. This means the normal displacement at the acute corners will move in the direction opposite that of the obtuse corners. When β is increased to the reversal in displacement is not observed. The reason for this shift is that as β is increased, the peak value of C_2 decreased (see Fig. 5), therefore the influence of rotation on the displace configuration is less significant. These results are consistent with the field monitoring studies reported Sanford,1993.

Impact of the unsymmetrical restraining springs stiffnesses on plate behavior

When the reference restraining springs on the boundaries (lines 1-4 and 2-3) of the plate are not identical($k_2^* > k_1^*$), in this case C_1 and C_3 will not be zero and will be determined by solving equations (12), (13), and (14) and then using equation (19) to determining normal and tangential displacements of the plate.

If we increase the stiffness on the boundary #2 of the plate

Some of the analytical study results finding showing the impact of the θ, a/b, β, and unsymmetrical restraining springs on the in-plane rotation and displacement of the plate caused by thermal expansion are presented and discussed in the following sections.

To get more insight some of the analytical formulations are plotted, tabulated and discussed in the following sections.

The plots in Figure 8 and Table 2 show the comparison of the impacvariation of the in-plane rotation of the plate, C_2 with the skew angle, θ (see equation(20)) caused by the thermal expansion , ΔT for ranges of β and a/b when the restraining spring on the boundaries are symmetrical, $k_1^* = k_2^* = k^*$. As Figure 5 shows when skew angle increases, the plate rotation increases from zero passing through a maximum, then decreases more gradually. This peak behavior is less pronounced for a smaller a/b and /or a larger β.

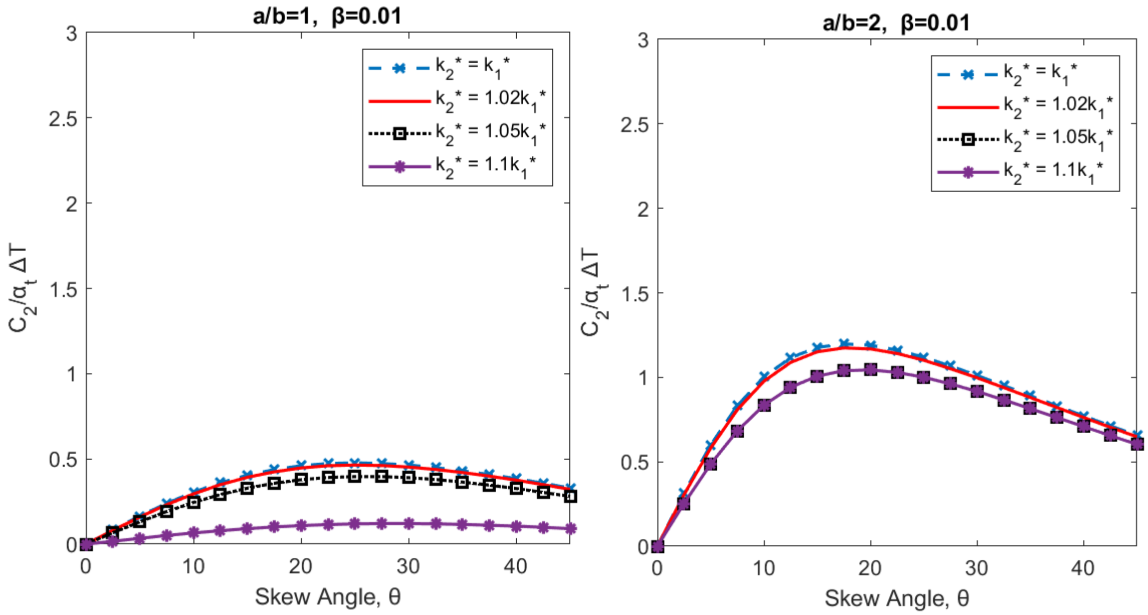

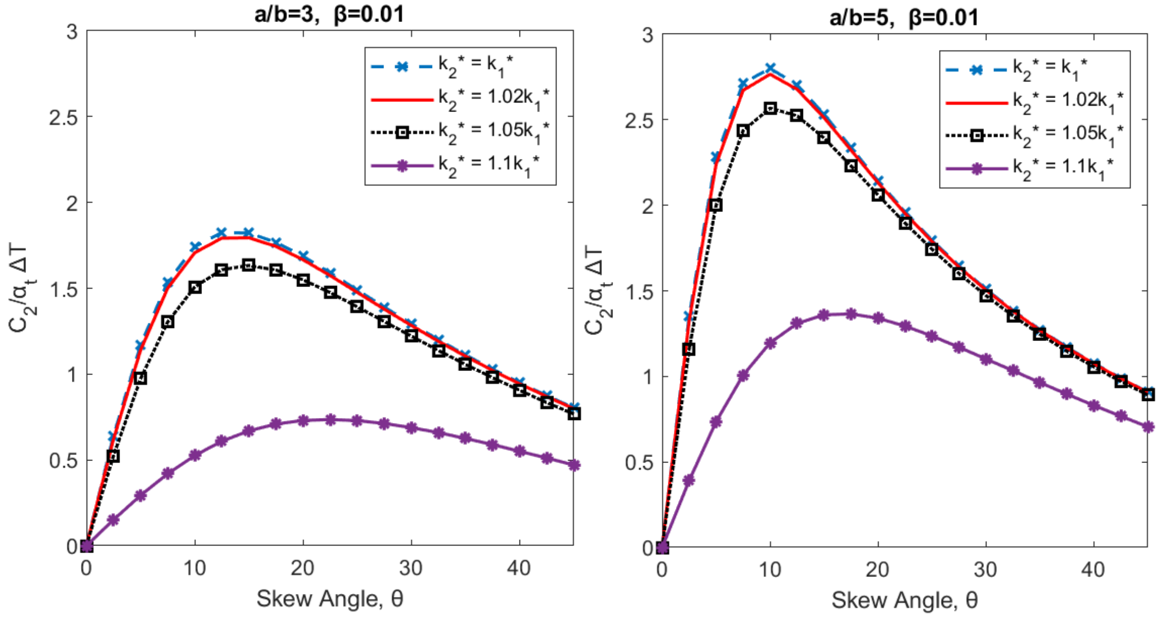

Fig. 9 Variation of C_2 with θ for β=0.01, range of k_2^* and a/b

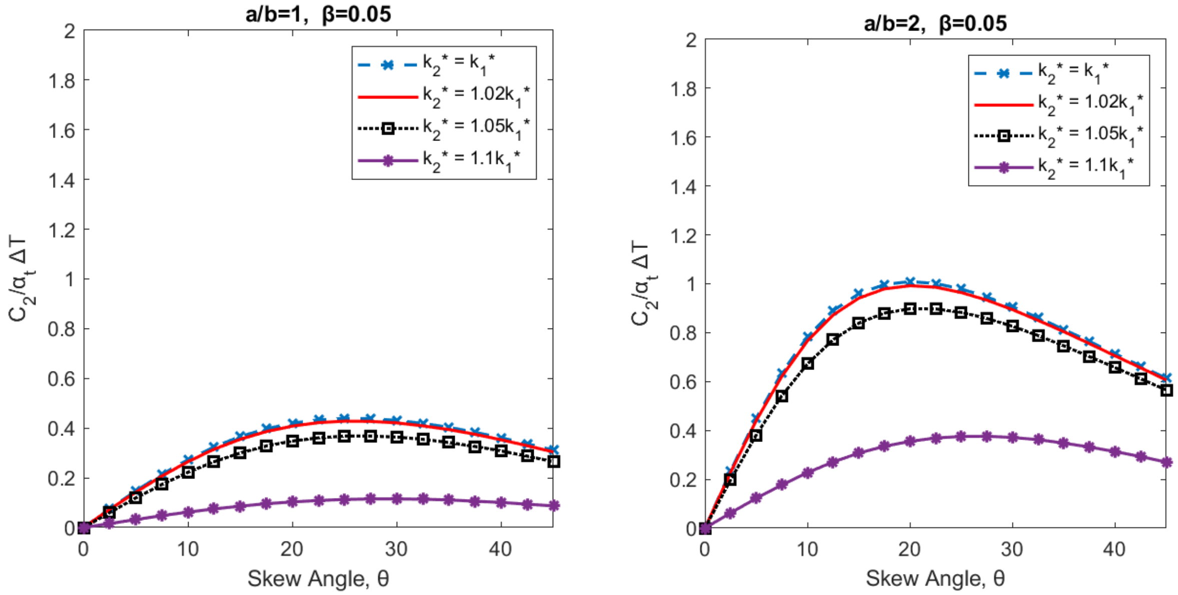

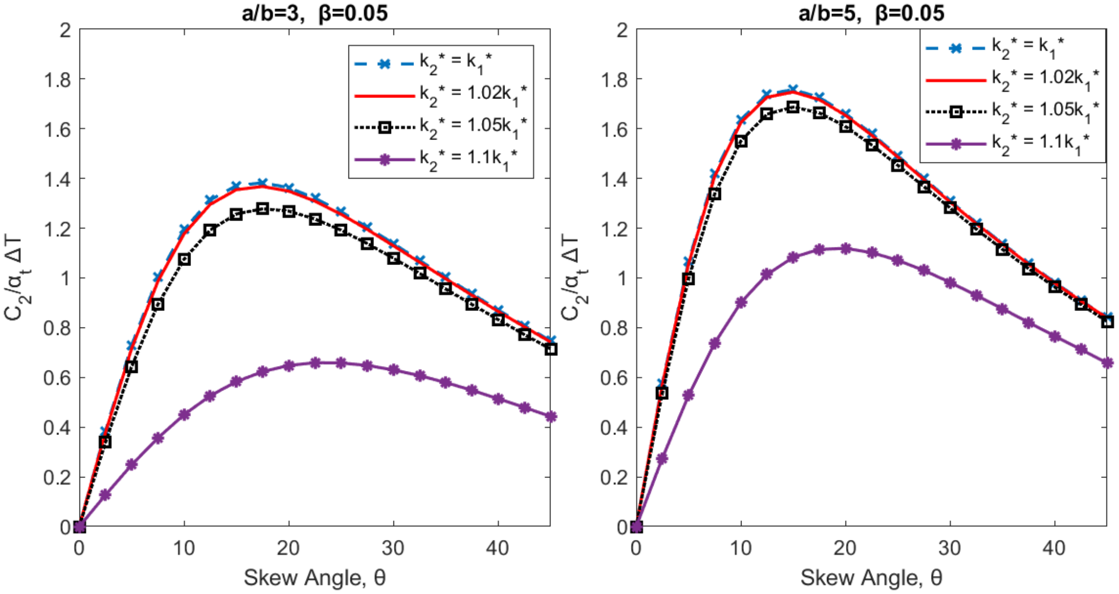

Fig. 10 Variation of C_2 vs. θ for β=0.05 and ranges of $\kappa_2{}^*$ and a/b

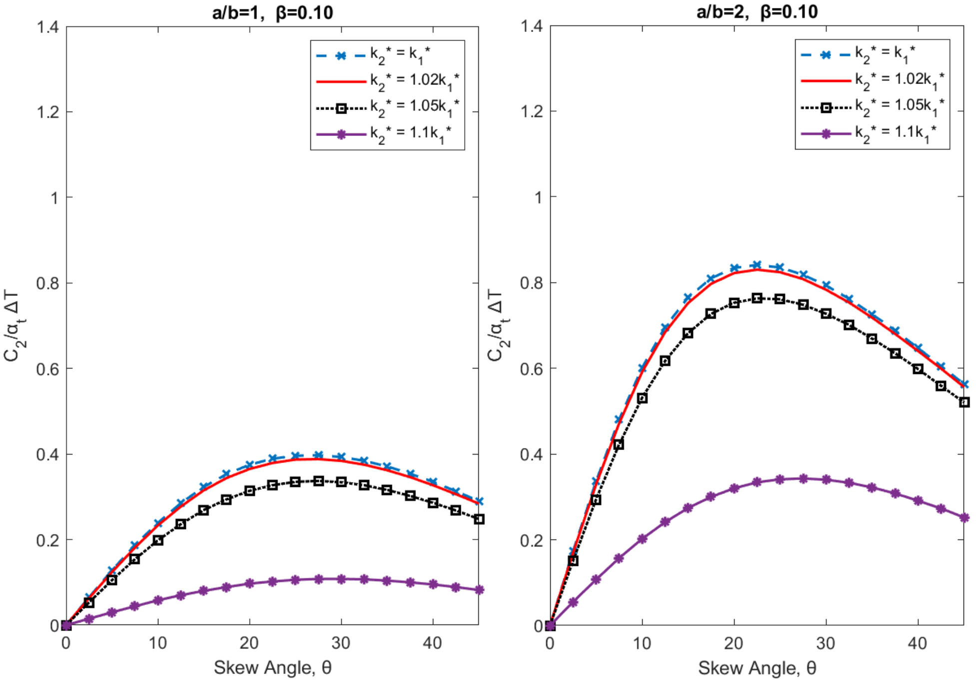

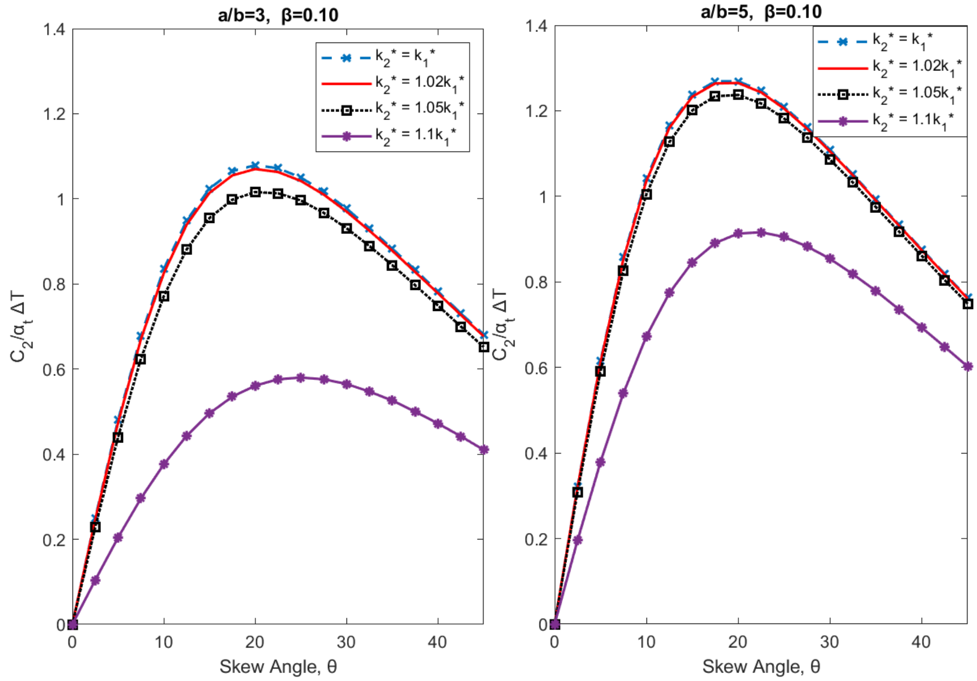

Fig. 11 Variation of C_2 vs. θ for β=0.1 and ranges of k_2^* and a/b

Table 2(a) Variation of C_2 with θ for a/b=1, β =0.05 and ranges of $k_2{}^*$

θ^0	$\frac{C_2}{\alpha_t\,\Delta T}$			
	$k_2^* = k_1^*$	$k_2^* = 1.02k_1^*$	$k_2^* = 1.05k_1^*$	$k_2^* = 1.1k_1^*$
0	0.000	0.000	0.000	0.000
2.5	0.075	0.073	0.060	0.016
5	0.147	0.142	0.119	0.032
7.5	0.214	0.207	0.173	0.048
10	0.273	0.265	0.222	0.062
12.5	0.324	0.315	0.265	0.075
15	0.366	0.355	0.300	0.086
17.5	0.397	0.386	0.328	0.096
20	0.42	0.408	0.348	0.103
22.5	0.433	0.422	0.361	0.109
25	0.439	0.428	0.368	0.113
27.5	0.438	0.427	0.368	0.115
30	0.431	0.421	0.364	0.115
32.5	0.419	0.409	0.355	0.114
35	0.403	0.394	0.342	0.111
37.5	0.383	0.375	0.326	0.106
40	0.361	0.353	0.308	0.101
42.5	0.337	0.329	0.287	0.094
45	0.311	0.304	0.265	0.087

Table 2(b) Variation of C_2 with θ for a/b=2, β =0.05 and ranges of $k_2{}^*$

θ^0	$\frac{C_2}{\alpha_t\ \Delta T}$			
	$k_2^* = k_1^*$	$k_2^* = 1.02k_1^*$	$k_2^* = 1.05k_1^*$	$k_2^* = 1.1k_1^*$
0	0.000	0.000	0.000	0.000
2.5	0.234	0.228	0.197	0.062
5	0.450	0.440	0.381	0.122
7.5	0.636	0.621	0.542	0.177
10	0.783	0.766	0.672	0.227
12.5	0.890	0.872	0.771	0.271
15	0.959	0.941	0.839	0.307
17.5	0.997	0.979	0.880	0.335
20	1.009	0.992	0.898	0.355
22.5	1.001	0.986	0.897	0.369
25	0.979	0.964	0.883	0.375
27.5	0.946	0.933	0.858	0.376
30	0.906	0.894	0.826	0.371
32.5	0.861	0.850	0.788	0.362
35	0.813	0.804	0.746	0.348
37.5	0.764	0.755	0.702	0.332
40	0.714	0.705	0.657	0.313
42.5	0.663	0.656	0.611	0.293
45	0.613	0.606	0.565	0.270

Table 2(c) Variation of C_2 with θ for a/b=3, β =0.05 and ranges of $k_2{}^*$

θ^0	$\frac{C_2}{\alpha_t\ \Delta T}$			
	$k_2^* = k_1^*$	$k_2^* = 1.02k_1^*$	$k_2^* = 1.05k_1^*$	$k_2^* = 1.1k_1^*$
0	0.000	0.000	0.000	0.000
2.5	0.385	0.378	0.339	0.127
5	0.729	0.716	0.644	0.248
7.5	1.002	0.986	0.893	0.356

10	1.195	1.177	1.075	0.450
12.5	1.314	1.296	1.193	0.526
15	1.371	1.355	1.257	0.583
17.5	1.383	1.368	1.278	0.623
20	1.363	1.349	1.269	0.648
22.5	1.321	1.309	1.237	0.659
25	1.266	1.256	1.192	0.658
27.5	1.204	1.195	1.138	0.648
30	1.138	1.129	1.079	0.630
32.5	1.070	1.063	1.018	0.607
35	1.002	0.996	0.955	0.579
37.5	0.936	0.930	0.893	0.548
40	0.871	0.865	0.832	0.514
42.5	0.808	0.803	0.772	0.479
45	0.747	0.742	0.714	0.443

Table 2(d) Variation of C_2 with θ for a/b=5, β =0.05 and ranges of $k_2{}^*$

θ^0	$\frac{C_2}{\alpha_t\ \Delta T}$			
	$k_2^* = k_1^*$	$k_2^* = 1.02k_1^*$	$k_2^* = 1.05k_1^*$	$k_2^* = 1.1k_1^*$
0	0.000	0.000	0.000	0.000
2.5	0.576	0.576	0.537	0.275
5	1.066	1.056	0.997	0.527
7.5	1.421	1.409	1.338	0.738
10	1.637	1.625	1.551	0.901
12.5	1.738	1.727	1.659	1.014
15	1.758	1.748	1.687	1.083
17.5	1.726	1.717	1.664	1.115
20	1.661	1.654	1.609	1.119
22.5	1.580	1.574	1.535	1.102
25	1.491	1.486	1.453	1.071
27.5	1.400	1.395	1.367	1.030
30	1.309	1.305	1.281	0.982

32.5	1.222	1.218	1.196	0.930
35	1.138	1.135	1.115	0.876
37.5	1.058	1.055	1.037	0.821
40	0.982	0.979	0.963	0.766
42.5	0.909	0.907	0.893	0.712
45	0.841	0.839	0.825	0.658

Table 3(a) Variation of C_2 with θ for a/b=1, and β =0.1, and ranges of k_2^*

θ^0	$\frac{C_2}{\alpha_t\ \Delta T}$			
	$k_2^* = k_1^*$	$k_2^* = 1.02k_1^*$	$k_2^* = 1.05k_1^*$	$k_2^* = 1.1k_1^*$
0	0.000	0.000	0.000	0.000
2.5	0.065	0.063	0.053	0.015
5	0.128	0.124	0.105	0.030
7.5	0.187	0.181	0.154	0.044
10	0.239	0.233	0.198	0.058
12.5	0.285	0.277	0.236	0.070
15	0.323	0.315	0.269	0.080
17.5	0.353	0.344	0.294	0.089
20	0.375	0.365	0.314	0.097
22.5	0.389	0.379	0.327	0.102
25	0.396	0.387	0.335	0.106
27.5	0.397	0.388	0.337	0.108
30	0.393	0.384	0.334	0.108
32.5	0.384	0.375	0.327	0.107
35	0.371	0.362	0.316	0.104
37.5	0.354	0.346	0.302	0.100
40	0.335	0.327	0.286	0.095
42.5	0.313	0.306	0.268	0.089
45	0.292	0.284	0.248	0.082

Table 3(b) Variation of C_2 with θ for a/b=2, and β =0.1, and ranges of $k_2{}^*$

θ^0	$\frac{C_2}{\alpha_t \, \Delta T}$			
	$k_2^* = k_1^*$	$k_2^* = 1.02k_1^*$	$k_2^* = 1.05k_1^*$	$k_2^* = 1.1k_1^*$
0	0.000	0.000	0.000	0.000
2.5	0.173	0.169	0.151	0.055
5	0.336	0.329	0.294	0.107
7.5	0.480	0.471	0.422	0.157
10	0.601	0.591	0.531	0.202
12.5	0.696	0.684	0.617	0.241
15	0.765	0.752	0.682	0.274
17.5	0.810	0.797	0.727	0.300
20	0.834	0.822	0.753	0.320
22.5	0.841	0.830	0.763	0.334
25	0.835	0.824	0.761	0.341
27.5	0.818	0.808	0.748	0.343
30	0.793	0.783	0.727	0.340
32.5	0.762	0.753	0.701	0.333
35	0.726	0.718	0.669	0.322
37.5	0.688	0.680	0.635	0.308
40	0.647	0.640	0.598	0.291
42.5	0.605	0.599	0.559	0.273
45	0.563	0.556	0.520	0.252

Table 3(c) Variation of C_2 with for a/b=3, and β =0.1, and ranges of $k_2{}^*$

θ^0	$\frac{C_2}{\alpha_t \, \Delta T}$			
	$k_2^* = k_1^*$	$k_2^* = 1.02k_1^*$	$k_2^* = 1.05k_1^*$	$k_2^* = 1.1k_1^*$
0	0.000	0.000	0.000	0.000
2.5	0.249	0.246	0.228	0.104

5	0.48	0.474	0.440	0.204
7.5	0.678	0.670	0.624	0.296
10	0.835	0.825	0.771	0.376
12.5	0.949	0.939	0.881	0.443
15	1.024	1.014	0.955	0.496
17.5	1.065	1.055	0.998	0.535
20	1.079	1.070	1.016	0.561
22.5	1.072	1.063	1.013	0.576
25	1.050	1.042	0.996	0.580
27.5	1.017	1.010	0.967	0.576
30	0.977	0.970	0.931	0.565
32.5	0.931	0.925	0.889	0.547
35	0.883	0.878	0.844	0.526
37.5	0.833	0.828	0.797	0.500
40	0.782	0.778	0.749	0.472
42.5	0.731	0.727	0.700	0.442
45	0.681	0.677	0.652	0.410

Table 3(d) Variation of C_2 with θ for a/b=5, and β =0.1, and ranges of $k_2{}^*$

θ^0	$\frac{C_2}{\alpha_t\ \Delta T}$			
	$k_2^* = k_1^*$	$k_2^* = 1.02k_1^*$	$k_2^* = 1.05k_1^*$	$k_2^* = 1.1k_1^*$
0	0.000	0.000	0.000	0.000
2.5	0.322	0.320	0.309	0.196
5	0.615	0.612	0.591	0.379
7.5	0.858	0.854	0.826	0.540
10	1.042	1.036	1.005	0.673
12.5	1.166	1.160	1.127	0.774
15	1.238	1.233	1.201	0.846
17.5	1.269	1.264	1.234	0.891
20	1.269	1.265	1.237	0.913
22.5	1.247	1.243	1.217	0.916

25	1.209	1.205	1.182	0.905
27.5	1.162	1.158	1.138	0.883
30	1.108	1.105	1.086	0.854
32.5	1.051	1.049	1.032	0.818
35	0.993	0.990	0.975	0.779
37.5	0.934	0.932	0.918	0.736
40	0.876	0.874	0.861	0.693
42.5	0.819	0.817	0.804	0.648
45	0.763	0.761	0.749	0.602

Table 4(a) Variations of u_n with θ for ranges of β, a/b=1, and $k_1^* = k_2^*$

θ^0	$\beta = 0.01$			$\beta = 0.05$			$\beta = 0.10$		
	$\frac{u_{n\ obtuse}}{a\ \alpha_t\ \Delta T}$	$\frac{u_{n\ center}}{a\ \alpha_t\ \Delta T}$	$\frac{u_{n\ acute}}{a\ \alpha_t\ \Delta T}$	$\frac{u_{n\ obtuse}}{a\ \alpha_t\ \Delta T}$	$\frac{u_{n\ center}}{a\ \alpha_t\ \Delta T}$	$\frac{u_{n\ acute}}{a\ \alpha_t\ \Delta T}$	$\frac{u_{n\ obtuse}}{a\ \alpha_t\ \Delta T}$	$\frac{u_{n\ center}}{a\ \alpha_t\ \Delta T}$	$\frac{u_{n\ acute}}{a\ \alpha_t\ \Delta T}$
0	1.000	1.000	1.000	1.000	1.000	1.000	1.000	1.000	1.000
2.5	1.080	0.995	0.911	1.071	0.996	0.921	1.061	0.996	0.931
5	1.147	0.982	0.816	1.131	0.983	0.836	1.113	0.985	0.857
7.5	1.202	0.960	0.719	1.179	0.964	0.748	1.155	0.967	0.779
10	1.241	0.932	0.622	1.215	0.937	0.660	1.186	0.943	0.700
12.5	1.267	0.898	0.53	1.238	0.906	0.574	1.207	0.915	0.622
15	1.280	0.861	0.433	1.25	0.871	0.493	1.217	0.882	0.548
17.5	1.281	0.822	0.364	1.251	0.834	0.418	1.218	0.848	0.477
20	1.272	0.782	0.293	1.243	0.796	0.349	1.210	0.811	0.412
22.5	1.254	0.743	0.232	1.227	0.758	0.289	1.196	0.775	0.354
25	1.231	0.705	0.179	1.205	0.721	0.236	1.176	0.739	0.301
27.5	1.202	0.668	0.135	1.179	0.685	0.191	1.152	0.703	0.255
30	1.170	0.634	0.098	1.148	0.65	0.153	1.123	0.67	0.216
32.5	1.135	0.602	0.069	1.115	0.618	0.121	1.092	0.637	0.182
35	1.098	0.572	0.047	1.080	0.588	0.096	1.0059	0.607	0.154
37.5	1.059	0.545	0.03	1.043	0.560	0.077	1.024	0.578	0.132
40	1.020	0.520	0.019	1.005	0.534	0.062	0.988	0.551	0.114
42.5	0.980	0.496	0.012	0.967	0.509	0.052	0.951	0.526	0.101
45	0.940	0.475	0.009	0.927	0.487	0.046	0.912	0.502	0.091

Table 4(b) Variations of u_n with θ for ranges of β, a/b=3, and $k_1^* = k_2^*$

θ^0	β = 0.01			β = 0.05			β = 0.10		
	$\frac{u_{n\,obtuse}}{a\,\alpha_t\,\Delta T}$	$\frac{u_{n\,center}}{a\,\alpha_t\,\Delta T}$	$\frac{u_{n\,acute}}{a\,\alpha_t\,\Delta T}$	$\frac{u_{n\,obtuse}}{a\,\alpha_t\,\Delta T}$	$\frac{u_{n\,center}}{a\,\alpha_t\,\Delta T}$	$\frac{u_{n\,acute}}{a\,\alpha_t\,\Delta T}$	$\frac{u_{n\,obtuse}}{a\,\alpha_t\,\Delta T}$	$\frac{u_{n\,center}}{a\,\alpha_t\,\Delta T}$	$\frac{u_{n\,acute}}{a\,\alpha_t\,\Delta T}$
0	1.000	1.000	1.000	1.000	1.000	1.000	1.000	1.000	1.000
2.5	1.184	0.971	0.758	1.111	0.982	0.854	1.071	0.974	0.905
5	1.286	0.894	0.503	1.177	0.933	0.689	1.115	0.903	0.794
7.5	1.307	0.791	0.274	1.198	0.861	0.524	1.131	0.806	0.675
10	1.272	0.682	0.092	1.182	0777	0.373	1.122	0.701	0.557
12.5	1.204	0.581	-0.041	1.141	0.692	0.243	1.095	0.600	0.447
15	1.123	0.494	-0.134	1.084	0.611	0.138	1.054	0.511	0.348
17.5	1.04	0.422	-0.196	1.021	0.538	0.054	1.006	0.435	0.262
20	0.961	0.363	-0.235	0.957	0.474	-0.010	0.953	0.371	0.188
22.5	0.889	0.315	-0.259	0.895	0.418	-0.058	0.900	0.319	0.127
25	0.825	0.277	-0.272	0.837	0.371	-0.095	0.849	0.276	0.077
27.5	0.768	0.245	-0.277	0.784	0.331	-0.121	0.800	0.241	0.035
30	0.717	0.220	-0.278	0.735	0.297	-0.141	0.754	0.211	0.002
32.5	0.673	0.199	-0.275	0.691	0.269	-0.154	0.711	0.187	-0.025
35	0.634	0.182	-0.271	0.652	0.244	-0.164	0.672	0.167	-0.047
37.5	0.599	0.168	-0.264	0.617	0.224	-0.169	0.636	0.150	-0.064
40	0.569	0.156	-0.257	0.585	0.206	-0.173	0.604	0.135	-0.077
42.5	0.542	0.147	-0.249	0.557	0.192	-0.174	0.574	0.123	-0.087
45	0.518	0.139	-0.240	0.531	0.179	-0.173	0.547	0.113	-0.095

Table 4(c) Variations of u_n with θ for ranges of β, a/b=5, and $k_1^* = k_2^*$

θ^0	β = 0.01			β = 0.05			β = 0.10		
	$\frac{u_{n\,obtuse}}{a\,\alpha_t\,\Delta T}$	$\frac{u_{n\,center}}{a\,\alpha_t\,\Delta T}$	$\frac{u_{n\,acute}}{a\,\alpha_t\,\Delta T}$	$\frac{u_{n\,obtuse}}{a\,\alpha_t\,\Delta T}$	$\frac{u_{n\,center}}{a\,\alpha_t\,\Delta T}$	$\frac{u_{n\,acute}}{a\,\alpha_t\,\Delta T}$	$\frac{u_{n\,obtuse}}{a\,\alpha_t\,\Delta T}$	$\frac{u_{n\,center}}{a\,\alpha_t\,\Delta T}$	$\frac{u_{n\,acute}}{a\,\alpha_t\,\Delta T}$
0	1.000	1.000	1.000	1.000	1.000	1.000	1.000	1.000	1.000
2.5	1.211	0.94	0.67	1.089	0.974	0.859	1.049	0.985	0.921
5	1.255	0.797	0.339	1.117	0.903	0.689	1.066	0.943	0.819
7.5	1.185	0.637	0.09	1.093	0.806	0.519	1.053	0.879	0.706
10	1.067	0.499	-0.070	1.033	0.701	0.368	1.015	0.804	0.592
12.5	0.945	0.391	-0.163	0.956	0.60	0.244	0.963	0.724	0.485
15	0.835	0.311	-0.214	0.875	0.511	0.147	0.902	0.645	0.389
17.5	0.741	0.251	-0.239	0.797	0.435	0.073	0.838	0.572	0.306
20	0.663	0.207	-0.249	0.725	0.371	0.018	0.776	0.506	0.236
22.5	0.598	0.173	-0.252	0.661	0.319	-0.023	0.717	0.447	0.177
25	0.544	0.147	-0.249	0.605	0.276	-0.053	0.662	0.395	0.128
27.5	0.498	0.127	-0.243	0.556	0.241	-0.075	0.613	0.351	0.089
30	0.460	0.112	-0.237	0.514	0.211	-0.091	0.568	0.312	0.056
32.5	0.428	0.099	-0.229	0.477	0.187	-0.103	0.528	0.279	0.029
35	0.400	0.089	-0.222	0.444	0.167	-0.111	0.492	0.250	0.007
37.5	0.376	0.081	-0.214	0.416	0.150	-0.117	0.460	0.225	-0.011
40	0.355	0.075	-0.206	0.391	0.135	-0.121	0.432	0.203	-0.026
42.5	0.337	0.069	-0.199	0.370	0.123	-0.124	0.406	0.184	-0.038
45	0.322	0.065	-0.192	0.350	0.113	-0.125	0.384	0.168	-0.048

Conclusions

There is a contrast in the behavior of the acute and obtuse corners of the plate. At the obtuse corners, as θ increases, the normal displacement increases, passes through a maximum and then decreases gradually. On the other hand, at the acute corners, as θ increases, the normal displacement decreases and by increasing a/b the normal displacement will move be negative. This means the normal displacement at the acute corner will move in the direction opposite that of the obtuse corner. When β is increased to the reversal in displacement is not observed. The reason for this shift is that as β is increased, the peak value of C_2 decreased (see Fig. 5), therefore the influence of rotation on the displace configuration is less significant. These results are consistent with the field monitoring studies reported Sanford,1993.

As figures 7-9 show there is a contrast in the behavior of the acute and obtuse corners of the plate. At the obtuse corners, as θ increases, the normal displacement increases, passes through a maximum and then decreases gradually. On the other hand at the acute corners, as θ increases, the normal displacement decreases and by increasing a / b the normal displacement will move be negative. This means the normal displacement at the acute corner will move in the direction opposite that of the obtuse corner. When β is increased to the reversal in displacement is not observed. The reason for this shift is that as β is increased, the peak value of C_2 decreased (see Fig. 5), therefore the influence of rotation on the displace configuration is less significant.

Figures 10-12 show the in-plane rotation of the plate, C_2 with the skew angle, θ caused by thermal expansion for a ranges of a / b =1, 2, 3,5 and β=0.01, 0.05, 0.1 and increase in the restraining spring on the boundary #2, $k_2^* / k_1^* =$ 1, 1.02,1.05,1.1. As θ increases, C_2 increases from zero passing through a maximum, then decreases more gradually. This peak behavior is less pronounced for a smaller a / b and /or a larger β. Tables 3(a)-(c) shows similar results.

Figures 13 illustrates the ratio of normal displacement at the acute corner to normal displacement at the obtuse corner of the plate ($u_{n\ acute} / u_{n\ Obtuse}$) with θ caused by thermal expansion of ΔT for ranges of a / b =1, 2, 3,and β= 0.05 and 0.1and $k_2^* / k_1^* =$ 1, 1.05

Figures 14 illustrates the ratio of normal displacement at the acute corner to normal displacement at the obtuse corner of the plate ($u_{n\ acute} / u_{n\ Obtuse}$) with θ caused by thermal expansion of ΔT for ranges of a / b =1, 2, 3,and β= 0.05 and 0.1and $k_2^* / k_1^* =$ 1, 1.1

The analytical study of the rigid plate revealed that, under thermal loading, the skewed rigid plate experiences a rotation, C_2 , in the horizontal plane about the origin of the plate.

The rotation of the plate depends on the skew angle, θ, the length to width ratio of the plate, a/b, the relative stiffness parameter, β (the ratio of the stiffness of the abutment and surrounding soil tangent to the skew to the stiffness of the abutment and surrounding soil normal to the skew) where β is major contributor.

The equations derived and the plots created based on the findings of this analytical study will provide bridge engineers with preliminary design guidelines to predict the response of skew IABs for a bridge for a given condition they are designing such as skew angle, the ratio of the length to width of the deck, wing-wall type, lack of symmetry at the abutments because of variation of soil conditions or pile stiffness at the abutments.

NOTATION

The following symbols are used in this paper

a = ½ plate length

b = ½ plate width

BDY1= boundary # 1, line 1-4

BDY2= boundary # 2, line 2-3

C_2 = in-plane rotation of the rigid plate about the origin

k^* = reference normal spring stiffness coefficient at the corners

k_1^* = normal spring stiffness coefficient at corners of boundary #1

k_2^* = normal spring stiffness coefficient at corners of boundary #2

u_n = normal displacement

u_s = tangent displacement

$u_{n\ acute}$ = normal displacement at acute corners of the plate

$u_{n\ obtuse}$ =normal displacement at obtuse corners of the plate

$u_{n\ center}$ =normal displacement at the center line of the plate boundary

ΔT = Uniform temperature expansion

α_t = thermal expansion coefficient

$\beta = \frac{k_s^*}{k_n^*}$ = ratio of the tangential to normal stiffness coefficients

θ = skew angle of the rigid plate

References

Alqarawi, A., Leo, C., Liyanapathirana, D. 2020. "Effects of wall movements on performance of integral abutment bridges." *International Journal of Geomechanics,* 20(2):04019157.

Davids, W., Sandford, T. , neé Hartt, S., DeLano, J., and Lyons, C. 2010." Field-measured response of an integral abutment bridge with short steel H-piles." *Journal of Bridge Eng.,* 15(1): 32-43.

Deng, Y. Phares, B. M., Greimann, L. Shryack, G. L. Hoffman, J. J. 2015. "Behavior of curved and skewed bridges with integral abutments," *Journal of Constructional Steel Research,* 109:115–136.

Dicleli, M. and Albhaisi, S. 2005. "Analytical formulation of maximum length of integral bridges supported on steel h-piles driven in sand." *Engineering Structures,* 25: 1491–1504.

Dicleli, M. and Albhaisi, S. 2004. " Performance of abutment–backfill system under thermal variations in integral bridges built on clay." *Engineering Structures*, 26: 949–962.

Faraji, S., Ting, J., Crovo, D., and Ernst, J. 2001. "Non-linear analysis of integral bridges: finite element model**."** *Geotech and Geoenviron Engineering*, 127(5):454-61.

Faraji-Hennessey, S. Parameters Controlling the In-plane Rotation of Skewed Integral Abutment Bridges Caused by Thermal Loading: An Analytical Study Engineering Institute (BEI-2025) Conference proceedings July 2025

Khodair, Y. A. Hassiotis, S. 2013." Rigidity of abutments in integral abutment bridges." *Structure and Infrastructure Engineering* , 9(2): 201–209.

Khard, R. Shreedhar, R. 2014. "Analysis of integral abutment bridge by grillage method." *NBM& CW,* 172–183.

Perić, D., Miletić, M., Shah, B.R., Esmaeily, A., Wang, H. 2016." Thermally induced soil structure interaction in the existing integral bridge." *Engineering Structures,* 106: 484–494.

Sanford, T. and Elgaaly, M. 1993. "Skew effects on backfill pressures at frame bridge abutments." *Transportation research record,* 1415: 1-11

Wright, Beth, LaFave, James, Fahnestock, Larry, Jarrrett, Riddle, Joseph, and Svatora, Jeffery, S. "Field monitoring of skewed integral abutment bridges." *6th international conference on advancedes in experimental structural engineering, 2015*

Xu, S., Kannangara, K., Taciroglu,E. 2018. "Analysis of the stress distribution across a retaining wall backfill." *Computers and Geotechnics,* 103: 13–25.

Zordan, T., Briseghella, B. Lan, C. 2011. " Parametric and pushover analyses on integral abutment bridge." *Engineering Structures*, 3392: 502–51

Zhao, Qiuhong, Dong, Shuo, and Wang, Quingwei. 2021. "Seismic Response of Skewed Integral Abutment Bridges under Near-Fault Ground Motions, Including Soil–Structure Interaction."*APPl. Sci*, 11(7), 3217

Chapter 2

Preliminary Design of Piles in Integral Abutment Bridges (IABs)

Introduction

Integral abutment bridges (IABs) are single-span or multi-span continuous deck-type bridges having the deck integral with the walls of the abutments and the walls supported on single rows of flexible piles. The thermal expansion of the deck is a major contributor to the total stress in integral abutment bridges. The reason is that, with an increase in temperature, the abutment walls move into the backfill soil and the interaction with the soil (passive pressure) will greatly impact the longitudinal forces that must be carried by the superstructure well as by the substructure. Which it will lend itself to longitudinal displacement of girders and abutment walls, and lateral displacement of abutment piles.

This Chapter presents a parametric study to evaluate the impact of parameters such as soil profile, pile size, orientation, axial load, imposed head displacement, and boundary conditions on moment profile of the pile, Using LPILE.

Methodology

Selected Soil profiles

Geotechnical properties were derived from soil report data for representative bridges in Massachusetts and Vermont. Three soil profile types were considered:

- **Soil Type 1(a):** Predrilled sand profile (looser upper layers)
- **Soil Type 1(b):** No-predrilled sand profile (medium to dense sand)
- **Soil Type 2:** Sand over weak rock
- **Soil Type 3:** Sand over clay layers

Each profile includes depth-dependent unit weight, friction angle or cohesion, and modulus of subgrade reaction, as presented in Tables 1–3 of Appendix A.

Selected Sample steel pile sections used for analysis

- **HP 12×74** (typical for short-span IABs)
- **W12×152** (typical for long-span IABs)

p–y Curve Development

Nonlinear p–y curves were created for sample piles (HP12x74 and W12x152) surrounded by selected soil profiles: type 1(a), type 1(b), type (2) and type (3). See Figures A.1-A.16 of Appendix A.

Material Properties

Material properties of the steel piles included a yield strength of 50 ksi and a modulus of elasticity of 29,000 ksi.

Analysis of HP and W piles under thermal loading, dead load, and live load

Analyses were conducted by using LPILE 10 software, imposing varying lateral pile head displacements (0.05 in -1.5 in), combined with varying axial loads (50 kip, 100 kip, and 150 kip), pile orientation (weak and strong), varying Pile head boundary conditions (Fully fixed, pin, and rotational stiffness). The pile fixity point was defined as the depth at which lateral displacement reduced to less than 0.01 in. LPILE-generated plots and tables were created. See Figures B.1-B.26 and Tables B.1-B.26 of Appendix B.

The following figure shows the sign convention for positive: displacement, axial force, shear, and moment in LIPE 10.0

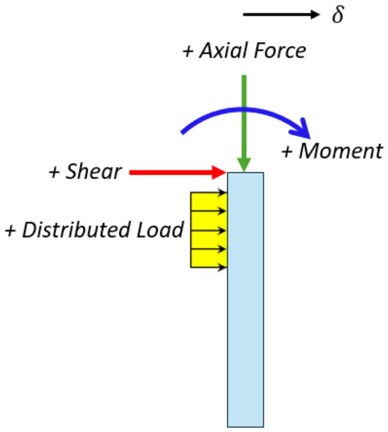

Summary and Conclusion

This parametric study provides a detailed evaluation of pile behavior in integral abutment bridges using nonlinear soil–structure interaction modeling provided by LPILE. The analysis demonstrates that pile head displacement, pile orientation, soil stiffness, and boundary conditions dominate pile response, while axial load plays a minimal role. Strong-axis pile orientation and stiffer soil conditions significantly increase bending demands and fixity depth, which has direct implications for IAB design limits. The results emphasize the need for careful consideration of pile orientation, installation method, and pile head connection detailing in IAB systems.

Variation of axial force of the HP or W piles has negligible impact on fixity points

Variation of axial force of the HP or W pile has negligible impact on pile maximum moment or maximum shear.

Increment in pile-head lateral displacement will increase the length of fixity point.

Increment in pile-head lateral displacement will increases the length of fixity point

Piles oriented in strong axis will have increased fixity length compared to weak axis

- p–y curves depend on pile size and soil profile, not pile orientation
- Axial load has negligible influence on fixity depth and bending moments
- Increasing pile head displacement increases fixity depth and moment demand
- Strong-axis orientation significantly increases pile stiffness and bending
- No-predrilled (stiffer) soils reduce fixity depth but increase moments
- Larger pile sections experience substantially higher bending demands
- Pile head boundary condition strongly affects fixity and moment response

Overall, the results offer a practical and reliable framework for estimating pile response in IABs during preliminary design stages, reducing reliance on full bridge-system modeling while maintaining engineering accuracy.

.

Appendix

A

Geotechnical Details for soil profiles surrounding HP and W piles

Table A.1 Soil profiles type 1(a) (Predrilled) and 1(b)

Soil Type	Layer Depth	Geotechnical Values
Sand	0.0’ – 8.0’	Unit weight (γ): 100 Pcf, Friction Angle (Φ): 30, Modulus of surcharge (k): 250 pci (pre-drilled)
		Unit weight (γ): 125 Pcf, Friction Angle (Φ): 38, Modulus of surcharge (k): 250 pci (No-predrilled)
Sand	8.0’ – 14.5’	Unit weight (γ): 120 Pcf, Friction Angle (Φ): 40, Modulus of surcharge (k): 125 pci
Sand	14.5’ – 36.0’	Unit weight (γ): 75 Pcf, Friction Angle (Φ): 38, Modulus of surcharge (k): 125 pci
Sand	36.0’- 50.0’	Unit weight (γ): 75 Pcf, Friction Angle (Φ): 40, Modulus of surcharge (k): 125 pci

Table A.2 Soil profile type 2

Soil Type	Layer Depth	Geotechnical Values
Sand	0’ – 12’	Unit weight (γ): 125 Pcf, Friction Angle (Φ): 38, Modulus of surcharge (k): 120 pci
Sand	12’ – 19’	Unit weight (γ): 120 Pcf, Friction Angle (Φ): 32, Modulus of surcharge (k): 40 pci
Sand (GW)	19’ – 20’	Unit weight (γ): 58 Pcf, Friction Angle (Φ): 32, Modulus of surcharge (k): 40 pci
Weak Rock	20’- 23’	Unit weight (γ): 88 Pcf, Strain Factor (k rm): 0.00125, Uniaxial comp. strength (qu): 1200 pci, Modulus of rock mass (k): 600000 pci

Table A.3 Soil profile type 3

Soil Type	Layer Depth	Geotechnical Values

Sand	0' – 18'	Unit weight (γ): 125 Pcf, Friction Angle (Φ): 32, Modulus of surcharge (k): 90 pci
Clay	18' – 42'	Unit weight (γ): 115 Pcf, Undrained Cohesion (c): 1500 pcf, Strain factor: 0.005
Clay (GW)	42' – 65'	Unit weight (γ): 55 Pcf, Undrained Cohesion (c): 1500 pcf, Strain factor: 0.005

P-y Cures HP and W Piles

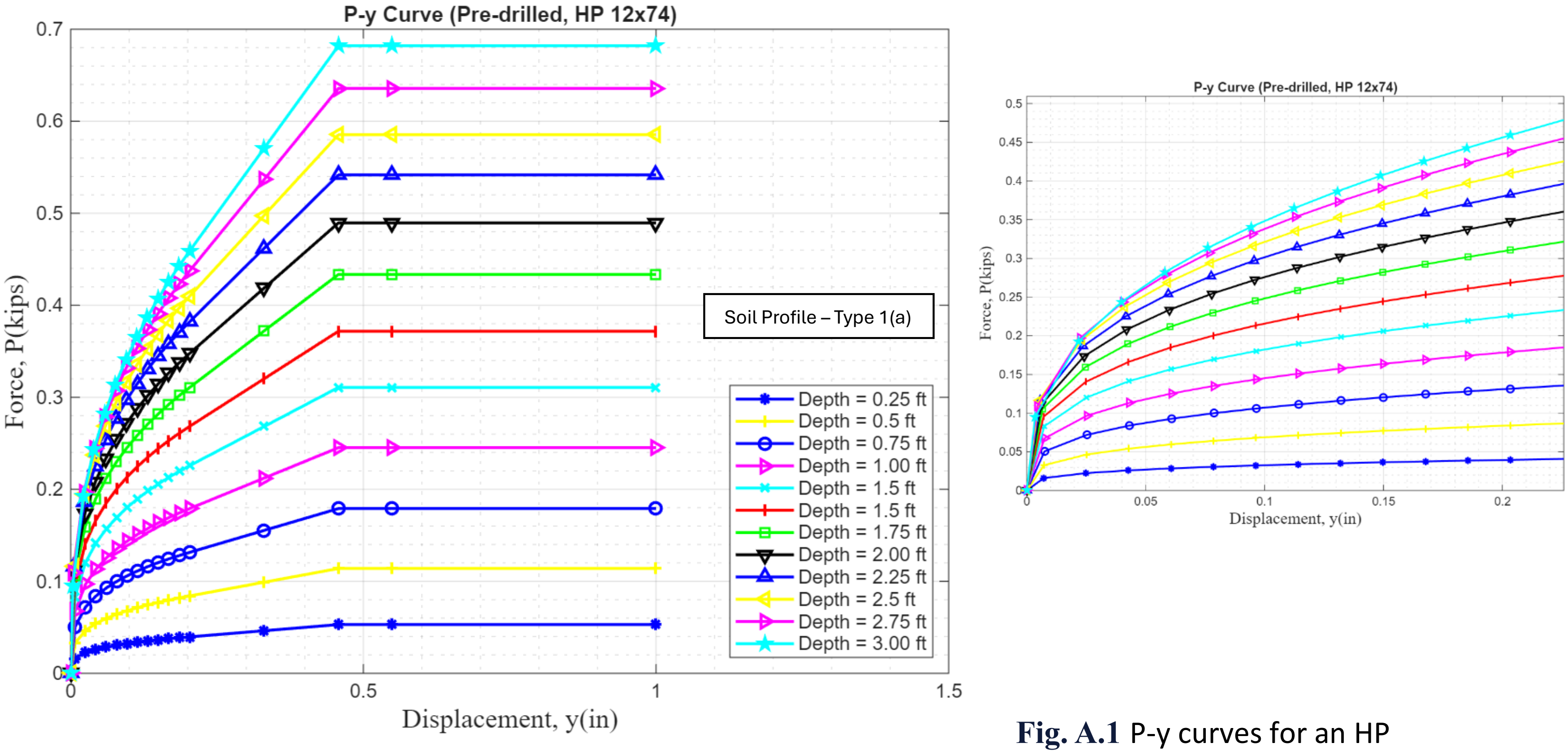

Fig. A.1 P-y curves for an HP 12x74 pile for soil profile type 1(a), with 3-inch nodal increments

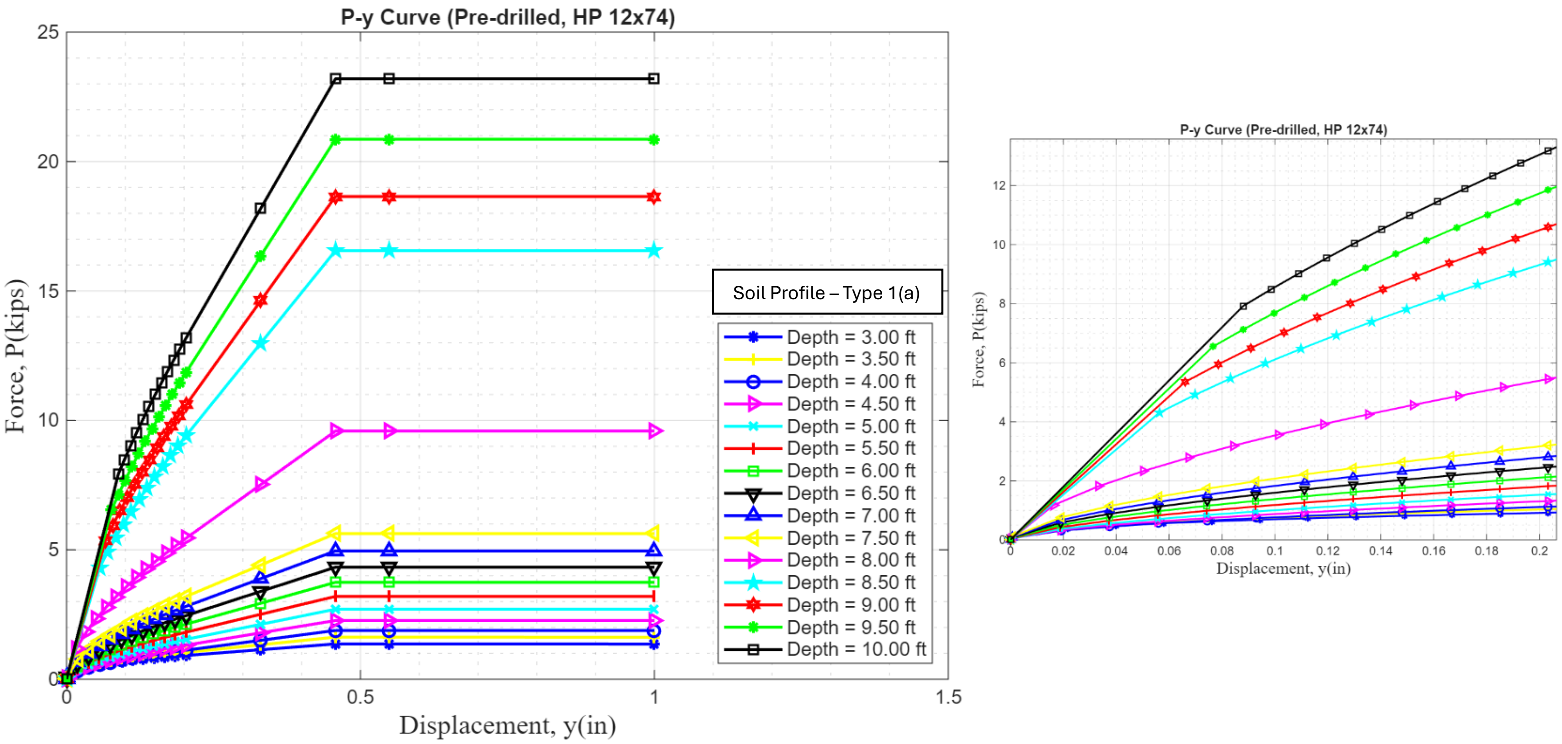

Fig. A.2 P-y curves for an HP 12x74 pile for soil profile type 1(a), with 3-inch nodal increments

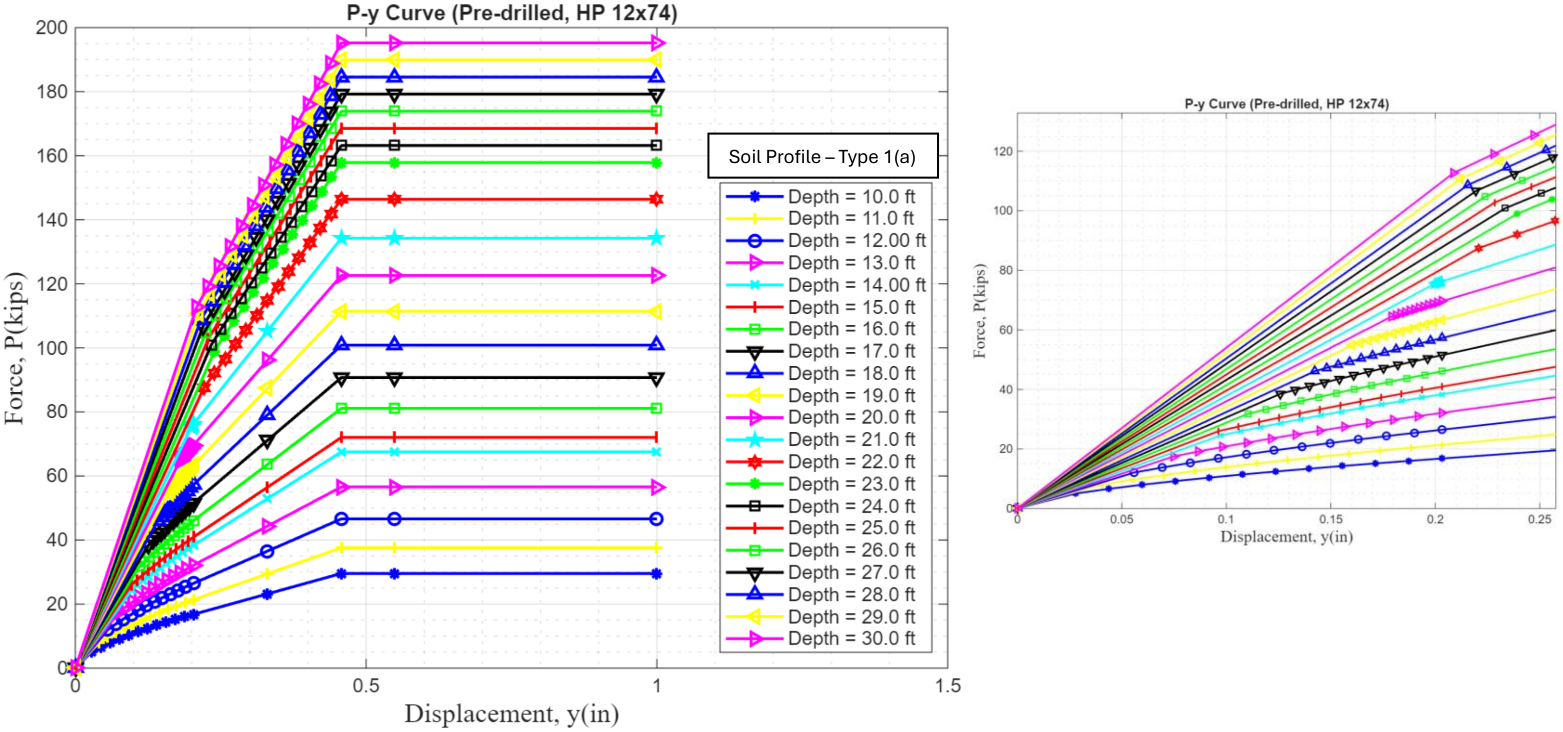

Fig. A.3 P-y curves for an HP 12x74 pile for soil profile type 1(a), with 12-inch nodal increments

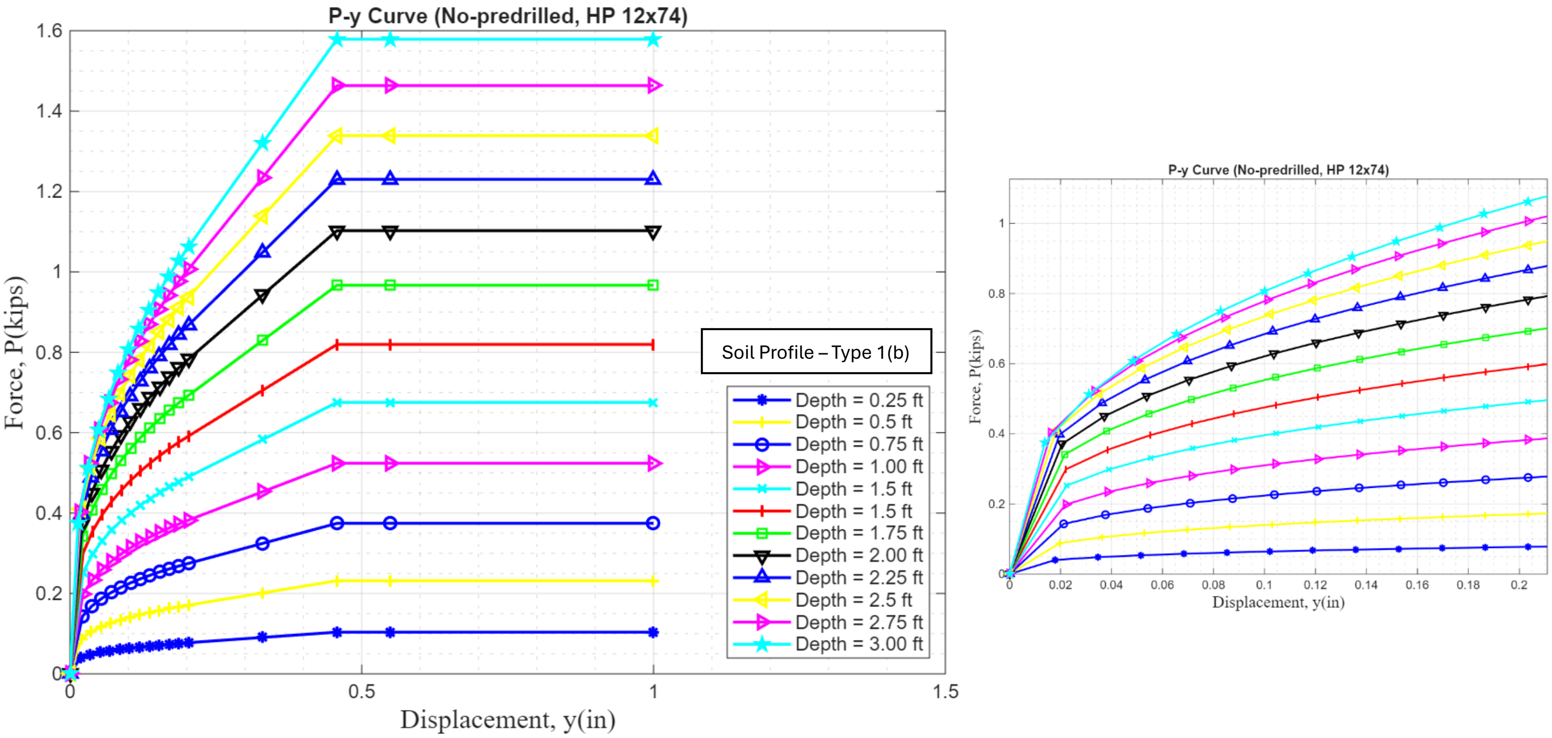

Fig. A.4 P-y curves for an HP 12x74 pile for soil profile type 1(b), with 3-inch nodal increments

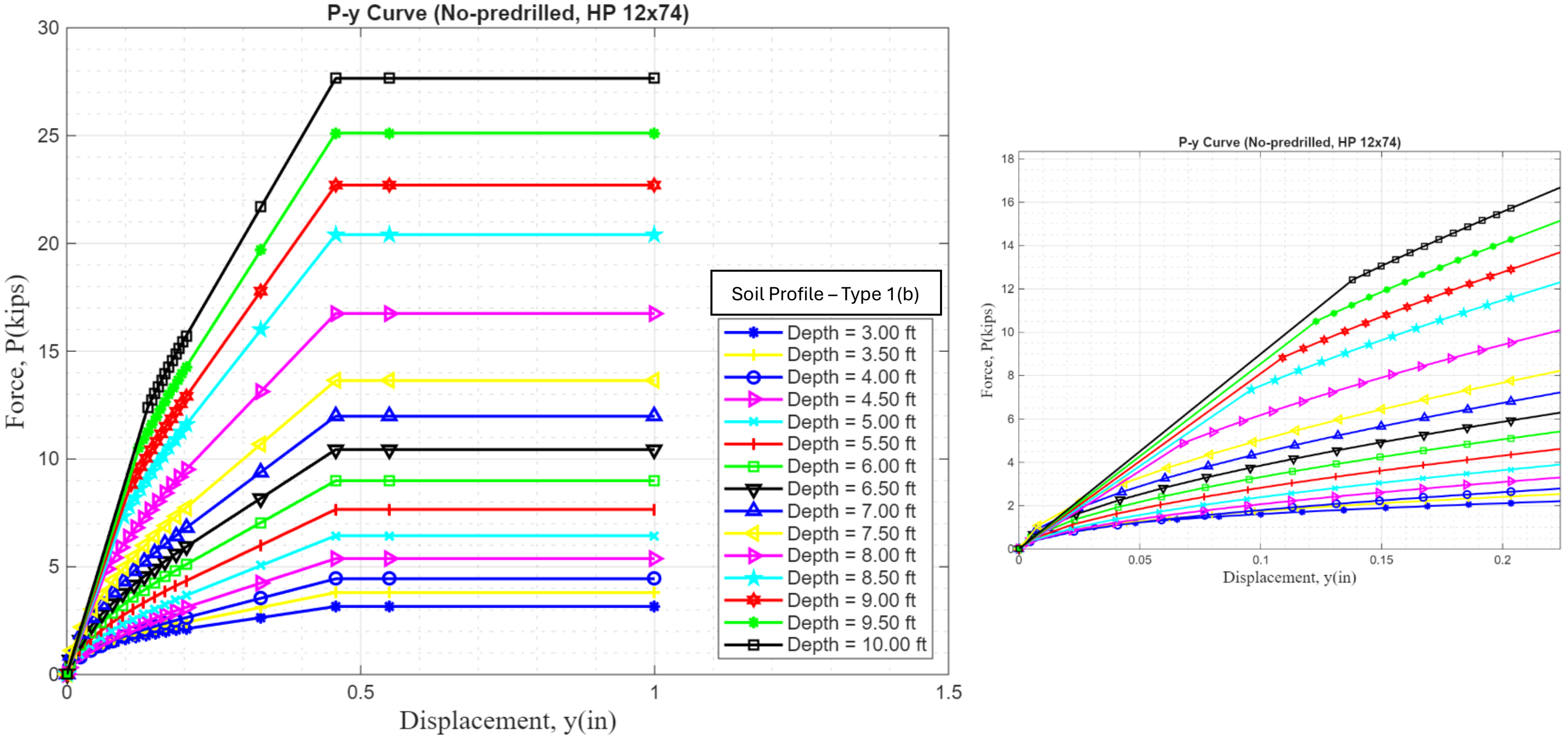

Fig. A.5 P-y curves for an HP 12x74 pile for soil profile type 1(b), with 6-inch nodal increments

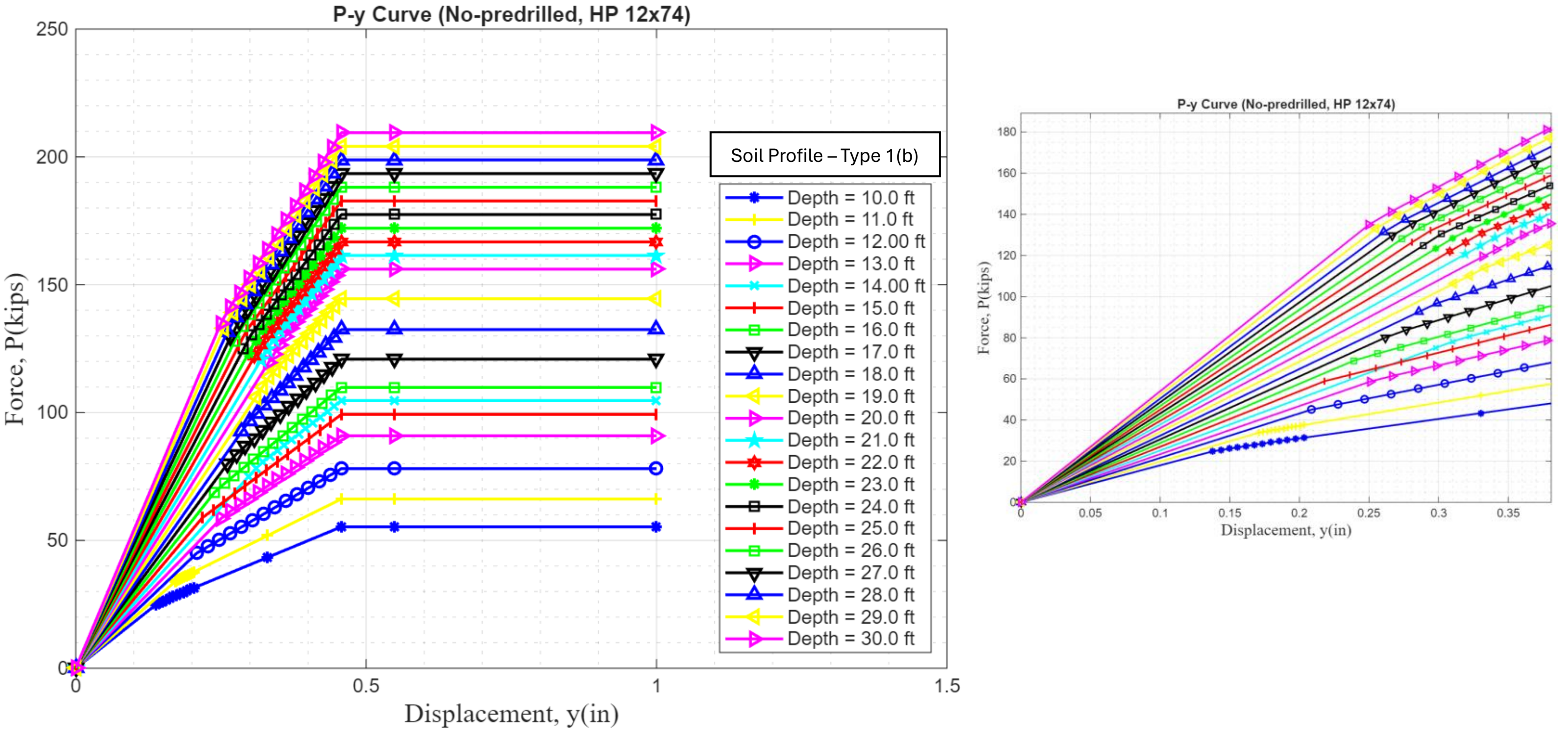

Fig. A.6 P-y curves for an HP 12x74 pile for soil profile type 1(b), with 12-inch nodal

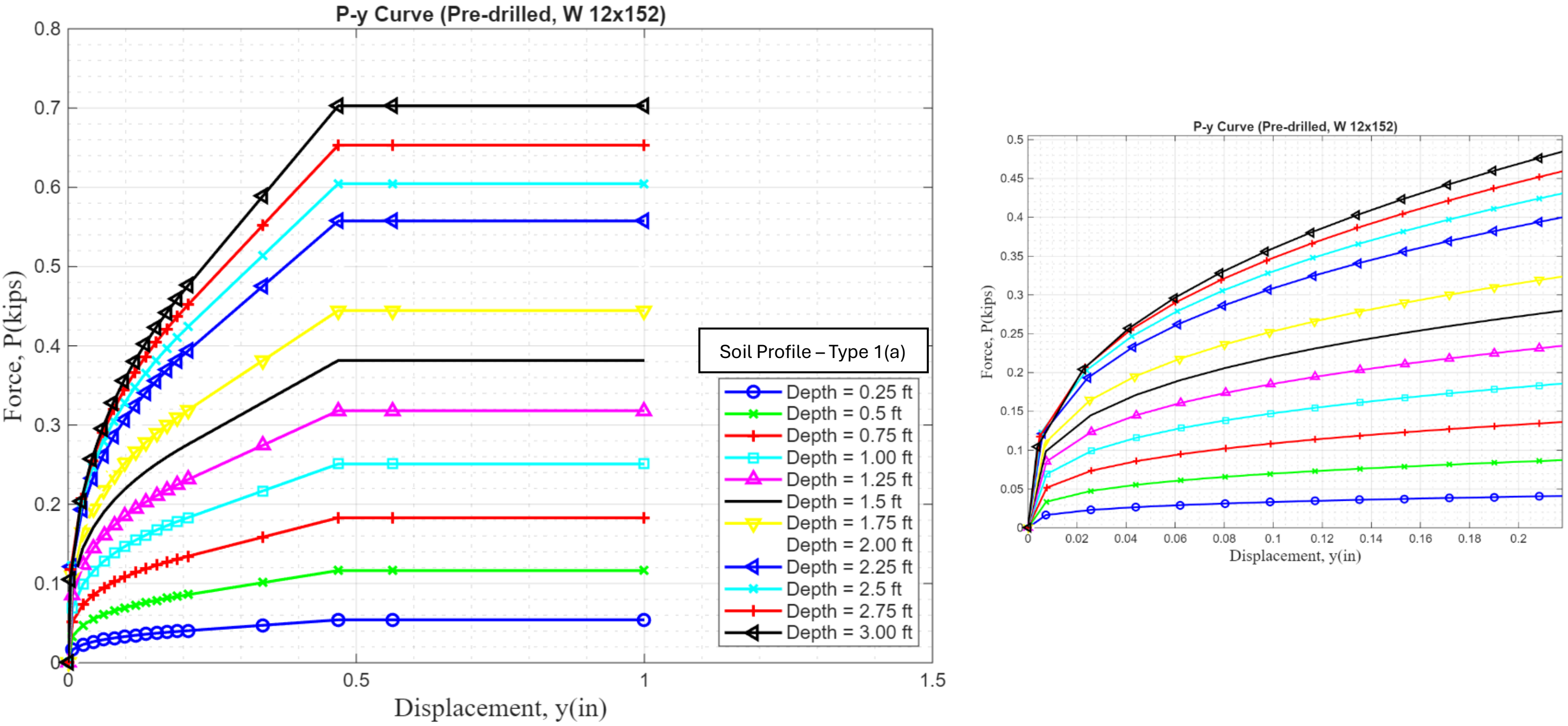

Fig. A.7 P-y curves for a W12x152 pile for soil profile type 1(a), with 3-inch nodal increments

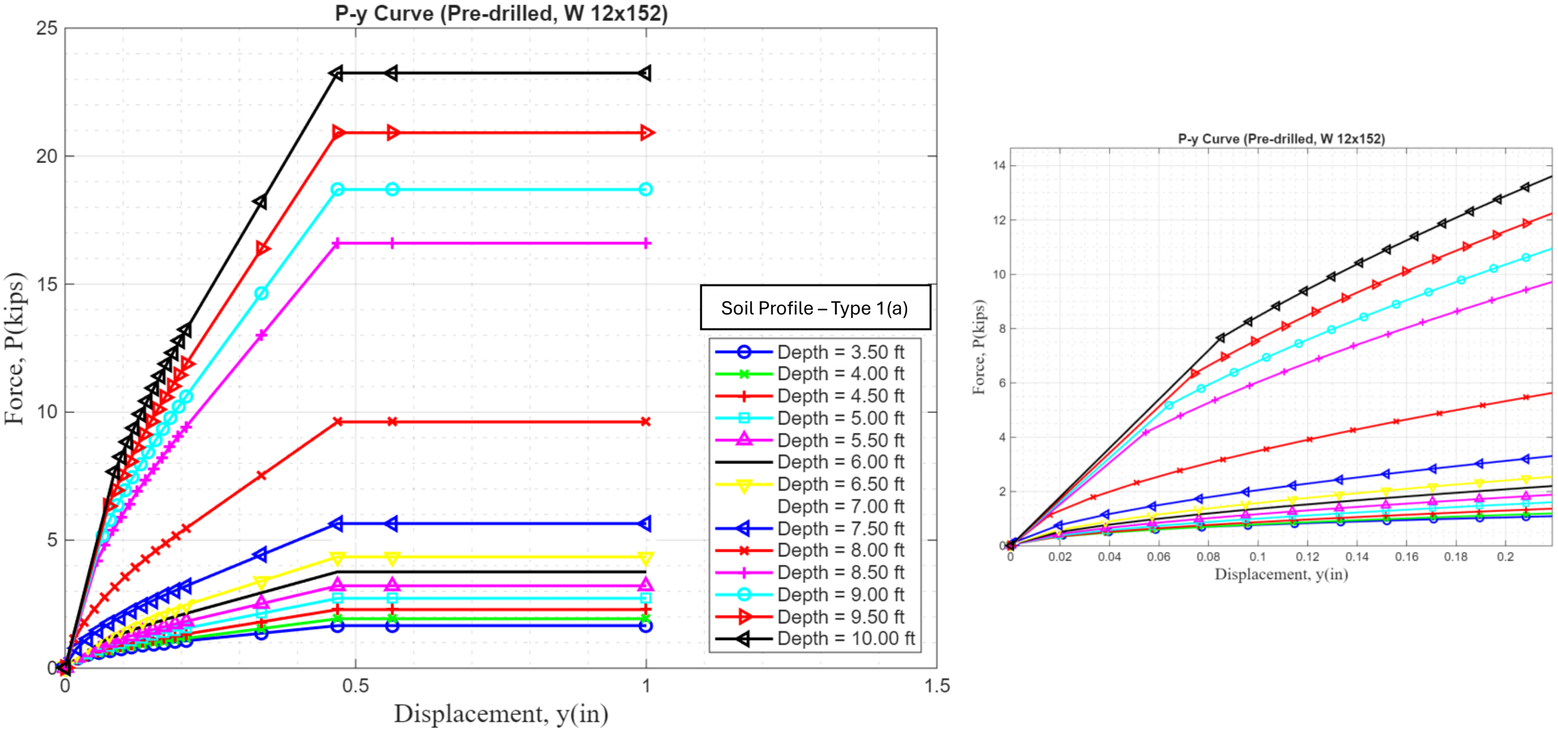

Fig. A.8 P-y curves for a W12x152 pile for soil profile type 1(a), with 6-inch nodal increments

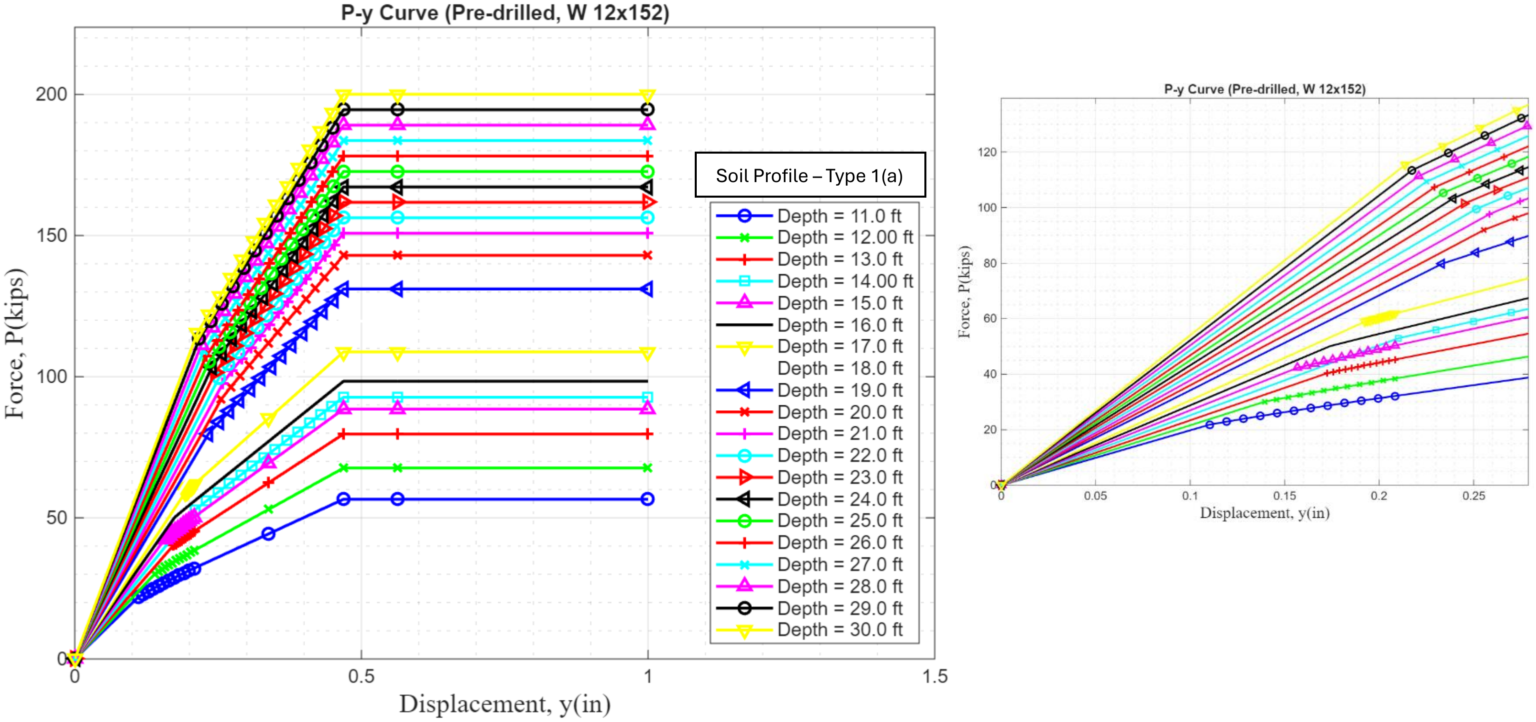

Fig. A.9 P-y curves for a W12x152 pile for soil profile type 1(a), with 12-inch nodal increments

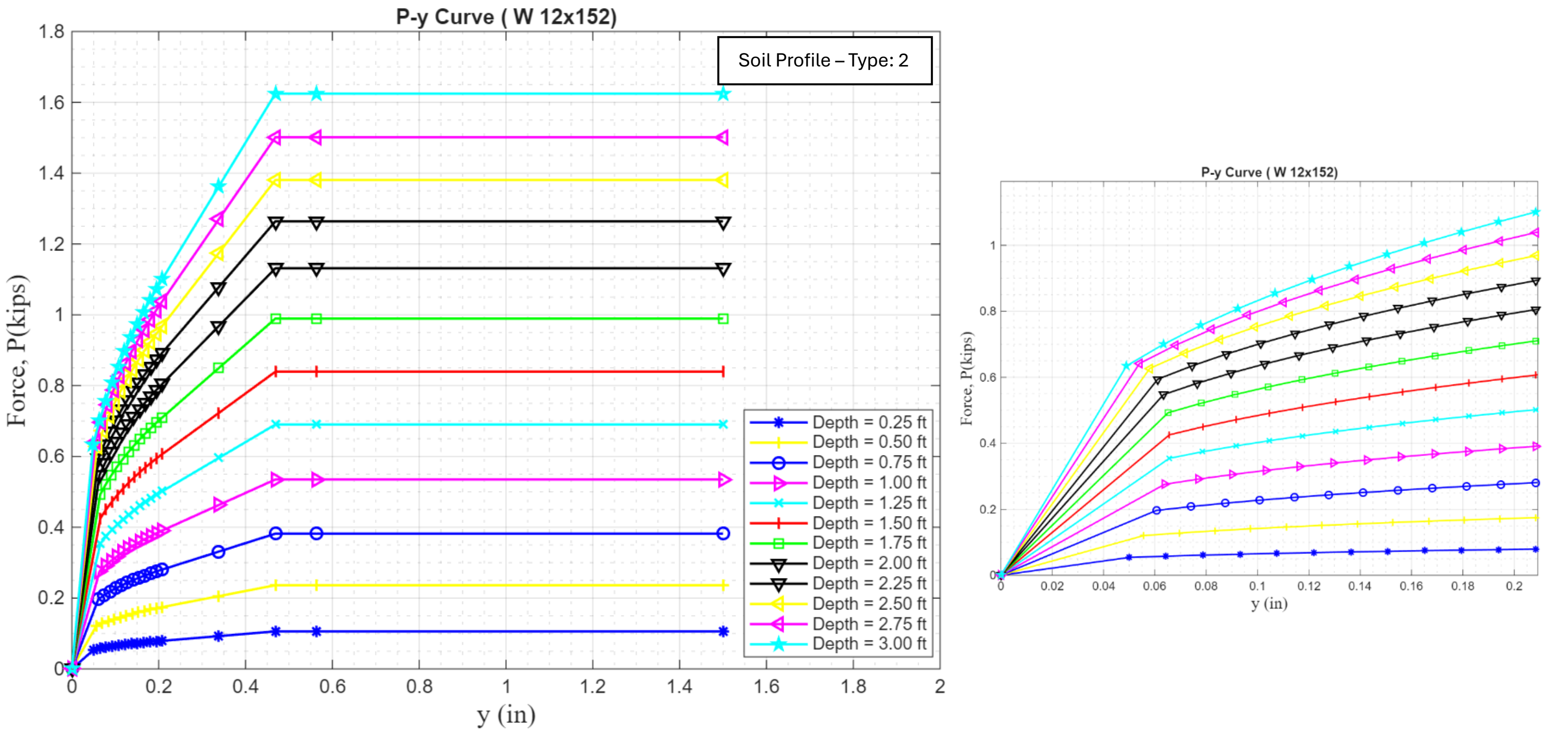

Fig. A.10 P-y curves for a W12x152 pile for soil profile type 2, with 3-inch nodal increments

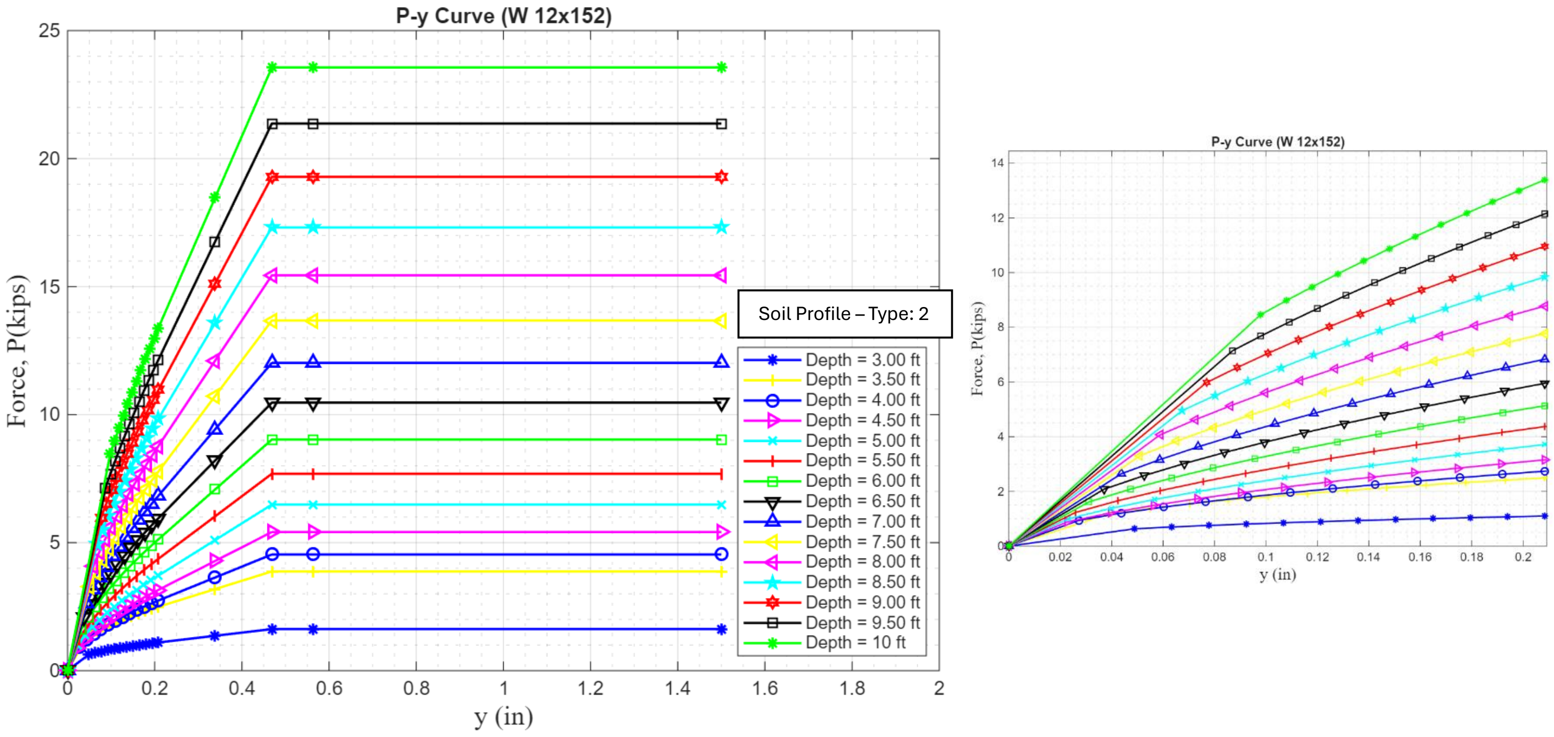

Fig. A.11 P-y curves for a W12x152 pile for soil profile type 2, with 6-inch nodal increments

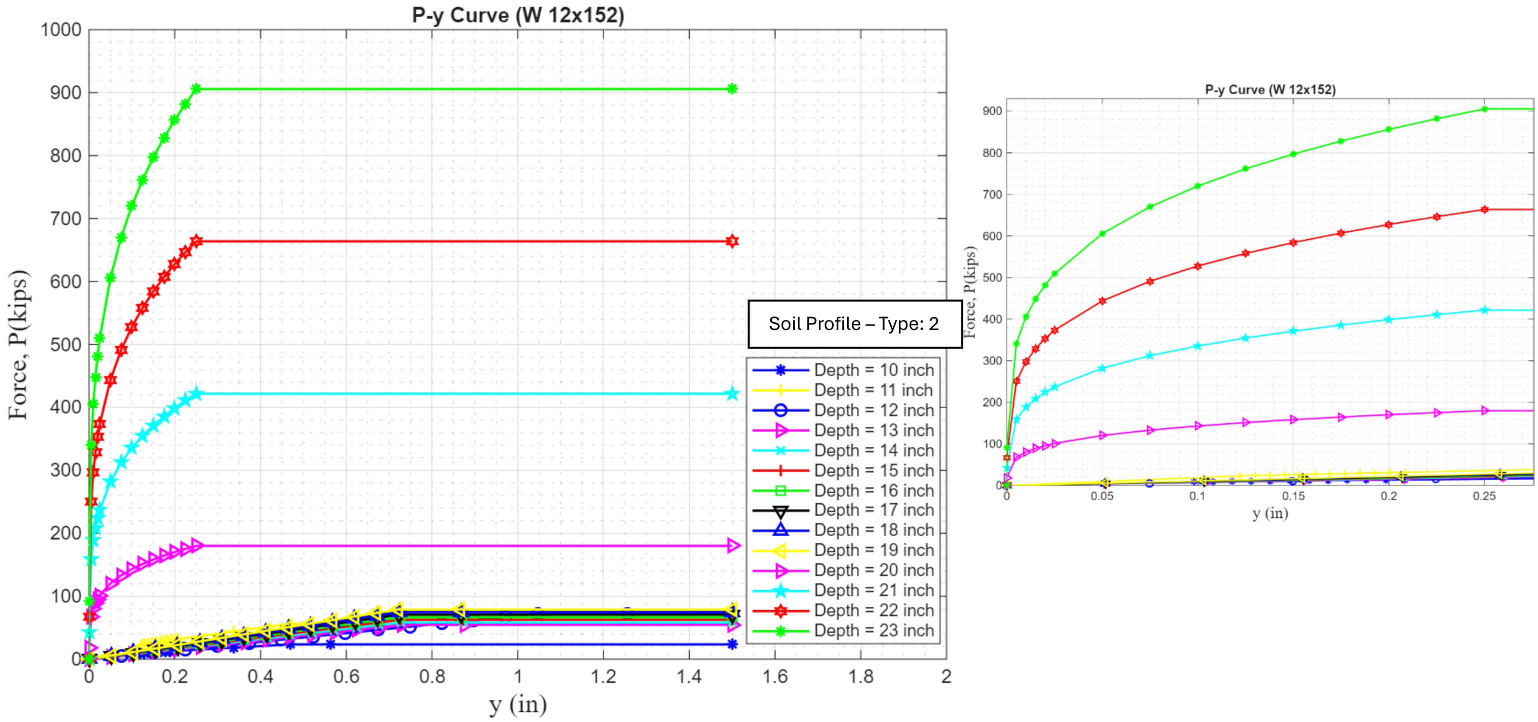

Fig. A.12. P-y curves for a W12x152 pile for soil profile type 2, with 12-inch nodal increments

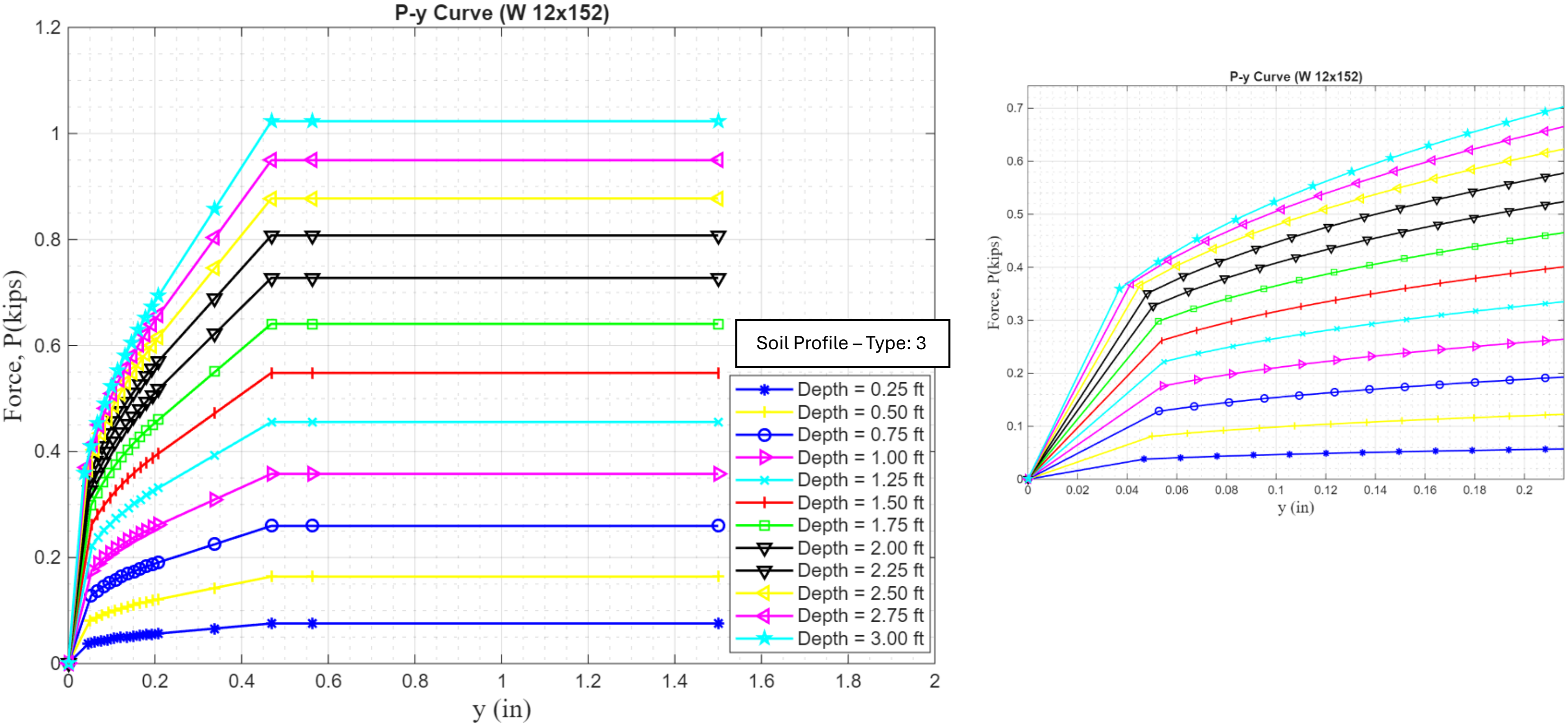

Fig. A.13 P-y curves for a W12x152 pile for soil profile type 3, with 3-inch nodal increments

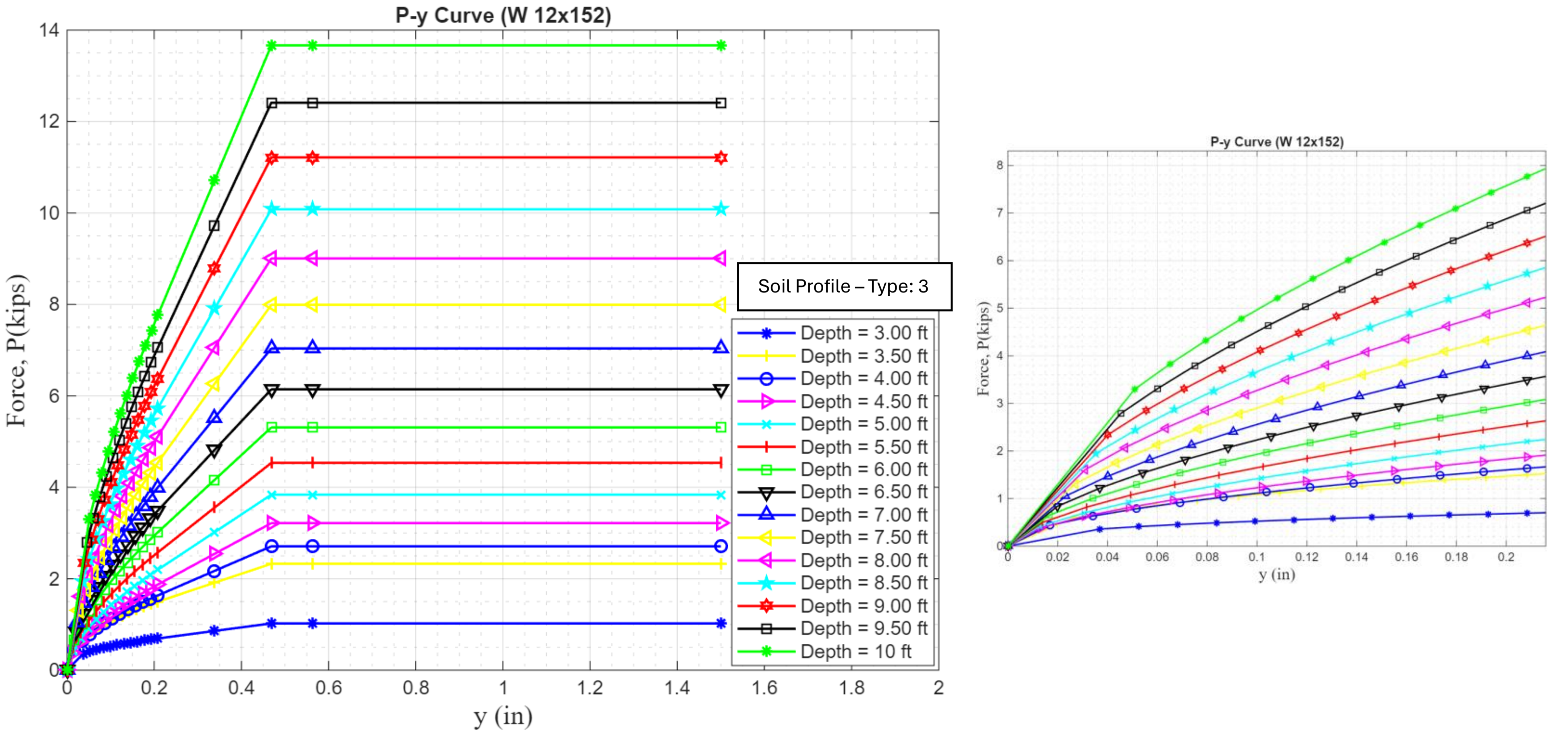

Fig. A.14 P-y curves for a W12x152 pile for soil profile type 3, with 6-inch nodal increments

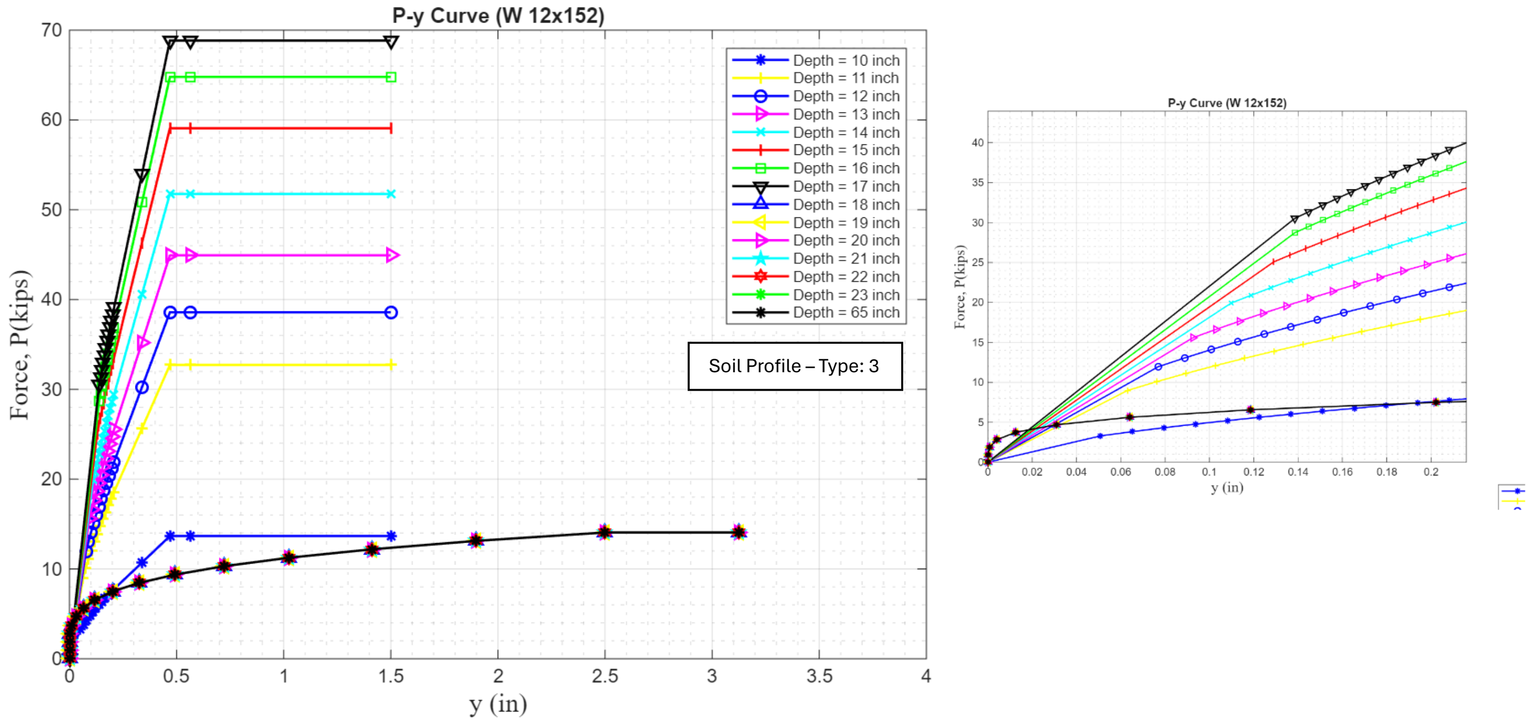

Fig. A.15 P-y curves for a W12x152 pile for soil profile type 3, with 12-inch nodal increments

Appendix B

displacement and moments profiles HP and W piles created by using LPILE 10.0 software

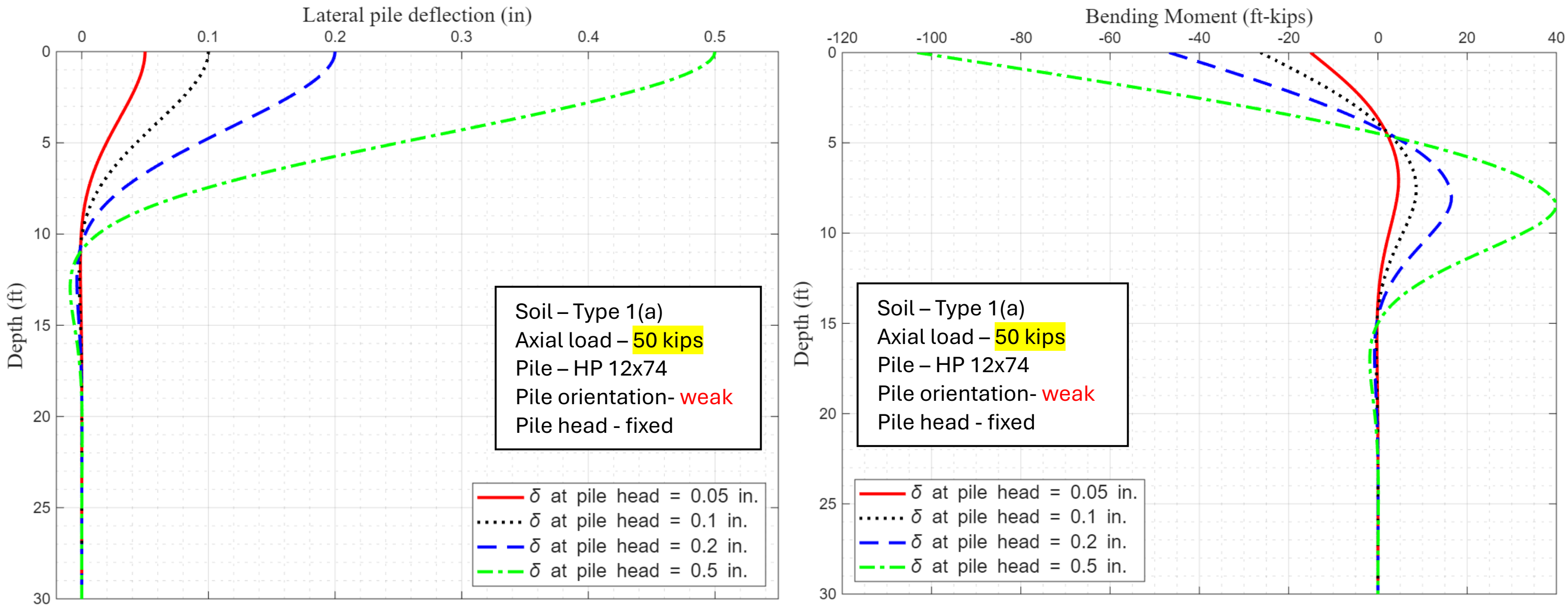

Fig. B.1 Lateral displacement and bending moment profiles for HP12x74 for the range of pile head displacements, δ

Table. B.1 Fixity points and maximum bending moments of the pile for the range of pile head displacements

Soil – Type 1(a), Axial load – 50-kip, Pile – HP 12x74, Pile orientation-weak, Pile head - fixed			
Pile head lateral displacement (in) δ	Fixity point (ft) (disp. <0.01 in)	$M_{max\|2nd}$ (kips-ft)	$M_{max\|pile\text{-}head}$ (kips-ft)
0.05	6.49	4.62	-15.07
0.1	7.96	8.59	-26.30
0.2	9.10	16.47	-46.76
0.5	10.16	39..92	-103.23

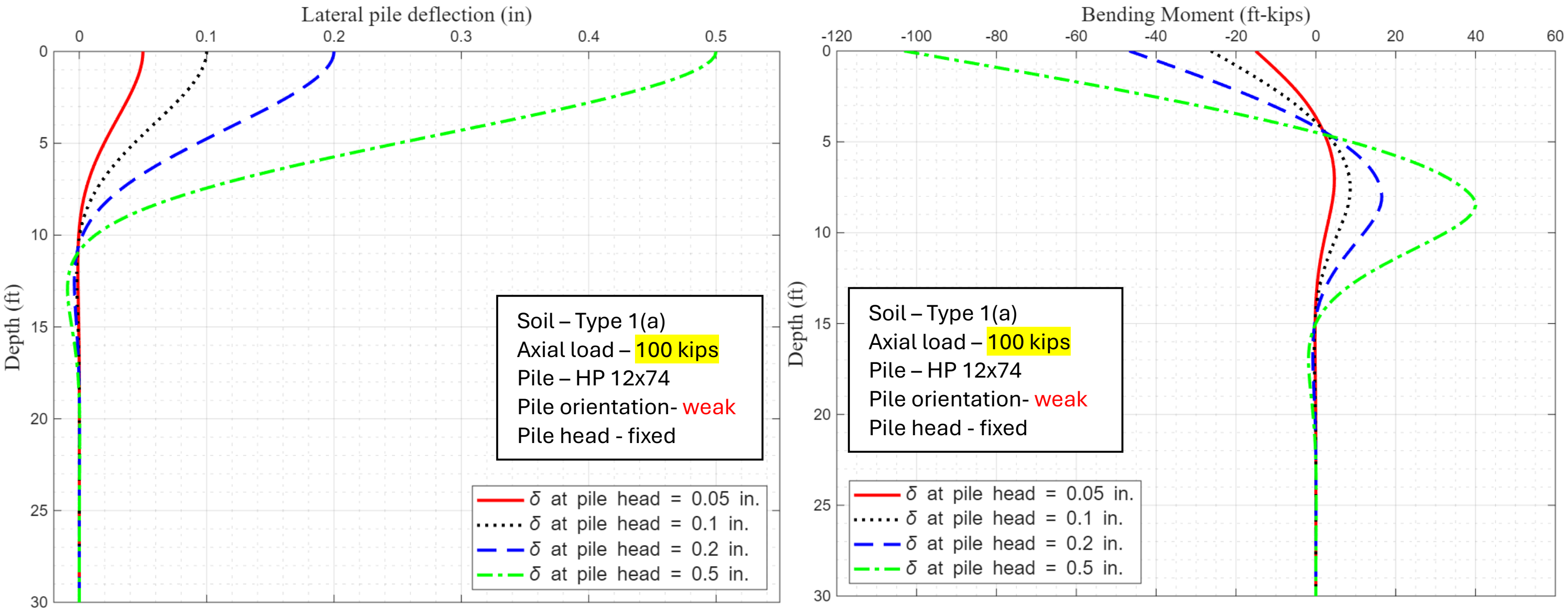

Fig. B.2 Lateral displacement and bending moment profiles for HP12x74 for the range of pile head displacements, δ

Table. B.2 Fixity points and maximum bending moments of the pile for the range of pile head displacements

Soil – Type 1(a), Pile axial load – 100-kip, Pile – HP 12x74, Pile orientation-weak, Pile head - fixed			
Pile head Lateral displacement (in) δ	Fixity point (ft) (disp. <0.01 in)	$M_{max\|2nd}$ (kips-ft)	$M_{max\|pile\text{-}head}$ (kips-ft)
0.05	6.48	4.63	-15.07
0.1	7.95	8.62	-26.28
0.2	9.09	16.52	-46.72
0.5	10.14	40.02	-103.12

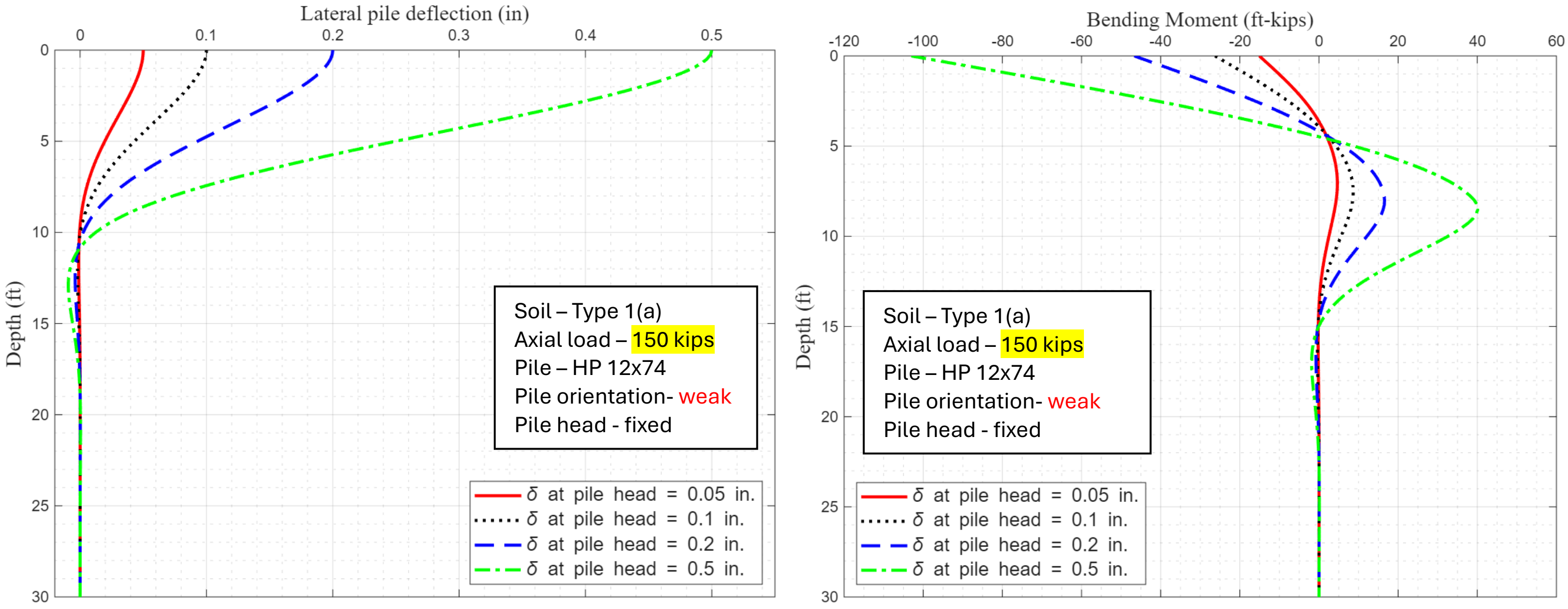

Fig. B.3 Lateral displacement and bending moment profiles for the range of pile head displacements, δ

Table. B.3 Fixity points and maximum bending moments for the range of pile head displacements

Soil – Type 1(a), Pile axial load – 150 kip, Pile – HP 12x74, Pile orientation-weak, Pile head - fixed			
Pile head Lateral displacement (in) δ	Fixity point (ft) (disp. <0.01 in)	$M_{max\vert 2nd}$ (kips-ft)	$M_{max\vert pile\text{-}head}$ (kips-ft)
0.05	6.48	4.63	-15.07
0.1	7.95	8.64	-26.27
0.2	9.07	16.56	-46.69
0.5	10.13	40.12	-103.02

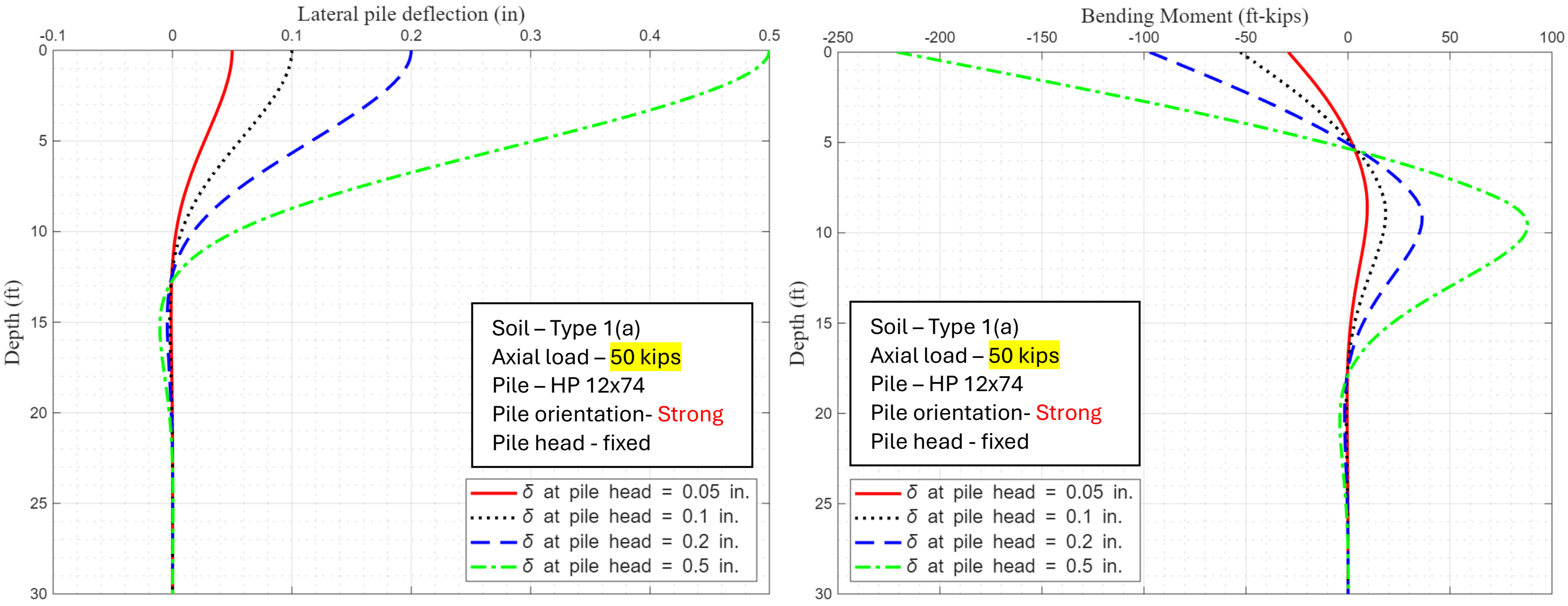

Fig. B.4 Lateral displacement and bending moment profiles for the range of pile head displacements, δ

Table. B.4 Fixity points and maximum bending moments of the pile for the range of pile head displacements

Soil – Type 1(a), Pile axial load – 50-kip, Pile – HP 12x74, Pile orientation- strong, Pile head - fixed			
Pile head Lateral displacement (in) δ	Fixity point (ft) (Disp. <0.01 in)	$M_{max\|2nd}$ (kips-ft)	$M_{max\|pile\text{-}head}$ (kips-ft)
0.05	7.98	9.46	-29.20
0.1	9.55	18.47	-52.84
0.2	10.16	36.36	-97.21
0.5	11.87	88.04	-221.01

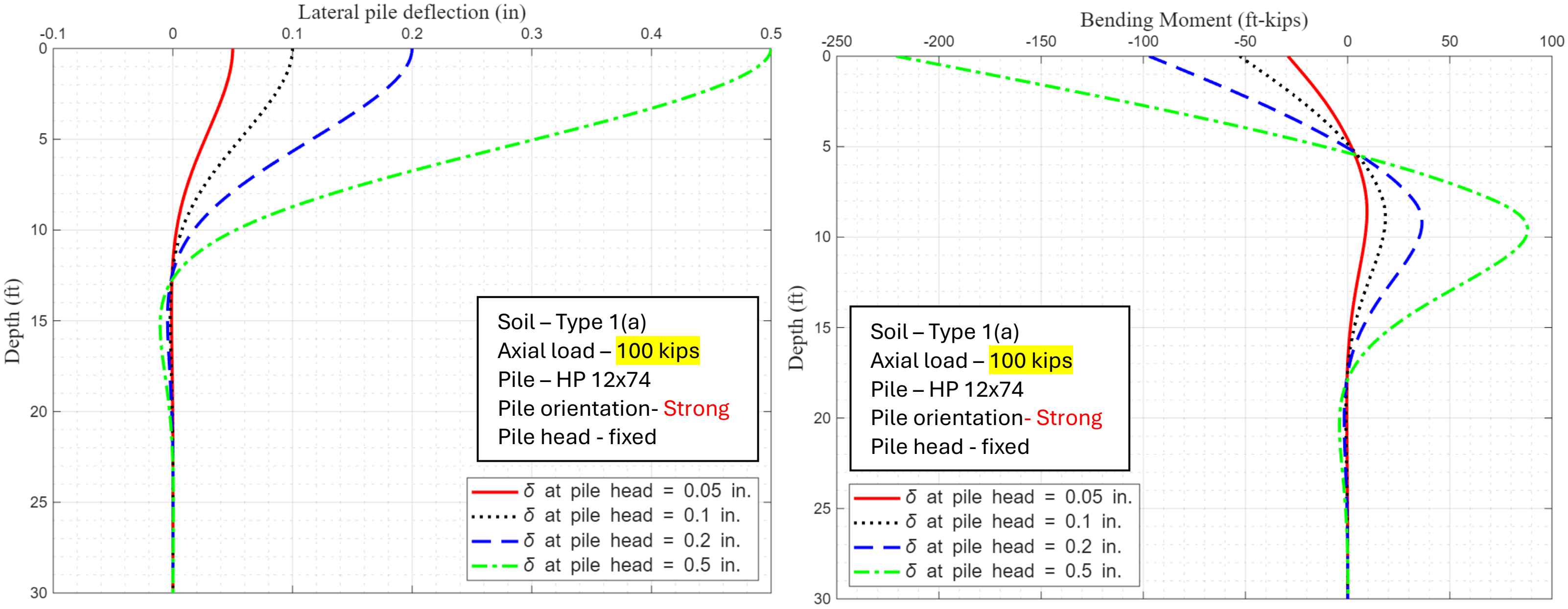

Fig. B.5 Lateral displacement and bending moment profiles for the range of pile head displacements, δ

Table. B.5 Fixity points and maximum bending moments of the pile for the range of pile head displacements

Soil – Type 1(a), Pile axial load – 100-kip, Pile – HP 12x74, Pile orientation- strong, Pile head – fixed			
Pile head Lateral displacement (in) δ	Fixity point (ft) (disp. <0.01 in)	$M_{max\|2nd}$ (kips-ft)	$M_{max\|pile\text{-}head}$ (kips-ft)
0.05	7.97	9.47	-29.20
0.1	9.55	18.49	-52.82
0.2	10.73	36.40	-97.17
0.5	11.86	88.15	-220.90

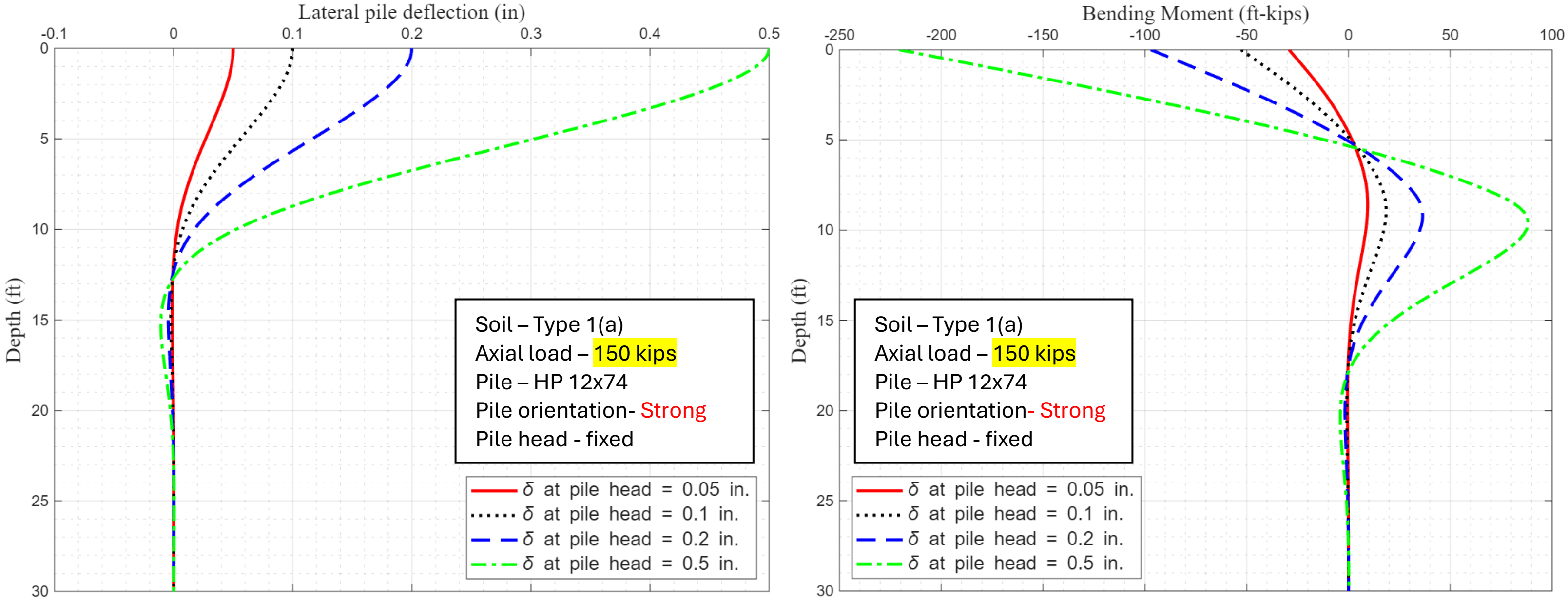

Fig. B.6 Lateral displacement and bending moment profiles for the range of pile head displacements, δ

Table. B.6 Fixity points and maximum bending moments of the pile for the range of pile head displacements

Soil – Type 1(a), Pile axial load – 150-kip, Pile – HP 12x74, Pile orientation- strong, Pile head – fixed			
Pile head Lateral displacement (in) δ	Fixity point (ft) (disp. <0.01 in)	$M_{max\|2nd}$ (kips-ft)	$M_{max\|pile\text{-}head}$ (kips-ft)
0.05	7.97	9.47	29.20
0.1	9.54	18.51	-52.81
0.2	10.73	36.44	-97.13
0.5	11.85	88.26	-220.79

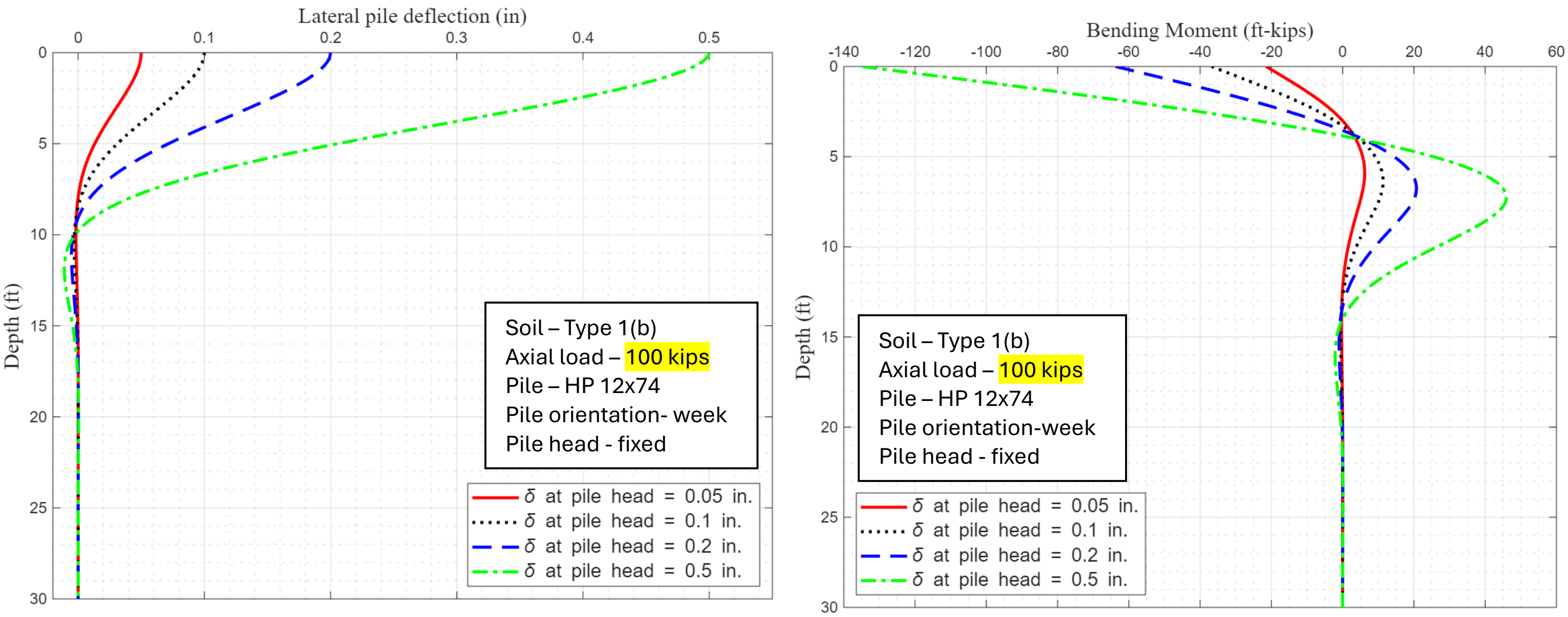

Fig. B.7 Lateral displacement and bending moment profiles for the range of pile head displacements, δ

Table. B.7 Fixity points and maximum bending moments of the pile for the range of pile head displacements

Soil – Type 1(b), Pile axial load – 100-kip, Pile – HP 12x74, Pile orientation- weak, Pile head – fixed			
Pile head Lateral displacement (in) δ	Fixity point (ft) (disp. <0.01 in)	$M_{max\|2nd}$ (kips-ft)	$M_{max\|pile\text{-}head}$ (kips-ft)
0.05	5.46	6.19	-21.47
0.1	6.77	11.35	-36.78
0.2	7.91	20.73	-63.72
0.5	9.14	45.98	-134.81

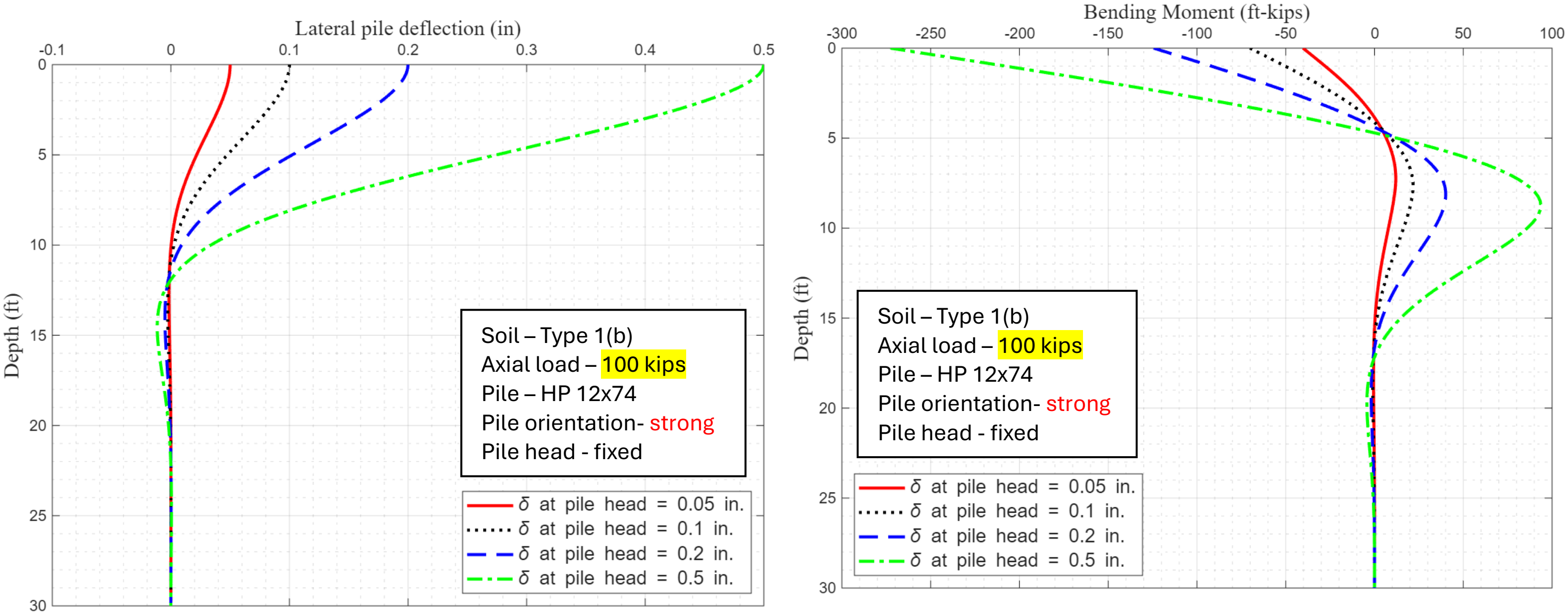

Fig. B.8 Lateral displacement and bending moment profiles for the range of pile head displacements, δ

Table. B.8 Fixity points and maximum bending moments of the pile for the range of pile head displacements

Soil – Type 1(b), Pile axial load – 100-kip, Pile – HP 12x74, Pile orientation- strong, Pile head – fixed			
Pile head displacement (in)	Fixity point (ft) (δ <0.01 in)	$M_{max\|2nd}$ (kips-ft)	$M_{max\|pile\text{-}head}$ (kips-ft)
0.05	6.91	11.99	-40.28
0.1	8.56	21.71	-70.22
0.2	9.89	40.09	-124.41
0.5	11.15	93.68	-272.66

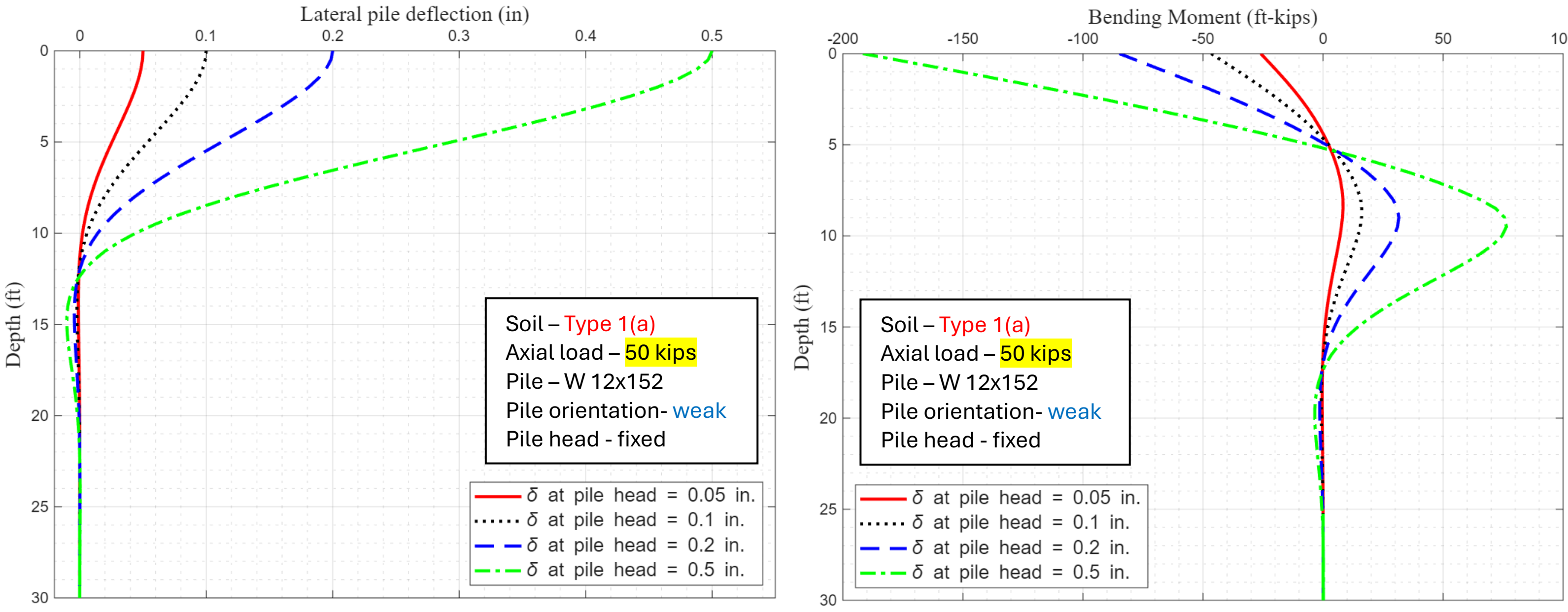

Fig. B.9 Lateral displacement and bending moment profiles for the range of pile head displacements, δ

Table. B.9 Fixity points and maximum bending moments of the pile for the range of pile head displacements

Soil – Type 1(a), Pile axial load – 50-kip, Pile – W 12x152, Pile orientation- weak, Pile head – fixed			
Pile head displacement (in) δ	Fixity point (ft) (disp.<0.01 in)	$M_{max\|2nd}$ (kips-ft)	$M_{max\|pile\text{-}head}$ (kips-ft)
0.05	7.69	8.28	-25.94
0.1	9.25	16.12	-46.58
0.2	10.43	31.54	-84.85
0.5	11.56	76.34	-191.68

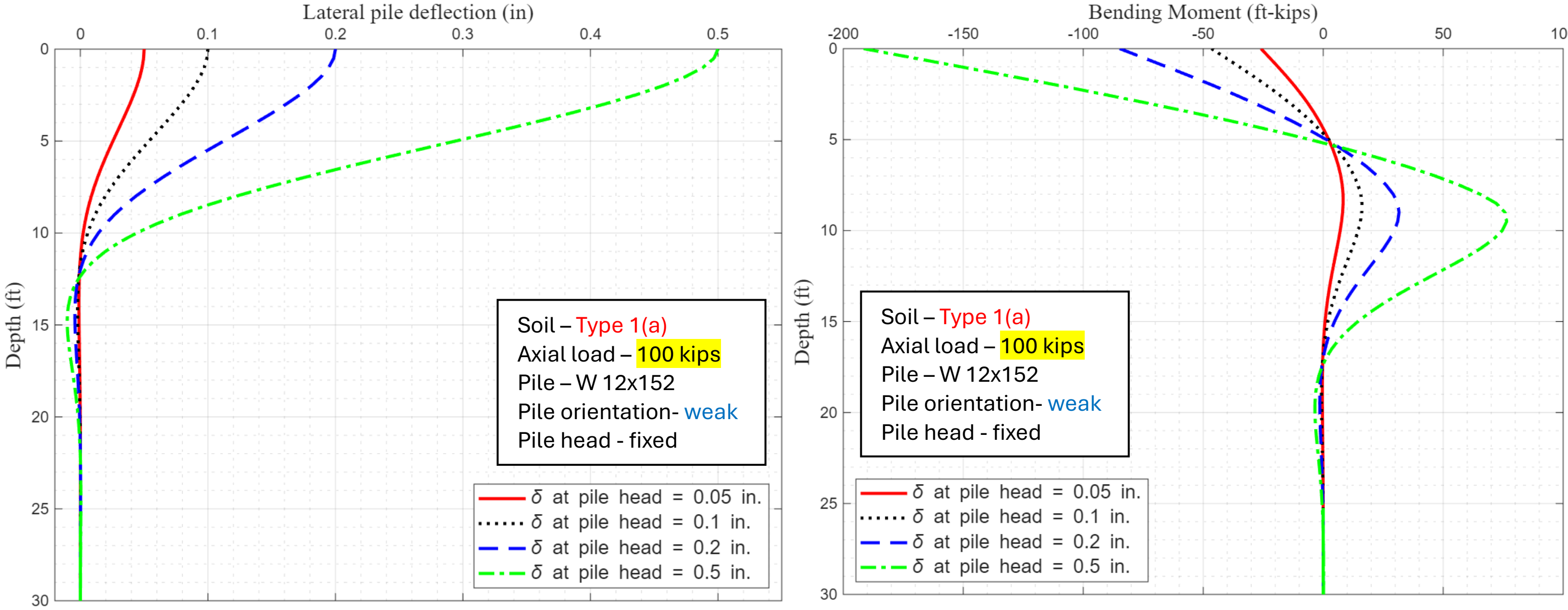

Fig. B.10 Lateral displacement and bending moment profiles for the range of pile head displacements, δ

Table. B.10 Fixity points and maximum bending moments of the pile for the range of pile head displacements

Soil – Type 1(a), Pile axial load – 100-kip, Pile – W 12x152, Pile orientation- weak, Pile head – fixed			
Pile head Lateral displacement (in) δ	Fixity point (ft) (disp. <0.01 in)	$M_{max\|2nd}$ (kips-ft)	$M_{max\|pile\text{-}head}$ (kips-ft)
0.05	7.68	8.29	-25.93
0.1	9.25	16.14	-46.56
0.2	10.43	31.58	-84.81
0.5	11.55	76.45	-191.57

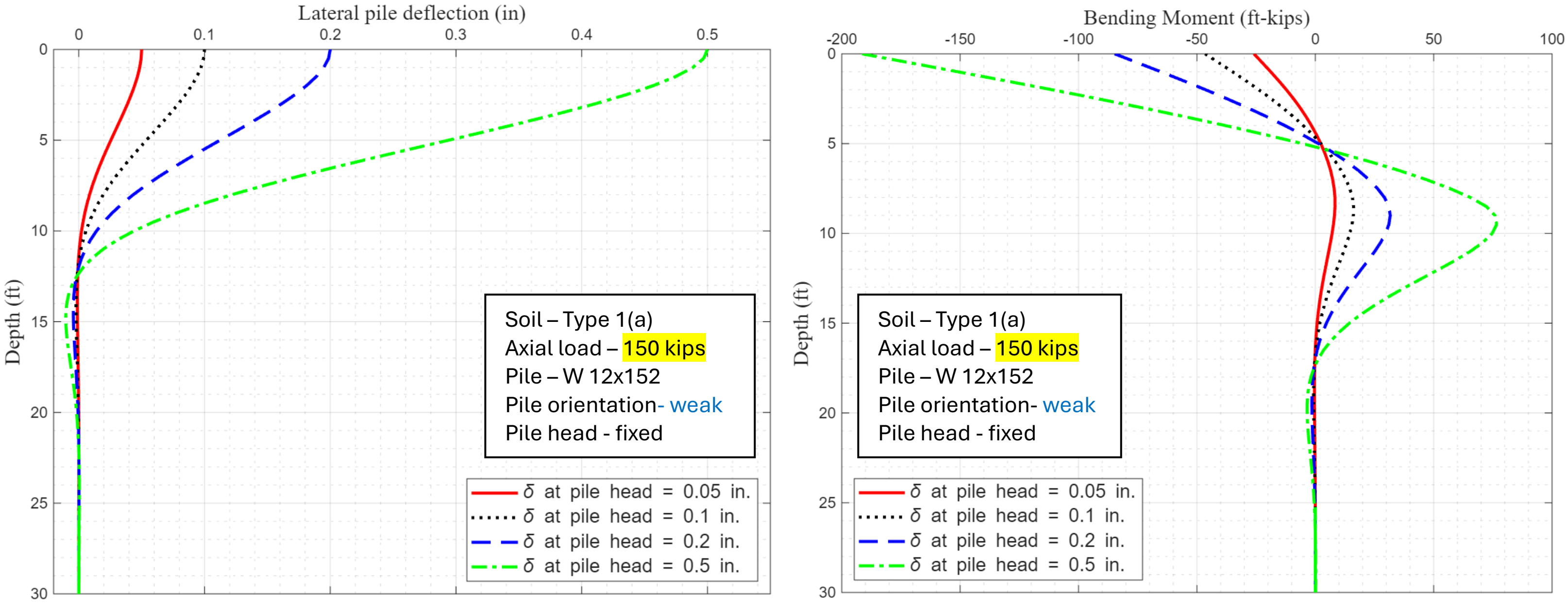

Fig. B.11 Lateral displacement and bending moment profiles for the range of pile head displacements, δ

Table. B.11 Fixity points and maximum bending moments of the pile for the range of pile head displacements

Soil – Type 1(a), Pile axial load – 150-kip, Pile – W12x152, Pile orientation- weak, Pile head – fixed			
Pile head Lateral displacement (in) δ	Fixity point (ft) (disp. <0.01 in)	$M_{max\|2nd}$ (kips-ft)	$M_{max\|pile\text{-}head}$ (kips-ft)
0.05	7.68	8.30	-25.92
0.1	9.24	16.17	-46.55
0.2	10.42	31.62	-84.77
0.5	11.54	76.55	-191.47

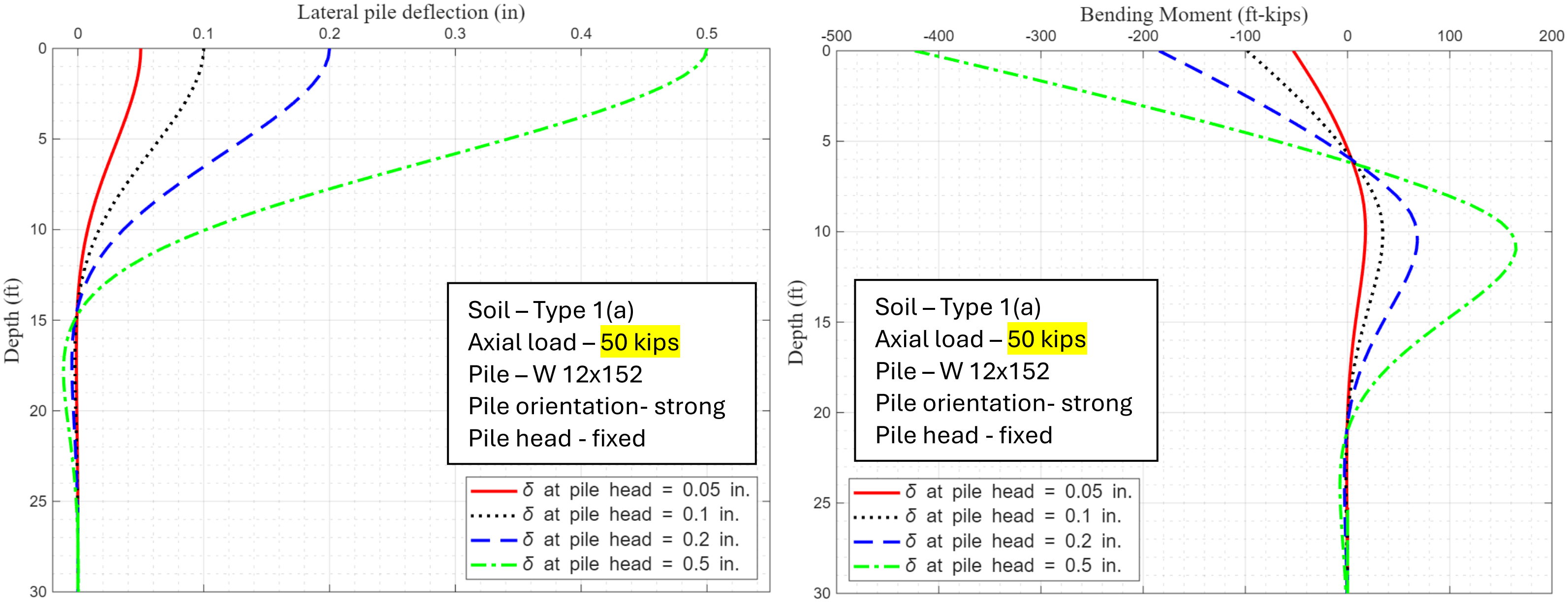

Fig. B.12 Lateral displacement and bending moment profiles for the range of pile head displacements, δ

Table. B.12 Fixity points and maximum bending moments of the pile for the range of pile head displacements

Soil – Type 1(a), Pile axial load – 50-kip, Pile – W 12x152, Pile orientation- strong, Pile head – fixed			
Pile head Lateral displacement (in) δ	Fixity point (ft) (disp. <0.01 in)	$M_{max\|2nd}$ (kips-ft)	$M_{max\|pile\text{-}head}$ (kips-ft)
0.05	9.37	17.51	-53.02
0.1	11.5	34.47	-98.16
0.2	12.43	68.35	-184.46
0.5	13.75	164.85	-423.53

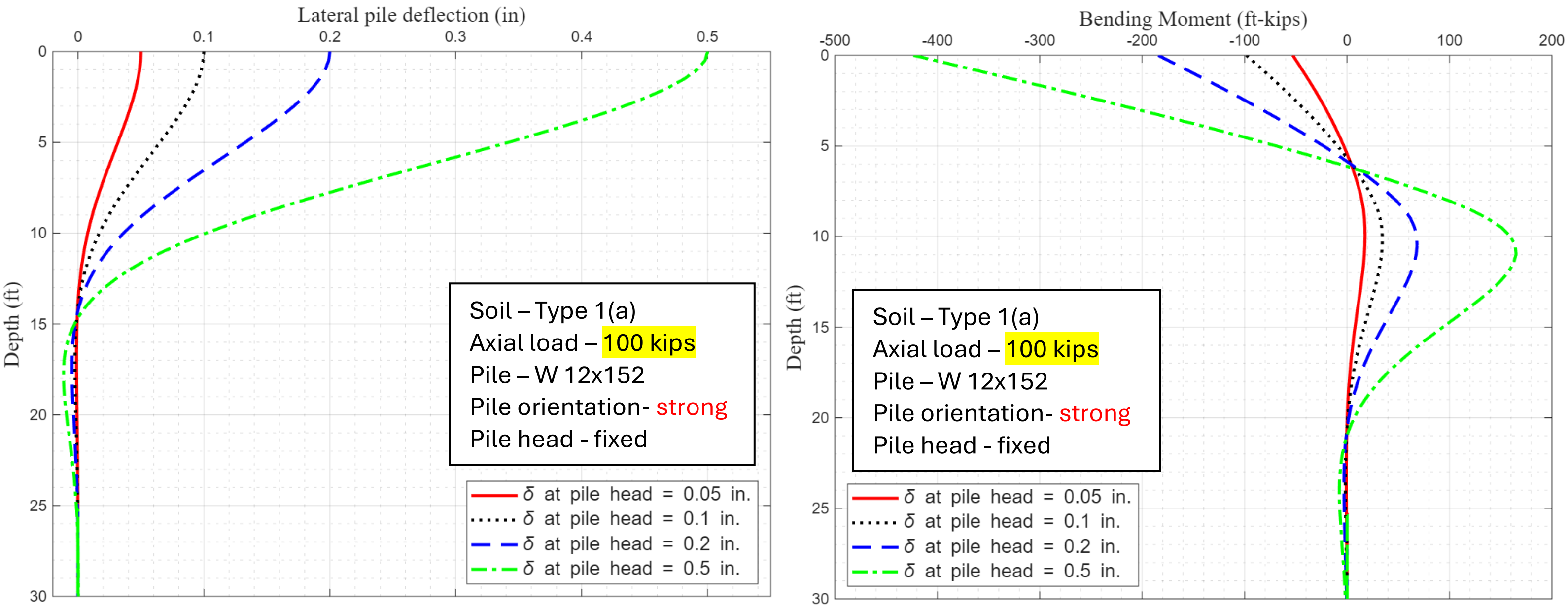

Fig. B.13 Lateral displacement and bending moment profiles for the range of pile head displacements, δ

Table. B.13 Fixity points and maximum bending moments of the pile for the range of pile head displacements

Soil – Type 1(a), Pile axial load – 100-kip, Pile – W 12x152, Pile orientation- strong, Pile head – fixed			
Pile head Lateral displacement (in) δ	Fixity point (ft) (disp.<0.01 in)	$M_{max\|2nd}$ (kips-ft)	$M_{max\|pile\text{-}head}$ (kips-ft)
0.05	9.36	17.53	-53.02
0.1	11.14	34.50	-98.14
0.2	12.43	68.40	-184.43
0.5	13.74	164.96	-423.42

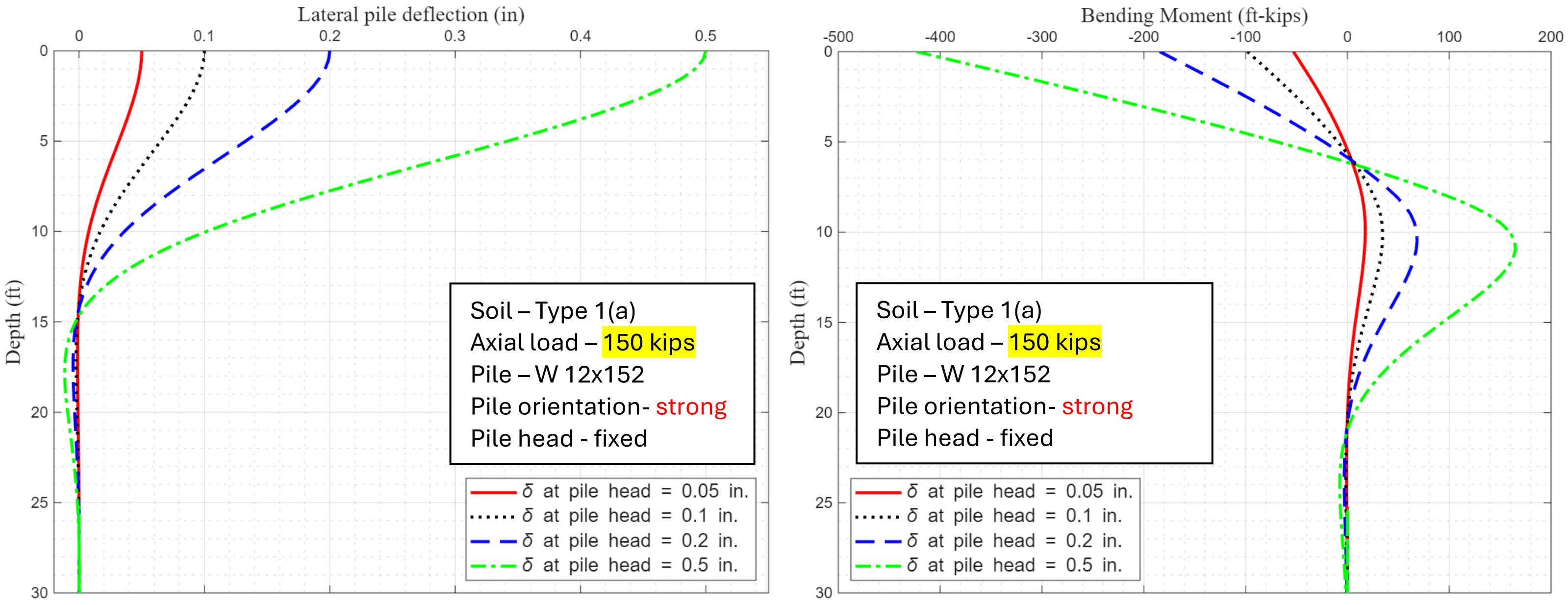

Fig. B.14 Lateral displacement and bending moment profiles for the range of pile head displacements, δ

Table. B.14 Fixity points and maximum bending moments of the pile for the range of pile head displacements

Soil – Type 1(a), Pile axial load – 150-kip, Pile – W 12x152, Pile orientation- strong, Pile head – fixed			
Pile head Lateral displacement (in) δ	Fixity point (ft) (disp. <0.01 in)	$M_{max\|2nd}$ (kips-ft)	$M_{max\|pile\text{-}head}$ (kips-ft)
0.05	9.35	17.54	-53.01
0.1	11.14	34.52	-98.12
0.2	12.42	68.45	-184.39
0.5	13.74	165.07	-423.32

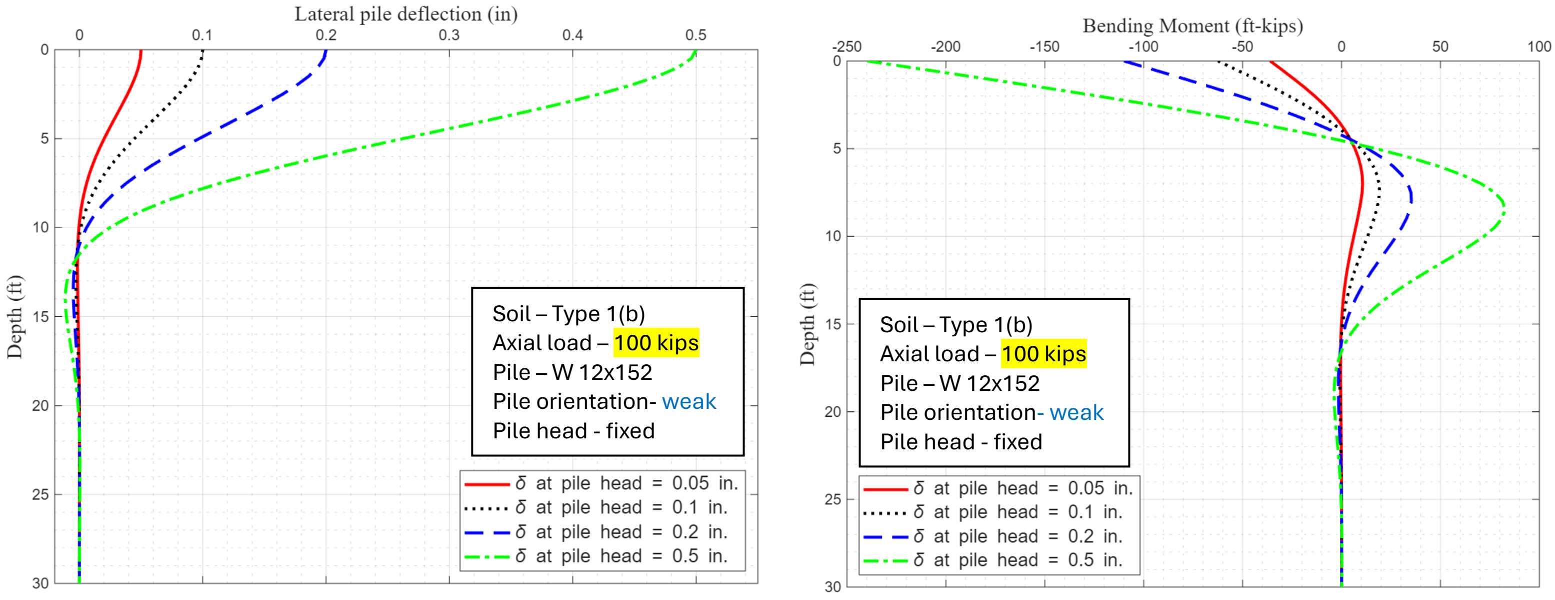

Fig. B.15 Lateral displacement and bending moment profiles for the range of pile head displacements, δ

Table. B.15 Fixity points and maximum bending moments of the pile for the range of pile head displacements

Soil – Type 1(b), Pile axial load – 100-kip, Pile – W 12x152, Pile orientation- weak, Pile head – fixed			
Pile head displacement (in) δ	Fixity point (ft) (disp. <0.01 in)	$M_{max\|2nd}$ (kips-ft)	$M_{max\|pile\text{-}head}$ (kips-ft)
0.05	6.61	10.64	-36.07
0.1	8.23	19.23	-62.46
0.2	9.52	35.30	-109.97
0.5	10.76	82.58	-239.78

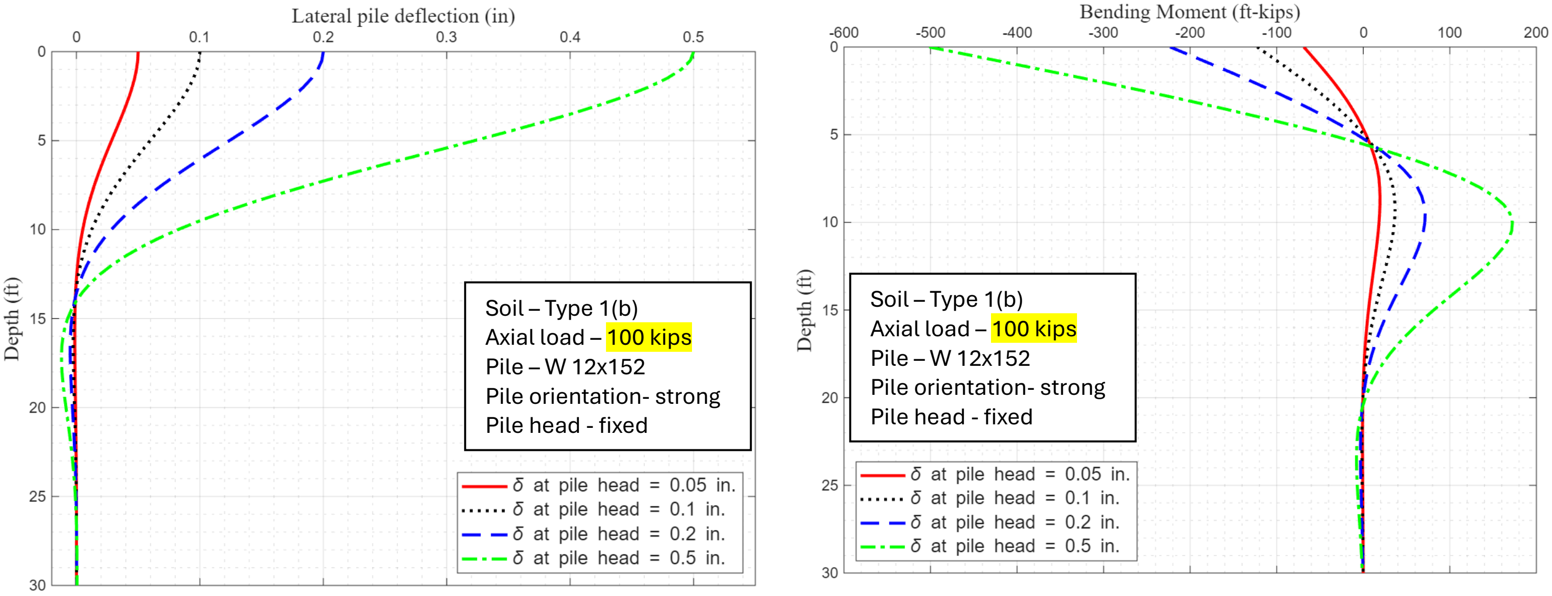

Fig. B.16 Lateral displacement and bending moment profiles for the range of pile head displacements, δ

Table. B.16 Fixity points and maximum bending moments of the pile for the range of pile head displacements

Soil – Type 1(b), Pile axial load – 100-kip, Pile – W 12x152, Pile orientation- strong, Pile head – fixed			
Pile head Lateral displacement (in) δ	Fixity point (ft) (disp. <0.01 in)	$M_{max\|2nd}$ (kips-ft)	$M_{max\|pile\text{-}head}$ (kips-ft)
0.05	8.54	19.28	-68.69
0.1	10.42	36.67	-122.57
0.2	11.80	71.49	-223.18
0.5	13.12	172.33	-501.44

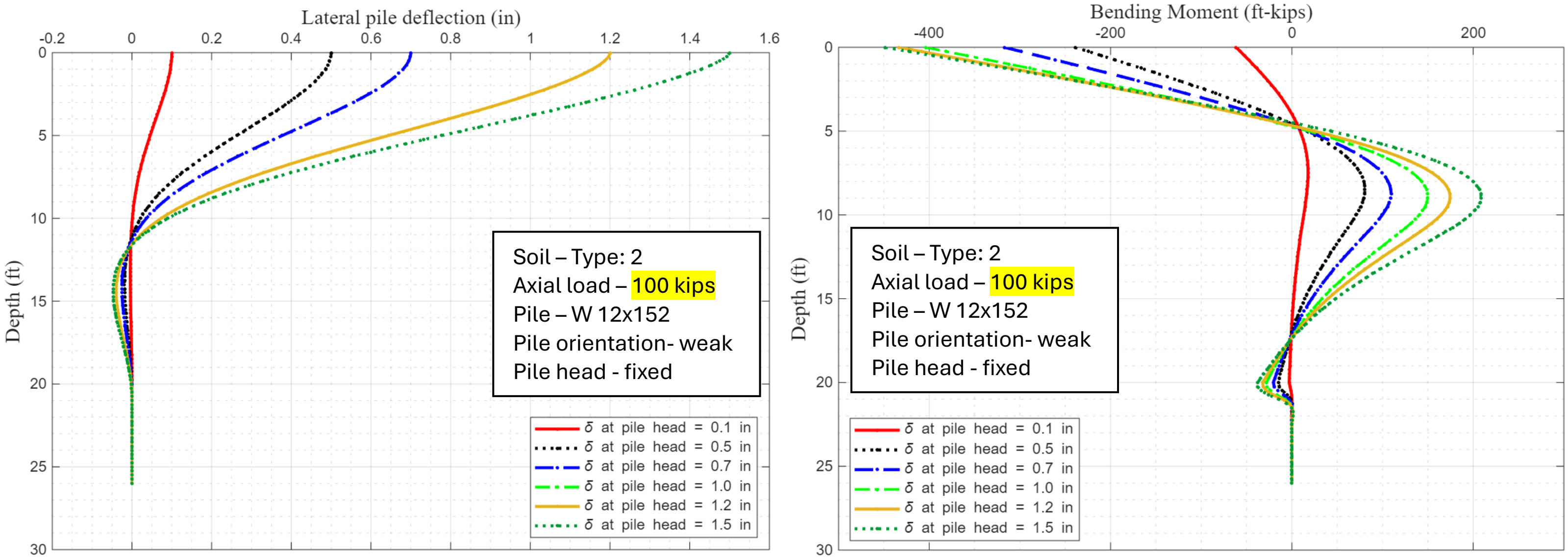

Fig. B.17 Lateral displacement and bending moment profiles for the range of pile head displacements, δ

Table. B.17 Fixity points and maximum bending moments of the pile for the range of pile head displacements

Soil – Type 2, Pile axial load – 100-kip, Pile – W 12x152, Pile orientation- weak, Pile head – fixed			
Pile head Lateral displacement (in) δ	Fixity point (ft) (disp. <0.01 in)	$M_{max\|2nd}$ (kips-ft)	$M_{max\|pile\text{-}head}$ (kips-ft)
0.1	8.31	17.82	-61.34
0.5	10.52	80.58	-238.98
0.7	10.87	109.41	-317.15
1.0	11.18	149.86	-404.23
1.2	11.28	174.52	-433.58
1.5	11.36	208.68	-448.27

Table. B.17 Pile deflection and bending moment at different pile head displacement– Axial load: 100 kips

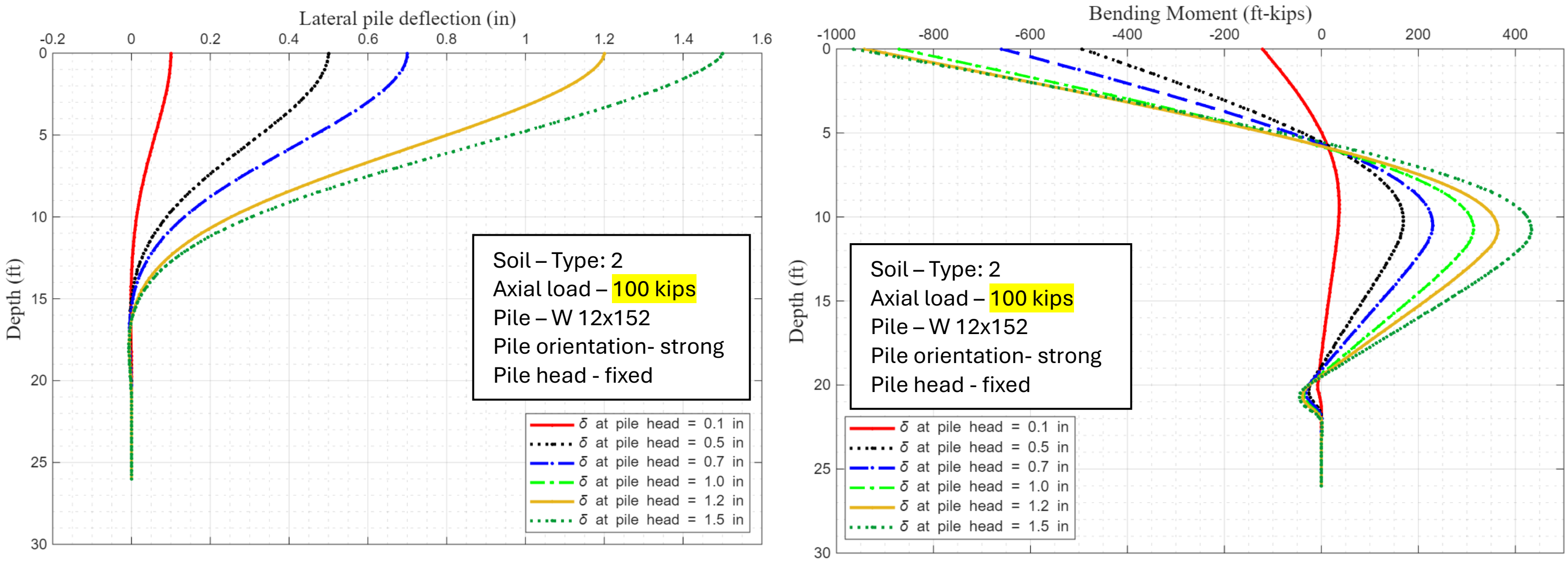

Fig. B.18 Lateral displacement and bending moment profiles for the range of pile head displacements, δ

Table. B.18 Fixity points and maximum bending moments of the pile for the range of pile head displacements

Soil – Type 2, Pile axial load – 100-kip, Pile – W12x152, Pile orientation- strong, Pile head – fixed			
Pile head displacement (in) δ	Fixity point (ft) (disp. <0.01 in)	$M_{max\|2nd}$ (kips-ft)	$M_{max\|pile\text{-}head}$ (kips-ft)
0.1	10.53	36.62	-121.69
0.5	13.68	169.23	-493.79
0.7	14.32	229.55	-659.34
1.0	15.09	313.72	-870.88
1.2	15.37	363.94	-942.88
1.5	15.52	433.13	-964.16

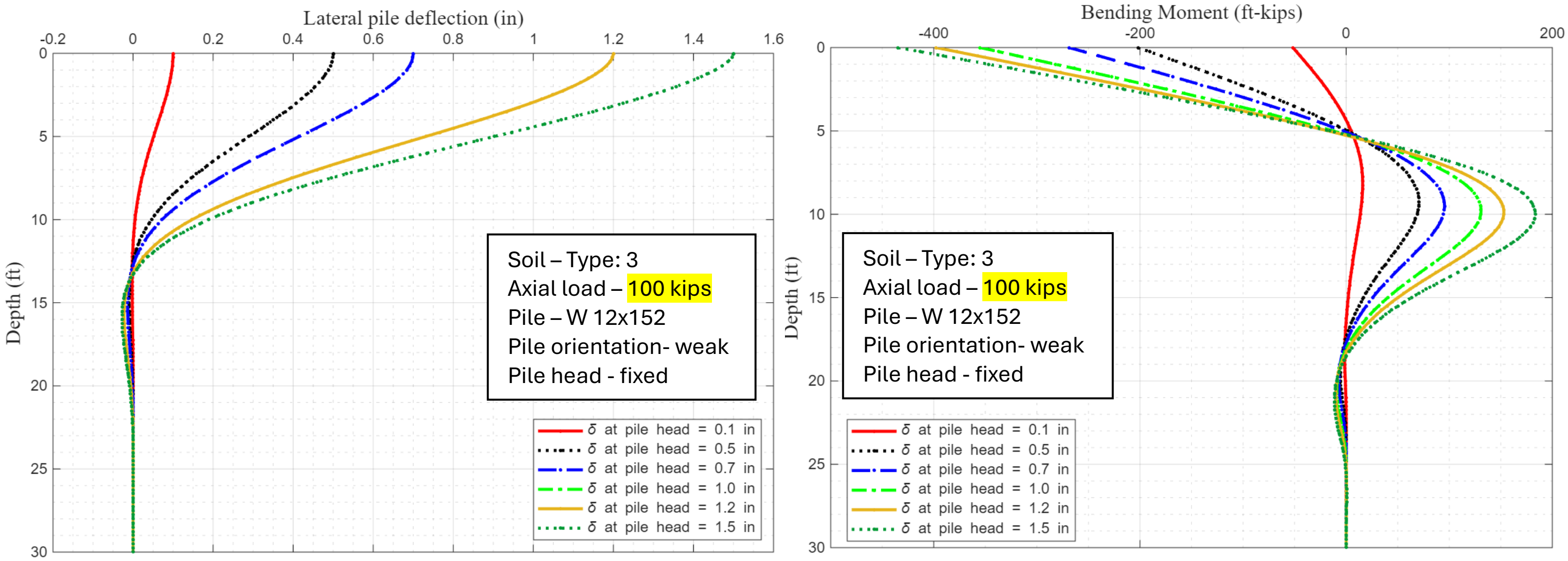

Fig. B.19 Lateral displacement and bending moment profiles for the range of pile head displacements, δ

Table. B.19 Fixity points and maximum bending moments of the pile for the range of pile head displacements

Soil – Type 3, Pile axial load – 100-kip, Pile – W 12x152, Pile orientation- weak, Pile head – fixed			
Pile head Lateral displacement (in) δ	Fixity point (ft) (disp. <0.01 in)	$M_{max\|2nd}$ (kips-ft)	$M_{max\|pile-head}$ (kips-ft)
0.1	9.03	15.98	-51.658
0.5	11.68	70.67	-201.98
0.7	12.12	95.48	-268.87
1.0	12.57	130.89	-354.95
1.2	12.77	152.91	-397.66
1.5	12.95	183.51	-434.65

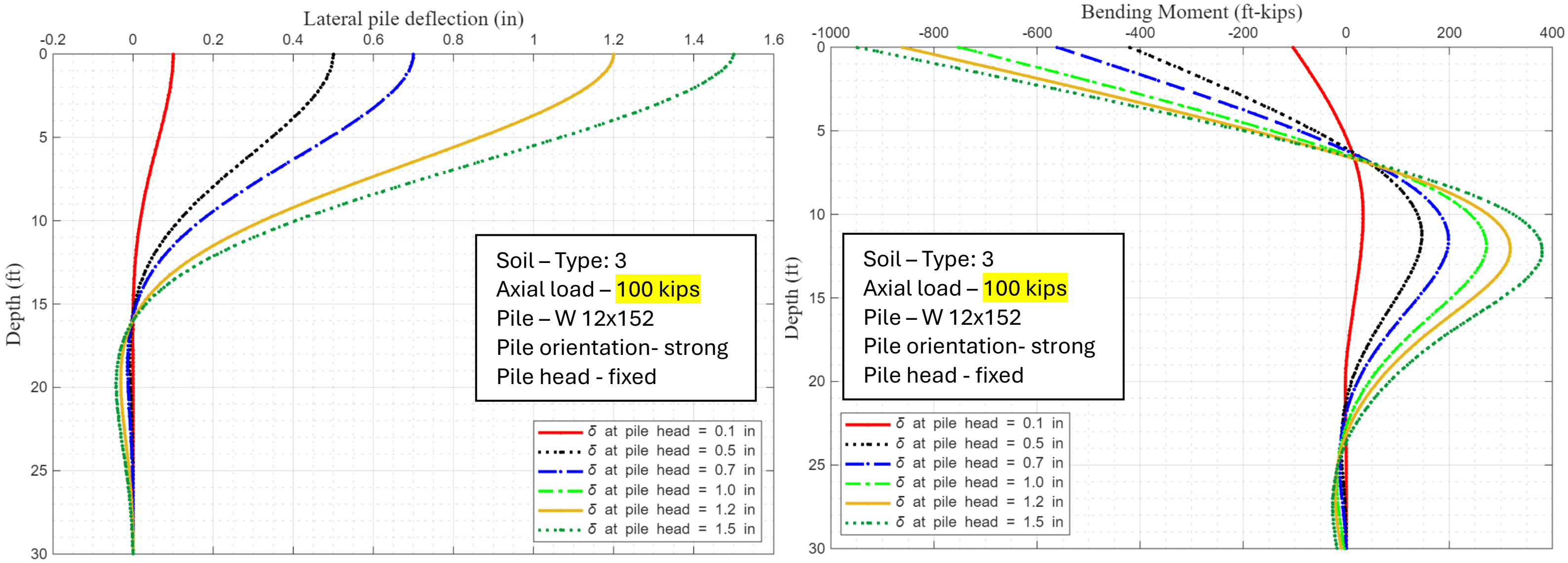

Fig. B.20 Lateral displacement and bending moment profiles for the range of pile head displacements, δ

Table. B.20 Fixity points and maximum bending moments of the pile for the range of pile head displacements

Soil – Type 3, Pile axial load – 100-kip, Pile – W 12x152, Pile orientation- strong, Pile head – fixed			
Pile head Lateral displacement (in) δ	Fixity point (ft) (disp. <0.01 in)	$M_{max\|2nd}$ (kips-ft)	$M_{max\|pile\text{-}head}$ (kips-ft)
0.1	11.34	32.67	-103.54
0.5	14.42	146.94	-420.06
0.7	14.72	198.47	-561.45
1.0	15.29	271.84	-751.71
1.2	15.50	318.32	-861.77
1.5	15.64	380.34	-948.83

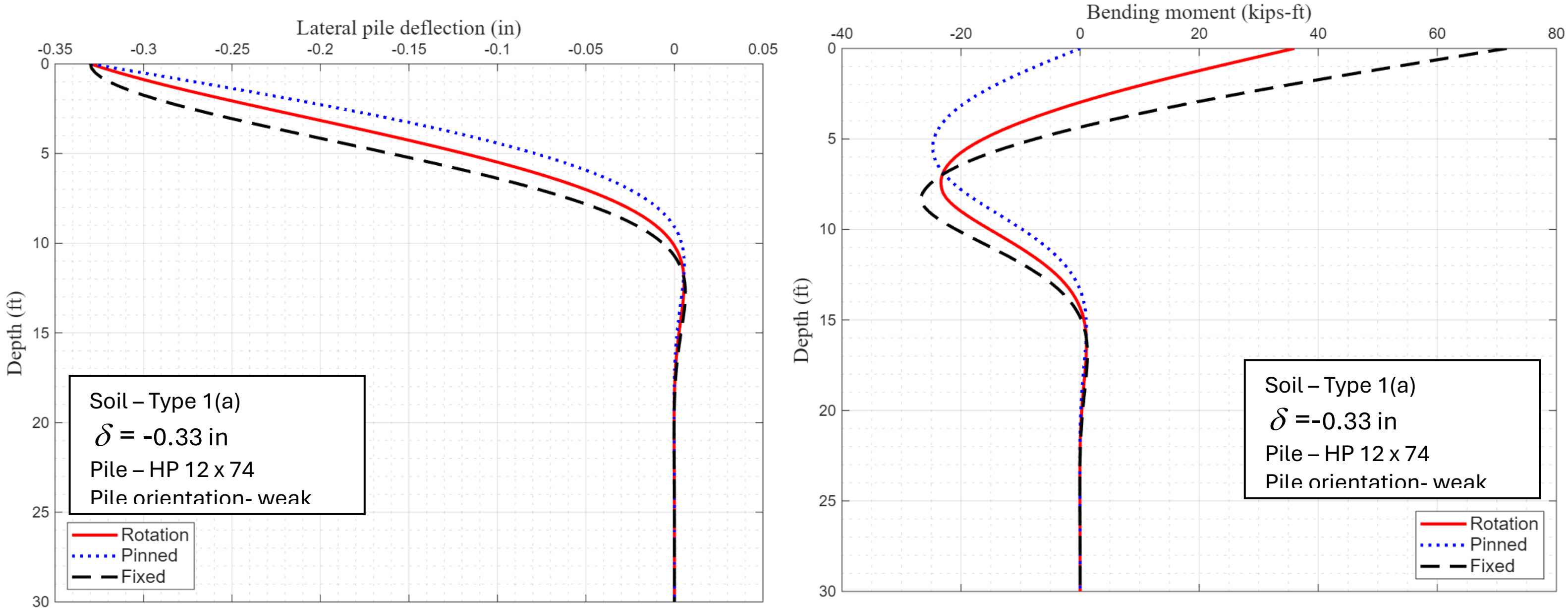

Fig. B.21 Lateral displacement and bending moment profiles of HP12x74 for different pile head connections and δ =- 0.33 in

Table B.21: Quantitative data of HP 12x74 pile for different pile head connections-LPILE

Pile Head Deflection, δ (inch)	Axial Force at Pile head (kips)	Pile Head Connection	Rotation at Pile Head	Max. Moment at Pile Head (kip-ft)	Max. Moment at Pile 2nd Segment (kip-ft)
-0.33	82.43	Fixed	0	71.65	-26.72
		Rotation	0.0025	36.00	-23.37
		Pinned	0.0049	0	-24.76

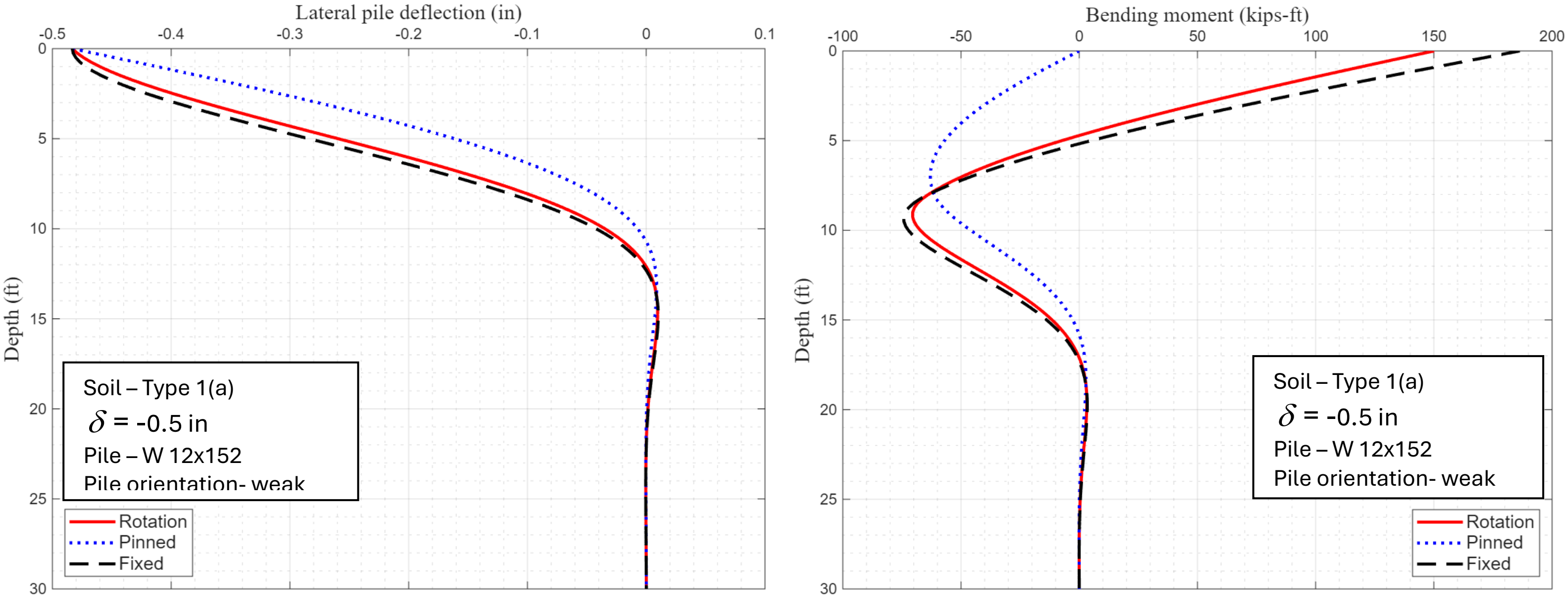

Fig. B.22 W 12 x 152 pile displacement and moment profile at δ= -0.5 in. – Fixed / Rotation / Pinned

Table B.22: Quantitative data of W12x152 pile for different pile head connection -LPILE

Pile Head Deflection (inch)	Axial Force at Pile head (kips)	Pile Head Connection	Rotation at Pile Head	Shear Force at Pile Head (kips)	Max. Moment at Pile Head (kip-ft)	Max. Moment at Pile 2nd Segment (kip-ft)
-0.5	97	Fixed	0	-39.70	191.68	-76.34
		Rotation	0.0012	-46.24	150.08	-74.65
		Pinned	0.0059	-14.11	0	-63.00

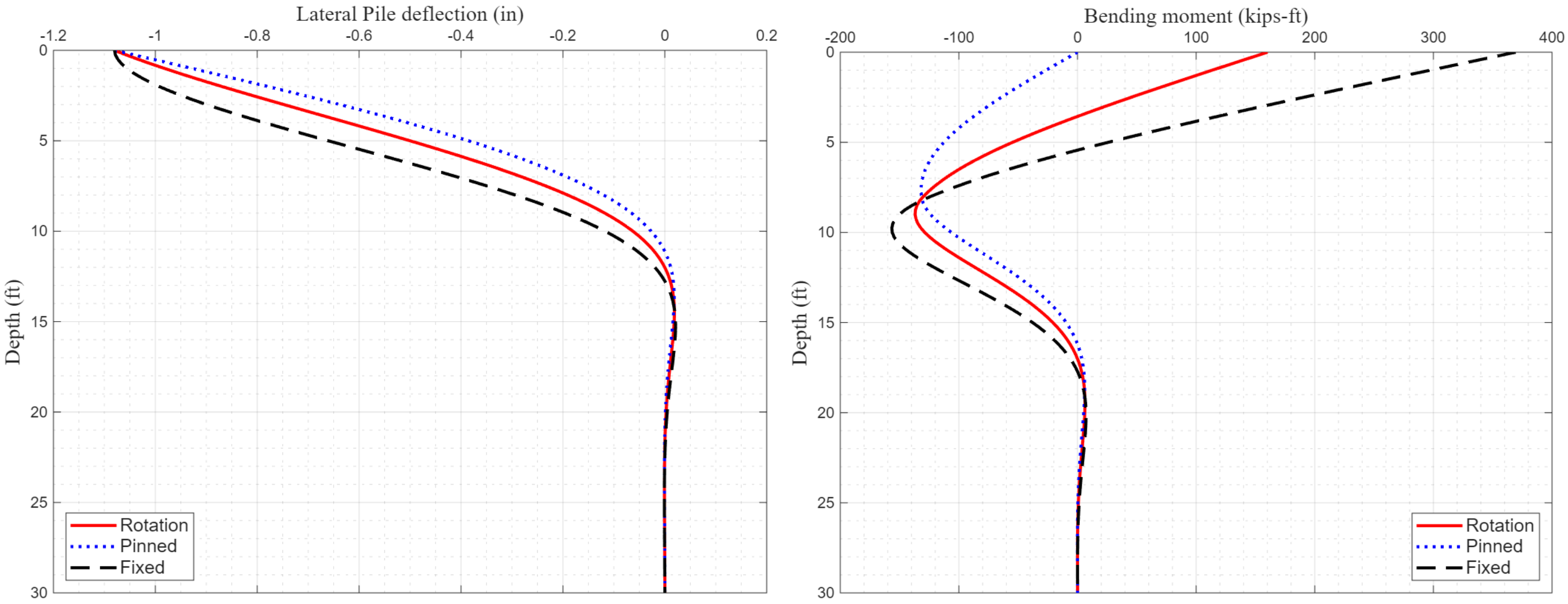

Fig. B.23 W12 x 152 pile displacement and moment profile at δ = -1.08 in. – Fixed / Rotation / Pinned

Table B.23 Quantitative data of W12x152 pile-weakfor different pile head connection-LPILE

Pile Head Deflection (inch)	Axial Force at Pile head (kips)	Pile Head Connection	Rotation at Pile Head	Max. Moment at Pile Head (kip-ft)	Max. Moment at Pile 2nd Segment (kip-ft)
-1.08	130.19	Fixed	0	369.36	-156.56
		Rotation	0.0073	160.17	-136.89
		Pinned	0.0127	0	-131.89

Chapter 3

Impact of the Abutment Wall Height, Unsymmetrical Backfill Stiffness, and the Span Length on the Behavior of an Integral Abutment Bridge

---

Abstract

Integral abutment bridges (IABs) are indeterminate framed structures. As in any indeterminate frames, the distribution of the forces among the frame members depends on the relative stiffness of their members. Therefore, parameters such as span length, abutment wall height, stiffness of soil behind the abutment walls and around the piles, roadway profile grade, use of short piles, use of Geofoam as a backfill material, and so on will control the distribution of forces among the superstructure and substructure members of IABs.

The aim of this work was to assess the impact of the variation in soil stiffness behind the backwalls caused by the sloping ground on the thermally induced displacements, forces, and moments in the foundation piles supporting the backwalls of IABs. In addition, the work aims to assess how the increase in backwall height and increase in bridge span length will effect this impact.

To conduct this assessment, full 3-D finite element models for forty-five sample multi-span IABs with nonlinear soil-structure interaction were created for use in this study. The results of the parametric study of the sample IABs show that the sloping ground can have a major impact on the thermally induced forces and moments of the piles supporting the backwalls. This impact is more critical for IABs with taller backwalls and longer spans.

Introduction

Integral abutment bridges (IABs) are indeterminate structures. Therefore, the distribution of the forces between the members of the superstructure and sub structure depends on the relative stiffness of its members. Therefore, parameters such as span length, abutment wall height, stiffness of soil behind the abutment walls and around the piles, roadway profile grade, use of short piles, use of Geofoam as a back-fill material, and so on will control the distribution of forces among thesuperstructure and substructure members of IAB.

The biggest uncertainty in the analysis and design of an integral abutment bridge (IAB) is the reaction of the soil behind the abutment walls and next to the foundation piles. The magnitude of the soil forces can become substantial during thermal expansion of the bridge system and can greatly affect the overall structural design of the bridge-wall-pile system.

In the past few decades, many researchers have studied IABs by means of finite element modeling and parametric studies [1, 2, 3, 4, 5, 6, 7, 8, 9], analytical studies [10, 11, 12, 13], experimental testing [14, 15], and field testing and data collecting [16, 17, 18, 19, 20, 21, 22], taking into account the impacts of parameters such as span length, stiffness of the soil behind the abutment walls, stiffness of the soil around piles, the abutment skew angle, short piles, orientation of piles, and so on. Many recommendations have been made which have helped bridge engineers to better understand IABs' behavior. This in turn lent itself to an increase in the construction of IABs. Many local agencies have developed their own design guidelines. However, the need still remains for a unified set of design guidelines for IABs, especially for the design of foundation piles that could be implemented by AASHTO [23].

The present study assesses the impact of the sloping ground, the backwall height range, and the bridge span length on the thermally induced displacements, forces, and moments of the piles supporting the backwalls of the IABs.

Methodology

The objective of this work has been to determine the impact of the sloping ground, the backwall height range, and the bridge span length range on the thermally induced displacements, forces, and moments in the foundation piles supporting the backwalls of IABs. To accomplish this objective, a parametric study was conducted using the commercially available finite element software, GTSTRUDL [24]. Full three-dimensional finite element models of forty-five sam- ple three-span IABs were created and analyzed.

All the sample multi-span IABs had the following assumptions in common:

- Seven girders were equally spaced 2.74 m (9 ft), where the middle girder was located at the deck center line.

- A row of seven steel piles at each abutment were equally spaced 2.74 m (9 ft), where the middle pile was located at the backwall center line.
- The back walls were 0.914 m (3 ft) wide.
- The connections between the back walls and girders were moment connections.
- The deck slab was 7.4 m (56.5 ft) wide and 0.216 m (8.5 in) thick and acting in composite with the girders.
- Steel piles supporting the backwalls were oriented in the weak direction and driven into 2.44 m (8 ft) pre-drilled holes backfilled with loose granular material.
- Solid pier caps were 1.067 m (3.5 ft) wide, 0.914 m (3.0 ft) deep, and 17.22 m (56.5 ft) long, and were supported on three concrete columns, each 0.914 m (3 ft) in diameter, with the middle column located at the bridge center line.
- The connections between the girders and pier caps were pin connections.
- The in-line wingwalls were cantilevered.
- The soils behind the backwalls were dense soils.
- The soils behind the backwalls were modeled with nonlinear springs.
- The soil stiffnesses around all piles were identical.
- The soils around the steel piles supporting the backwalls were modeled with nonlinear springs.

- The soils around the concrete piles at the bents were modeled with nonlinear springs.

- The analyses of the sample IABs were conducted for a thermal expansion of $\Delta T = 37.7^{0/c}$ ($100^{0/F}$).

And the varying factors between the sample IABs were:

- The backwall height variation, with ranges of 2.44 m (8 ft), 3 m (10 ft), and 3.7 m (12 ft).

- The total span length variation, with ranges of 45.72 m (150 ft), 83.8 m (275 ft), 121.9 m (400 ft), and 167.7 m (550 ft).

- The variation in soil stiffness, behind one backwall of $k_2 = 1.05k_1$ and $k_2 = 1.10k_1$ (See Fig.1).

- The variation in the inertias of the girders and the steel piles.

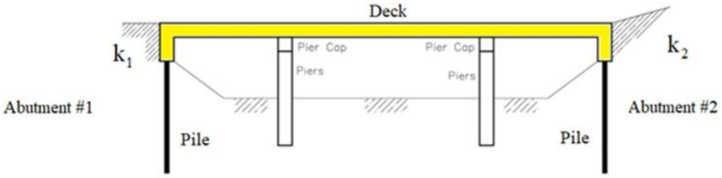

Fig. 1. Elevation view of a sample three-span IAB

Figs. 1 show the typical elevation view of the sample IABs for this study. Fig. 2 shows the displacement contour of the superstructure of a sample IAB under thermal expansion.

Fig. 3 shows the force-deflection relations, NCHRP design curves for the soil

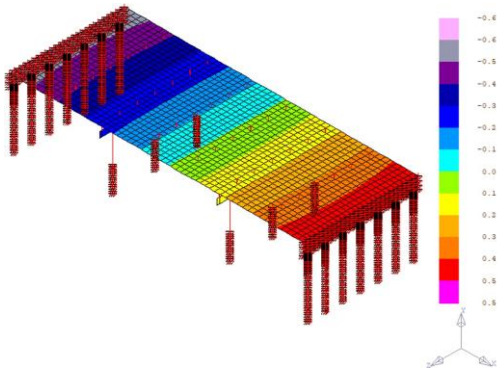

Fig. 2. Displacement contour of superstructure of a sample three-span IAB

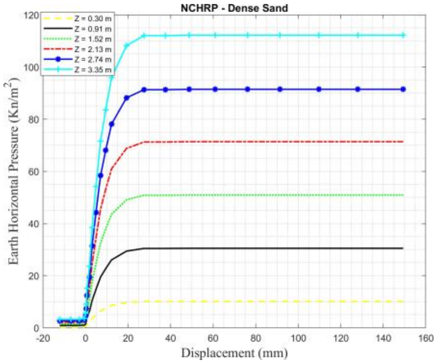

Fig. 3. Soil-abutment wall interaction design curves (NCHRP (1991)).

Table 1. Geotechnical properties of soil around piles

Soil	Layer Depth $m(ft)$	γ kg/m^3 (lb/ft^3)	ϕ (deg)	k N/mm^3 (lb/in^3)
Sand	0 – 2.44 (0 – 8) (pre-drilled)	1602 (100)	30	0.068 (250)
	2.44 – 4.42 (8.0 – 14.5)	1922 (120)	40	0.034 (125)
	4.42 – 10.97 (14.5 – 36.0)	1201 (75)	38	0.034 (125)
	10.97 – 15.24 (36.0 - 50.0)	1201 (75)	40	0.034 (125)

behind the abutment walls [25], for the typical interior node of the abutment walls used in the FE models of the sample IABs.

Table 1 shows the properties of the soil surrounding the piles for all sample IABs. LPILE 10.0 [26] software was used to create the force-deflection relations for the pile's nodes. The force-deflection relations for the top 0.9 m (3 ft) below the ground surface are shown in Fig. 4.

The impact of the wall height and span length, combined with symmetrical or un-symmetrical soil stiffnesses behind the back walls, on the thermally induced

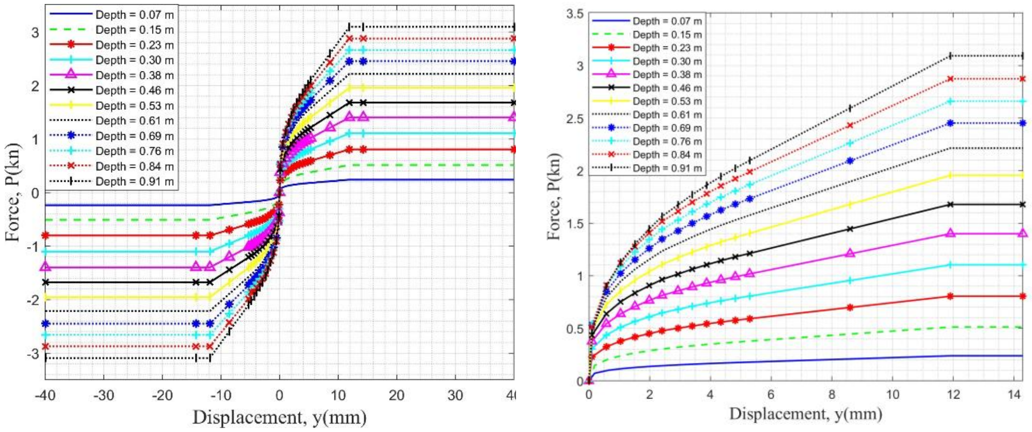

Fig. 4. P-y curves for the top 0.91 m (3 ft) of the abutment steel piles (Lpile 10.0).

forces, moments, and the displacements of the piles supporting the back walls are discussed next.

Parametric study results and discussion

Symmetrical case: Identical soil stiffnesses behind the abutment walls

For sample IABs with any given span length, an increase in the abutment wall height will cause decreases in the thermally induced forces, moments, and displacements in the piles supporting the backwalls. On the other hand, for sample IABs with a given backwall height, an increase in span length will increase the thermally induced forces, moments, and displacements in the piles supporting the abutment walls.

Figs. 5(a) and 5(b) show the displacement and moment profiles for the piles of sample IABs with a span length of 167.7 m and the abutment wall height ranges of H= 2.4, 3.0, and 3.7 m, caused by thermal expansion of $\Delta T = +37.7^{0/c}$ $(100^{0/F})$. A curve-fitting tool was used to generate 2nd degree polynomial equations to be

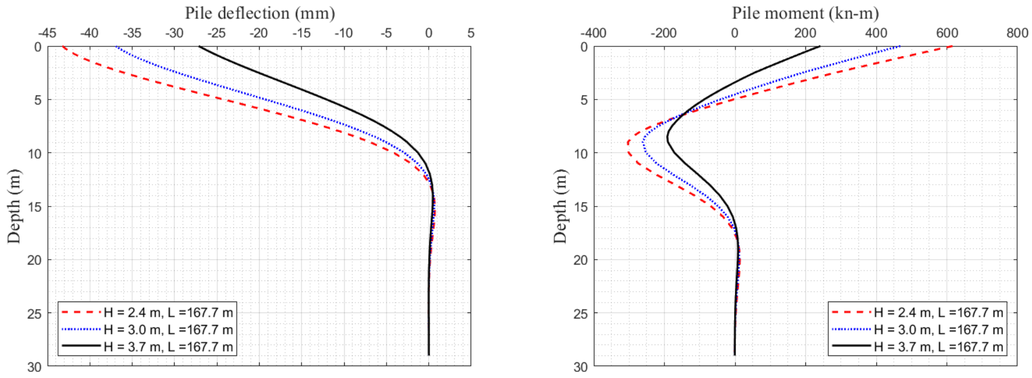

(a) **(b)**

Fig. 5. (a) Displacement and (b) moment profiles of the abutment pile for sample IABs of *L*= 167.7 m

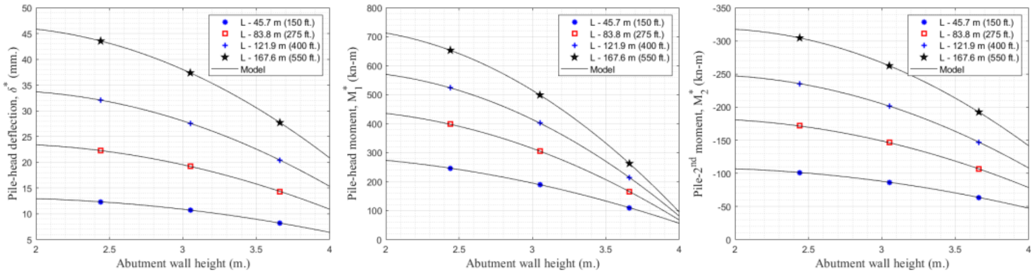

(a) **(b)** **(c)**

Fig. 6. Variations of (a) $\delta*$ (b) M_1^* (c) M_2^* vs. H, for $k_2 = k_1 = k*$

used in creating response models based on the parametric study of the sample IABs with the varying factors among them being backwall height and span length, while the other parameters were identical. These polynomial equations were used to create the plots for the pile head displacement, the pile head moment, and the pile's 2nd moment, as shown in Figs. 6 , 7, and 8. These plots will be very useful in preliminary pile design.

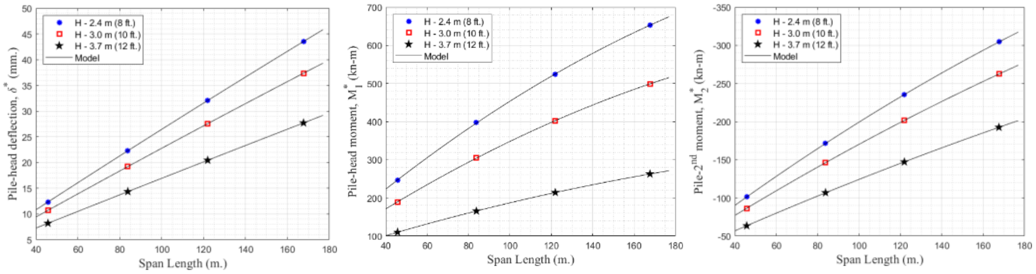

(a) **(b)** **(c)**

Fig. 7. Variations of (a) δ^* (b) M_1^* (c) M_2^* vs. L, for $k_2 = k_1 = k^*$

3.2. Unsymmetrical cases: An increase in the soil stiffness behind one abutment wall

For sample IABs with unsymmetrical soil stiffnesses behind their backwalls, $k_2 > k_1 = k^*$ (see Fig. 1), the thermally induced displacements, forces, and moments of the piles supporting the backwall with increased soil stiffness ($k_2 > k^*$) will decrease. On the other hand, the piles supporting the other backwall ($k_1 = k^*$) will experience increases in their displacements, forces, and moments when compared to the sample IABs with identical soil stiffnesses behind their backwalls ($k_2 = k_1 = k^*$).

Figs. 9 (a-f) show the impact of unsymmetrical soil stiffness behind the backwalls ($k_2 = k_1 = k^*$, $k_2 = 1.05k^*$, and $k_2 = 1.10k^*$) and variation in backwall height on the pile head, displacement, the pile head moment, and the pile's 2nd moment for sample IABs with a span length of 83.8 meters under thermal expansion.

Figs. 10 (a-f) show the ratios of the pile head displacements (non-symmetrical /symmetrical, $\frac{\delta}{\delta^*}$), the ratios of pile head moments (non-symmetrical /symmetrical, $\frac{M1}{M_1^*}$), and the rations of the piles' 2nd moments (non-symmetrical/symmetrical,

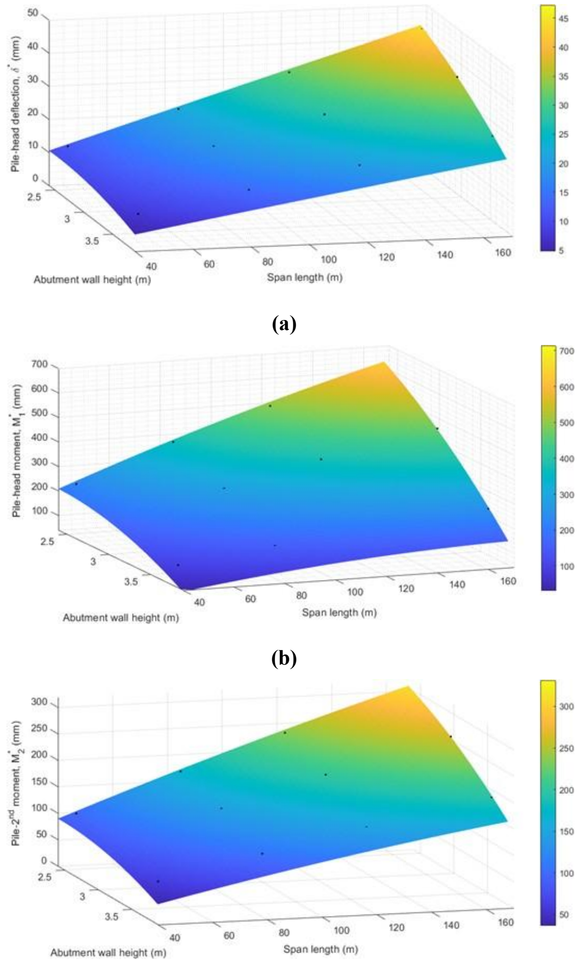

(a)

(b)

(c)

Fig. 8. 3-D presentations of (a) $\delta*$ (b) M_1^* (c) M_2^* vs. H and L, for $k_2 = k_1 = k^*$

$\frac{M_2}{M^*_2}$) vs. abutment wall height, for sample IABs with a span length of 45.7 meters, and soil stiffness increases of 5% and 10% behind one backwall ($k_2 = 1.05k*$ and $k_2 = 1.10k*$) under thermal expansion. Figs. 11 (a-f) and Figs. 12 (a-f) show similar results for sample IABs with span lengths of 83.8 and 167.7 meters.

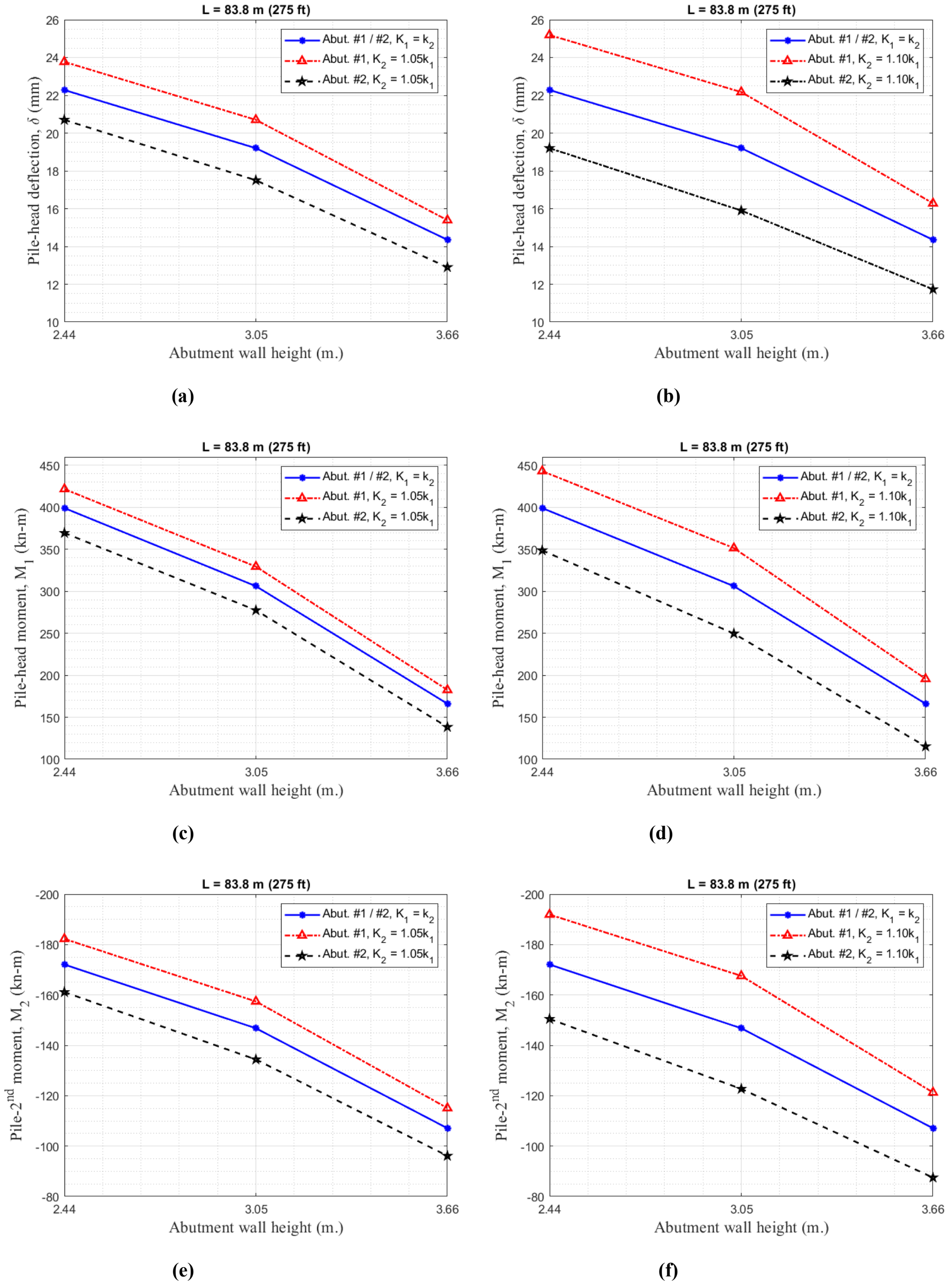

Fig. 9. Comparisons of (a-b) δ, δ^* , (c-d) M_1, M_1^*, and (e-f) M_2, M_2^* vs. H, at abutments #1 and

#2, for sample IABs of *L*= 83.8 m

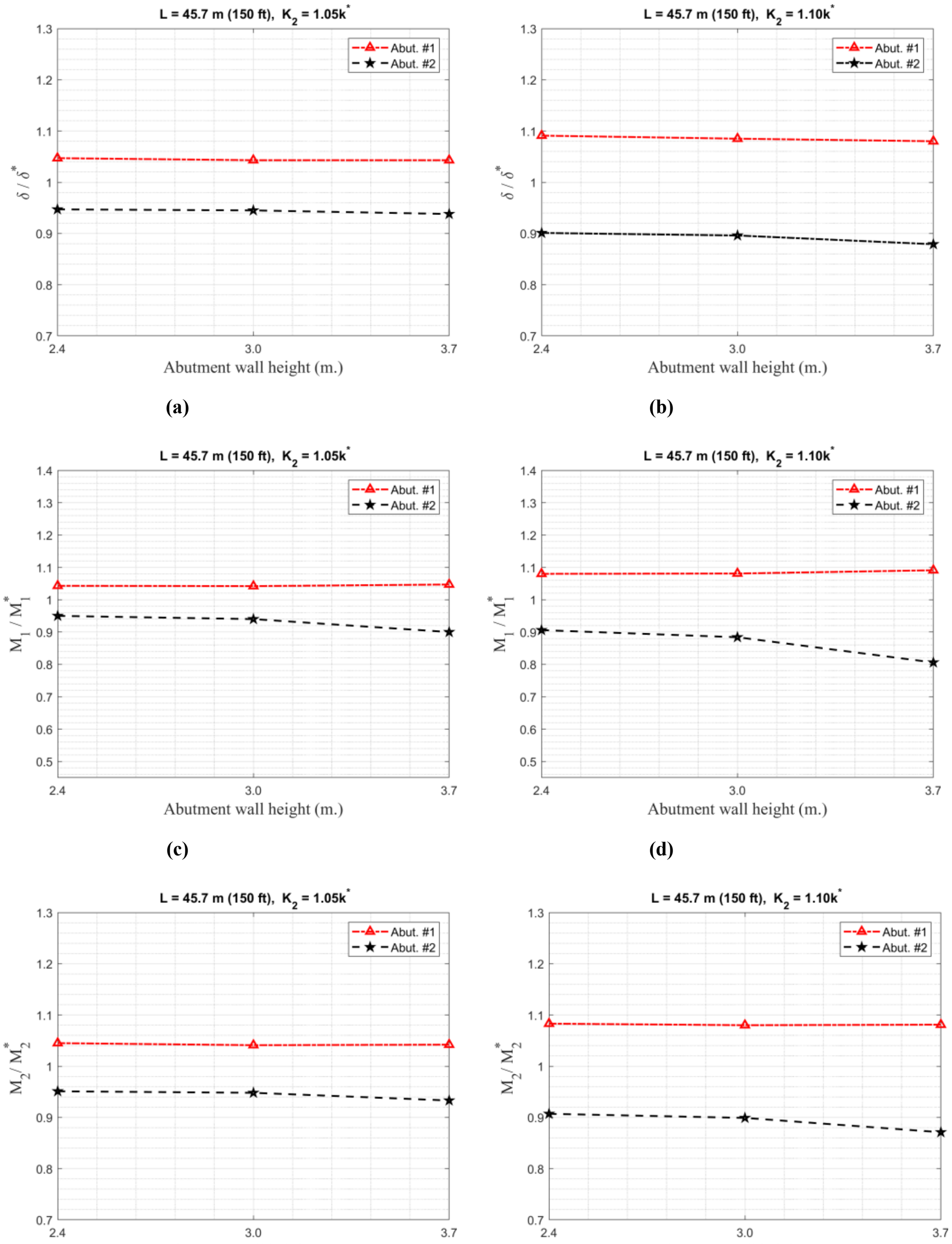

(a) (b)

(c) (d)

(e) (f)

Fig. 10. Comparison of ratios of (a-b) δ/δ^*, (c-d) M_1/M_1^*, and (e-f) M_2/M_2^* vs H, at abutment #1 and #2, for sample IABs of L= 45.7 m

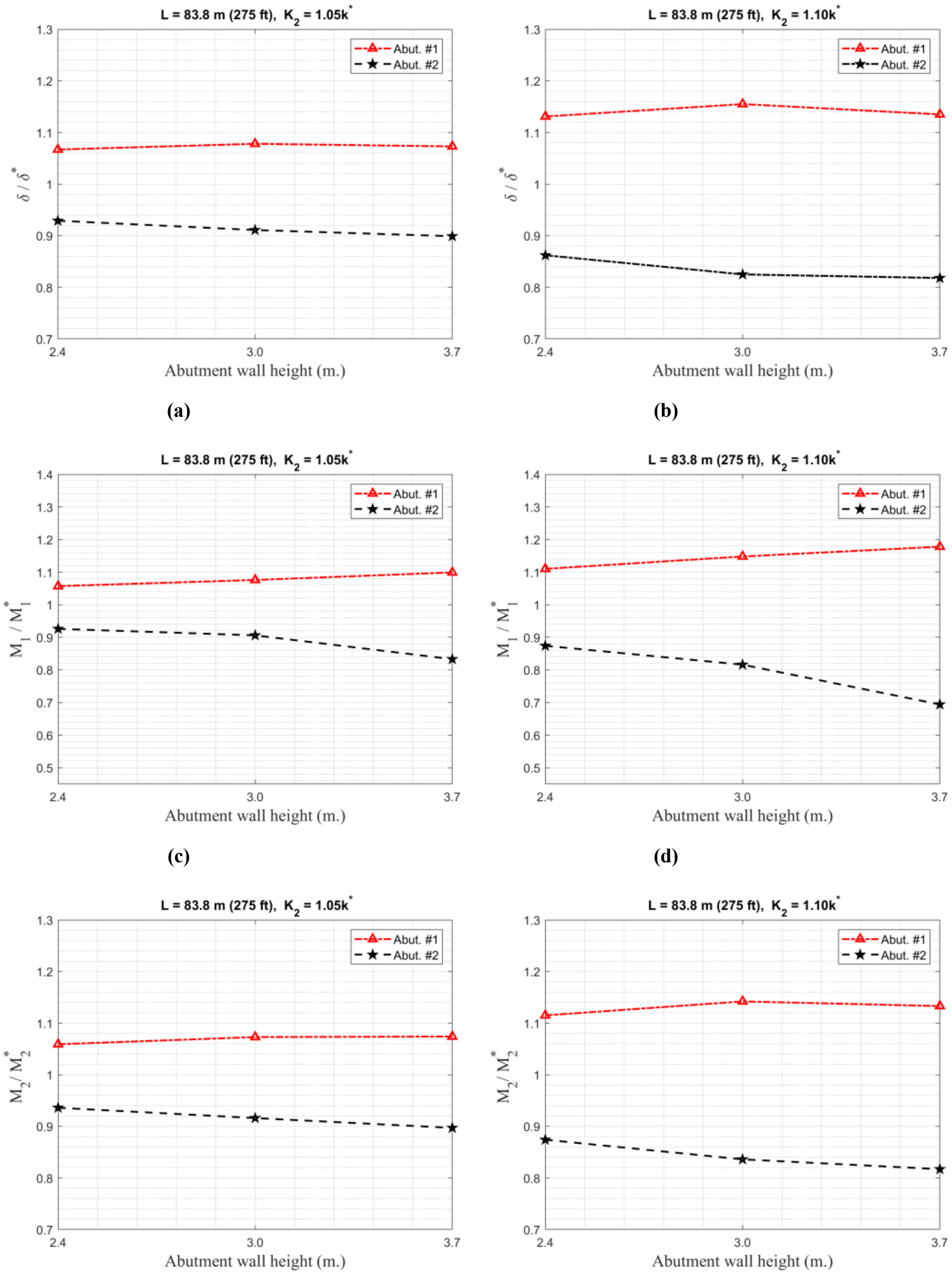

(a) **(b)**

(c) **(d)**

(e) **(f)**

Fig. 11. Comparison of ratios of (a-b) δ/δ^*, (c-d) M_1/M_1^*, and (e-f) M_2/M_2^* vs H, at abutment #1 and #2, for sample IABs of L= 83.8 m

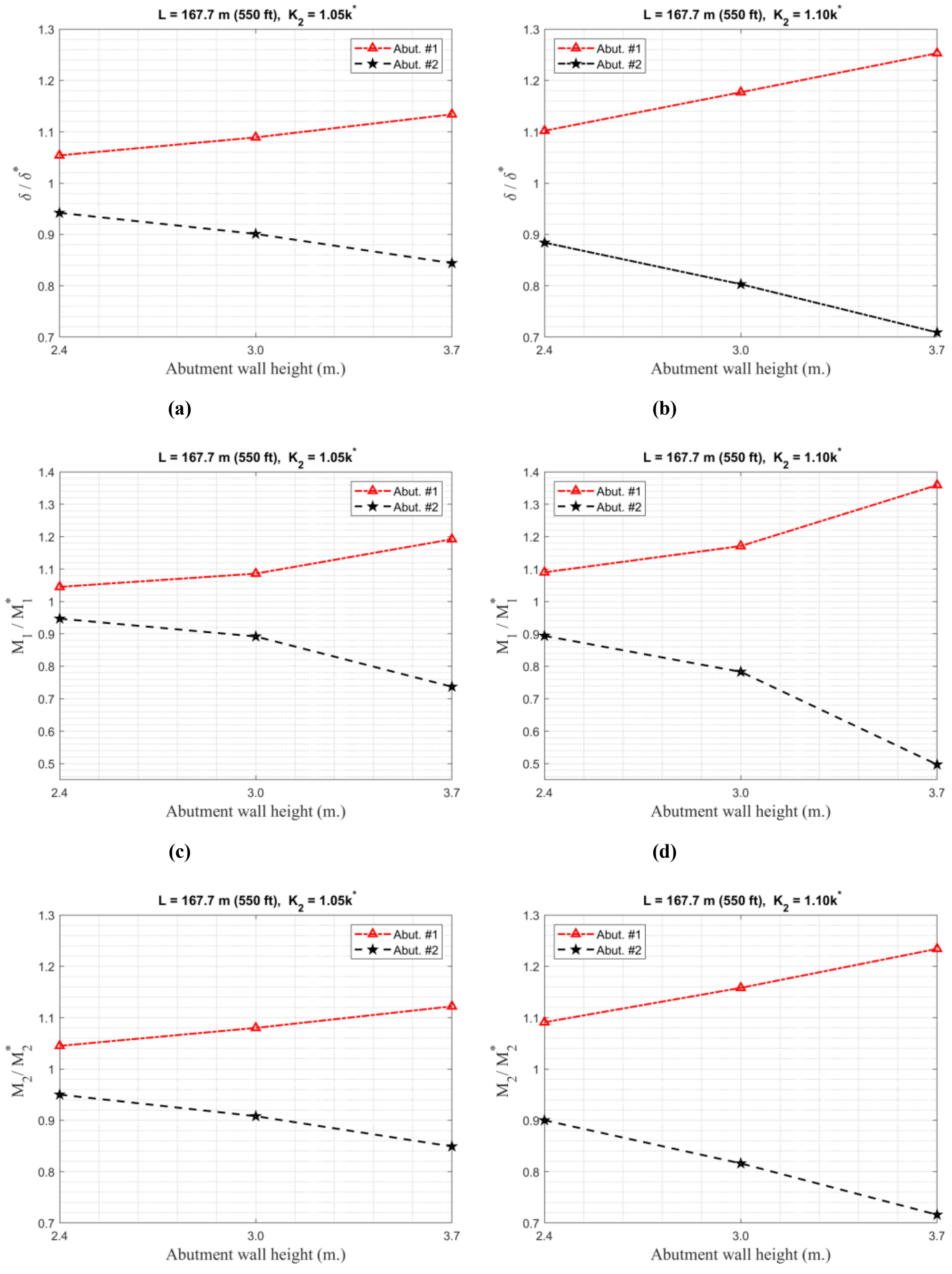

(a) (b) (c) (d) (e) (f)

Fig. 12. Comparison of ratios of (a-b) δ/δ^*, (c-d) M_1/M_1^*, and (e-f) M_2/M_2^* vs H, at abutment #1 and #2, for sample IABs of L= 167.7 m

Table 2. Data comparison for abutment piles of sample IABs of L= 167.7 m

Wall height m (ft)	Stiffness of backfill	Abutment source	$\Delta/\ \Delta*$	Pile					
				$\delta/\delta*$	v/v*	$M_1/\ M_1*$	$M_2/\ M_2*$	F/F*	$L_e/\ L_e*$
H= 2.4 (8)	$k_2 = k_1 = k*$	# 1 , # 2	1.00	1.00	1.00	1.00	1.00	1.00	1.00
	$k_1 = k*,\ k_2 = 1.02k*$	# 1	1.02	1.02	1.01	1.02	1.02	1.00	1.00
		# 2	0.98	0.98	0.98	0.98	0.98	1.00	0.99
	$k_1 = k*,\ k_2 = 1.05k*$	# 1	1.05	1.05	1.03	1.04	1.04	0.99	1.00
		# 2	0.94	0.94	0.96	0.94	0.95	1.00	0.99
	$k_1 = k*,\ k_2 = 1.10k*$	# 1	1.10	1.10	1.06	1.09	1.09	0.99	1.01
		# 2	0.89	0.88	0.91	0.89	0.90	1.00	0.98
H= 3 (10)	$k_2 = k_1 = k*$	# 1 , # 2	1.00	1.00	1.00	1.00	1.00	1.00	1.00
	$k_1 = k*,\ k_2 = 1.02k*$	# 1	1.03	1.03	1.03	1.03	1.03	1.00	1.00
		# 2	0.97	0.96	0.97	0.96	0.96	1.00	0.99
	$k_1 = k*,\ k_2 = 1.05k*$	# 1	1.07	1.09	1.06	1.08	1.08	0.99	1.01
		# 2	0.92	0.90	0.92	0.89	0.90	1.00	0.98
	$k_1 = k*,\ k_2 = 1.10k*$	# 1	1.15	1.17	1.12	1.17	1.15	0.99	1.02
		# 2	0.84	0.80	0.84	0.78	0.81	1.00	0.96
H= 3.7 (12)	$k_2 = k_1 = k*$	# 1 , # 2	1.00	1.00	1.00	1.00	1.00	1.00	1.00
	$k_1 = k*,\ k_2 = 1.02k*$	# 1	1.04	1.06	1.06	1.09	1.06	1.00	1.01
		# 2	0.96	0.93	0.92	0.88	0.93	1.00	0.98
	$k_1 = k*,\ k_2 = 1.05k*$	# 1	1.09	1.13	1.11	1.19	1.12	0.99	1.02
		# 2	0.90	0.84	0.84	0.73	0.84	1.00	0.96
	$k_1 = k*,\ k_2 = 1.10k*$	# 1	1.17	1.25	1.21	1.35	1.23	0.99	1.04
		# 2	0.82	0.70	0.69	0.49	0.71	1.00	0.96

Table 2 presents the analysis results for sample IABs with a span length of 167.7 meters, abutment wall height ranges of H= 2.4, 3.0, and 3.7 meters, and a range of

Table 3. Data comparison for abutment piles of sample IABs of L= 45.7 m

Wall height m (ft)	Stiffness of backfill	Abutment source	Δ/ Δ*	Pile				
				δ/δ^*	v/v*	M_1/M_1^*	M_2/M_2^*	F/F*
H= 2.4 (8)	$k_2 = k_1 = k^*$	# 1 , # 2	1.00	1.00	1.00	1.00	1.00	1.00
	$k_1 = k^*,\ k_2 = 1.05k^*$	# 1	1.04	1.05	1.04	1.04	1.04	0.99
		# 2	0.95	0.95	0.96	0.95	0.95	1.00
	$k_1 = k^*,\ k_2 = 1.10k^*$	# 1	1.09	1.09	1.07	1.08	1.08	0.99
		# 2	0.91	0.90	0.92	0.91	0.91	1.00
H= 3.7 (12)	$k_2 = k_1 = k^*$	# 1 , # 2	1.00	1.00	1.00	1.00	1.00	1.00
	$k_1 = k^*,\ k_2 = 1.05k^*$	# 1	1.04	1.04	1.04	1.05	1.04	0.99
		# 2	0.96	0.93	0.93	0.90	0.93	1.00
	$k_1 = k^*,\ k_2 = 1.10k^*$	# 1	1.07	1.08	1.07	1.09	1.08	0.97
		# 2	0.93	0.87	0.88	0.80	0.87	0.99

soil stiffness behind the backwalls ($k_2 = k_1 = k^*$, $k_2 = 1.02k^*$, $k_2 = 1.05k^*$, and $k_2 = 1.10k^*$) caused by a thermal expansion.

Table 3 presents similar results for sample IABs with a span length of L= 45.7 meters, abutment wall heights of H = 2.4 and 3.7 meters, and a range of soil stiffness behind the backwalls ($k_2 = k_1 = k^*$, $k_2 = 1.05k^*$, and $k_2 = 1.10k^*$) caused by a thermal expansion.

The parametric study of sample IABs (see Figs. 9 - 12 and Tables 2 - 3) show that under thermal expansion, an increase in the soil stiffness behind only one backwall caused by sloping ground or more denser soil, will cause the piles supporting the backwall with increased soil stiffness to experience decreases in their thermally induced displacements, shear, and moments when compared to the case of backwalls with identical soil stiffnesses. On the other hand, the piles supporting the other backwall will experience increases in their thermally induced displacements, shear, and moments compared to the case of backwalls with identical soil stiffnesses behind them. This increase or decrease in pile's displacements, shear, and moments is more critical for IABs with taller backwalls and longer spans. As shown in Figs. 9 - 12 and Tables 2 - 3 this increase specially in pile' pile head moment can increased more than 30% for IABs with long span and tall backwall height.

Also the parametric study show that the impact of the sloping ground on thermally induced axial forces of the pile and it's the fixity point is negligible. (see Table 3). All the data presented in the plots and tables are for piles located on the centerline of the bridge.

Table 4. Data comparison for abutment piles of sample IABs of *L*= 45.7 m and *H*= 2.4 m

Stiffness of backfill	Abutment source	Case: 1*				Case: 2*			
		Δ/Δ^*	Pile			Δ/Δ^*	Pile		
			δ/δ^*	v/v*	M_l/M_l^*		δ/δ^*	v/v*	M_l/M_l^*
$k_2 = k_1 = k^*$	# 1 , # 2	1.00	1.00	1.00	1.00	1.00	1.00	1.00	1.00
$k_1 = k^*,\ k_2 = 1.05k^*$	# 1	1.03	1.03	1.02	1.03	1.04	1.05	1.04	1.04
	# 2	0.97	0.95	0.95	0.93	0.95	0.95	0.96	0.95
$k_1 = k^*,\ k_2 = 1.10k^*$	# 1	1.06	1.06	1.04	1.06	1.09	1.09	1.07	1.08
	# 2	0.94	0.90	0.91	0.85	0.91	0.90	0.92	0.91

*Case : 1 Based on actual design inertias of the girders and piles

*Case : 2 Based on assumed inertias of the girders and piles

In IABs, the thermally induced axial force, shear, and moment varies from pile

Table 5. Data for abutment piles of sample IABs of *L*= 167.7 m - More flexible superstructure

Wall height m (ft)	Stiffness of backfill	Abutment source	Δ/Δ^*	Pile				
				δ/δ^*	v/v*	M_1/M_1^*	M_2/M_2^*	F/F*
H= 2.4 (8)	$k_2 = k_1 = k^*$	# 1 , # 2	1.00	1.00	1.00	1.00	1.00	1.00
	$k_1 = k^*,\ k_2 = 1.05k^*$	# 1	1.10	1.13	1.12	1.16	1.13	0.99
		# 2	0.89	0.85	0.85	0.79	0.85	1.00
	$k_1 = k^*,\ k_2 = 1.10k^*$	# 1	1.19	1.25	1.21	1.29	1.24	0.98
		# 2	0.80	0.71	0.71	0.62	0.71	1.00

to pile. The variation in shear and moment values are small but the variation in the pile's axial force is major. Therefore, a full three-dimensional finite element modeling of IABs for thermal loading is necessary.

Note that in all of the above findings the inertias of girders and inertias piles were kept the same for all of the sample IABs. The selected inertias for the girders and piles were based on the design requirements for the girders and piles of the longest sample IAB. This assumption made both the superstructure and substructure of shorter span IABs stiffer than they needed to be but did not change the relative stiffness of superstructure to substructure and therefore did not impact our findings. This was verified by comparing the data from the analysis of the shorter sample span IABs, using the inertias for the girders and the piles that they were originally designed for, with the data from the analysis using the inertias for the girders and piles used in this study. Table 4 shows this comparison for IABs with a span length of *L*= 45.7 meters and an abutment wall height of *H*= 2.4 meters, and a range of soil stiffness behind the backwalls ($k_2 = k_1 = k^*$, $k_2 = 1.05k^*$, and $k_2 = 1.10k^*$)

caused by a thermal expansion.

Conclusion

The goal of this parametric study was to examine the impact of the variation in soil stiffness behind the backwalls caused by the sloping ground, abutment wall height ranges, and the span length ranges on the thermally induced forces, the moments, and the displacements of the steel piles supporting the backwalls of the three-span IABs. Full three-dimensional finite element models of forty- five sample three-span IABs were created and analyzed. In order to limit the number of variables, the inertias of the girders and the piles were kept the same for the all sample IABs. The selected inertias for the girders and piles were basedon the design requirements for the girders and piles of the longest sample IAB. This assumption made both the superstructure and substructure of shorter span IABs stiffer than they needed to be but did not change the relative stiffness of superstructure to substructure and therefore did not impact our findings. This was verified by comparing the data from the analysis of the shorter sample span IABs, using the inertias for the girders and the piles that they were originally designed for, with the data from the analysis using the inertias for the girders and piles used in this study.

The following are the summary of findings based on this parametric study of sample IABs under thermal expansion.

In IABs, the thermally induced axial force, shear, and moment varies from pileto pile. The variation in shear and moment values are small but the variation in the pile's axial force is major. Therefore, a full three-dimensional finite element modeling of IABs for thermal loading is necessary.

The plots that have been created, based on 2nd degree polynomial equations for pile head displacement, the pile head moment, and the pile's 2nd moment vs. ranges of abutment wall height and span length ranges, will be very useful in the preliminary design of piles supporting the backwall.

The impact of the sloping ground on thermally induced axial forces of the pile and it's fixity point is negligible. Under thermal expansion, an increase in the soil stiffness behind one backwall caused by sloping ground or denser soil, will cause the piles supporting the backwall with increased soil stiffness to experience decreases in their thermally induced displacements, forces, and moments when compared to the case of backwalls with identical soil stiffnesses. On the other hand, the piles supporting the other backwall will experience increases in their thermally induced displacements, forces, and moments compared to the case of backwalls with identical soil stiffnesses behind them.

The variation in soil stiffness behind the backwalls caused by the sloping ground can have a major impact on the thermally induced lateral displacement, shear, and moment of the piles supporting the backwalls of IABs. This impact is more critical for IABs with taller backwalls and longer spans. Therefore, we should design accordingly, to optimize the design, reduce construction costs, increase safety, and enable the construction of longer span IABs.

Notation

The following symbols are used in this paper:

H = Wall height

k = Soil subgrade reaction

k^*, k_1, k_2 = Stiffness spring parameter

L = Total span length of sample IABs

L_e^*, L_e = Effective pile length

M_1^*, M_1 = Pile head moment

M_2^*, M_2 = Pile's 2nd segment moment

V^*, V = Pile head shear

ΔT = Temperature change

Δ^*, Δ = Wall displacement at the deck level

ϕ = Internal friction angle of soil material

γ = Weight density of soil material

δ^*, δ = Pile head displacement

θ^*, θ = Pile head rotation

References

[1] D. W. Conboy, E. J. Stoothoff, Integral abutment design and construction: The new england experience, Proceedings of the Integral Abutment and Jointless Bridges Conference, Federal Highway Administration (2005) 50–60.

[2] S. Faraji, J. Ting, D. Crovo, J. Ernst, Non-linear analysis of integral bridges: finite element model, Geotech Geoenviron Engineering 127(5) (2001) 454–461.

[3] D. Gama, J. Almeida, Concrete integral abutment bridges with reinforced concrete piles, Structural Concrete 15 (2014) 292–304.

[4] R. Khard, R. Shreedhar, Analysis of integral abutment bridge by grillage method, NBM& CW 172–183.

[5] Y. A. Khodair, S. Hassiotis, Analysis of soil–pile interaction in integral abutment, Computers and Geotechnics 32 (2005) 201–209.

[6] W. Kim, J. Laman, Integral abutment bridge response under thermal loading, Engineering Structures 32 (2010) 1495–1508.

[7] D. Perić, M. Miletić, B. R. Shah, A. Esmaeily, H. Wang, Thermally induced soil structure interaction in the existing integral bridge, Engineering Structures 106 (2016) 484–494.

[8] T. Shaikh, K. L.G., Behavior of integral abutment bridge by different end conditions, International Journal of Current Engineering and Technology 4 (2014) 2875–2879.

[9] T. Zordan, B. Briseghella, C. Lan, Parametric and pushover analyses on integral abutment bridge, Engineering Structures 3392) (2011) 502–515.

[10] M. Dicleli, S. Albhaisi, Analytical formulation of maximum length limits of integral bridges on cohesive soils, Canadian Journal of Civil Engineering 32 (2005) 726–738.

[11] M. Dicleli, S. Albhaisi, Performance of abutment–backfill system under thermal variations in integral bridges built on clay, Engineering Structures 26 (2004) 949–962.

[12] J. Kunin, S. Alampalli, Integral abutment bridges: Current practice in united states and canada, Journal of Performance of Constructed Facilities 14(3) (2000) 104.

[13] S. Xu, K. Kannangara, E. Taciroglu, Analysis of the stress distribution across a retaining wall backfill, Computers and Geotechnics 103 (2018) 13–25.

[14] A. Alqarawi, C. Leo, D. Liyanapathirana, Effects of wall movements on performance of integral abutment bridges, International Journal of Geomechanics 20(2) (2020) 04019157.

[15] C. Jiang, Z. Zhang, H. Jiali, Nonlinear analysis of combined loaded rigid piles in cohesionless soil slope, Computers and Geotechnics 117 (2020) 103225.

[16] W. Davids, T. Sandford, S. neé Hartt, J. DeLano, C. Lyons, Field-measured response of an integral abutment bridge with short steel h-piles, Journal of Bridge Engineering 15(1) (2010) 32–43.

[17] Y. Deng, B. M. Phares, L. Greimann, G. L. Shryack, J. J. Hoffman, Behavior of curved and skewed bridges with integral abutments, Journal of Constructional Steel Research 109 (2015) 115–136.

[18] M. Dicleli, S. Albhaisi, Maximum length of integral bridges supported on steel h-piles driven in sand, Engineering Structures 25 (2003) 1491–1504.

[19] J. Huang, C. Shield, C. French, Behavior of an integral abutment bridge in minnesota, Structural Engineering International 21(3) (2011) 320–331.

[20] Y. A. Khodair, S. Hassiotis, Rigidity of abutments in integral abutment bridges, Structure and Infrastructure Engineering 9(2) (2013) 201–209.

[21] S.-H. Kim, J.-H. Ahn, C.-Y. Jung, J.-W. Jang, P. Young-Ho, Behavior of steel-box semi-integral abutment bridge considering temperature-earth pressure change, International Journal of Steel Structures 14 (2014) 117–140.

[22] T. Sanford, M. Elgaaly, Skew effects on backfill pressures at frame bridge abutments, Transportation research record 1145 (1993) 1–11.

[23] AASHTO, LRFD Bridge Design Specifications, Washington, D.C. (2020).

[24] GT STRUDL, Hexagon/Intergraph Corp., Madison, AL (2022).

[25] J. Barker, R.M. and Duncan, K. Rojiani, C. Tan, K. S.G., Manuals for the Design of Bridge Foundations, National Cooperative Highway Research Program (NCHRP), Washington, D.C. (1991).

[26] LPILE 22.0, Ensoft Inc., Austin, Texas.

Appendix C

GTSTRUDL & LPILE Data and Plots

Appendix C presents the three-dimensional finite element analyses conducted to evaluate the response of integral abutment bridges under thermal loading using GTStrudl. The analyses build directly on the geotechnical characterization and pile–soil interaction modeling established in Appendix I. The same soil profiles and nonlinear p–y springs defined in Appendix I were implemented consistently in the structural models, ensuring continuity between local pile response and system-level bridge behavior.

The numerical models represent single-span and multi-span integral abutment bridges with span lengths of 150 ft, 275 ft, 400 ft, and 550 ft. Structural geometry, pile configuration, and material properties were based on the Fitchburg Bridge, Massachusetts, allowing the study to reflect realistic construction and subsurface conditions. Nonlinear soil springs were assigned to the piles and abutment backwalls using the p–y relationships previously developed. Thermal loading was applied to simulate seasonal expansion and contraction of the superstructure, inducing longitudinal displacements at the abutments and corresponding demands on the foundation piles.

The parametric study focused on three key variables that directly influence pile demand in integral abutment bridges: (1) the variation of backfill stiffness of one abutment with respect to the other within the range of 0% to 10%, (2) different backwall heights ranging from 8 ft, 10 ft, and 12 ft; and (3) bridge span lengths varying from 150 ft to 550 ft. These parameters were selected to isolate their combined and individual effects on thermally induced pile displacements, bending moments, and axial forces within a fully three-dimensional framework.

The justification for analyzing these parameters lies in their direct relevance to current design uncertainties. Differences in backfill stiffness between abutments are common in practice due to construction sequencing, compaction variability, and aging effects, yet their influence on pile demand is not well quantified. Abutment height and span length govern thermal displacement magnitude and restraint stiffness, making them primary drivers of pile response. By examining these variables within a unified 3D model using field-derived soil properties, Appendix III provides insight into how realistic variations in boundary conditions influence pile behavior and overall integral abutment bridge performance.

Effect of Abutment Wall Height – 150 ft (Dense – backfill)

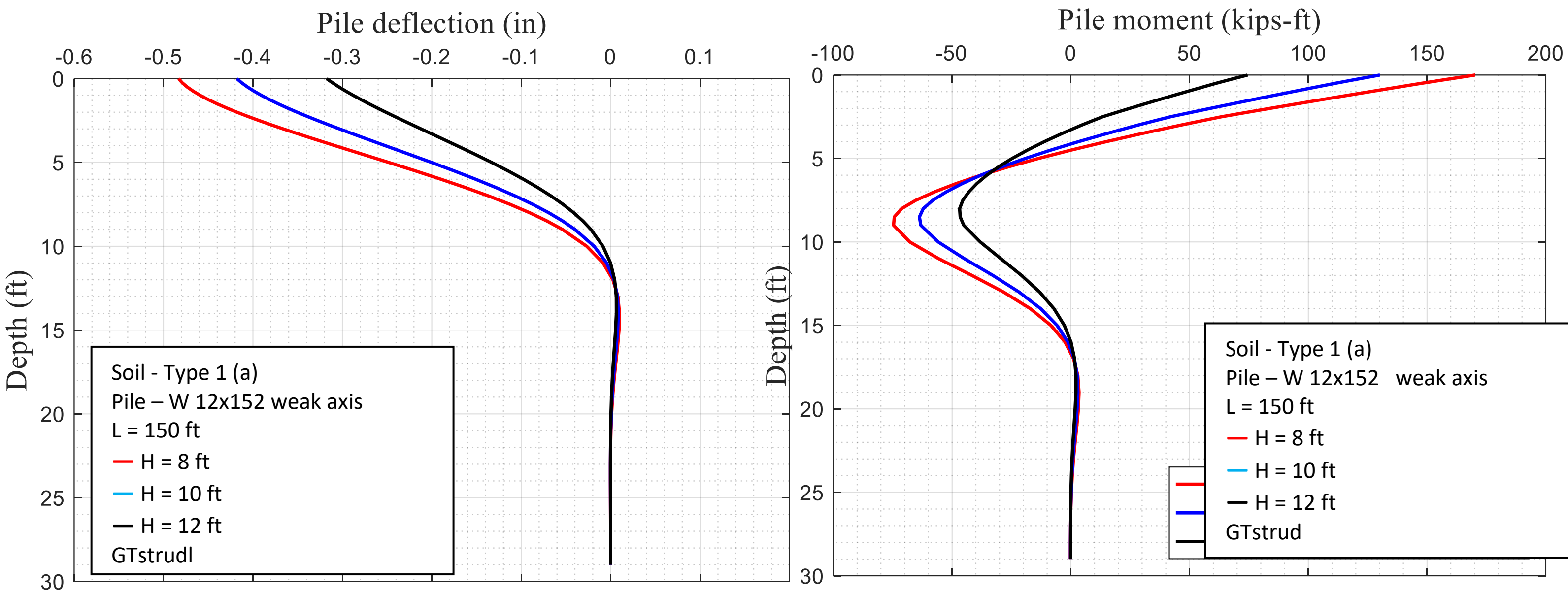

Fig. C.1 Lateral displacement and bending moment profiles of the W12x152 pile caused by $\Delta T = 100^{0F}$

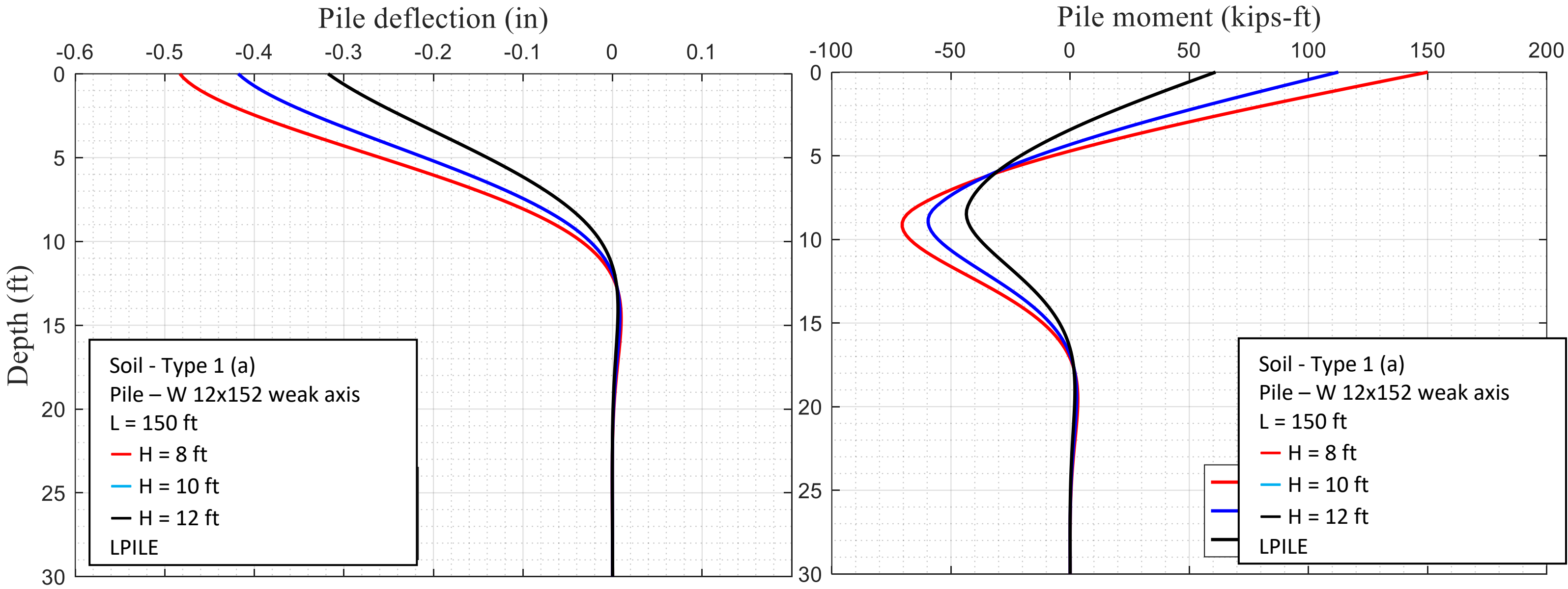

Fig. C.2 Comparison of lateral displacement and bending moment profiles of the W12x152 pile for L=150 ft, a range of abutment wall height, H, caused by $\Delta T = 100^{0F}$,

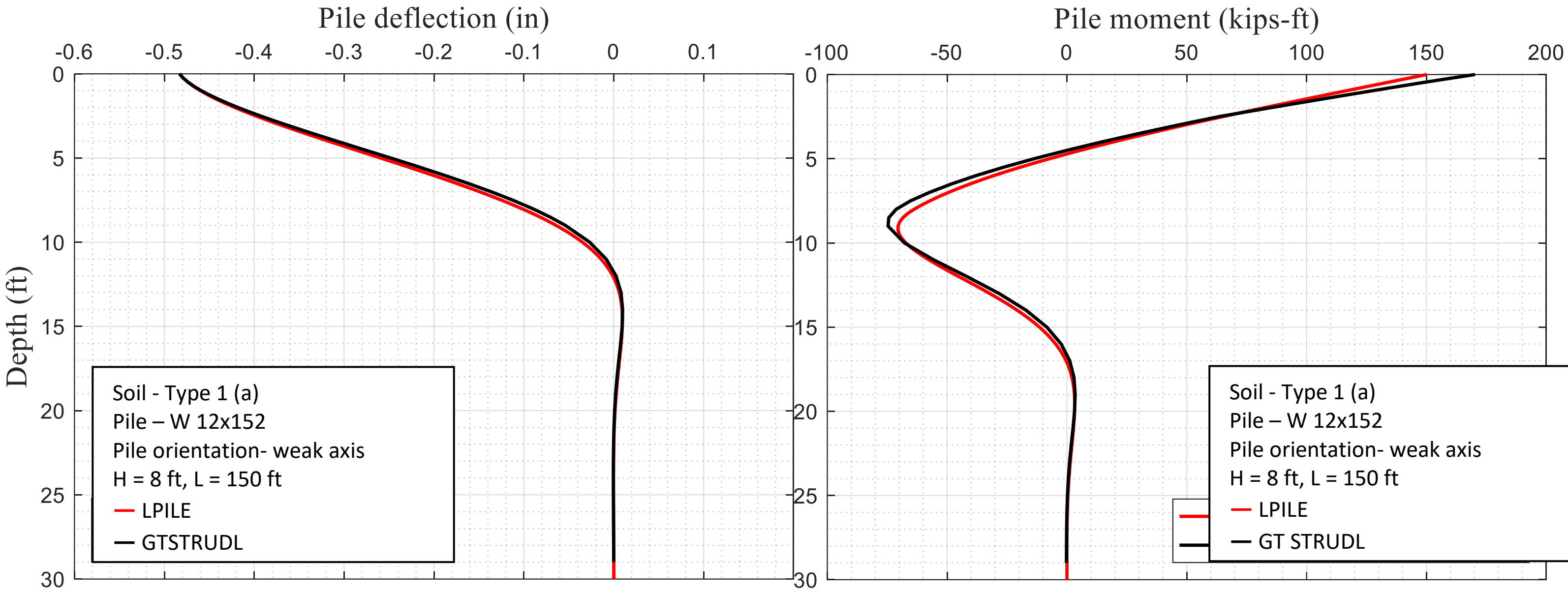

Fig. C.3 W 12x152 pile displacement and moment due to temp. – 150 ft span / H=8 / Lpile vs. GTSrudl

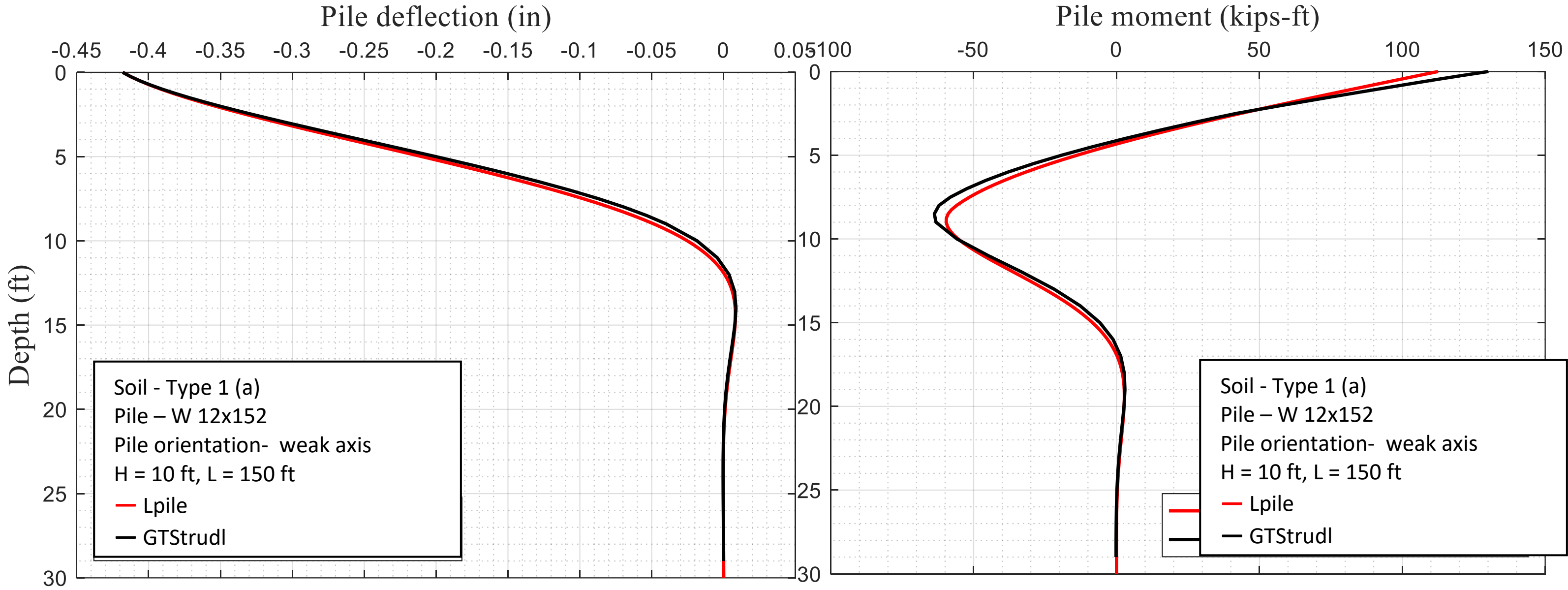

Fig. C.4 W 12x152 pile displacement and moment due to temp. – 150 ft span / H=10 / Lpile vs. GTSrudl

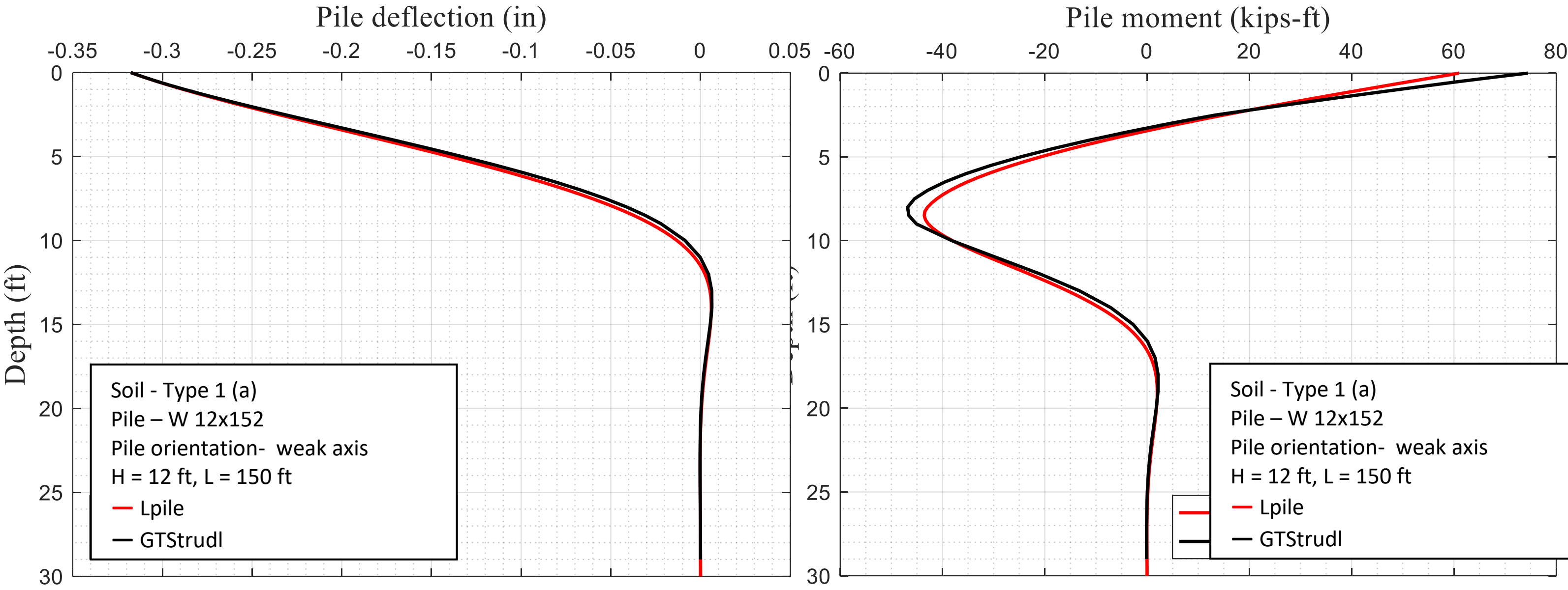

Fig. C.5 W 12x152 pile displacement and moment due to temp. – 150 ft span / H=12 / Lpile vs. GTSrudl

Effect of Abutment Wall Height – 275 ft (Dense – backfill)

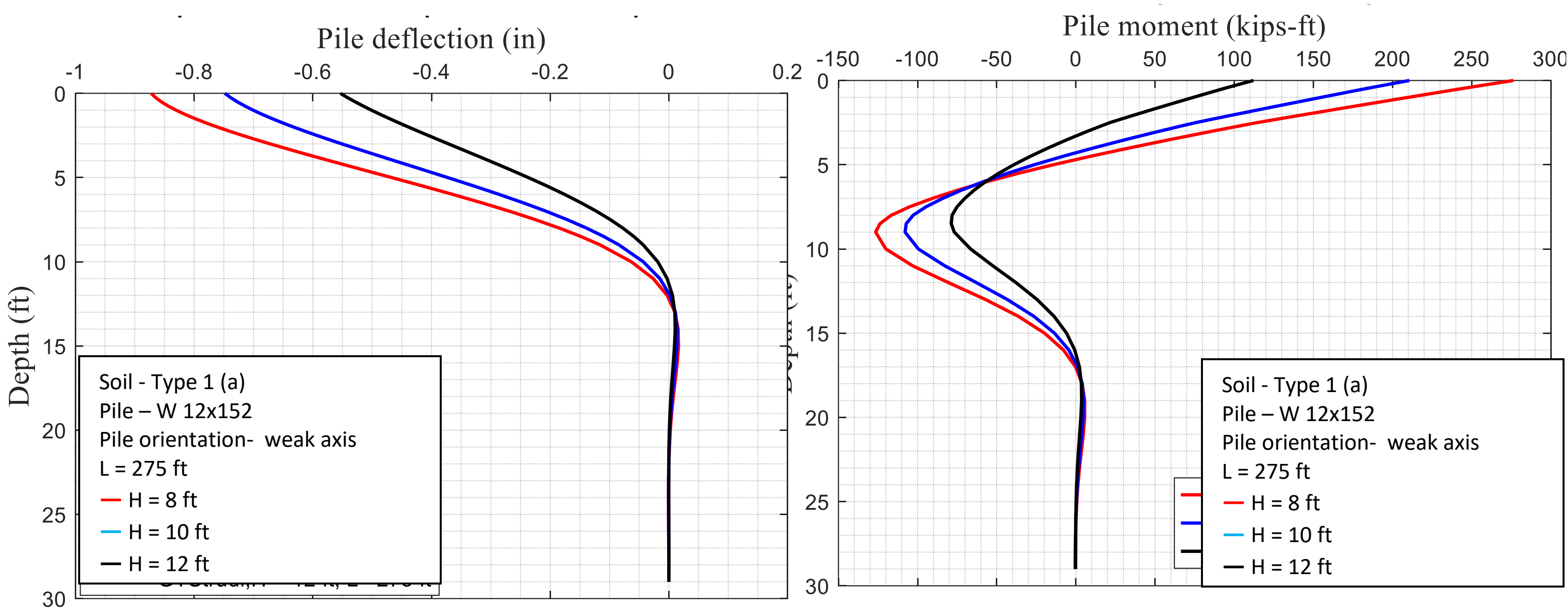

Fig. C.6 W 12x152 pile displacement and moment due to temp. – 275 ft span / weak axis / GTStrudl

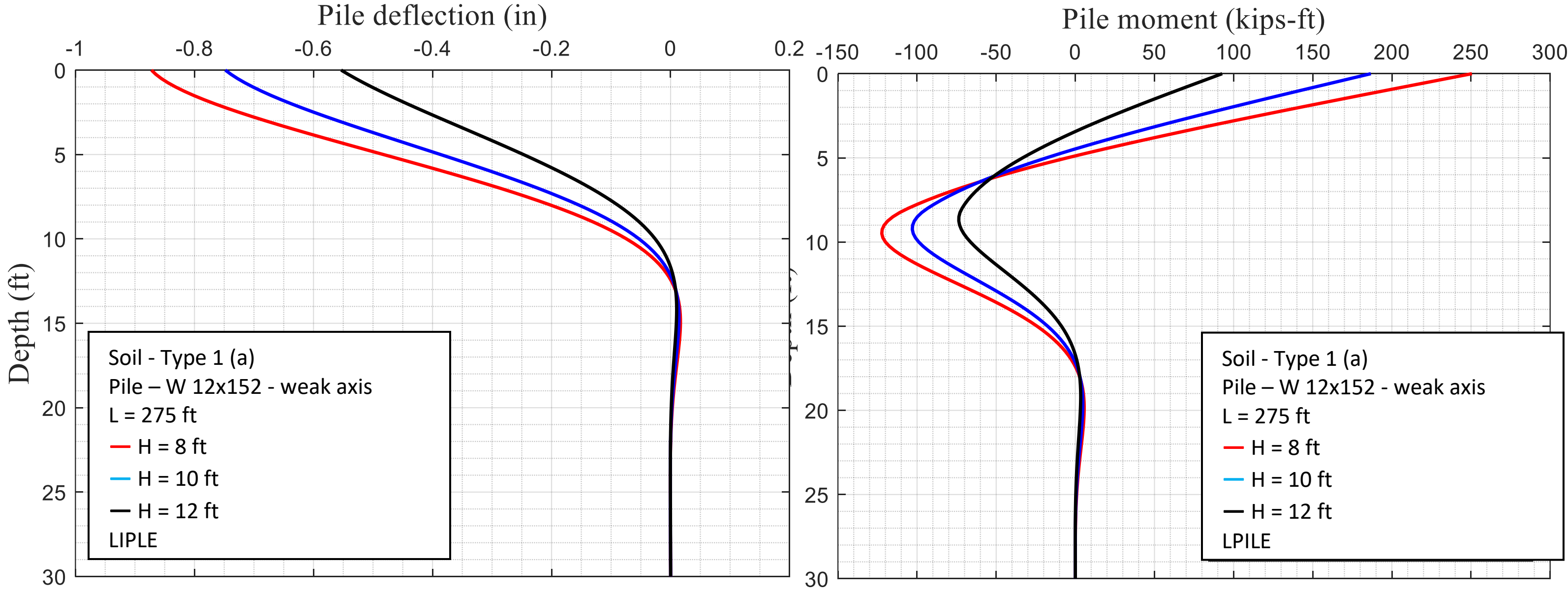

Fig. C.7 W 12x152 pile displacement and moment due to temp. – 275 ft span / weak axis / LPILE

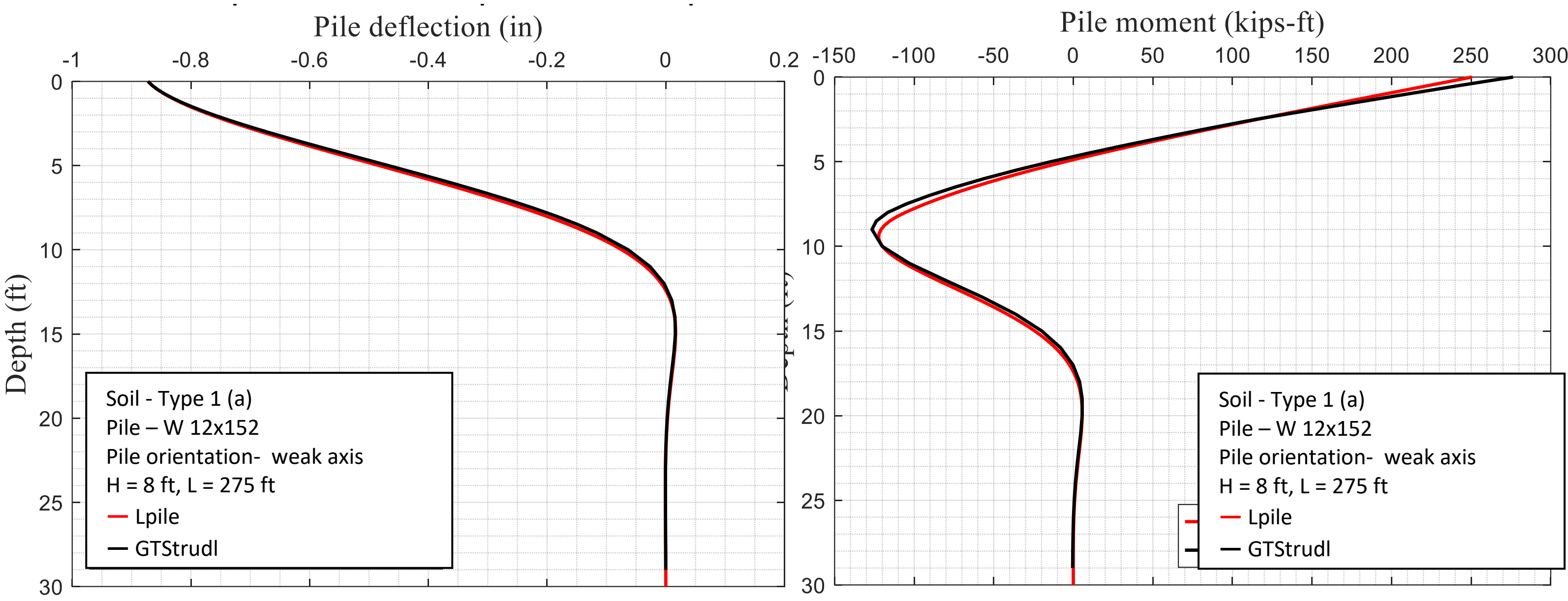

Fig. C.8 W 12x152 pile displacement and moment due to temp. – 275 ft span / H=8 , Lpile vs. GTStrudl

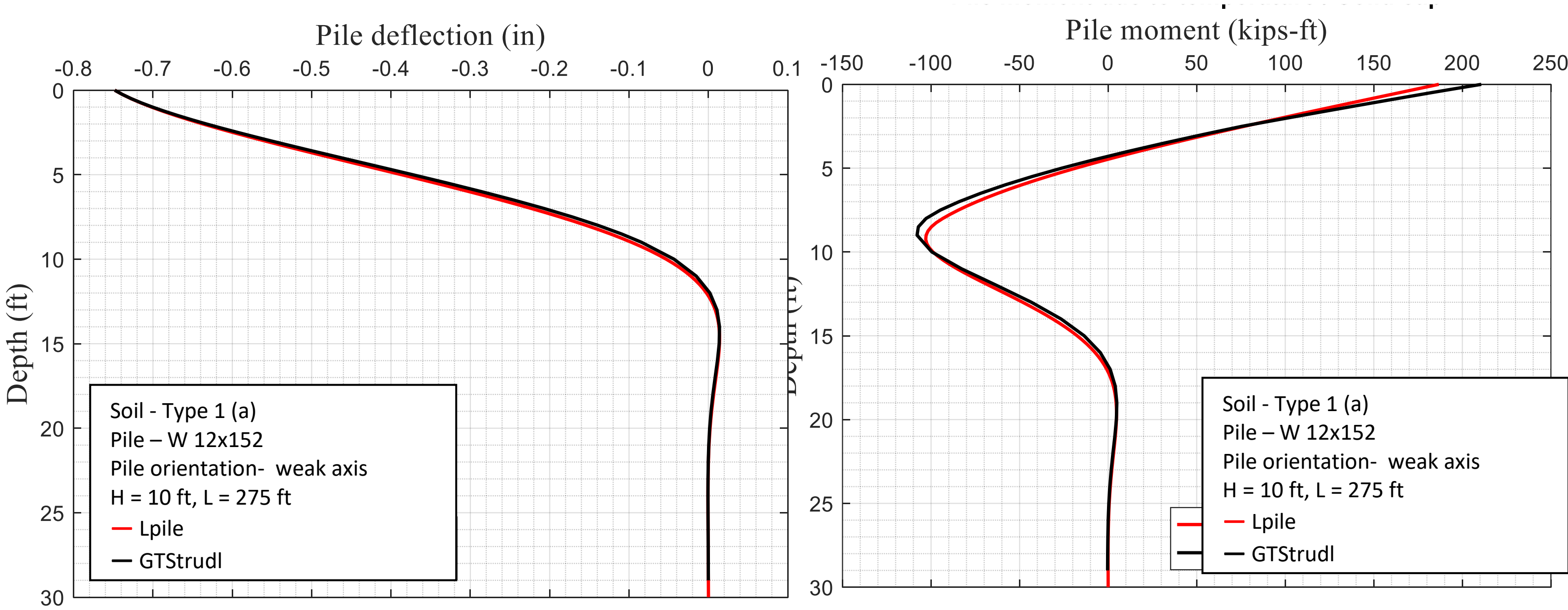

Fig. C.9 W 12x152 pile displacement and moment due to temp. – 275 ft span / H=10, Lpile vs. GTStrudl

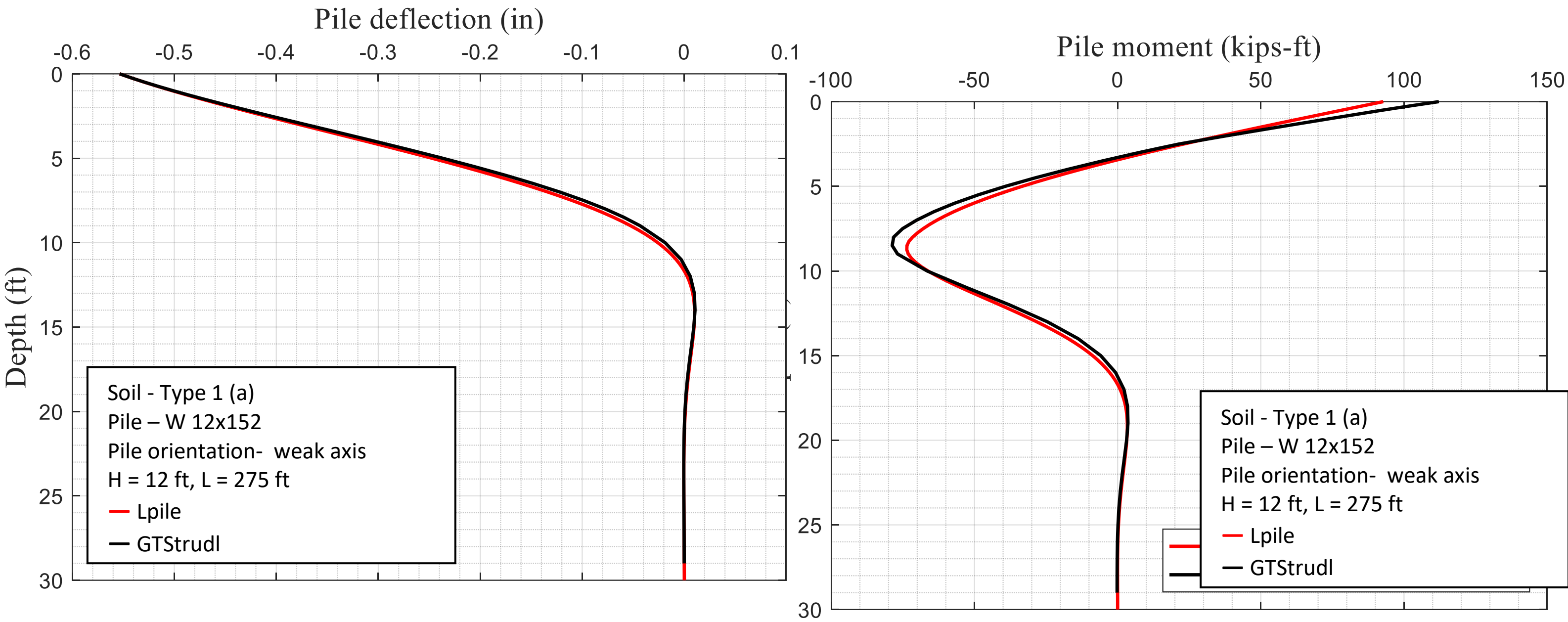

Fig. C.10 W 12x152 pile displacement and moment due to temp. – 275 ft span / H=12, Lpile vs. GTStrudl

Effect of Abutment Wall Height – 400 ft (Dense – backfill)

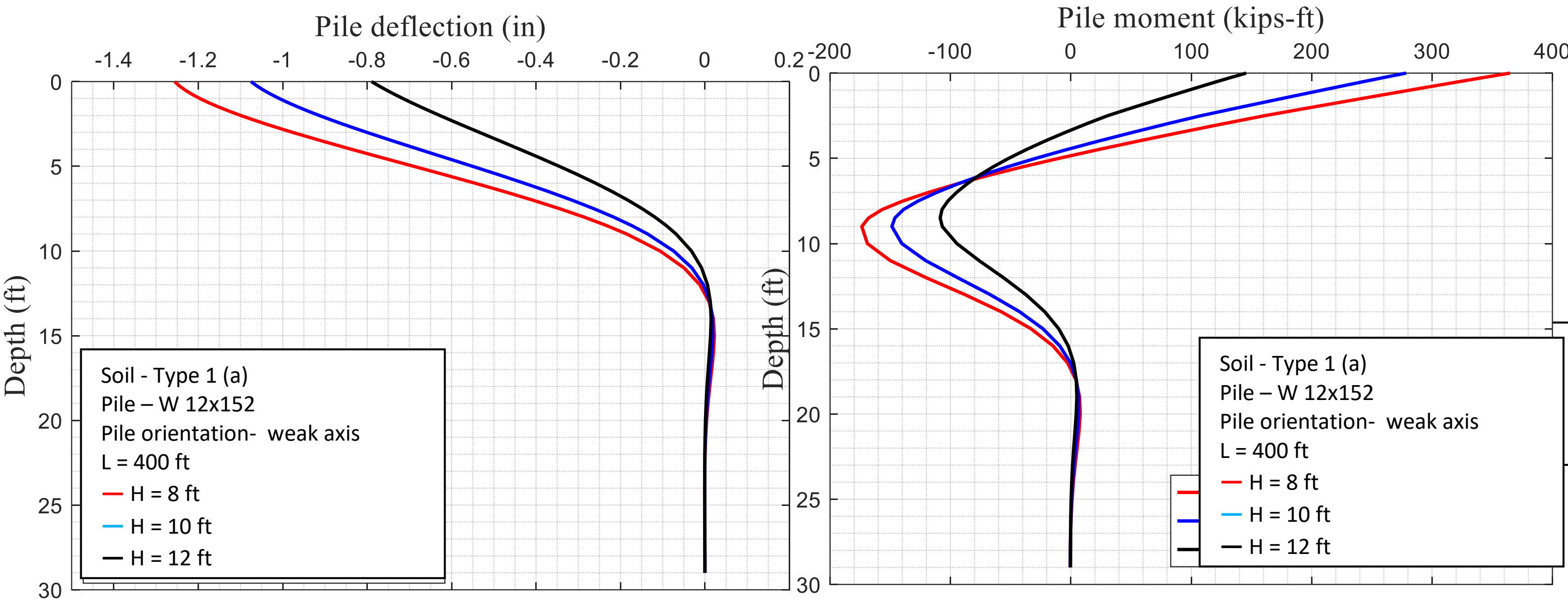

Fig. C.11 W 12x152 pile displacement and moment due to temp. – 400 ft span / weak axis / GTStrudl

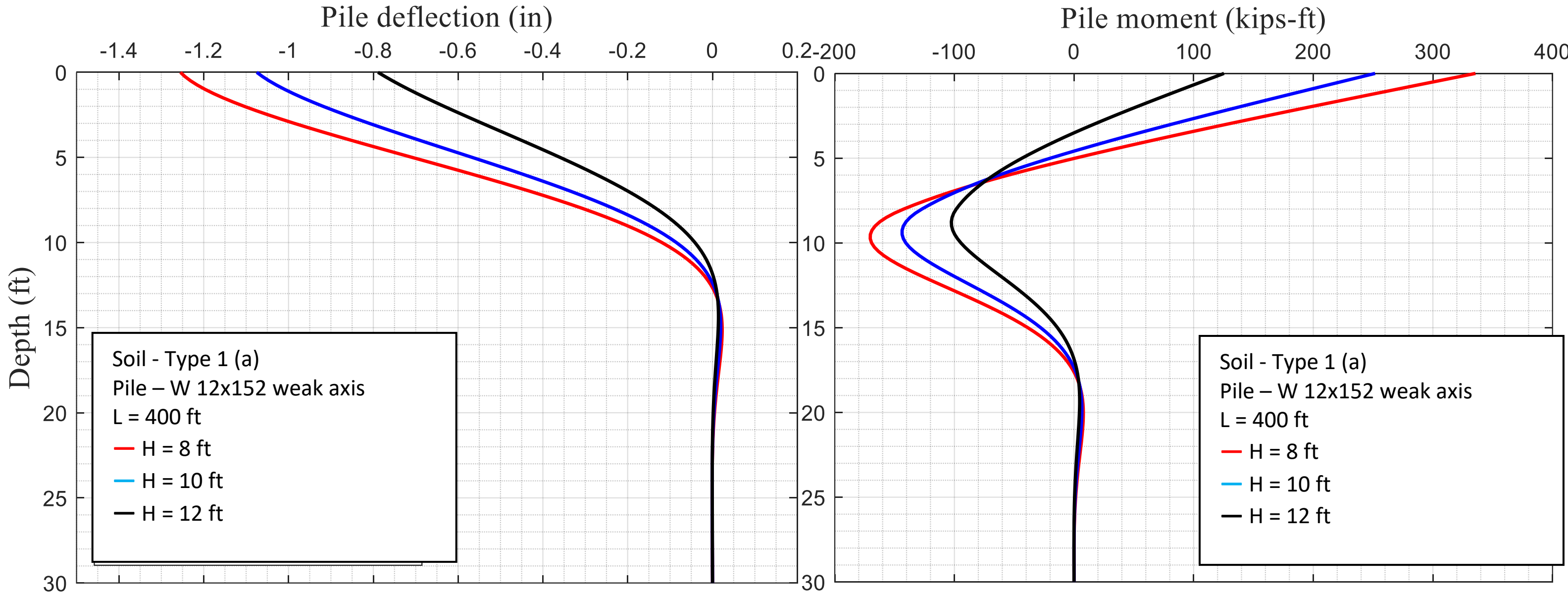

Fig. C.12 W 12x152 pile displacement and moment due to temp. – 400 ft span / weak axis / LPILE

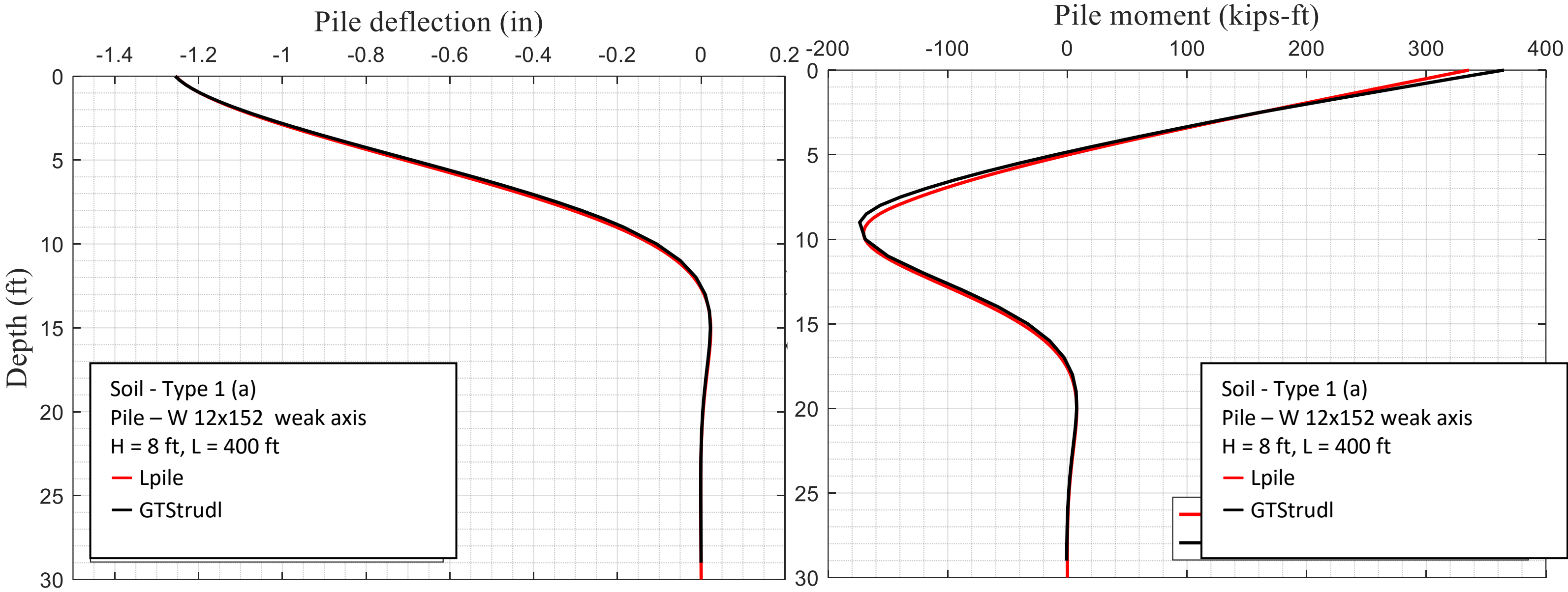

Fig. C.13 W 12x152 pile displacement and moment due to temp. – 400 ft span / H=8, Lpile vs. GTStrudl

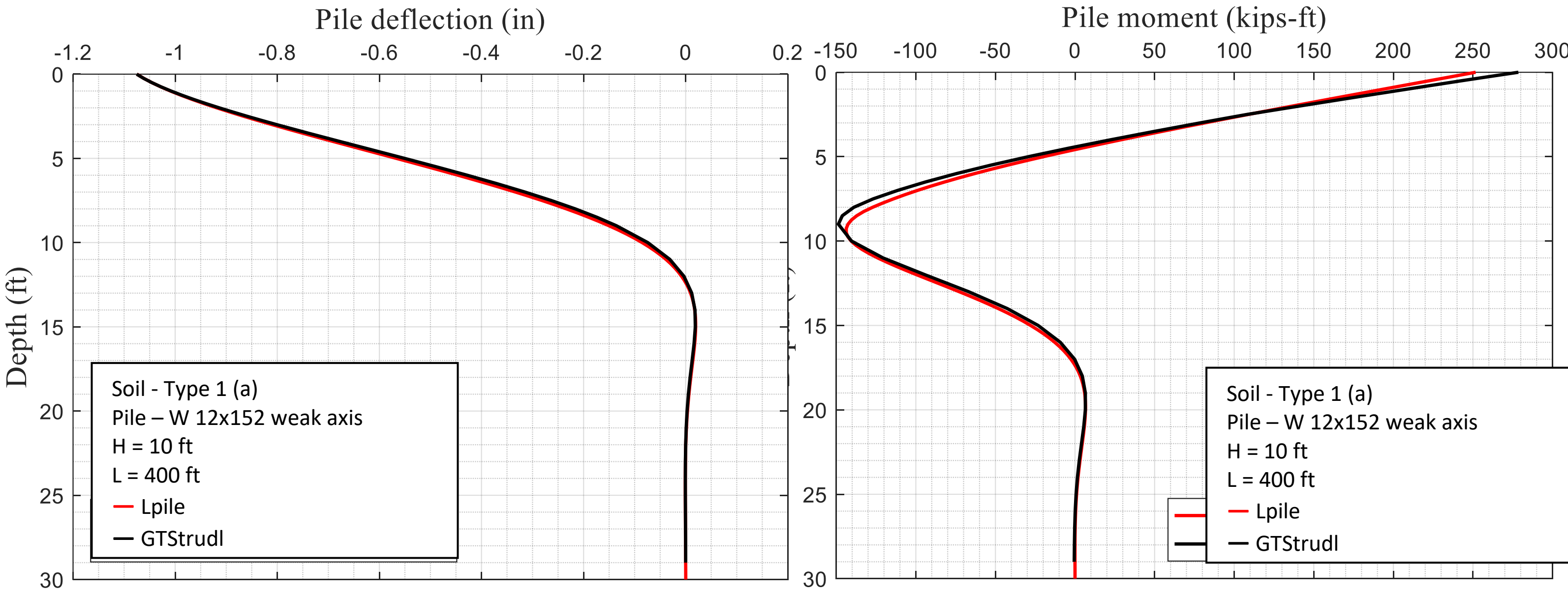

Fig. C.14 W 12x152 pile displacement and moment due to temp. – 400 ft span / H=10, Lpile vs. GTStrudl

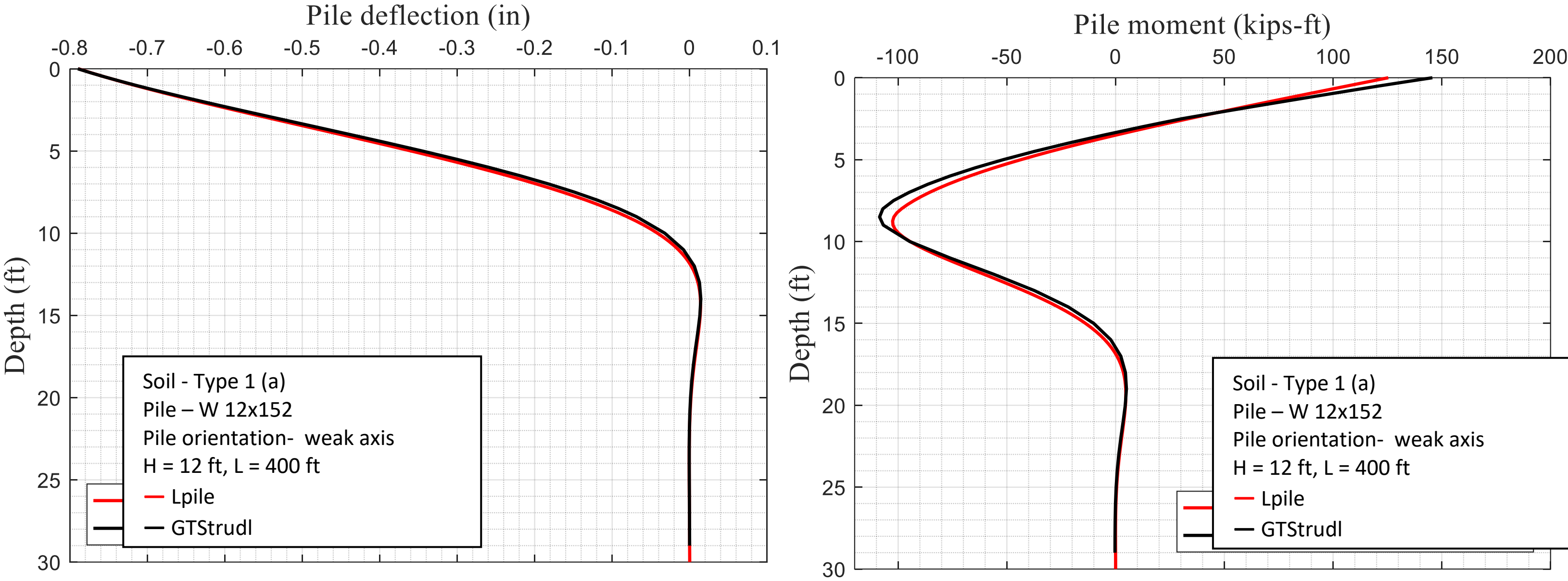

Fig. C.15 W 12x152 pile displacement and moment due to temp. – 400 ft span / H=12, Lpile vs. GTStrudl

Effect of Abutment Wall Height – 550 ft (Dense – backfill)

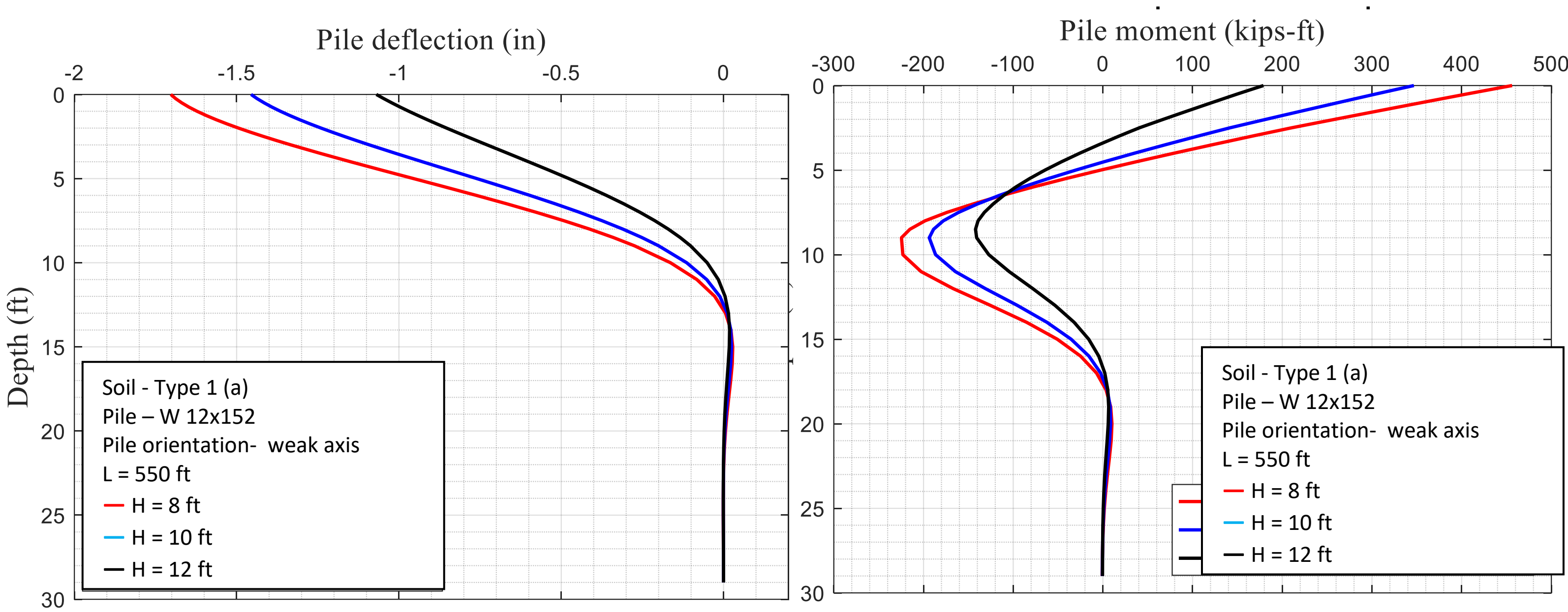

Fig. C.16 W 12x152 pile displacement and moment due to temp. – 550 ft span / weak axis / GTStrudl

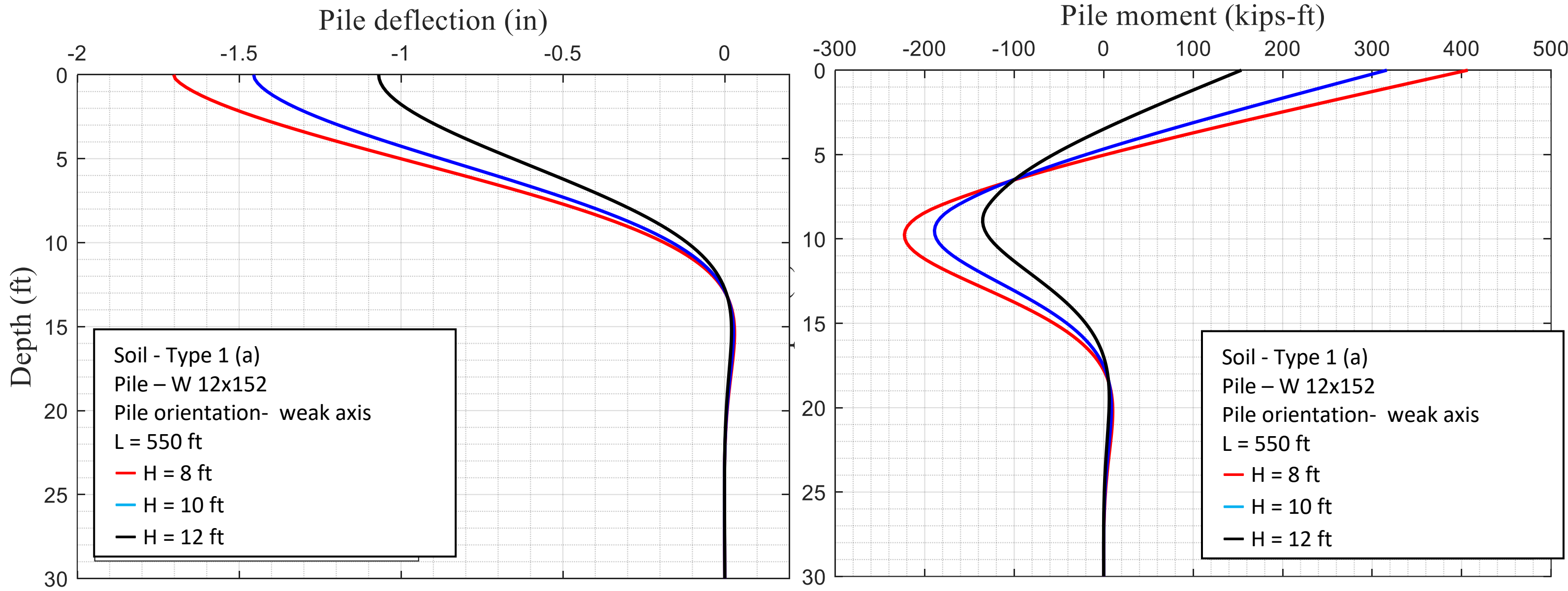

Fig. C.17 W 12x152 pile displacement and moment due to temp. – 550 ft span / weak axis / LPILE

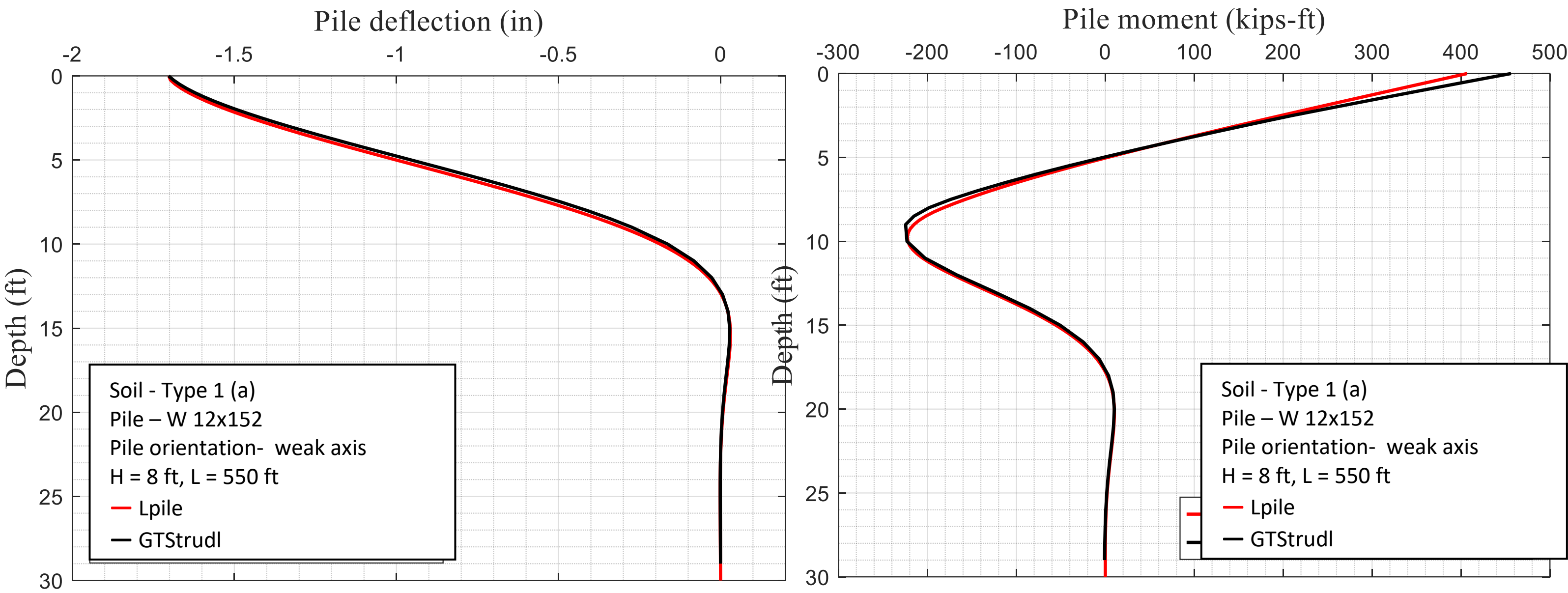

Fig. C.18 W 12x152 pile displacement and moment due to temp. – 550 ft span / H=8, Lpile vs. GTStrudl

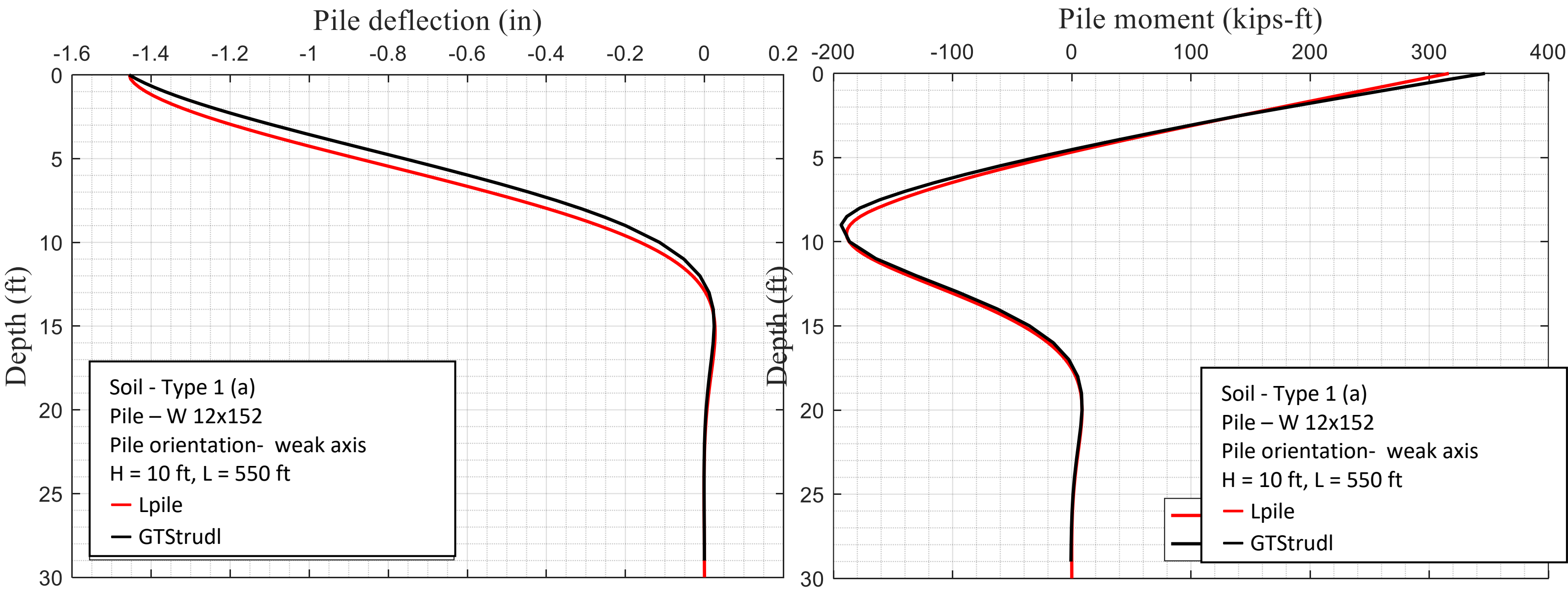

Fig. C.19 W 12x152 pile displacement and moment due to temp. – 550 ft span / H=10, Lpile vs. GTStrudl

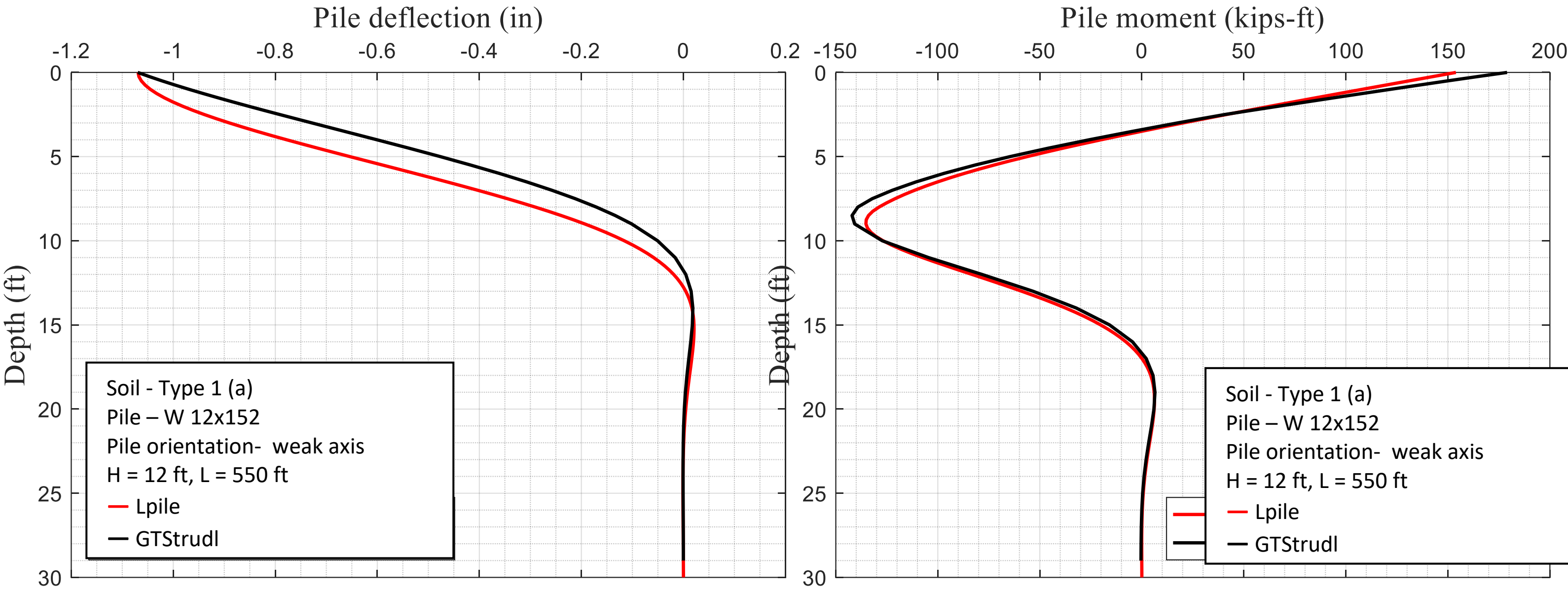

Fig. C.20 W 12x152 pile displacement and moment due to temp. – 550 ft span / H=12, Lpile vs. GTStrudl

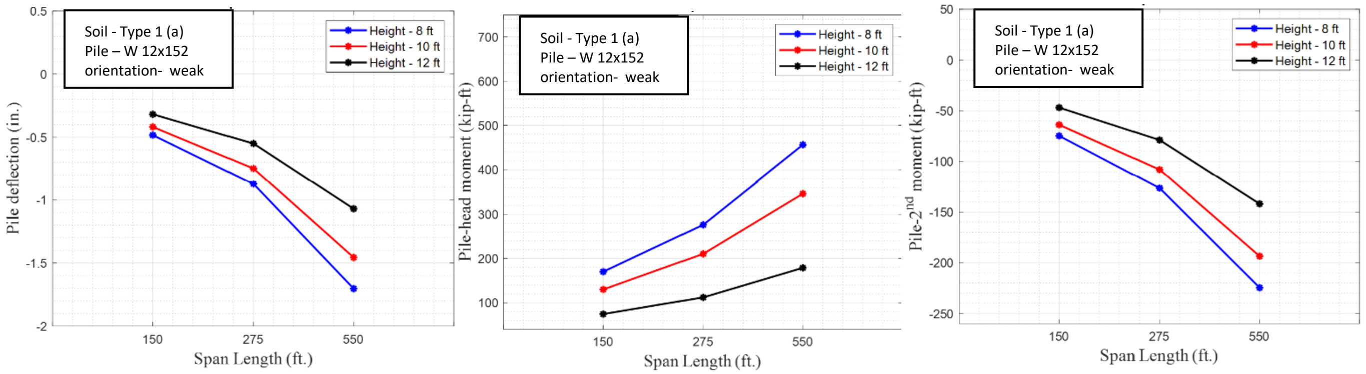

(a) **(b)** **(c)**

Fig. C.21 W 12x152 (a) pile head displacement (b) head moment (c) 2nd moment due to temp. – dense sand behind abutment - 8/10/12 ft / GTStrudl

Table C1: Quantitative data of W12x152 pile for dense sand around abutment wall

Soil Behind Abutment	Abutment Height (inch)	Span Length (ft)	Pile Head Deflection (inch)	Rotation at Pile Head	Axial Force at Pile head (kips)	Output Source	Abutment Head Deflection (inch)	Abutment Bottom Deflection (inch)	Shear Force at Pile Head (kips)	Max. Moment at Pile Head (kip-ft)	Max. Moment a Pile 2^{nd} Segment (kip-ft)
Dense	H = 8	150	-0.483	0.0011	-97.1	GTStrudl	-0.522	-0.486	-46.24	170.25	-74.65
						LPile	-	-	-34.79	150.08	-70.46
		275	-0.872	0.0024	-103.9	GTStrudl	-0.954	-0.877	-68.28	276.36	-126.50
						LPile	-	-	-54.62	250.55	-122.29
		400	-1.255	0.0031	-99.25	GTStrudl	-1.390	-1.263	-85.11	364.84	-173.63
						LPile	-	-	-70.11	335.55	-170.35
		550	-1.702	0.0044	-101.6	GTStrudl	-1.913	-1.714	-101.92	456.23	-224.60
						LPile	-	-	-83.77	406.81	-222.73
	H = 10	150	-0.418	0.0016	-112.0	GTStrudl	-0.522	-0.422	-38.58	130.14	-63.75
						LPile	-	-	-28.24	112.53	-59.60
		275	-0.748	0.0029	-123.4	GTStrudl	-0.949	-0.756	-57.53	210.68	-107.90
						LPile	-	-	-44.38	186.69	-103.00
		400	-1.075	0.0042	-128.7	GTStrudl	-1.377	-1.086	-71.72	278.52	-148.64
						LPile	-	-	-57.29	251.67	-143.71
		550	-1.455	0.0058	-133.3	GTStrudl	-1.891	-1.471	-85.59	346.76	-193.61
						LPile	-	-	-69.80	316.45	-189.12
	H = 12	150	-0.317	0.0021	-103.8	GTStrudl	-0.523	-0.323	-27.36	74.44	-46.82
						LPile	-	-	-18.96	61.00	-43.57
		275	-0.553	0.0038	-113.8	GTStrudl	-0.945	-0.564	-39.80	112.17	-78.73
						LPile	-	-	-28.39	92.76	-73.63
		400	-0.789	0.0054	-122.0	GTStrudl	-1.366	-0.805	-49.58	145.65	-108.55
						LPile	-	-	-36.95	125.37	-102.55
		550	-1.069	0.0074	-129.2	GTStrudl	-1.873	-1.091	-58.89	179.02	-142.03
						LPile	-	-	-44.89	153.92	-135.24

- Pile head deflection, moment and 2nd segment moment significantly reduced with the increment of the abutment heigh Table B.5 represents the qualitative data of all the key parameters from GTStrudl and LPILE for w 12x152 pile oriented in weak axis for dense sand behind the Abutment wall. Axial force has minimal affect with the increment of abutment height.
- Similarly, Span length have major impact on pile head displacement, shear moment and 2nd segment moment. All the above mentioned key parameters are increasing with the increment of length of bridge span. Moreover, influence of spa

length is greater with smaller abutment height as shown in Fig. B35. As abutment height increase the effect of span length on key parameters are reducing. Also, for all the cases mentioned in Table B.5.

Effect of Abutment Wall Height – 150 ft (Loose – backfill)

Fig. C22 W 12x152 pile displacement and moment due to temp. – 150 ft span / weak axis / GTStrudl

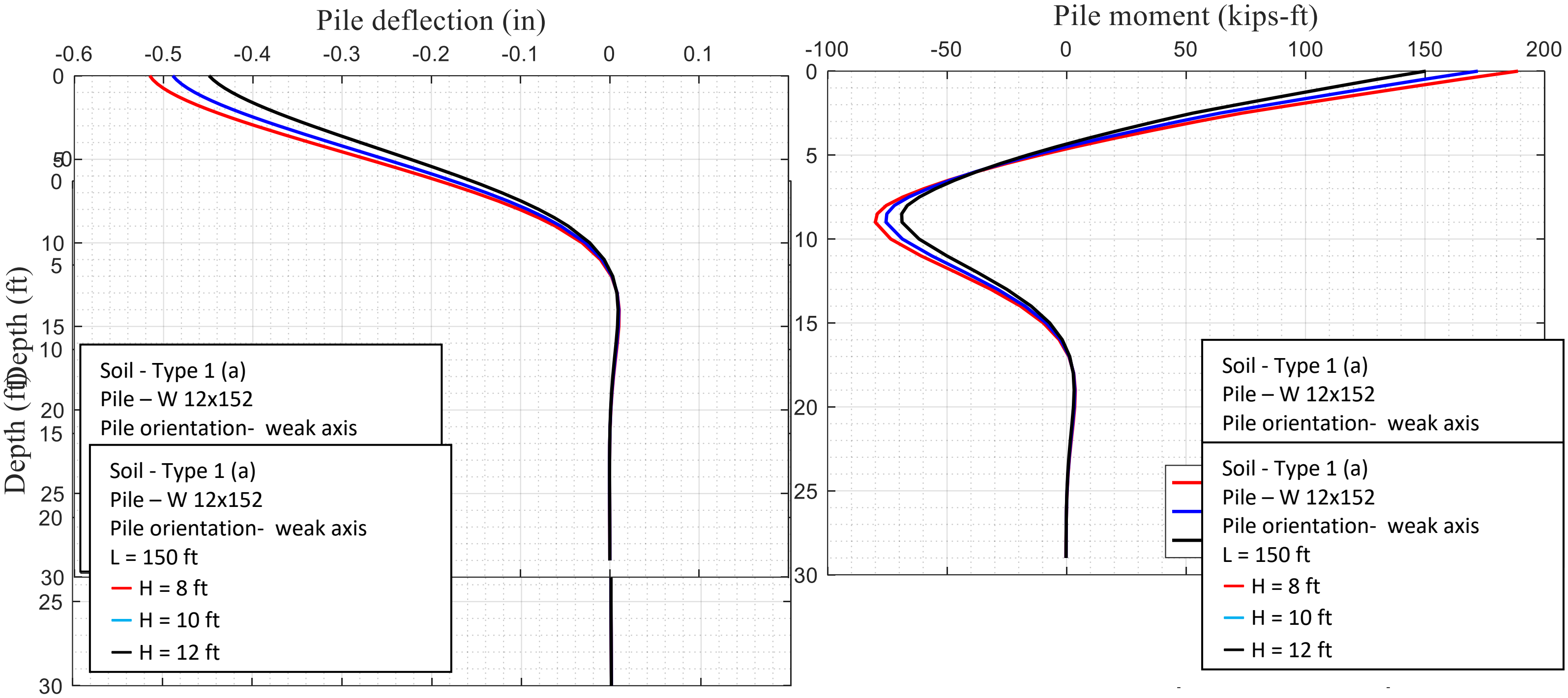

Fig. C.23 W 12x152 pile displacement and moment due to temp. – 150 ft span / weak axis / LPILE

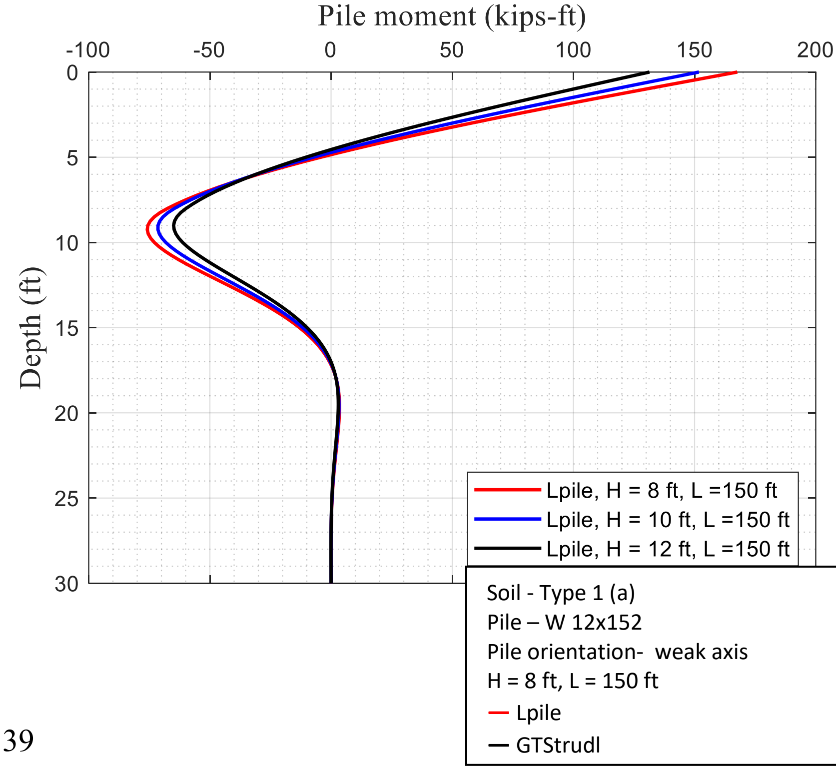

Soil - Type 1 (a)
Pile – W 12x152
Pile orientation- weak axis
H = 8 ft, L = 150 ft
— Lpile
— GTStrudl

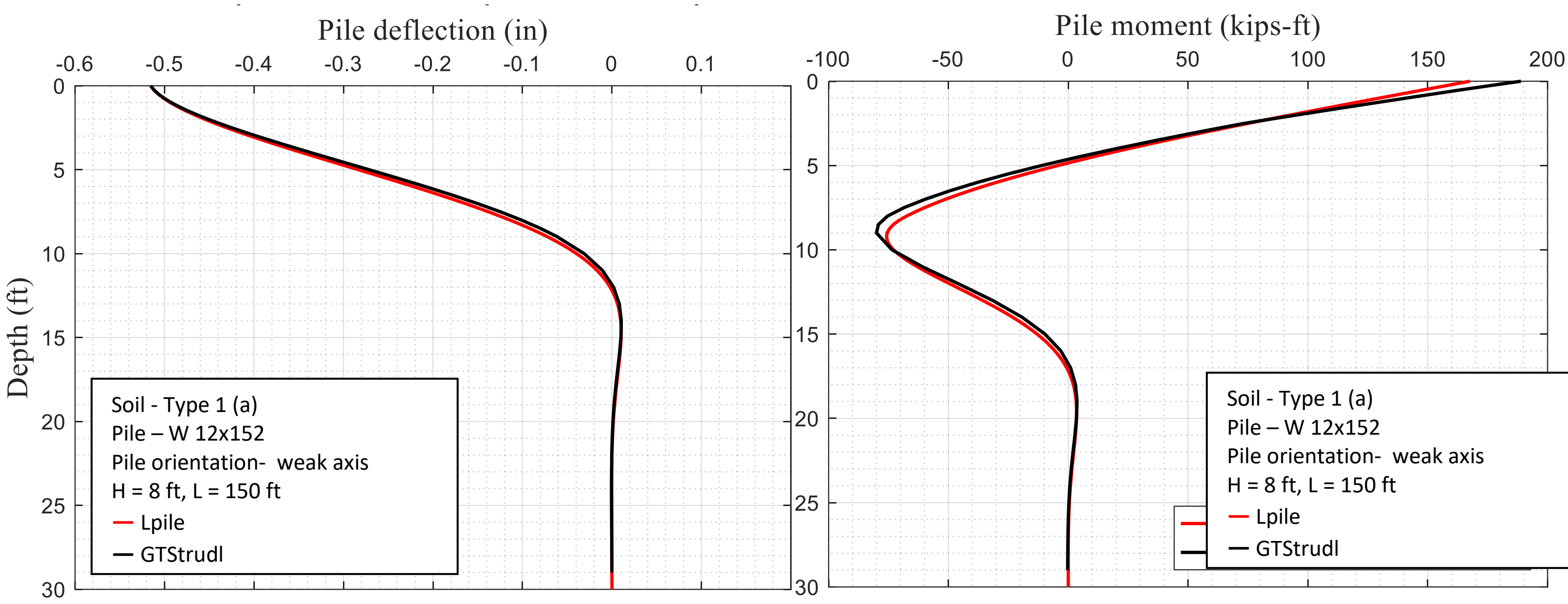

Fig. C.24 W 12x152 pile displacement and moment due to temp. – 150 ft span / H=8, Lpile vs. GTStrudl

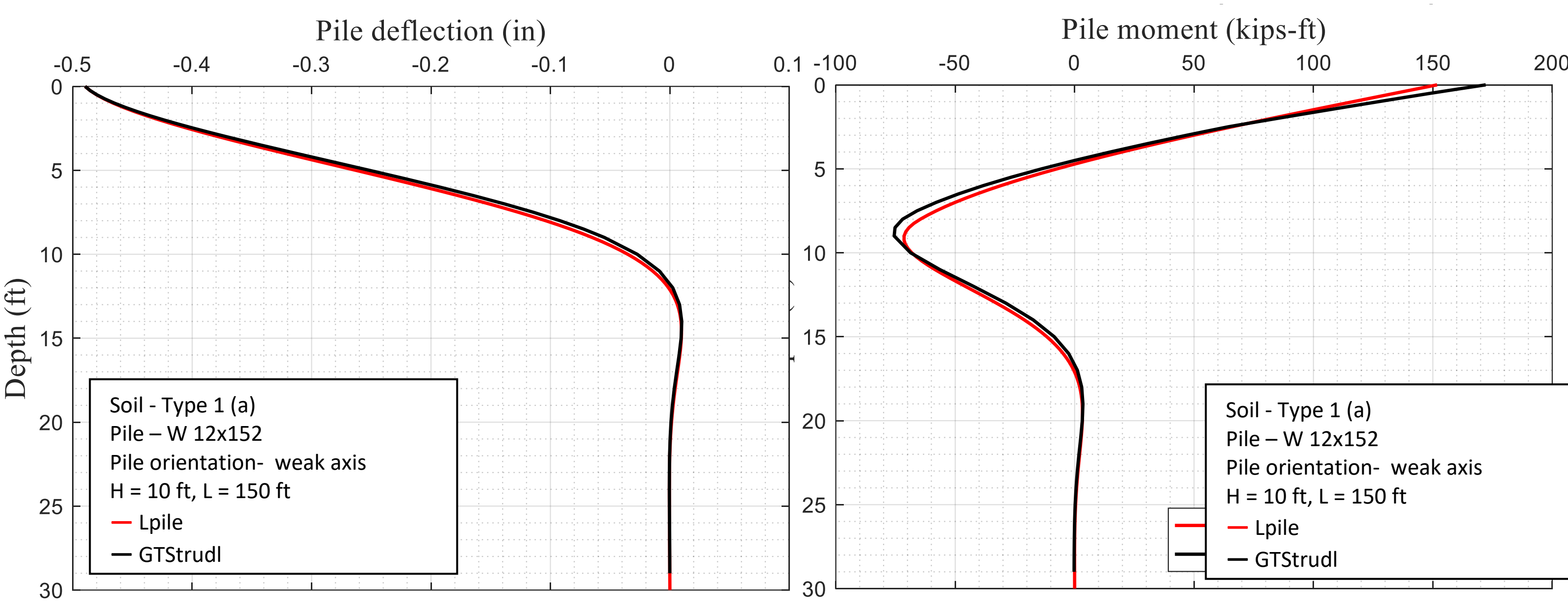

Fig. C.25 W 12x152 pile displacement and moment due to temp. – 150 ft span / H=10, Lpile vs. GTStrudl

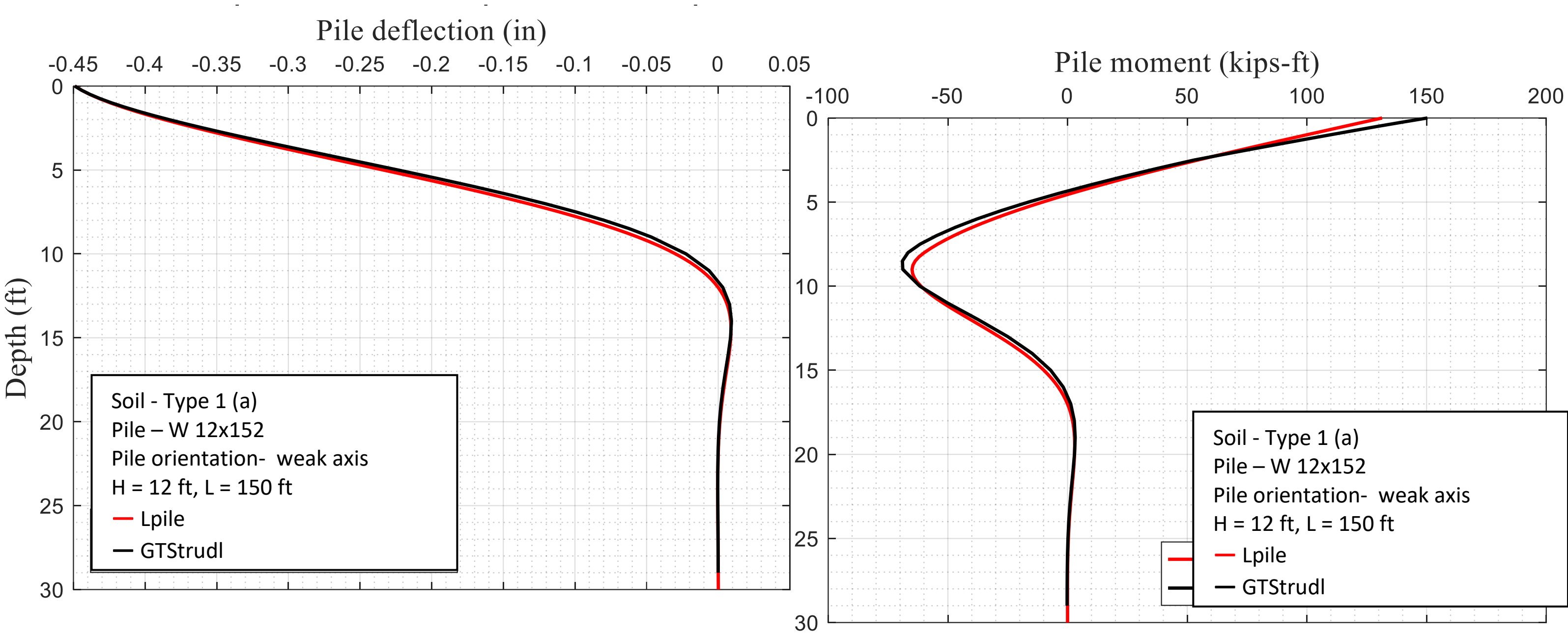

Fig. C.26 W 12x152 pile displacement and moment due to temp. – 150 ft span / H=12, Lpile vs. GTStrudl

Effect of Abutment Wall Height – 275 ft (Loose – backfill)

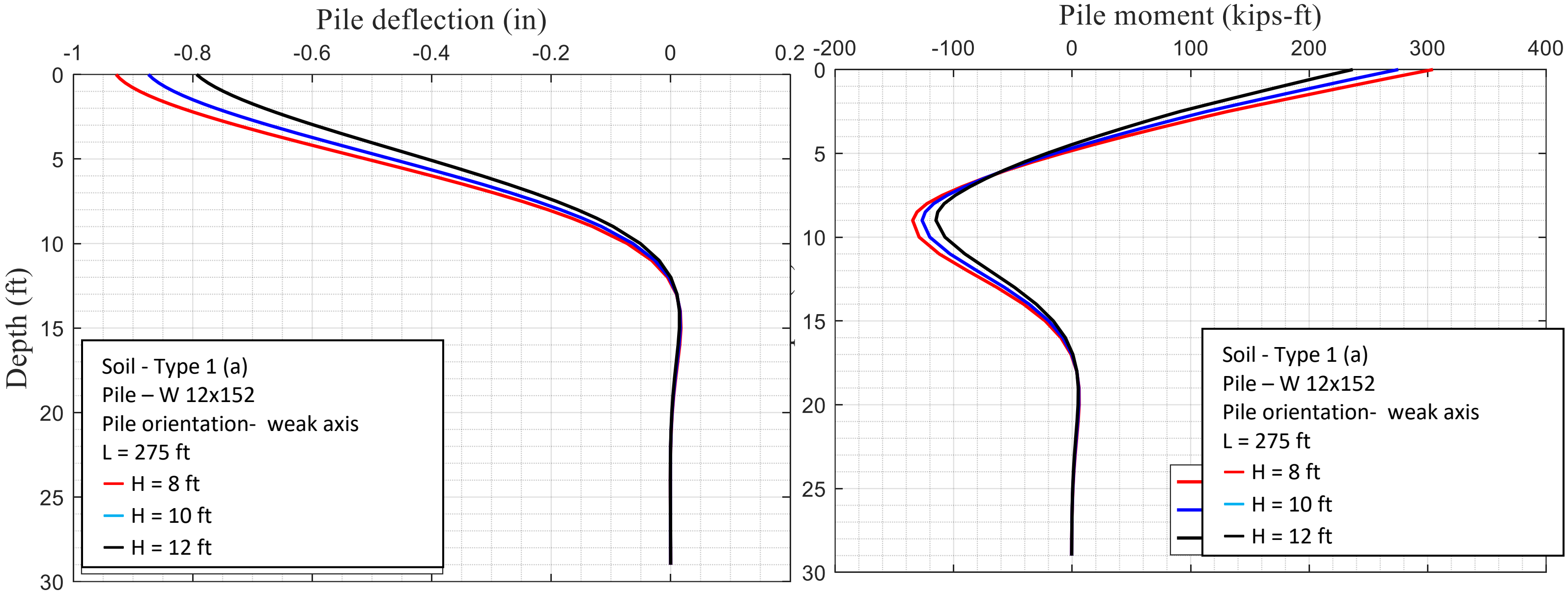

Fig. C.27 W 12x152 pile displacement and moment due to temp. – 275 ft span / weak axis / GTStrudl

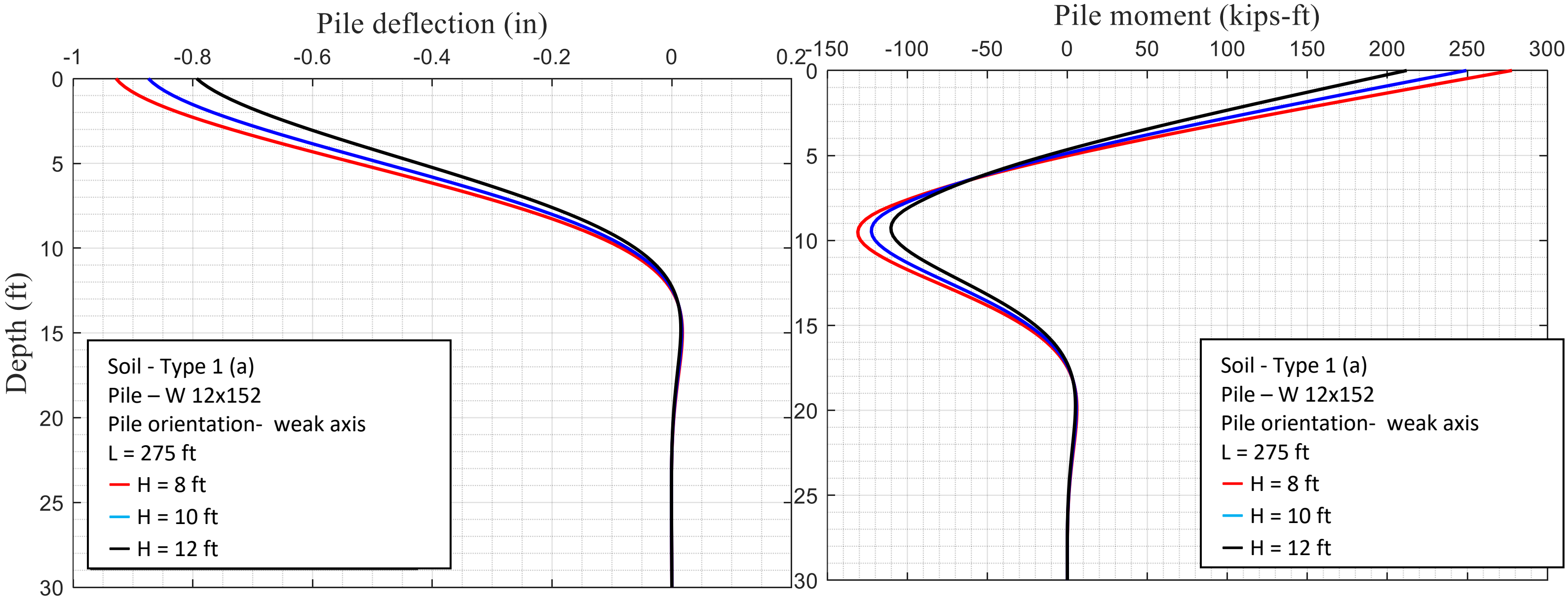

Fig. C.28 W 12x152 pile displacement and moment due to temp. – 275 ft span / weak axis / LPILE

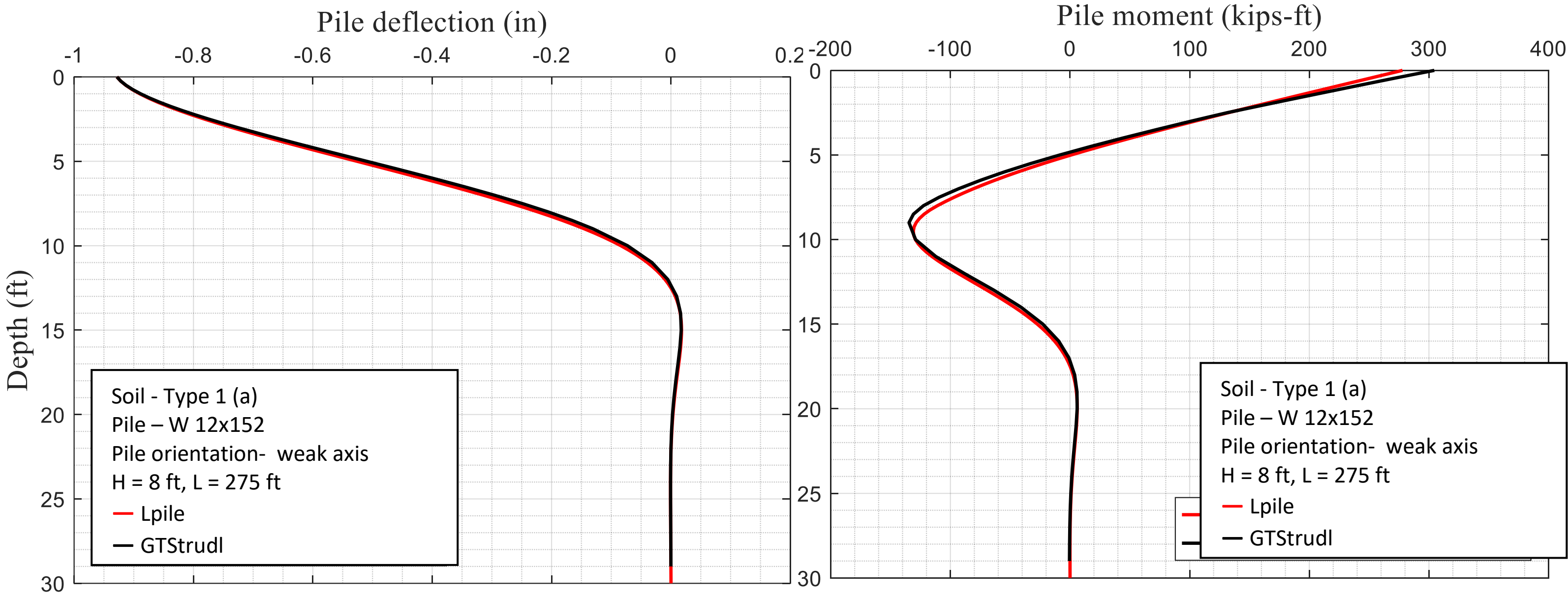

Fig. C.29 W 12x152 pile displacement and moment due to temp. – 275 ft span / H=8, Lpile vs. GTStrudl

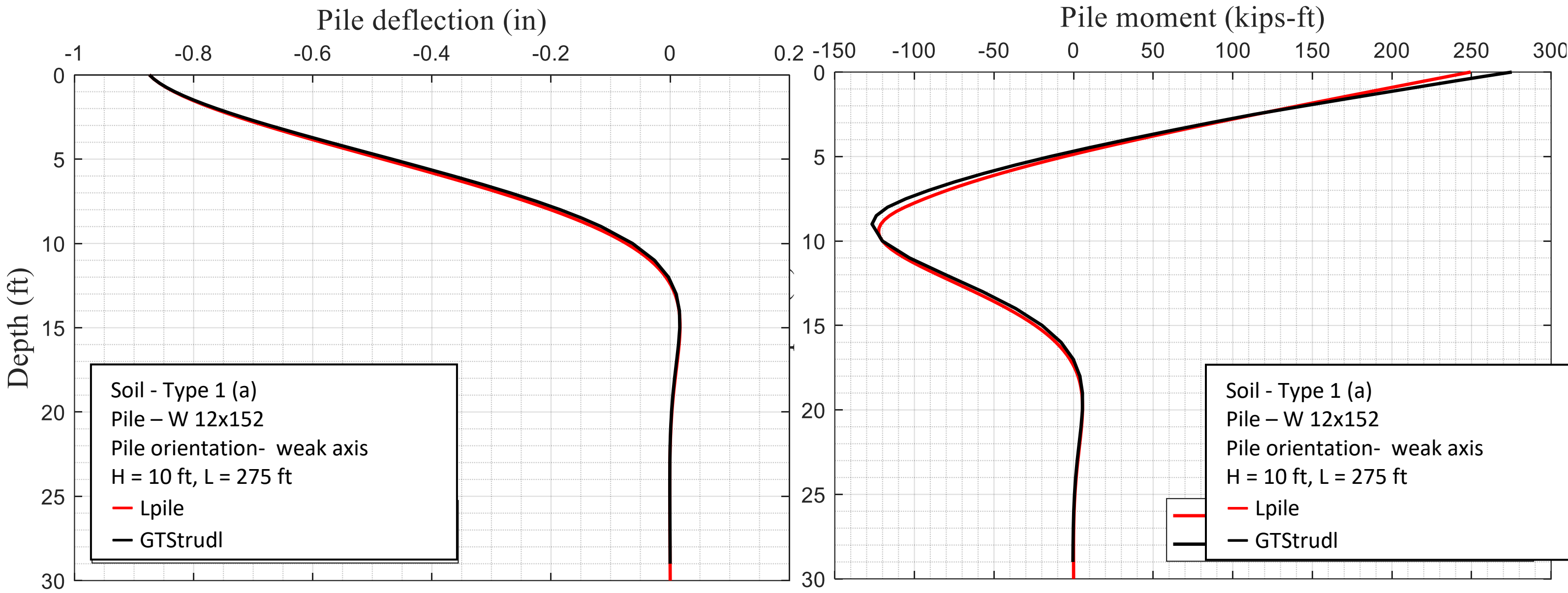

Fig. C.30 W 12x152 pile displacement and moment due to temp. – 275 ft span / H=10, Lpile vs. GTStrudl

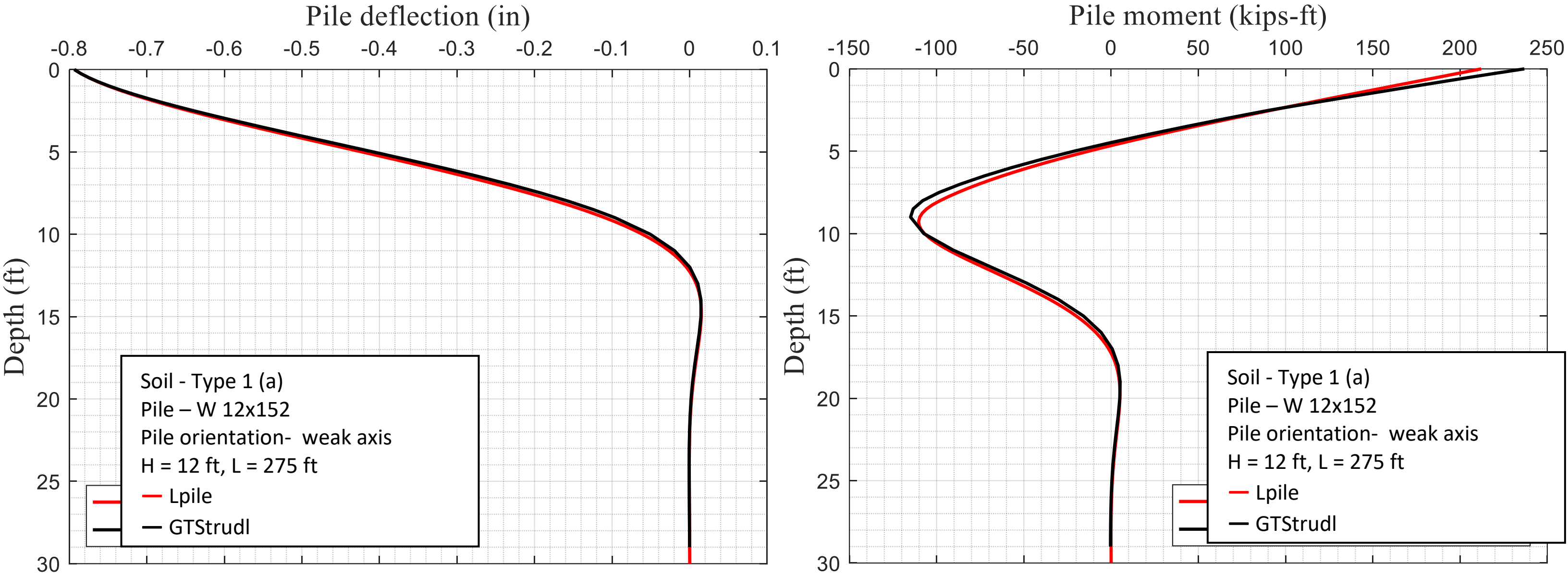

Fig. C.31 W 12x152 pile displacement and moment due to temp. – 275 ft span / H=12, Lpile vs. GTStrudl

<u>Effect of Abutment Wall Height – 550 ft (Loose – backfill)</u>

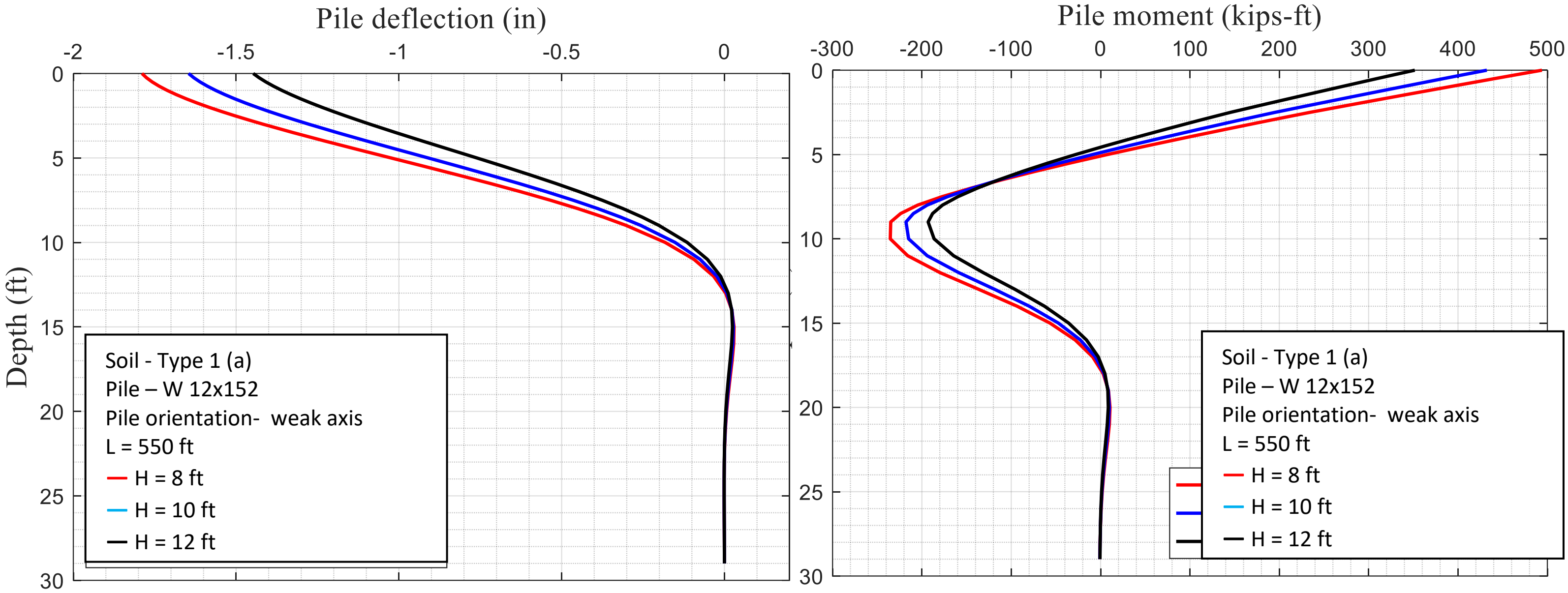

Fig. C.32 W 12x152 pile displacement and moment due to temp. – 550 ft span / weak axis / GTStrudl

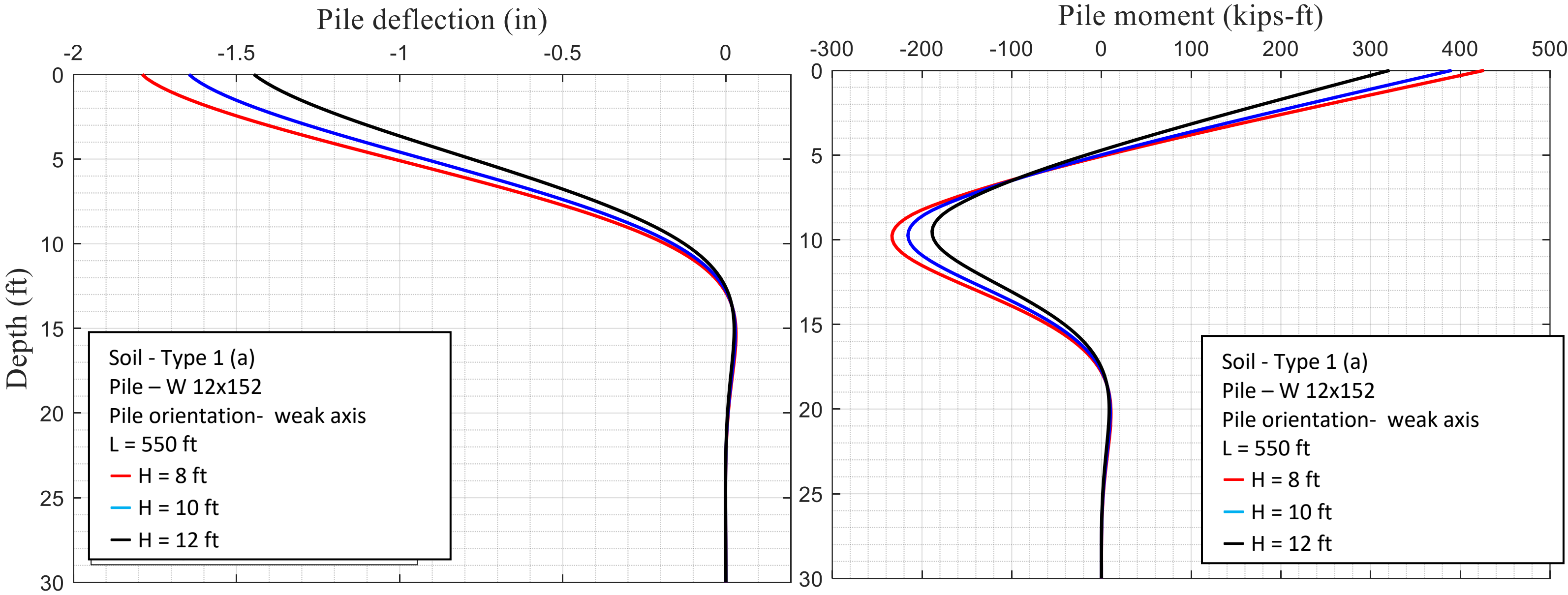

Fig. C.33 W 12x152 pile displacement and moment due to temp. – 550 ft span / weak axis / LPILE

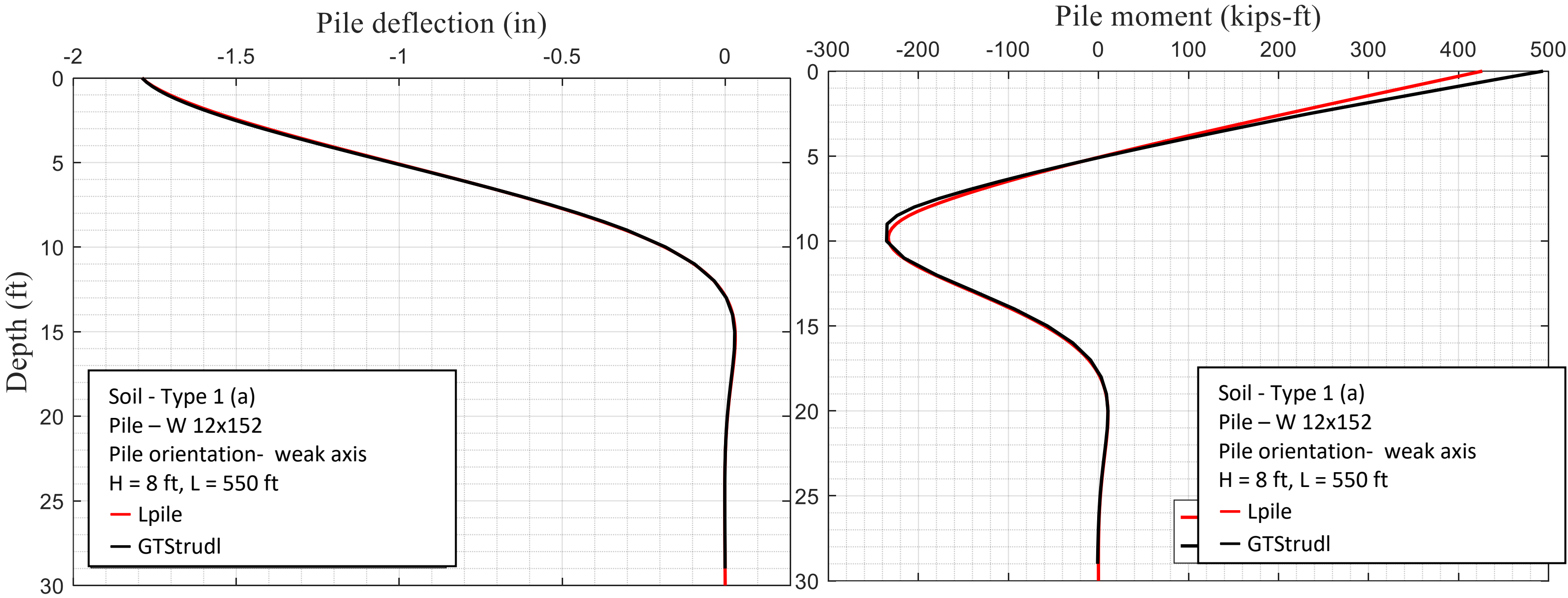

Fig. C.34 W 12x152 pile displacement and moment due to temp. – 550 ft span / H=8, Lpile vs. GTStrudl

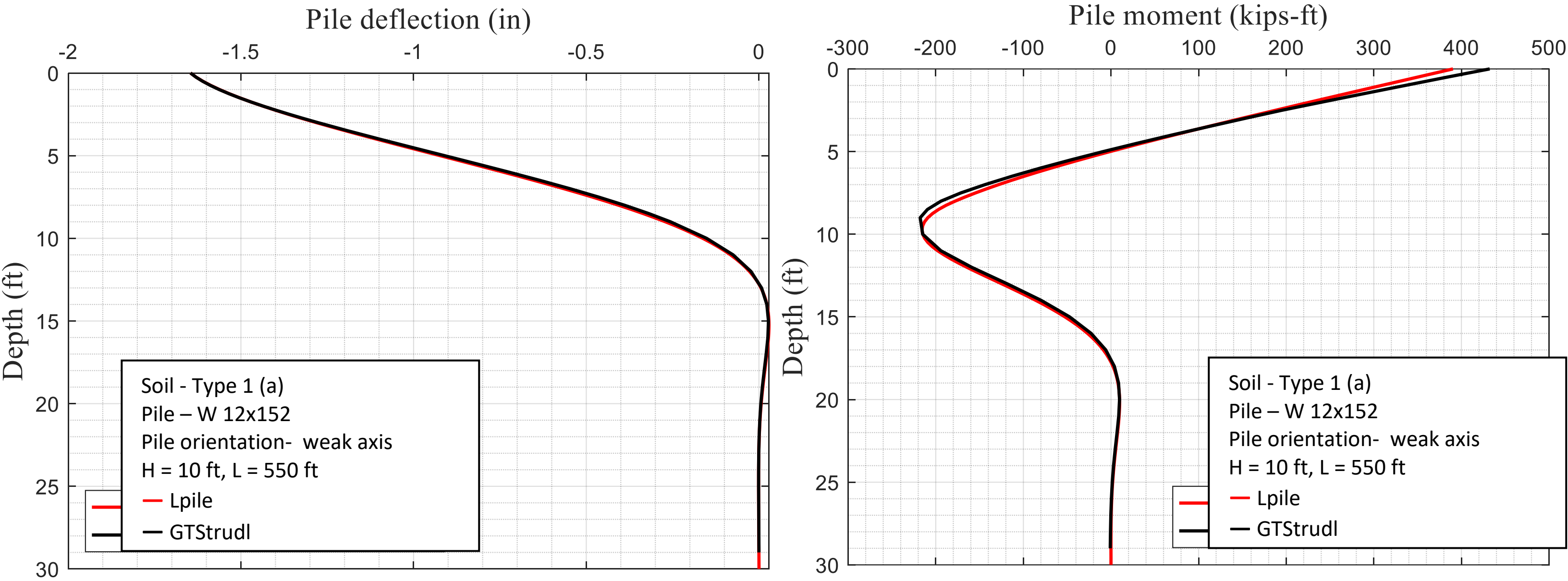

Fig. C.35 W 12x152 pile displacement and moment due to temp. – 550 ft span / H=10, Lpile vs. GTStrudl

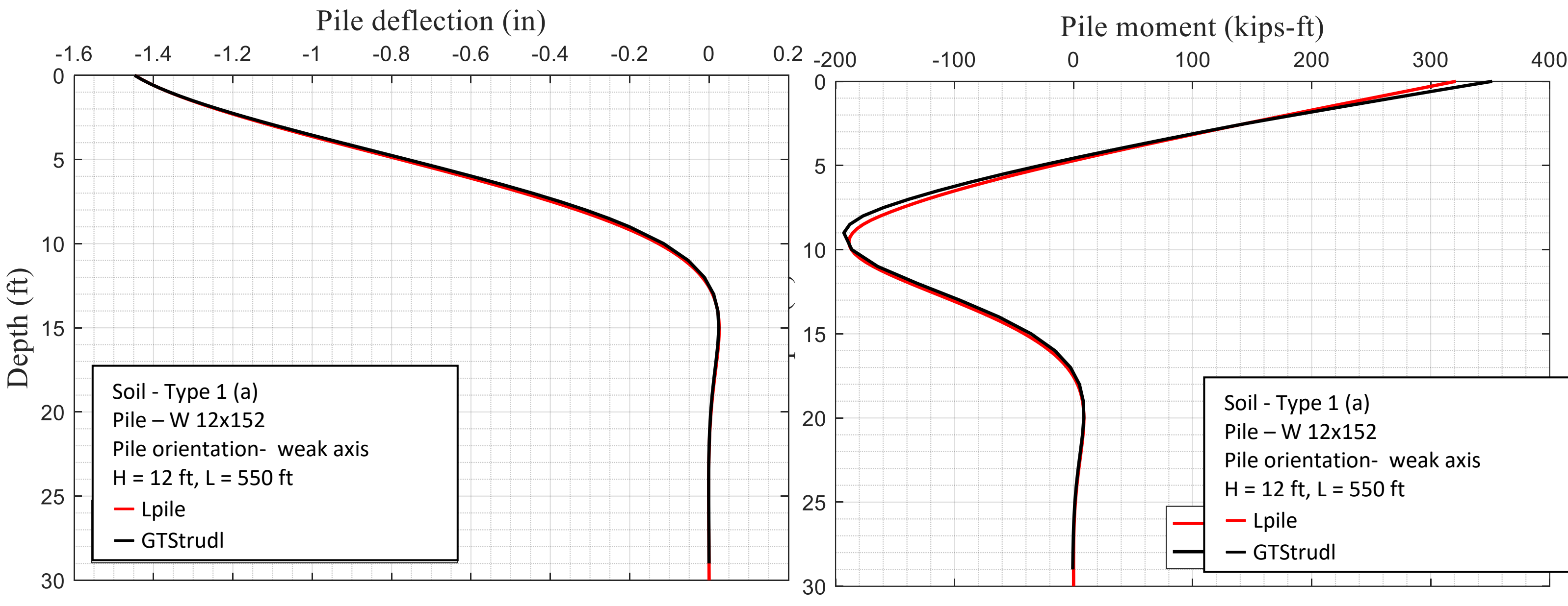

Fig. C.36 W 12x152 pile displacement and moment due to temp. – 550 ft span / H=12, Lpile vs. GTStrudl

Table C.2: Quantitative data of W12x152 pile for loose sand around abutment wall

Soil Behind Abutment	Abutment Height (inch)	Span Length (ft)	Pile Head Deflection (inch)	Rotation at Pile Head	Axial Force at Pile head (kips)	Output Source	Abutment Head Deflection (inch)	Abutment Bottom Deflection (inch)	Shear Force at Pile Head (kips)	Max. Moment at Pile Head (kip-ft)	Max. Moment a Pile 2nd Segment (kip-ft)
Loose	H = 8	150	-0.52	0.0009	-108.7	GTStrudl	-0.536	-0.514	-49.73	188.92	-80.02
						LPile	-	-	-37.77	167.63	-75.83
		275	-0.92	0.0017	-110.9	GTStrudl	-0.979	-0.932	-72.79	304.48	-134.60
						LPile	-	-	-58.71	277.88	-130.99
		550	-1.78	0.0039	-104.7	GTStrudl	-1.952	-1.798	-107.43	493.95	-235.41
						LPile	-	-	-87.04	426.41	-233.48
	H = 10	150	-0.48	0.0011	-134.5	GTStrudl	-0.539	-0.492	-46.86	172.13	-75.56
						LPile	-	-	-35.01	151.79	-71.42
		275	-0.87	0.0021	-137.8	GTStrudl	-0.981	-0.879	-68.17	275.25	-126.63
						LPile	-	-	-54.20	249.42	-122.50
		550	-1.64	0.0047	-139.7	GTStrudl	-1.947	-1.658	-98.39	432.27	-217.78
						LPile	-	-	-80.73	390.36	-215.69
	H = 12	150	-0.44	0.0013	-138.4	GTStrudl	-0.539	-0.452	-42.42	150.33	-68.99
						LPile	-	-	-31.38	131.39	-64.96
		275	-0.79	0.0025	-137.2	GTStrudl	-0.983	-0.800	-61.81	236.83	-114.94
						LPile	-	-	-48.26	212.11	-110.29

		550	-1.44	0.0055	-140.4	GTStrudl	-1.945	-1.462	-86.08	351.66	-193.03
						LPile	-	-	-70.23	321.16	-188.78

- Backfill material influence the stiffness of the abutment wall behavior. Table B6. illustrates quantitative data of W 12x152 pil oriented in weak axis for the loose sand behind the abutment wall. Due to loose sand behind abutment wall, stiffness was reduced hence, pile head experienced the slight increment in the displacement. Thus, increment in pile head displacement contributed into increment in pile head moment, shear, and 2nd segment moment. Hence, loose abutment backfill has more impact on pile head displacement, shear force, bending moments than dense abutment backfill.

Effect of Different Soil Behind Abutment– 5/10% Stiffer Abutment #2 – 150 ft

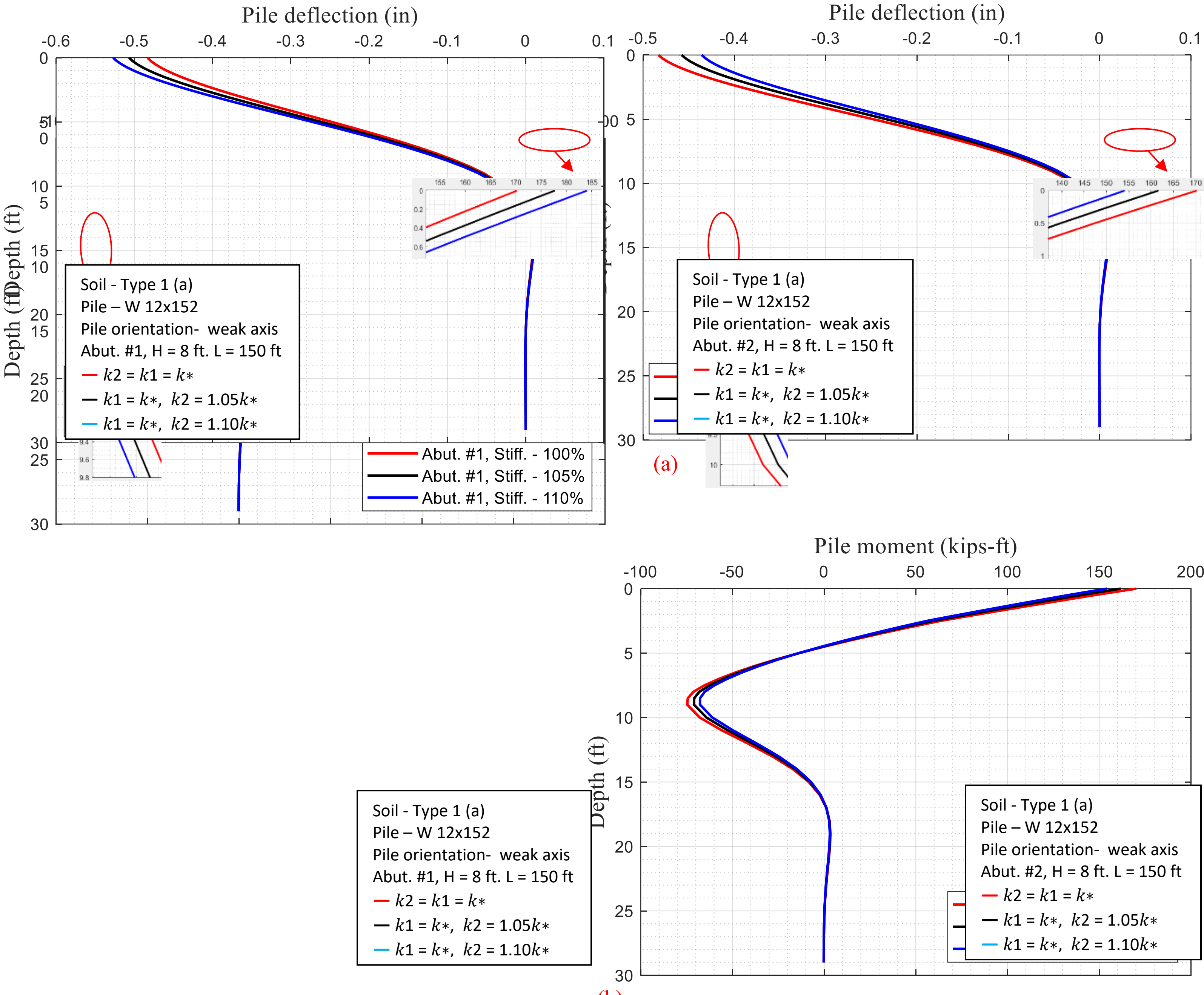

(a)

(b)

Fig. C.37 W 12x152 pile, Abut. #1, #2 (a) displacement and (b) moment due to temp. – 150 ft span / weak axis / H = 8 ft / GTStrudl

(a)

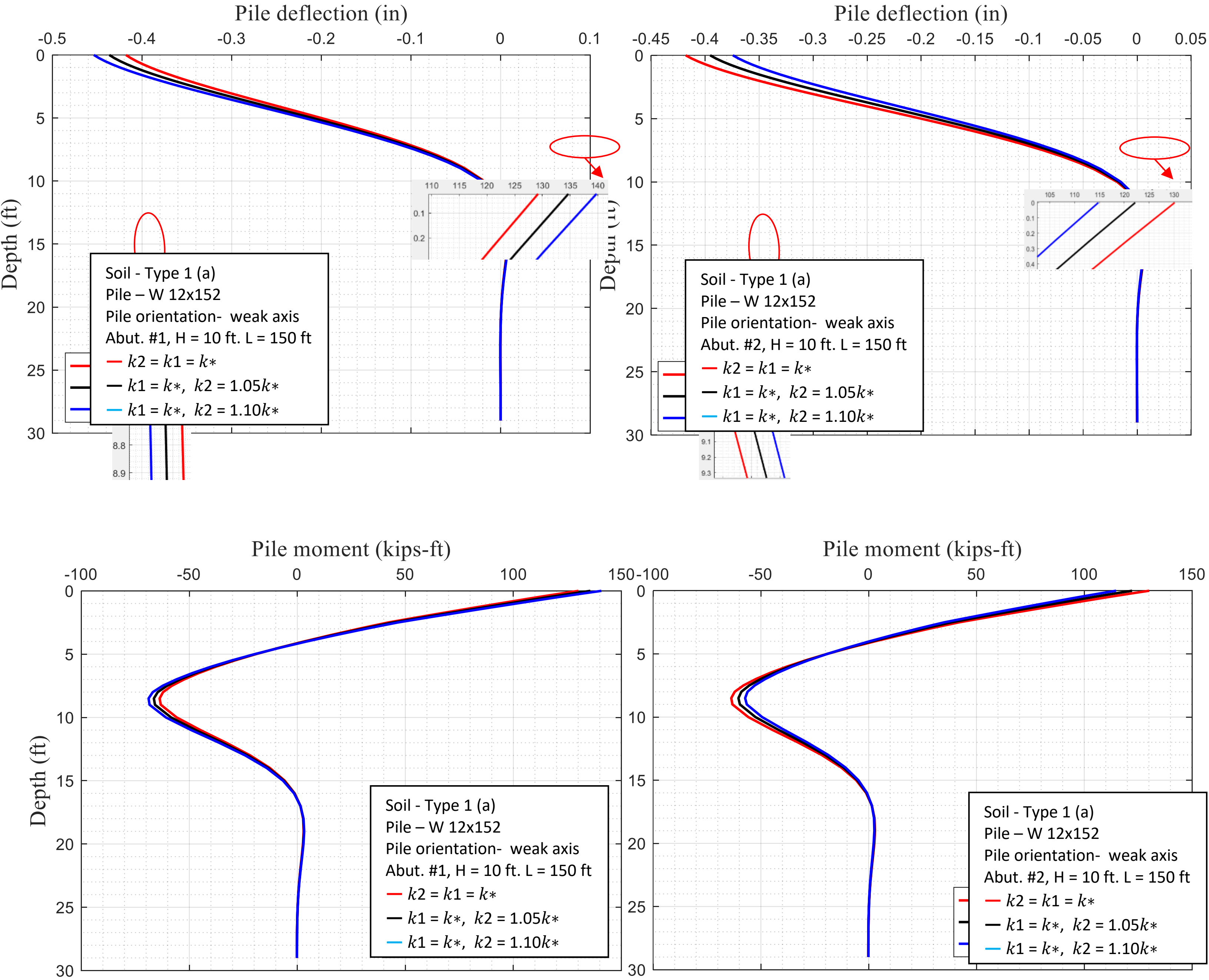

(b)

Fig. C.38 W 12x152 pile, Abut. #1, #2 (a) displacement and (b) moment due to temp.. – 150 ft span / weak axis / H = 10 ft/ GTStrudl

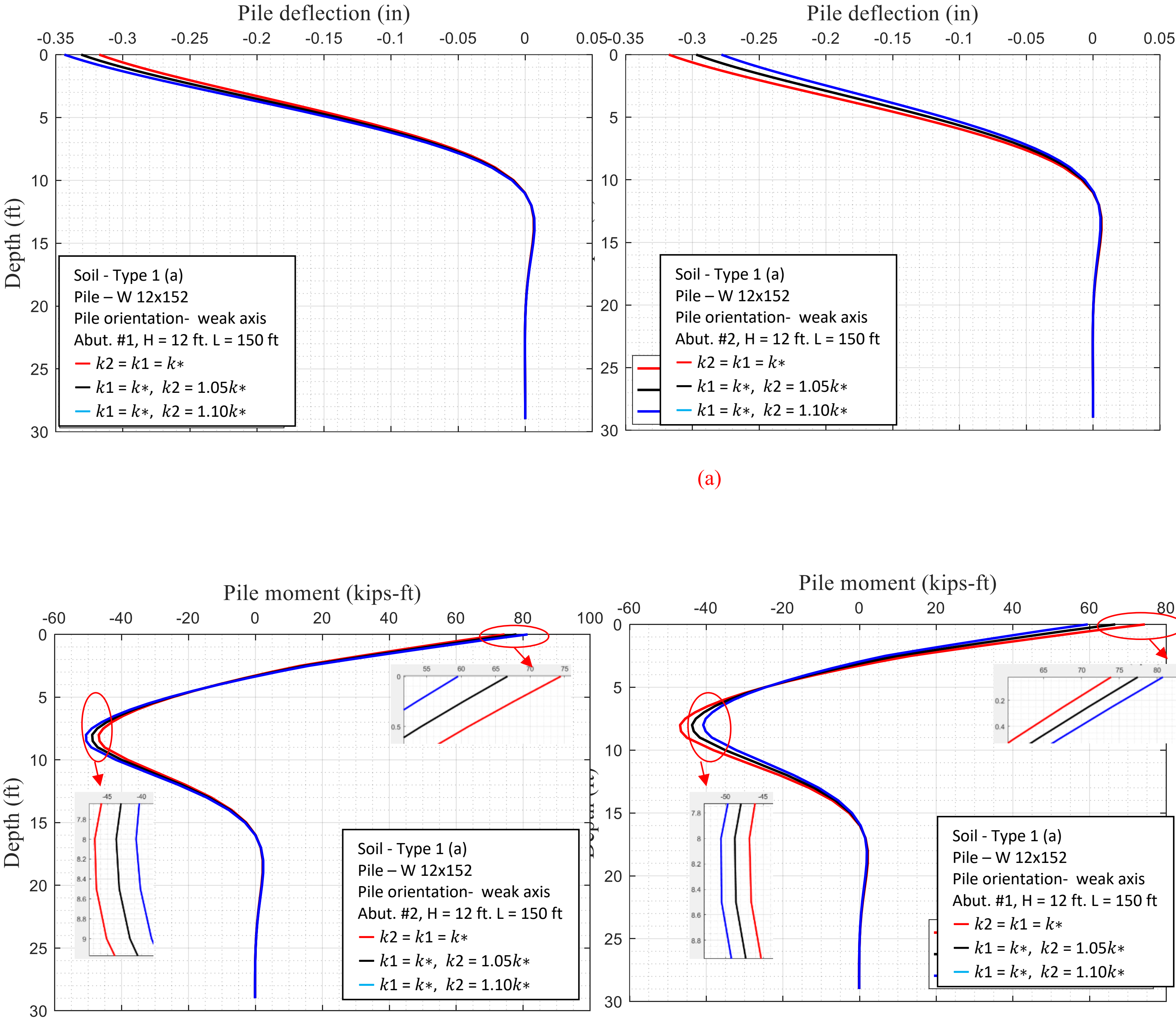

(a)

(b)

Fig. C.39 W 12x152 pile, Abut. #1, #2 (a) displacement and (b) moment due to temp. – 150 ft span / weak axis / H = 12 ft/ GTStrudl

Table C.3: Quantitative data of W12x152 pile for different sand stiffness around abutment wall, L = 150 ft / weak axis/ H =8, 10, 12 ft/ GTStrudl

Abutment Height (inch)	Span Length (ft)	Stiffness of Soil Behind Abutment Wall #2	Abut. Source	Pile Head Deflection (inch)	Rotation at Pile Head	Axial Force at Pile head (kips)	Abutment Head Deflection (inch)	Abutment Bottom Deflection (inch)	Shear Force at Pile Head (kips)	Max. Moment at Pile Head (kip-ft)	Max. Moment at Pile 2^{n} Segment (kip-ft)
H = 8	150	$k_2 = k_1 = k*$	#1, #2	-0.483	0.0012	-97.1	-0.523	-0.486	46.2	170.25	-74.66
		$k_2 = 1.05k*$	#1	-0.506	0.0012	-96.4	-0.547	-0.509	47.9	177.68	-77.99
			#2	-0.457	0.0011	-97.0	-0.497	-0.460	44.3	161.66	-70.99
		$k_2 = 1.10k*$	#1	-0.527	0.0012	-95.9	-0.569	-0.530	49.3	184.06	-80.86
			#2	-0.435	0.0011	-97.0	-0.474	-0.438	42.5	154.10	-67.72
H=10	150	$k_2 = k_1 = k*$	#1, #2	-0.418	0.0016	-112.0	-0.523	-0.422	38.58	130.14	-63.76
		$k_2 = 1.05k*$	#1	-0.436	0.0017	-111.0	-0.544	-0.441	39.93	135.64	-66.40
			#2	-0.395	0.0016	-111.7	-0.500	-0.399	36.74	122.20	-60.41
		$k_2 = 1.10k*$	#1	-0.453	0.0017	-110.0	-0.564	-0.458	41.19	140.74	-68.86
			#2	-0.374	0.0016	-111.5	-0.479	-0.378	35.03	114.78	-57.29
H=12	150	$k_2 = k_1 = k*$	#1, #2	-0.318	0.0021	-103.8	-0.523	-0.324	27.3	74.44	-46.83
		$k_2 = 1.05k*$	#1	-0.331	0.0021	-102.4	-0.542	-0.337	28.3	77.99	-48.78
			#2	-0.297	0.0021	-103.3	-0.504	-0.303	25.5	66.70	-43.69
		$k_2 = 1.10k*$	#1	-0.343	0.0022	-101.1	-0.559	-0.349	29.1	81.33	-50.61
			#2	-0.278	0.0020	-102.9	-0.486	-0.284	23.9	59.53	-40.79

Effect of Different Soil Behind Abutment– 5/10% Stiffer Abutment #2 – 275 ft

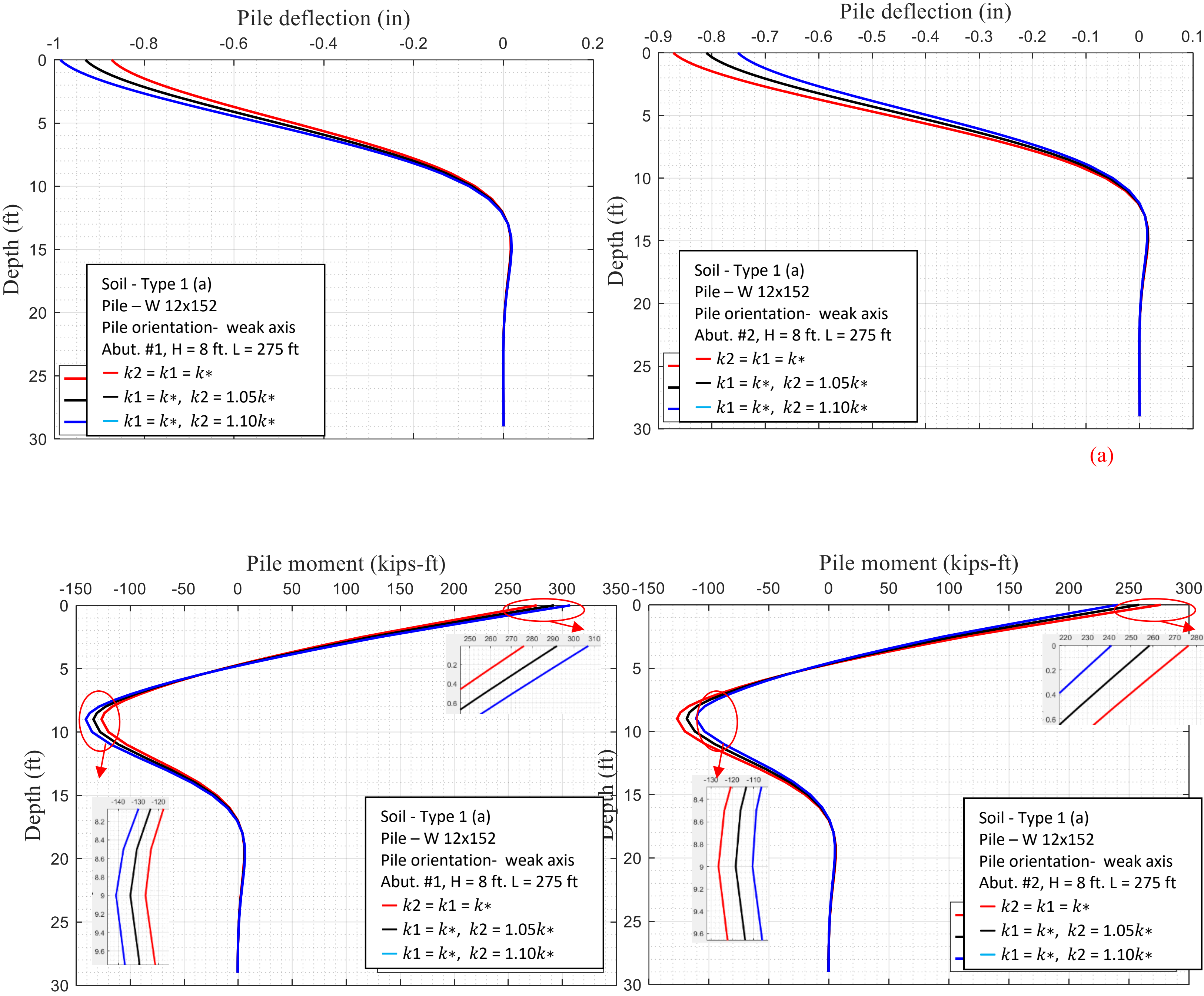

(a)

(b)

Fig. C.40 W 12x152 pile, Abut. #1, #2 (a) displacement and (b) moment due to temp. – 275ft span / weak axis / H = 8 ft/ GTStrudl

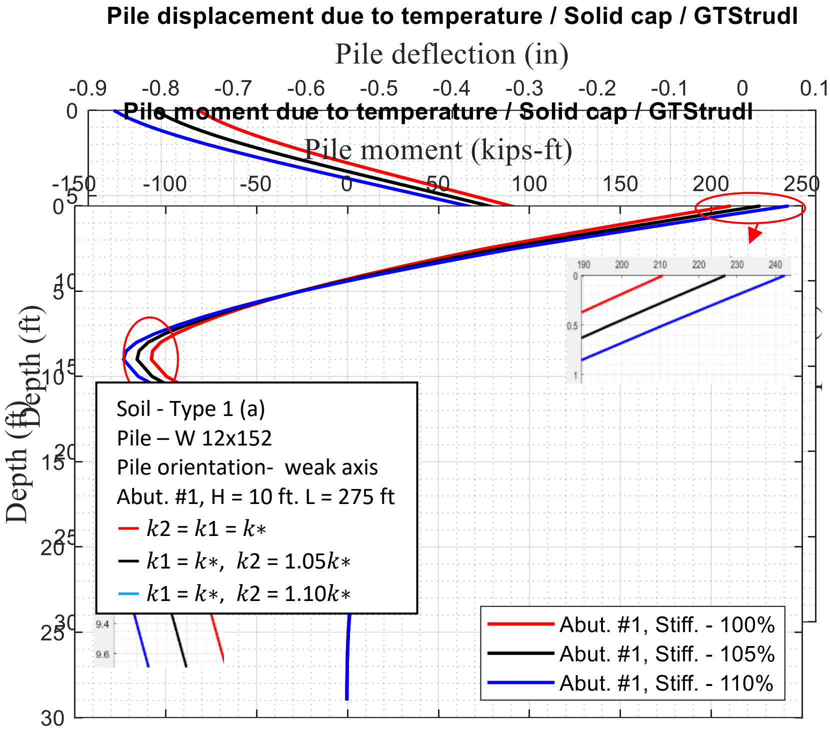

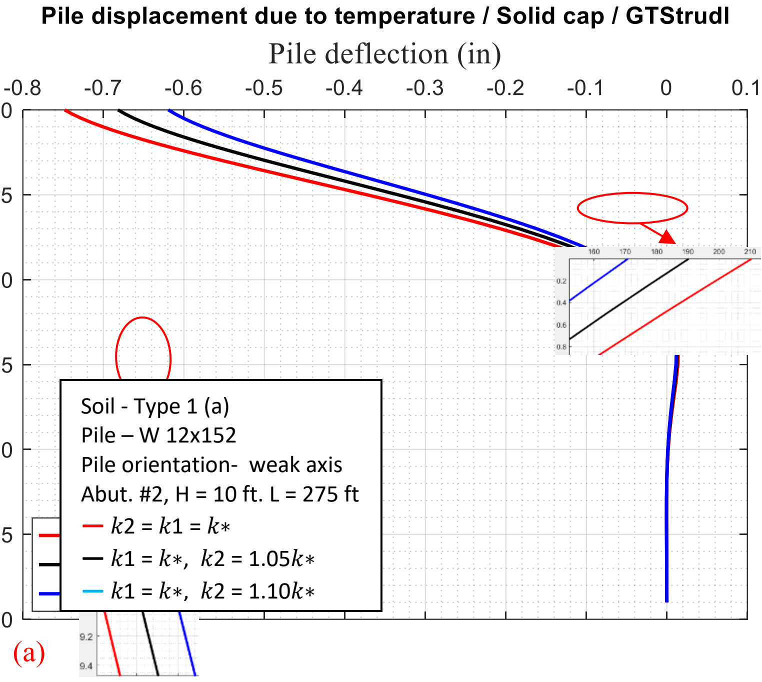

(a)

(b)

Fig. C.41 W 12x152 pile, Abut. #1, #2 (a) displacement and (b) moment due to temp. – 275 ft span / weak axis / H = 10 ft/ GTStrudl

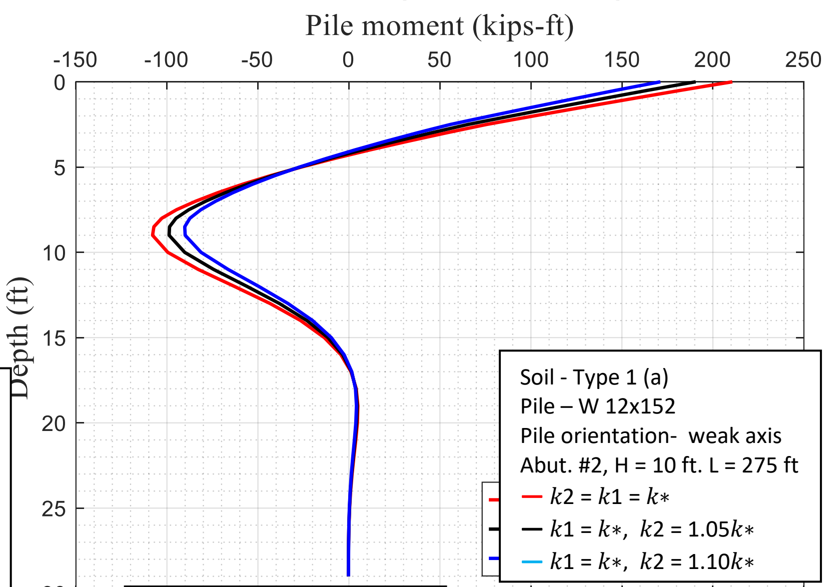

Soil - Type 1 (a)
Pile – W 12x152
Pile orientation- weak axis
Abut. #1, H = 10 ft. L = 275 ft
— $k2 = k1 = k*$
— $k1 = k*,\ k2 = 1.05k*$
— $k1 = k*,\ k2 = 1.10k*$

Soil - Type 1 (a)
Pile – W 12x152
Pile orientation- weak axis
Abut. #1, H = 12 ft. L = 275 ft
— $k2 = k1 = k*$
— $k1 = k*,\ k2 = 1.05k*$
— $k1 = k*,\ k2 = 1.10k*$

Soil - Type 1 (a)
Pile – W 12x152
Pile orientation- weak axis
Abut. #2, H = 12 ft. L = 275 ft
— $k2 = k1 = k*$
— $k1 = k*,\ k2 = 1.05k*$
— $k1 = k*,\ k2 = 1.10k*$

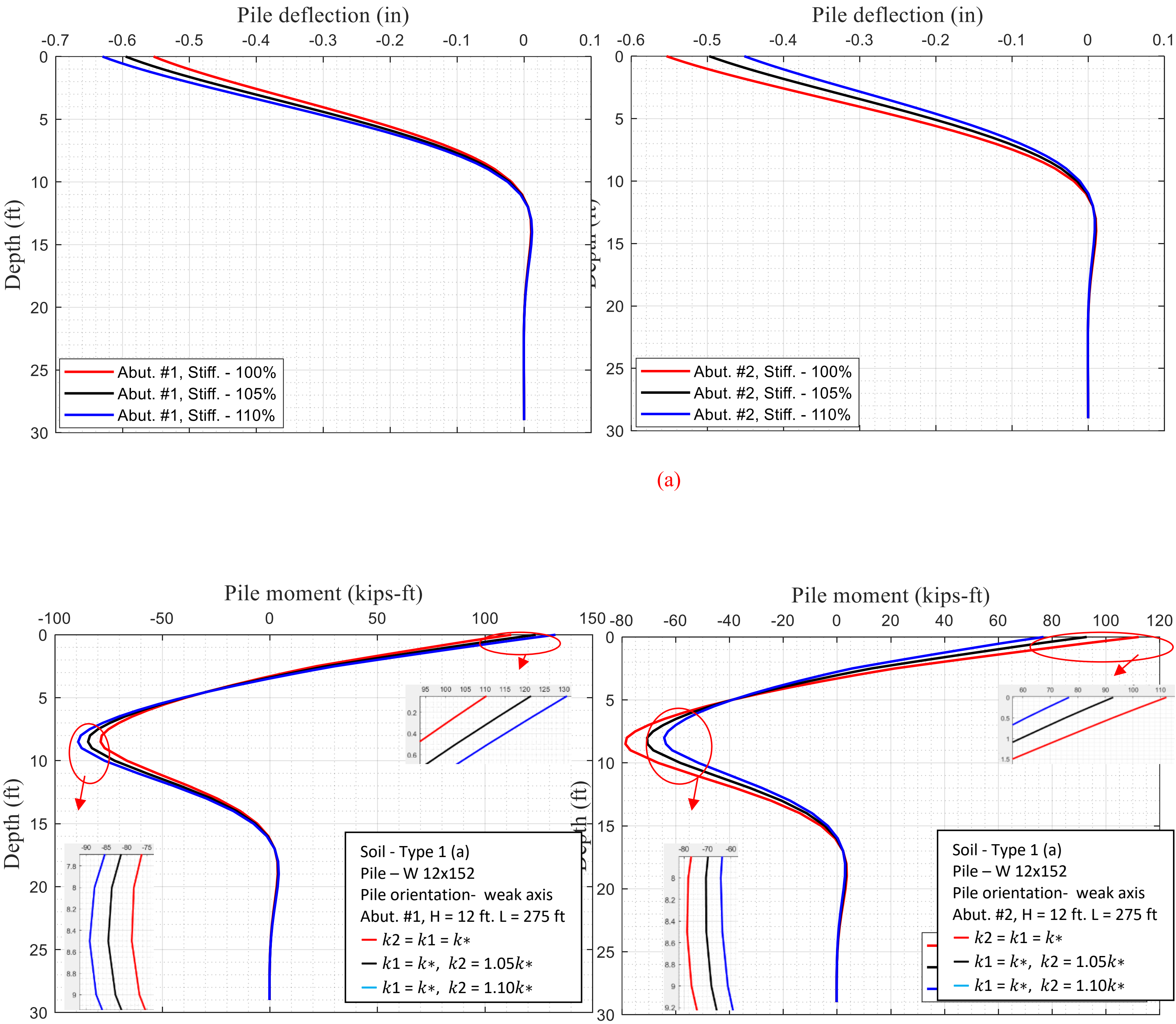

(a)

(b)

Fig. C.42 W 12x152 pile, Abut. #1, #2 (a) displacement and (b) moment due to temp. – 275 ft span / weak axis / H = 12 ft/ GTStrudl

Table C.4: Quantitative data of W12x152 pile for different sand stiffness around abutment wall

Abutment Height (inch)	Span Length (ft)	Stiffness of Soil Behind Abutment Wall #2	Abut. Source	Pile Head Deflection (inch)	Rotation at Pile Head	Axial Force at Pile head (kips)	Abutment Head Deflection (inch)	Abutment Bottom Deflection (inch)	Shear Force at Pile Head (kips)	Max. Moment at Pile Head (kip-ft)	Max. Moment at Pile 2nd Segment (kip-ft)
H = 8	275	$k_2 = k_1 = k*$	#1, #2	-0.872	0.0021	-104.0	-0.955	-0.877	68.3	276.36	-126.51
		$k_2 = 1.05k*$	#1	-0.930	0.0022	-103.4	-1.015	-0.936	71.2	292.26	-134.00
			#2	-0.810	0.0020	-104.1	-0.891	-0.815	64.9	258.45	-118.46
		$k_2 = 1.10k*$	#1	-0.986	0.0022	-102.8	-1.074	-0.992	74.0	307.31	-141.10
			#2	-0.751	0.0019	-104.2	-0.831	-0.756	61.6	240.98	-110.62
H=10	275	$k_2 = k_1 = k*$	#1, #2	-0.748	0.0029	-123.4	-0.949	-0756	57.5	210.68	-107.91
		$k_2 = 1.05k*$	#1	-0.807	0.0030	-122.5	-1.014	-0.815	60.7	227.00	-115.74
			#2	-0.681	0.0028	-123.5	-0.881	-0.689	53.5	190.55	-98.80
		$k_2 = 1.10k*$	#1	-0.864	0.0031	-121.8	-1.077	-0.873	63.7	242.47	-123.20
			#2	-0.619	0.0027	-123.7	-0.817	-0.626	49.6	171.12	-90.22
H=12	275	$k_2 = k_1 = k*$	#1, #2	-0.554	0.0038	-113.8	-0.945	-0.564	39.8	112.17	-78.73
		$k_2 = 1.05k*$	#1	-0.595	0.0039	-112.6	-0.998	-0.606	42.5	123.55	-84.57
			#2	-0.497	0.0037	-113.7	-0.889	-0.508	35.53	92.83	-70.66
		$k_2 = 1.10k*$	#1	-0.630	0.0040	-111.6	-1.042	-0.641	44.61	132.74	-89.17
			#2	-0.451	0.0037	-113.5	-0.843	-0.462	31.87	76.77	-64.32

Effect of Different Soil Behind Abutment– 5/10% Stiffer Abutment #2 – 550 ft

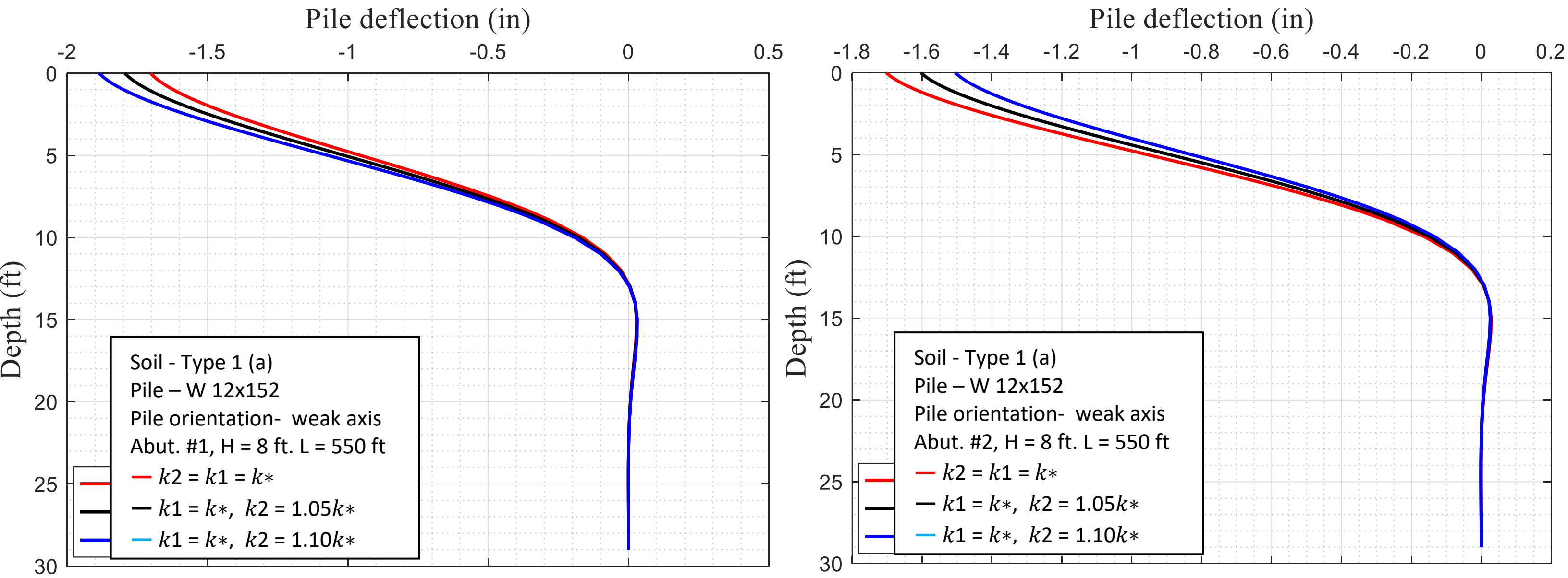

(a)

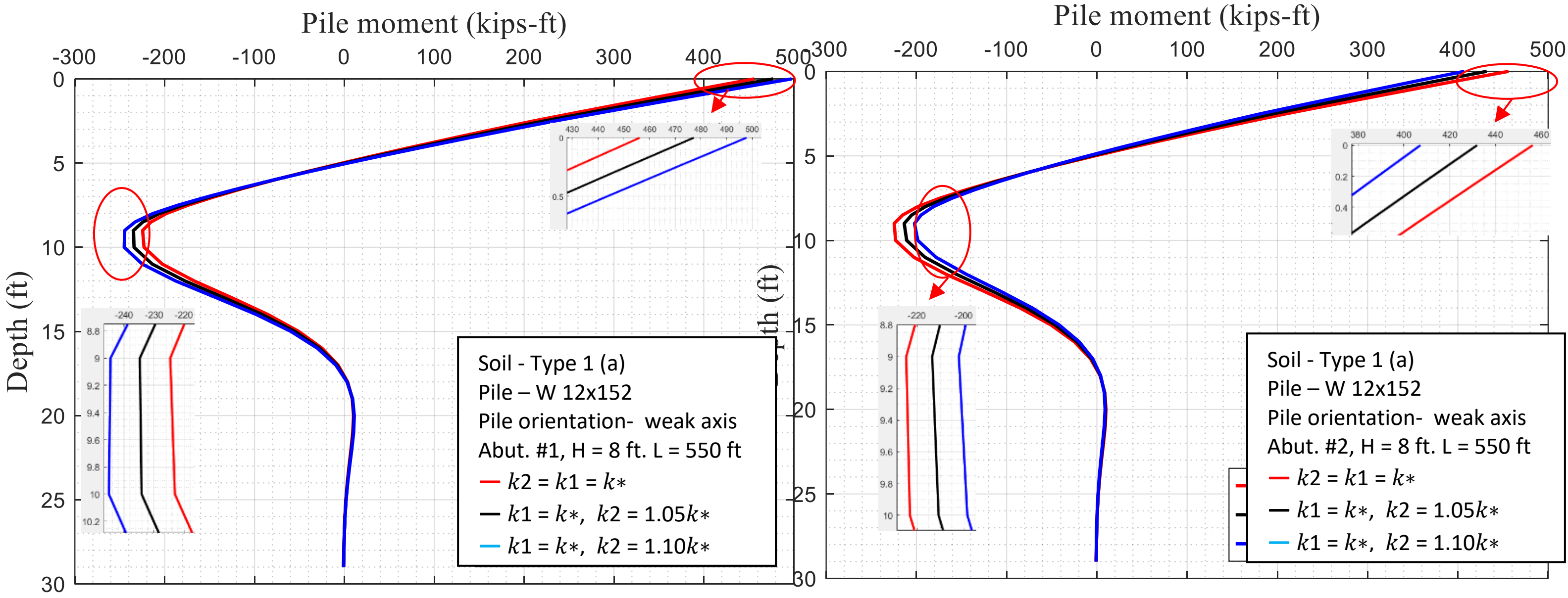

(b)

Fig. C.43 W 12x152 pile, Abut. #1, #2 (a) displacement and (b) moment due to temp. – 550ft span / weak axis / H = 8 ft / GTStrudl

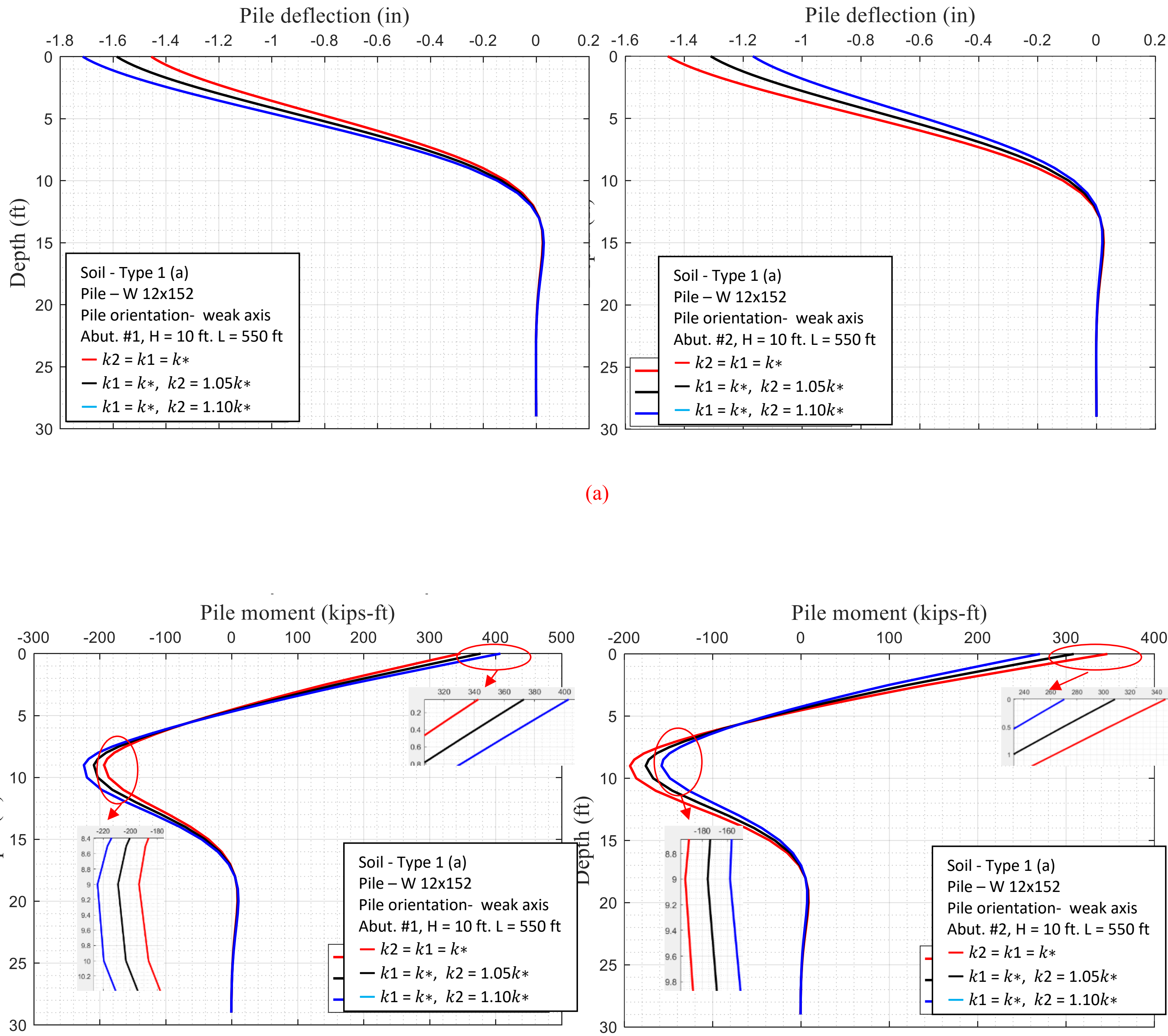

(b)

Fig. C.44 W 12x152 pile, Abut. #1, #2 (a) displacement and (b) moment due to temp. – 550 ft span / weak axis / H = 10 ft / GTStrudl

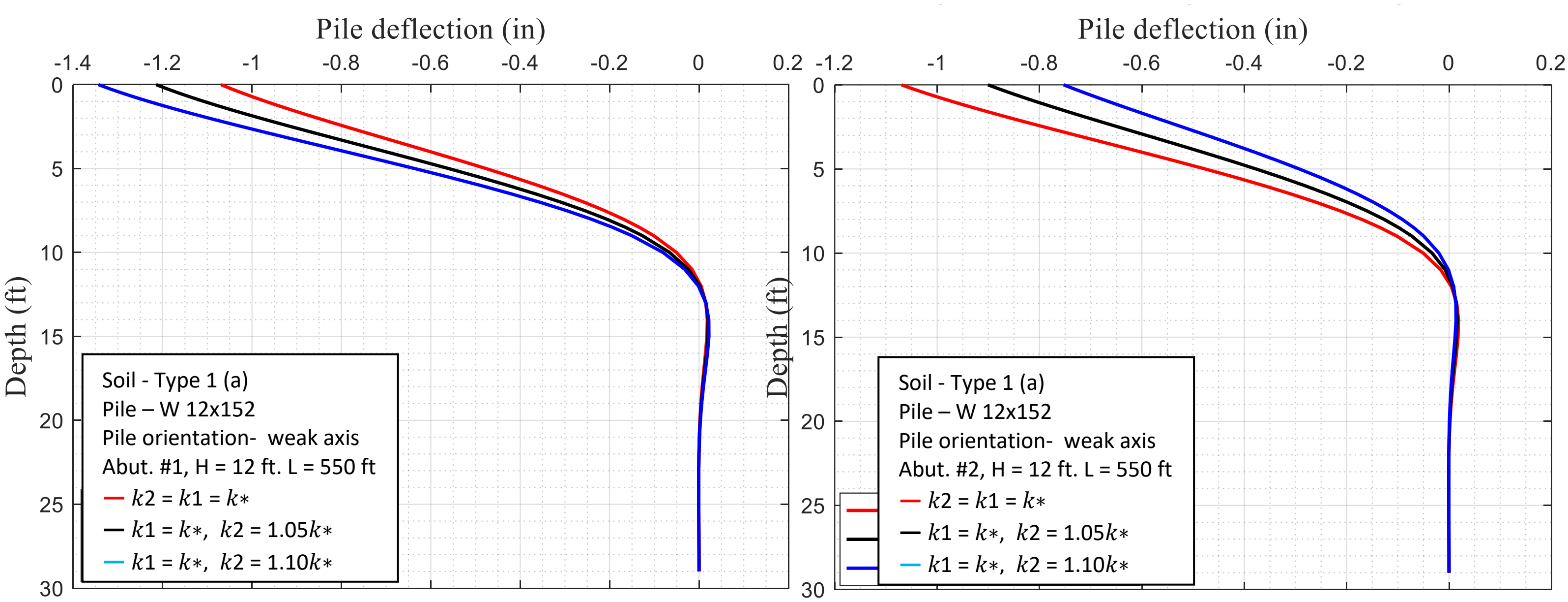

(a)

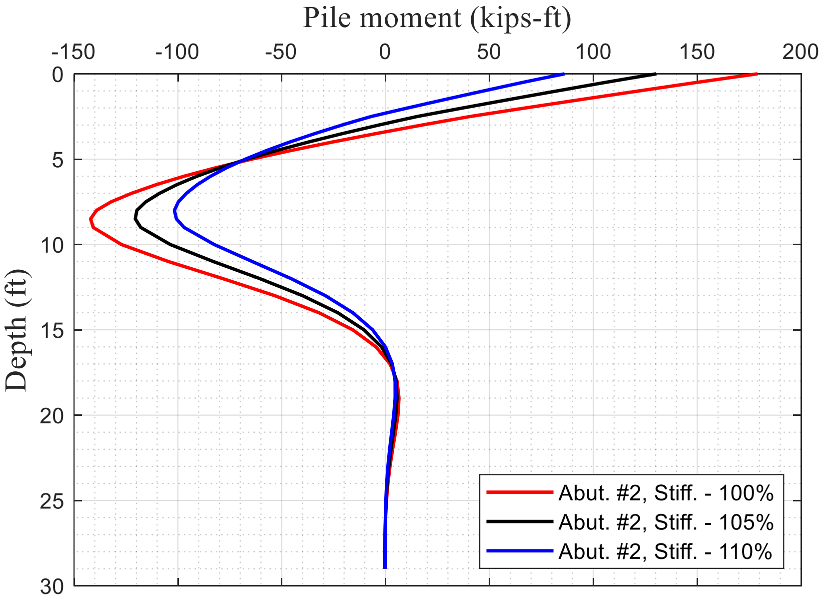

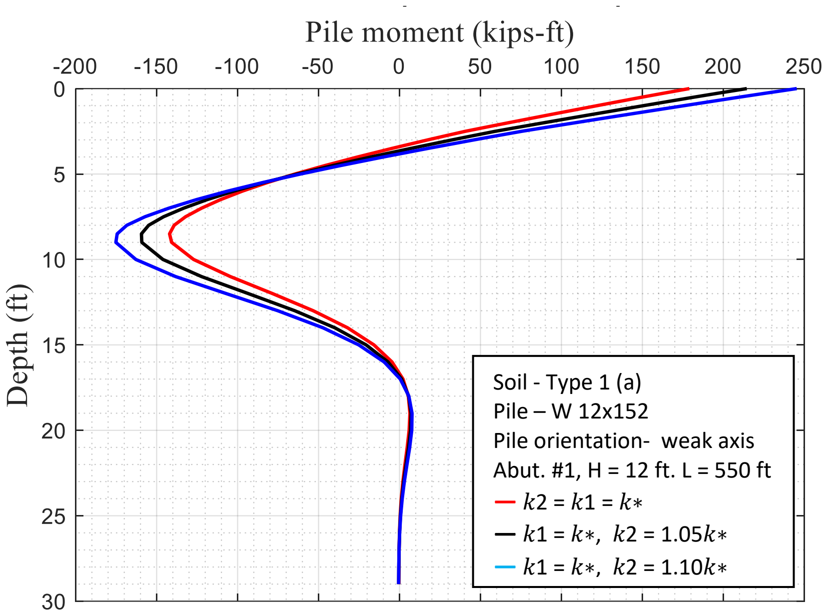

(b)

Fig. C.45 W 12x152 pile, Abut. #1, #2 (a) displacement and (b) moment due to temp. – 550 ft span / weak axis / H = 12 ft / GTSrudl

Table C.5: Quantitative data of W12x152 pile for different sand stiffness around abutment wall

Soil - Type 1 (a)
Pile – W 12x152
Pile orientation- weak axis
Abut. #2, H = 12 ft. L = 550 ft
— $k2 = k1 = k*$
— $k1 = k*,\ k2 = 1.05k*$
— $k1 = k*,\ k2 = 1.10k*$

Abutment Height (inch)	Span Length (ft)	Stiffness of Soil Behind Abutment Wall #2	Abut. Source	Pile Head Deflection (inch)	Rotation at Pile Head	Axial Force at Pile head (kips)	Abutment Head Deflection (inch)	Abutment Bottom Deflection (inch)	Shear Force at Pile Head (kips)	Max. Moment at Pile Head (kip-ft)	Max. Moment a Pile 2nd Segment (kip-ft)
H = 8	550	$k_2 = k_1 = k*$	#1, #2	-1.703	0.0044	-101.7	-1.911	-1.714	101.9	456.24	-224.60
		$k_2 = 1.05k*$	#1	-1.791	0.0045	-101.3	-2.000	-1.806	105.5	477.23	-234.75
			#2	-1.605	0.0043	-101.7	-1.809	-1.614	97.8	431.96	-213.48
		$k_2 = 1.10k*$	#1	-1.882	0.0047	-100.9	-2.107	-1.898	108.9	497.73	-245.08
			#2	-1.506	0.0041	-101.9	-1.708	-1.516	93.5	407.23	-202.08
H=10	550	$k_2 = k_1 = k*$	#1, #2	-1.456	0.0058	-133.3	-1.891	-1.471	85.6	346.76	-193.61
		$k_2 = 1.05k*$	#1	-1.586	0.0060	-132.6	-2.036	-1.602	91.0	377.23	-209.08
			#2	-1.309	0.0056	-133.4	-1.741	-1.325	78.9	308.67	-175.79
		$k_2 = 1.10k*$	#1	-1.714	0.0063	-132.0	-2.180	-1.731	96.3	407.09	-224.22
			#2	-1.166	0.0054	-133.6	-1.593	-1.181	72.0	270.42	-157.91
H=12	550	$k_2 = k_1 = k*$	#1, #2	-1.070	0.0075	-129.2	-1.873	-1.091	58.9	179.02	-142.04
		$k_2 = 1.05k*$	#1	-1.214	0.0078	-128.3	-2.045	-1.237	65.7	214.49	-159.40
			#2	-0.900	0.0072	-129.5	-1.696	-0.921	49.5	130.32	-120.52
		$k_2 = 1.10k*$	#1	-1.343	0.0081	-127.5	-2.197	-1.367	71.4	245.35	-175.21
			#2	-0.752	0.0069	-129.7	-1.539	-0.773	40.7	86.13	-101.69

Effect of Span Length – L = 150, 275, 550 ft

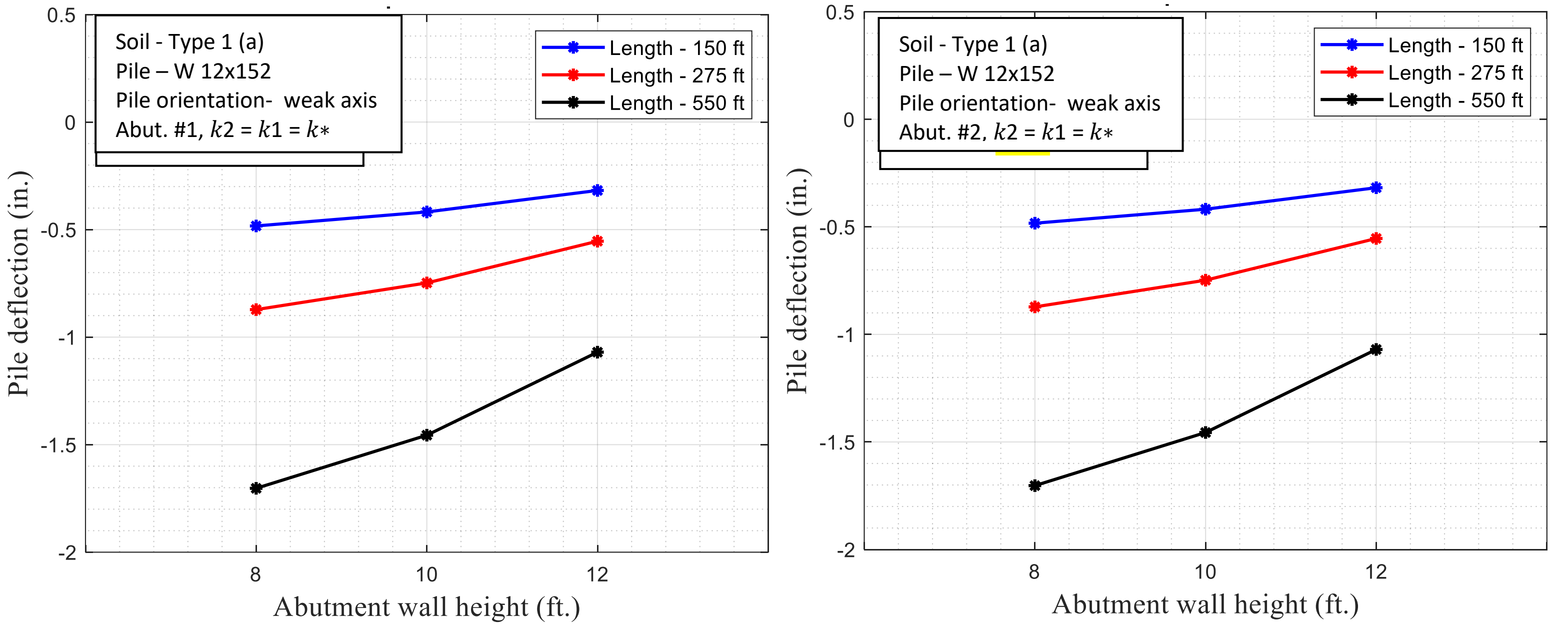

Fig. C.46 W 12x152 pile displacement due to temp. – 150/275/550 ft – $k_2 = k_1 = k*$/ GTStrudl

Size – W 12x152
Orientation- weak axis
Stiffness -105%

Size – W 12x152
Orientation- weak axis
Stiffness -105%

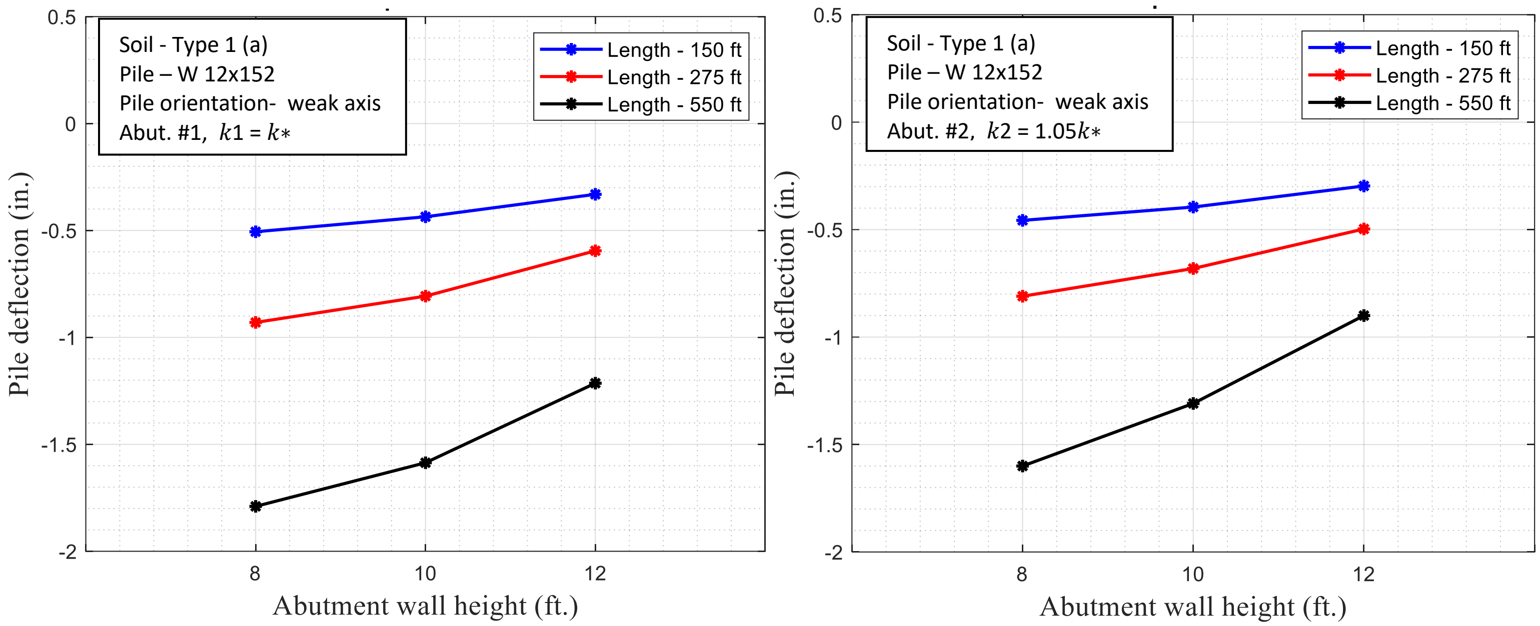

Fig. C.47 W 12x152 pile displacement due to temp. – 150/275/550 ft - $k_1 = k*$, $k_2 = 1.05k*$/ GTStrudl

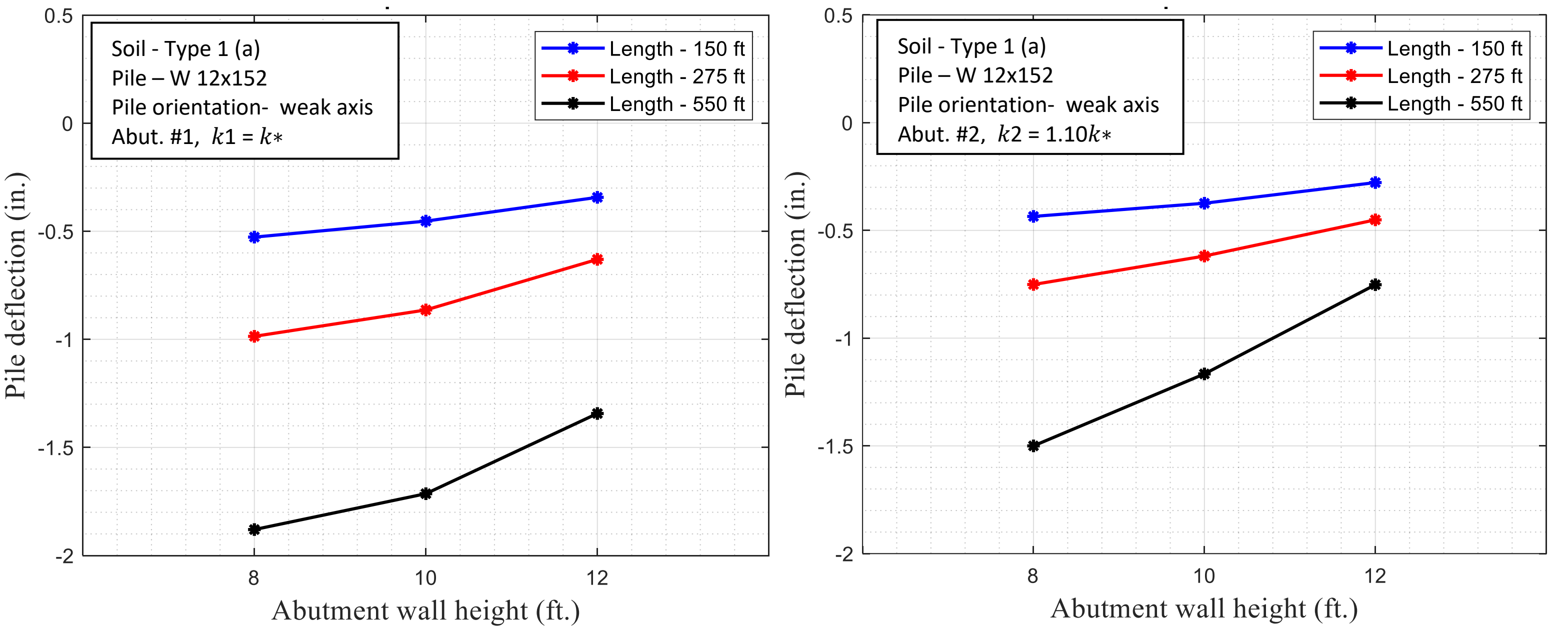

Fig. C.48 W 12x152 pile displacement due to temp. – 150/275/550 ft $k_1 = k*$, $k_2 = 1.10k*$/ GTStrudl

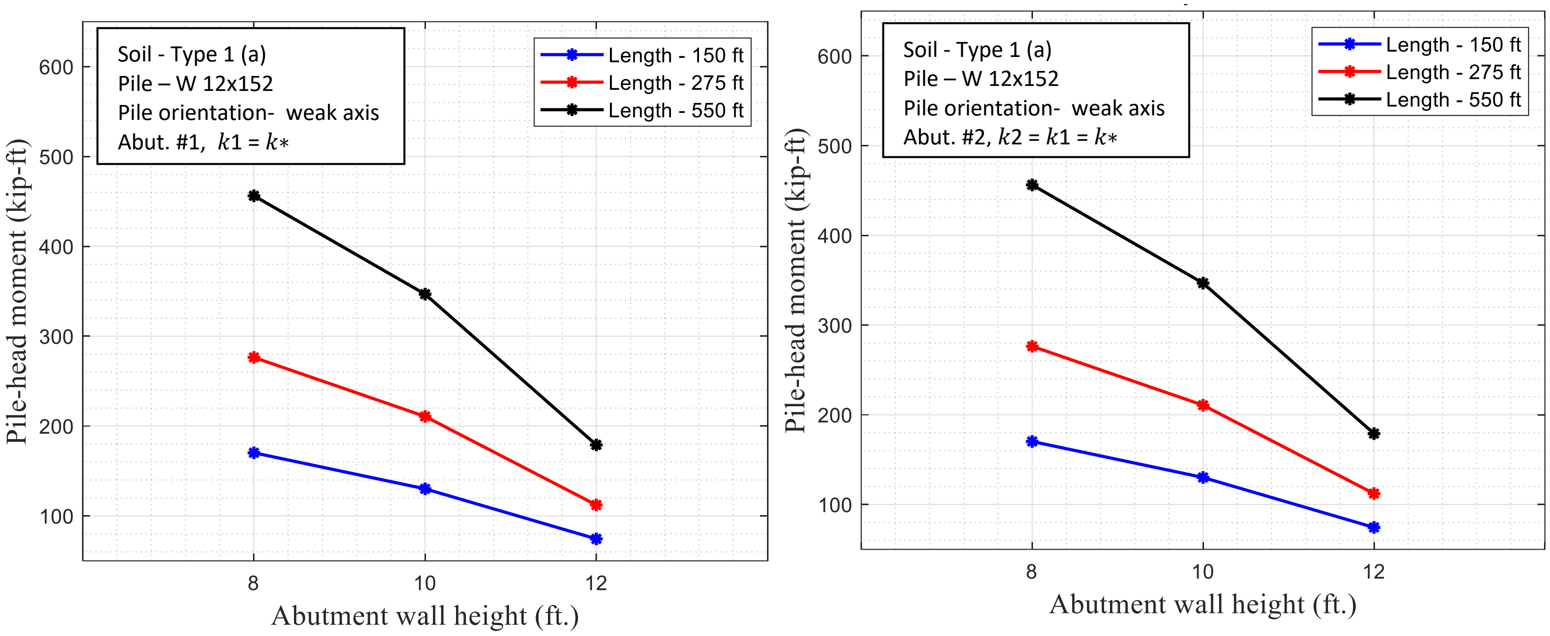

Fig. C.49 W 12x152 pile-head moment due to temp. -150/275/550 ft – $k_2 = k_1 = k*$/ GTStrudl

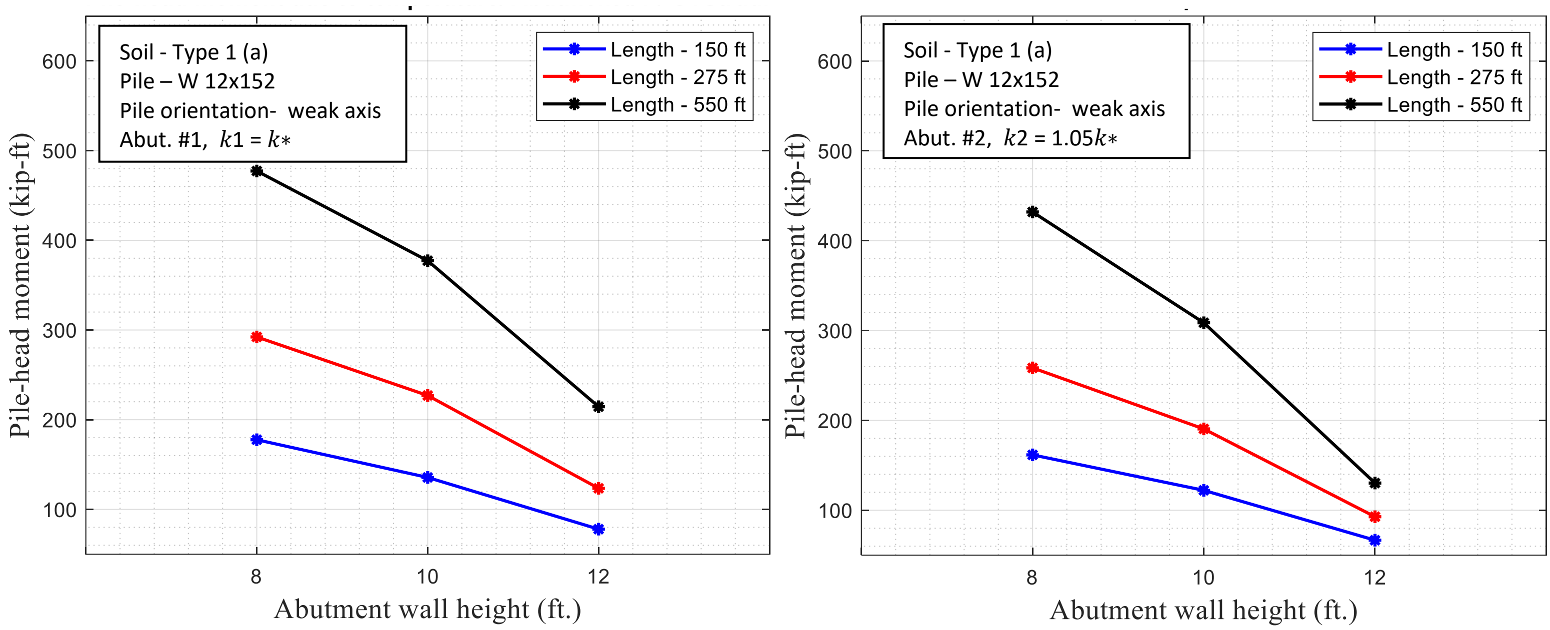

Fig. C.50 W 12x152 pile-head moment due to temp. – 150/275/550 ft - $k_1 = k*$, $k_2 = 1.05k*$/ GTStrudl

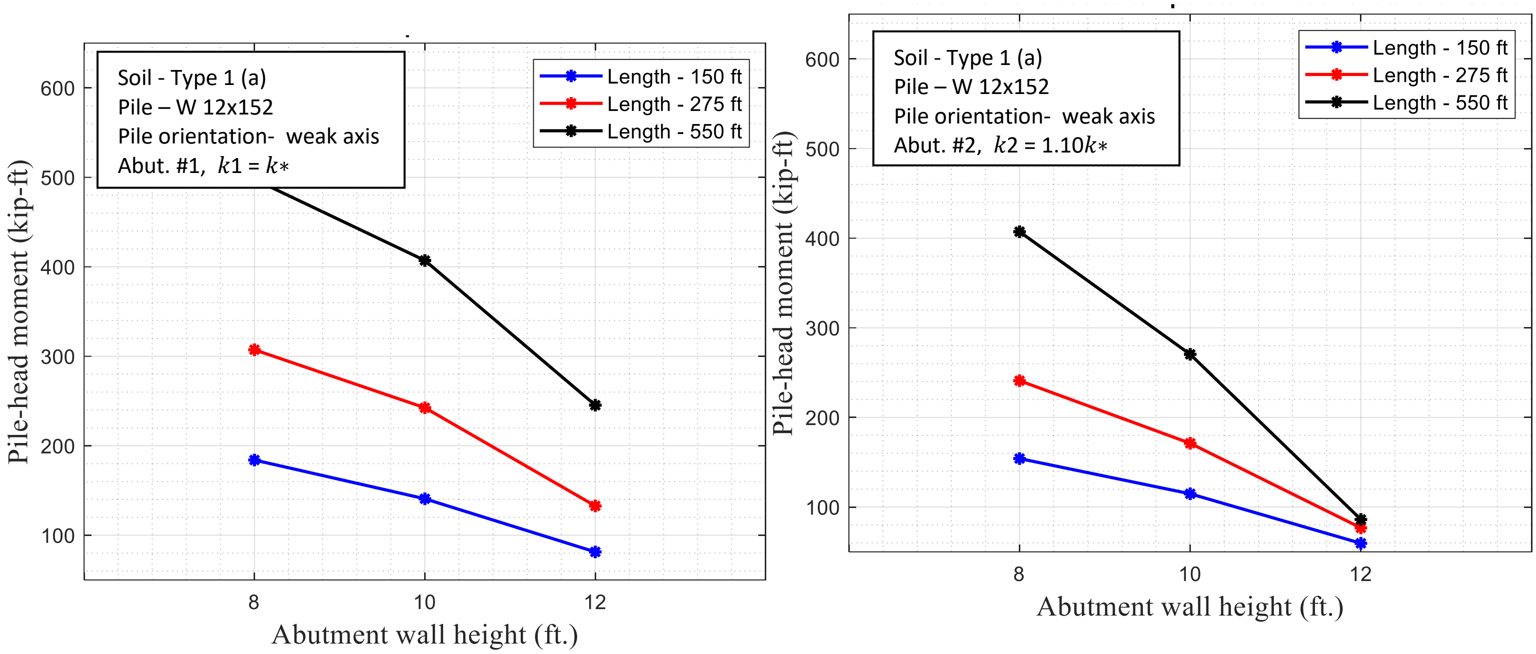

Fig. C.51 W 12x152 pile-head moment due to temp. – 150/275/550 ft - $k_1 = k*$, $k_2 = 1.10k*$/ GTStrudl

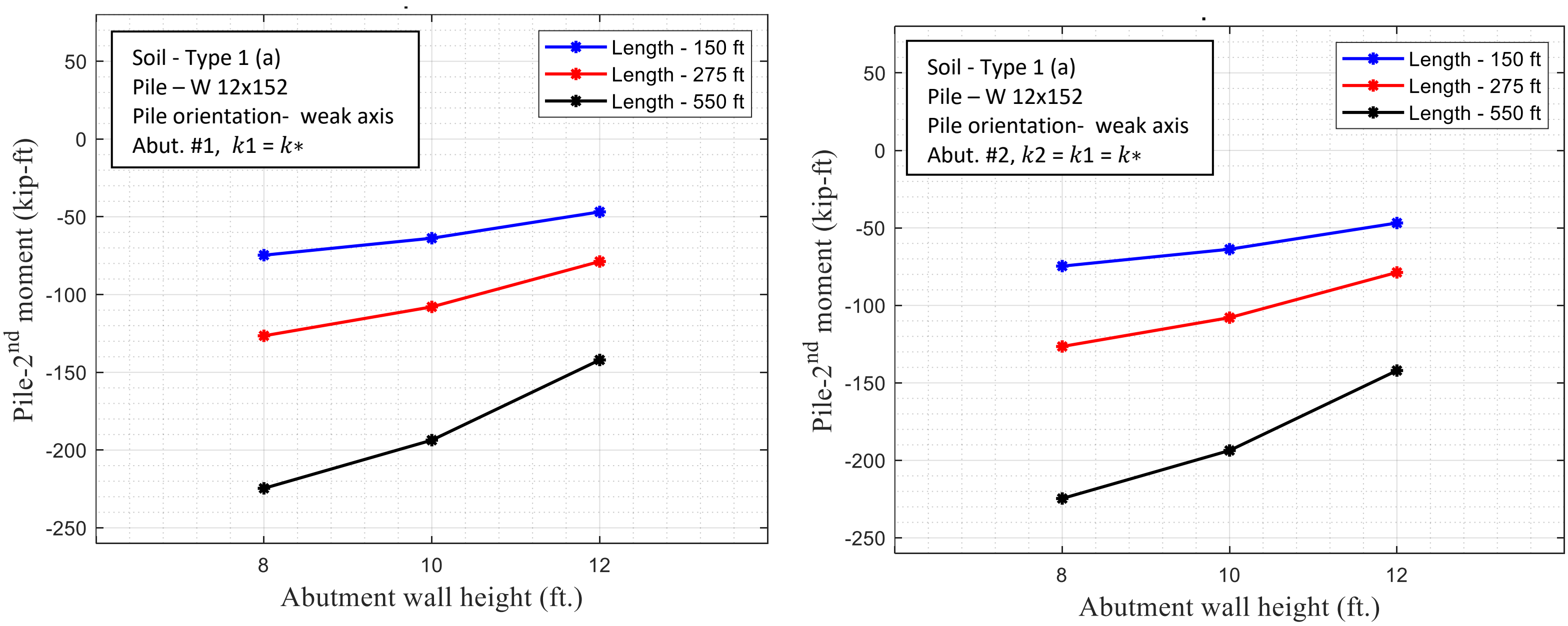

Fig. C.52 W 12x152 pile-2nd moment due to temp. – 150/275/550 ft – $k_2 = k_1 = k*$/ GTStrudl

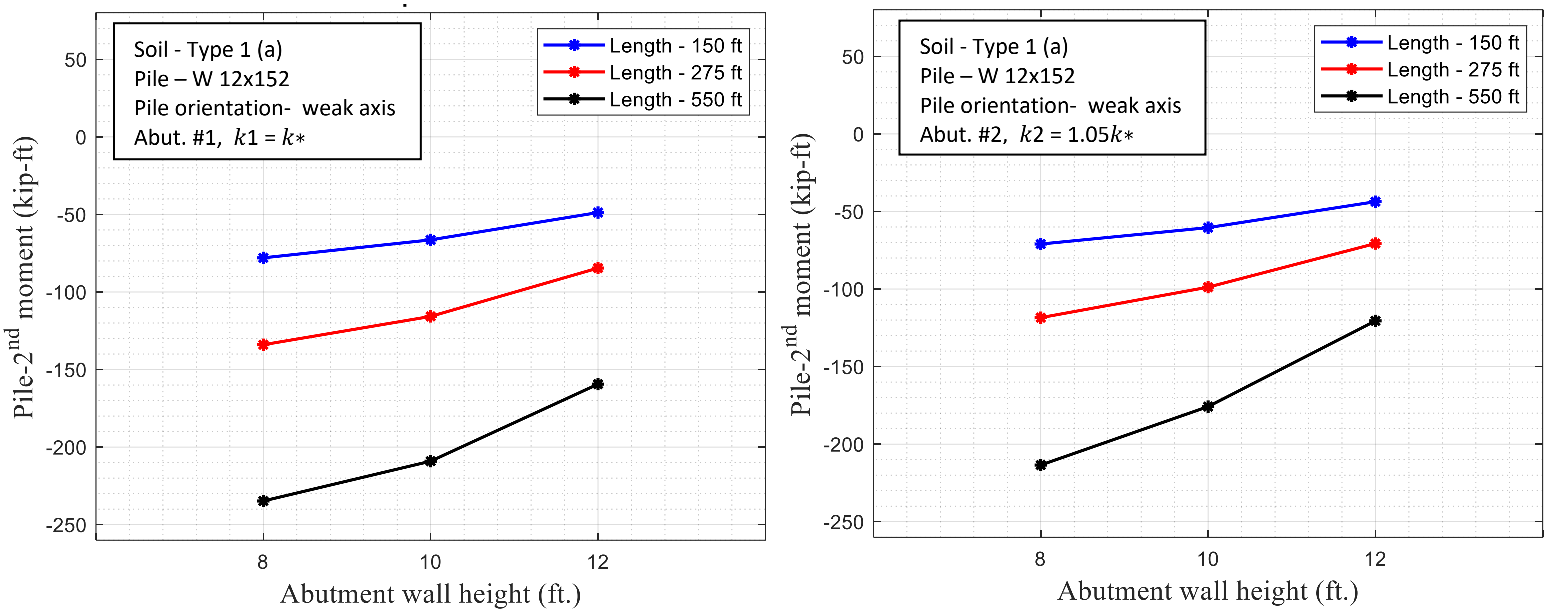

Fig. C.53 W 12x152 pile-2nd moment due to temp. – 150/275/550 ft - $k_1 = k*$, $k_2 = 1.05k*$/ GTStrudl

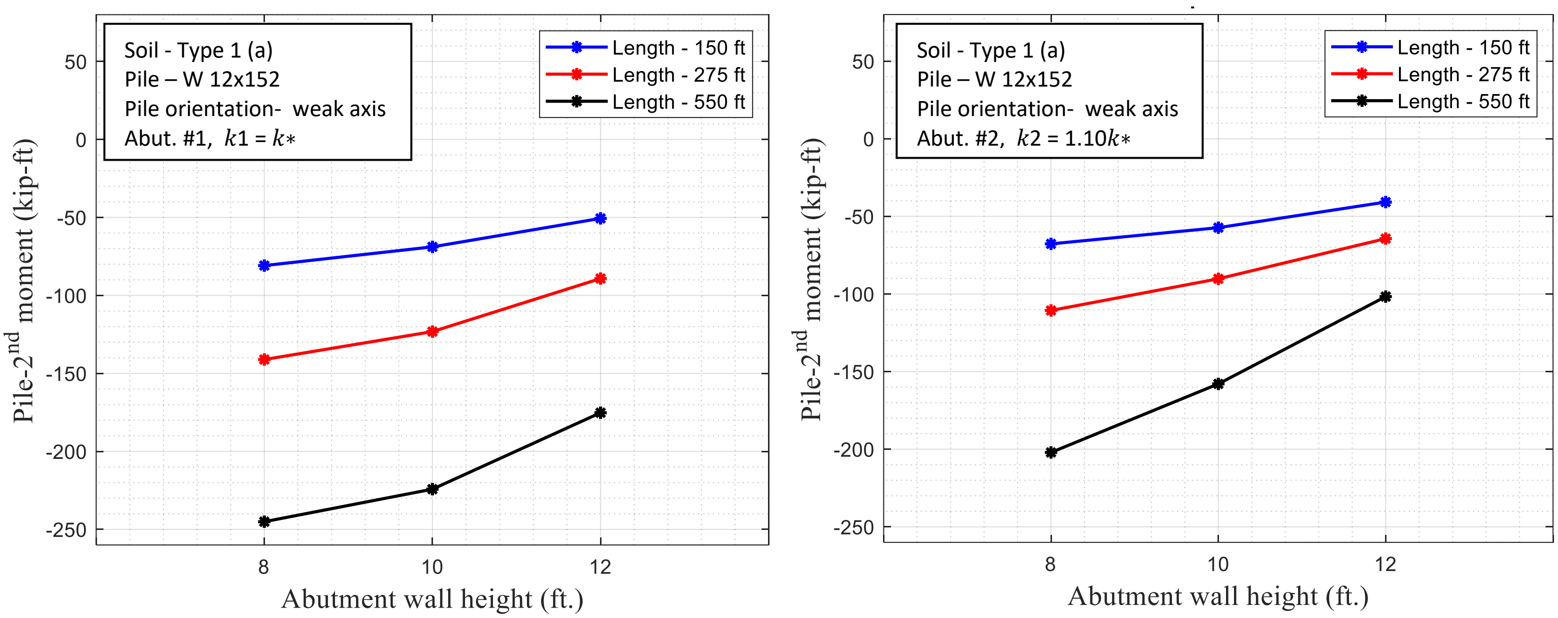

Fig. C.54 W 12x152 pile-2nd moment due to temp. – 150/275/550 ft - $k_1 = k*$, $k_2 = 1.10k*$/ GTStrudl

<u>**Effect of Abutment Height – H = 8, 10, 12 ft**</u>

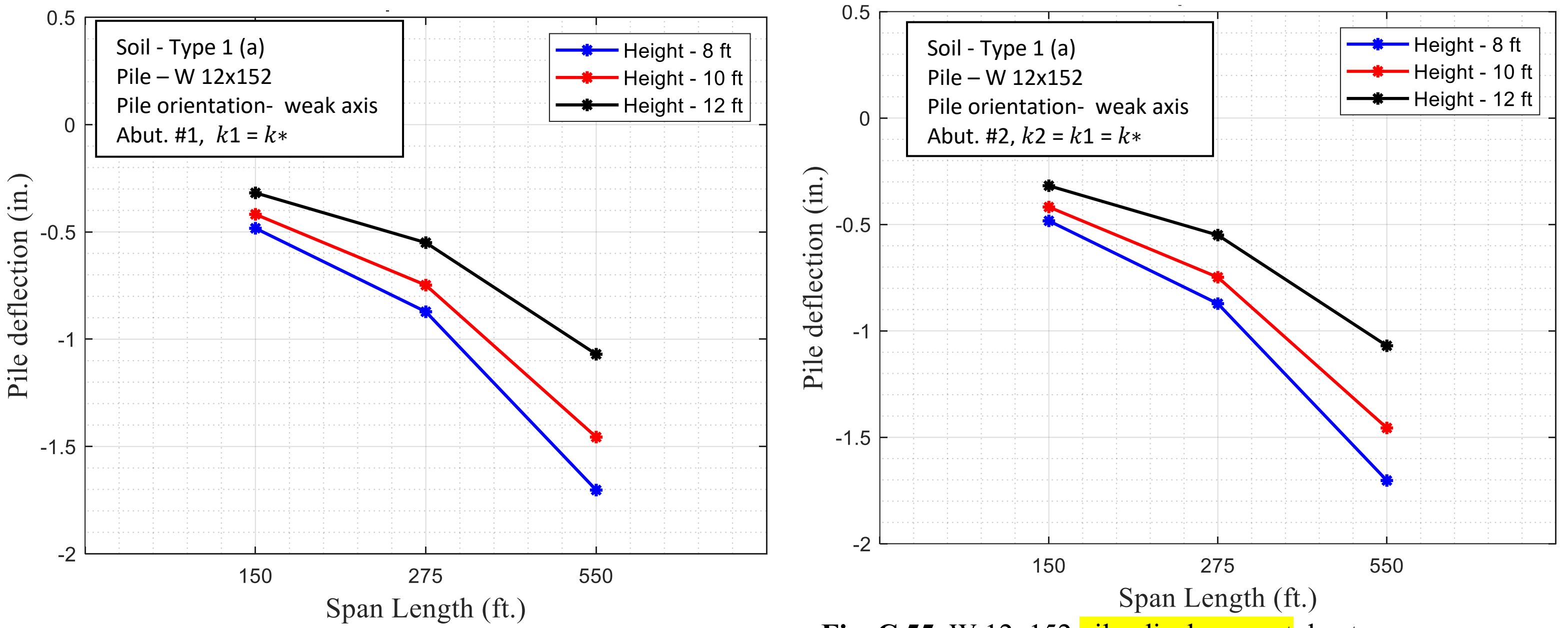

Fig. C.55 W 12x152 pile displacement due to temp. – 8/10/12 ft – $k_2 = k_1 = k^*$/ GTStrudl

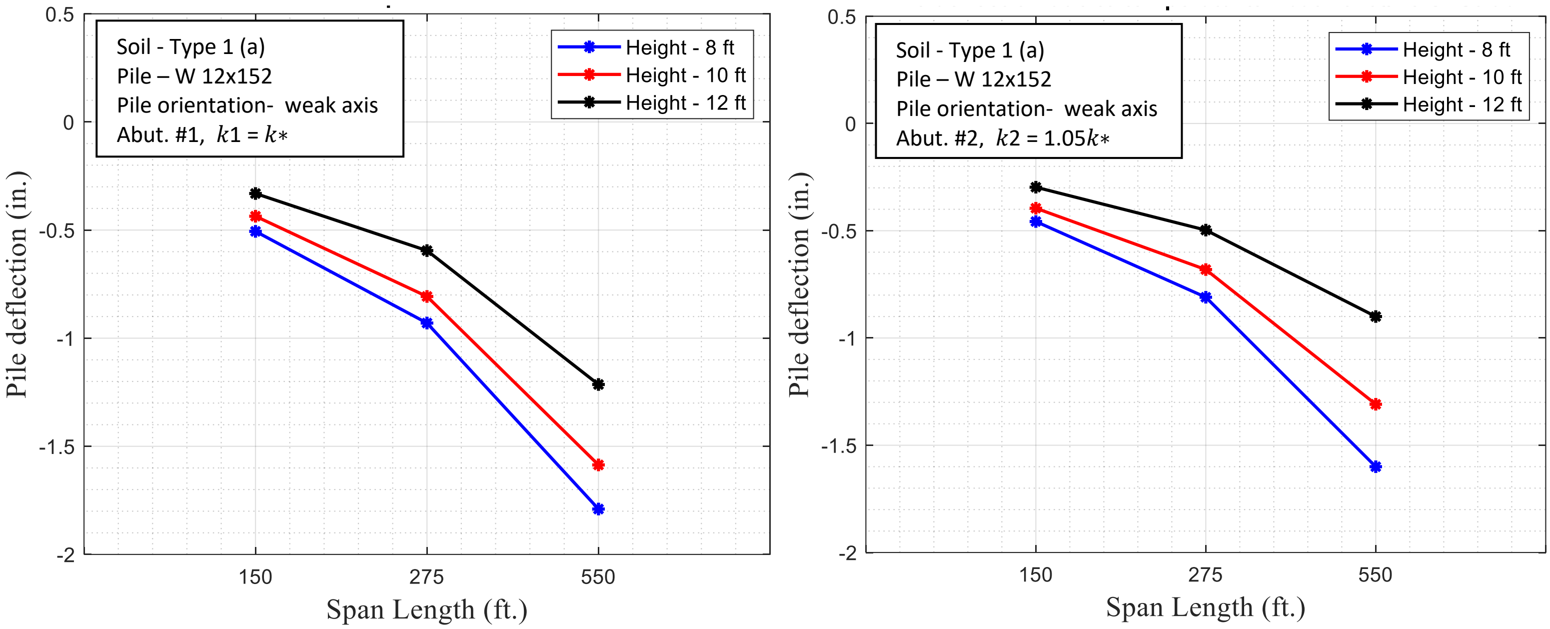

Fig. C.56 W 12x152 pile displacement due to temp. – 8/10/12 ft - $k_2 = k_1 = k*$, $k_2 = 1.05k*$/ GTStrudl

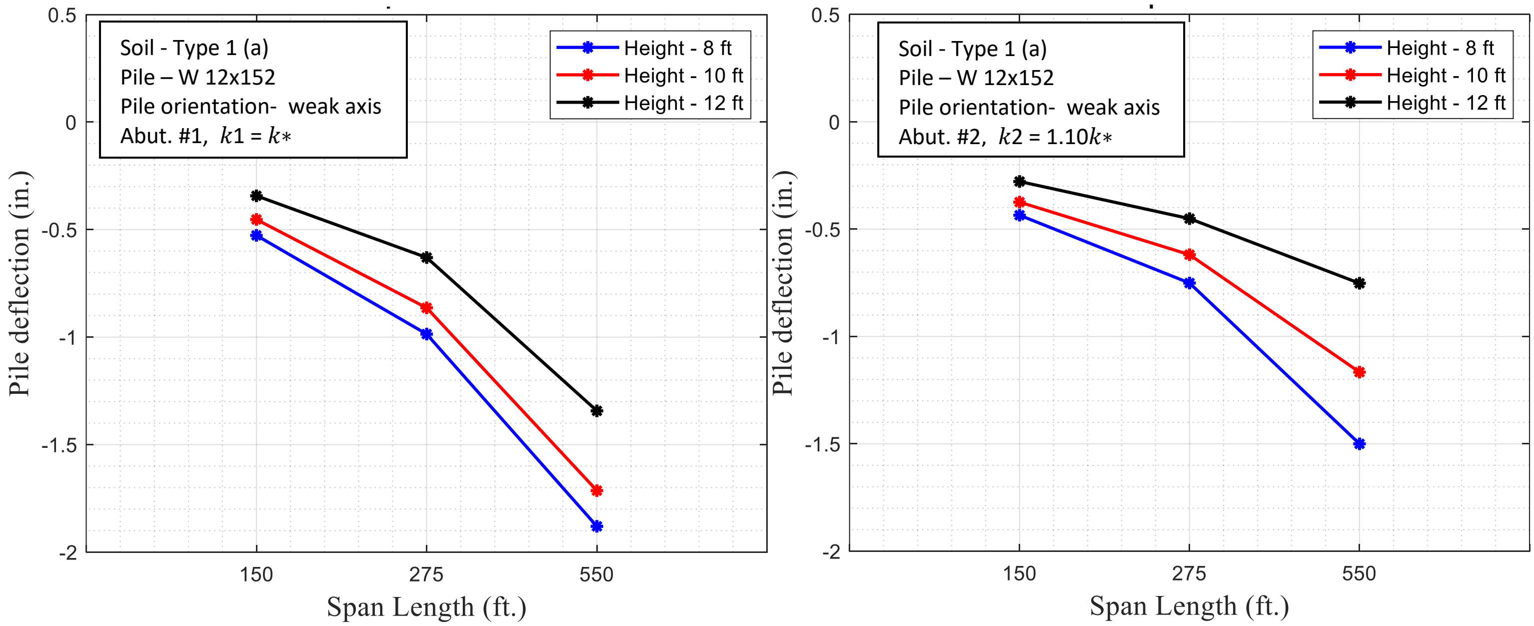

Fig. C.57 W 12x152 pile displacement due to temp. – 8/10/12 ft - $k_2 = k_1 = k*$, $k_2 = 1.10k*$/ GTStrudl

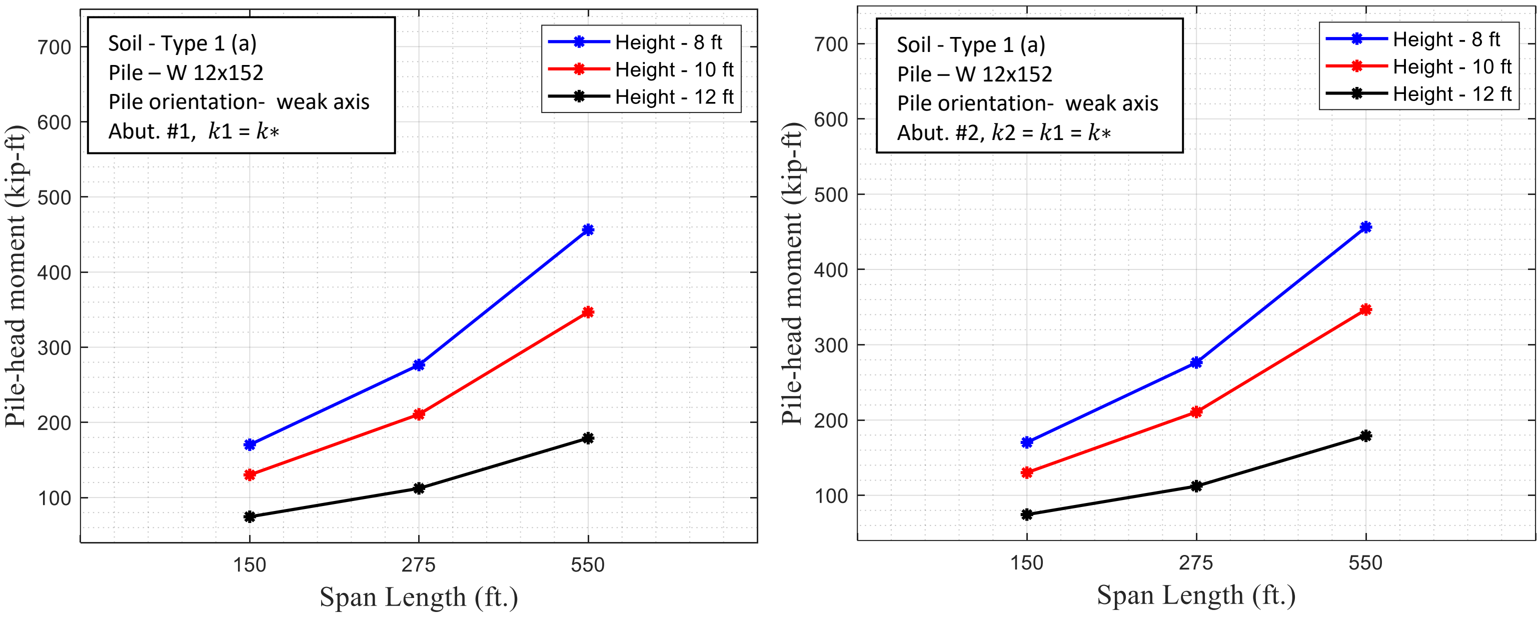

Fig. C.58 W 12x152 pile-head moment due to temp. – 8/10/12 ft - $k_2 = k_1 = k*$/ GTStrudl

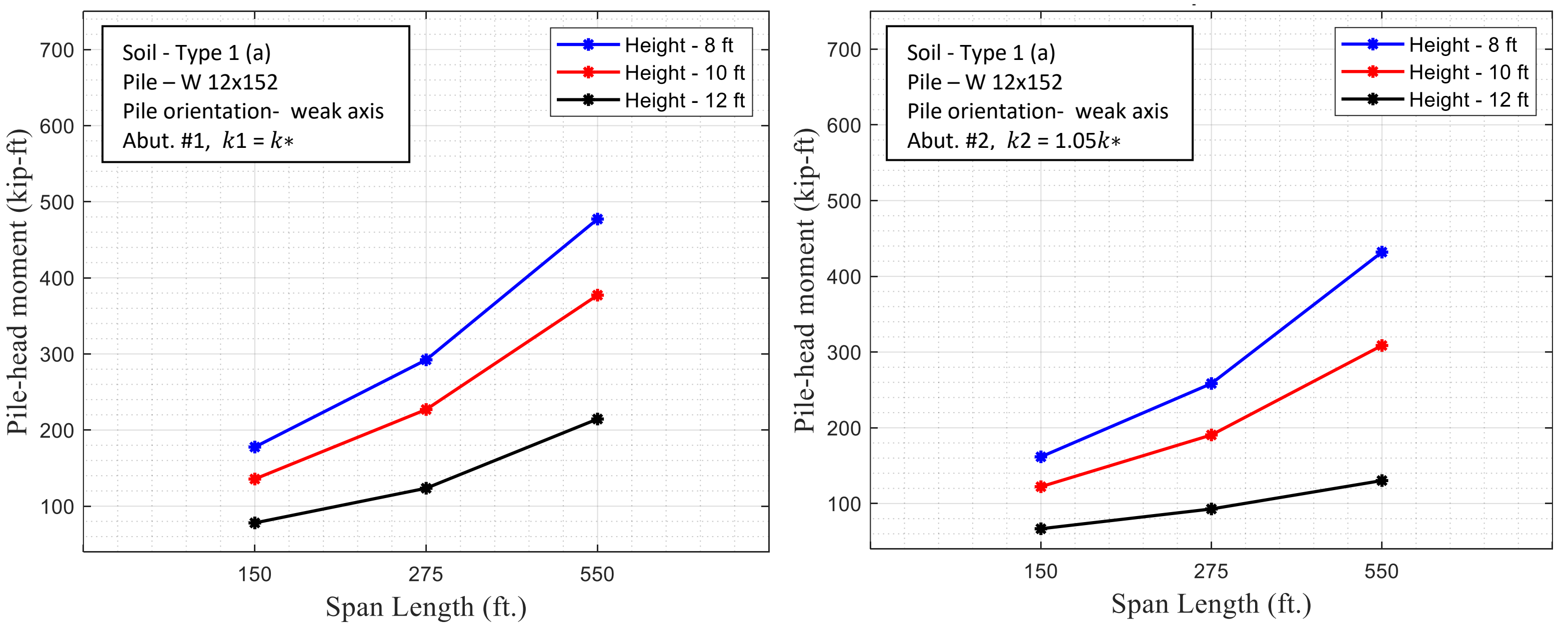

Fig. C.59 W 12x152 pile-head moment due to temp. – 8/10/12 ft - $k_2 = k_1 = k*$, $k_2 = 1.05k*$/ GTStrudl

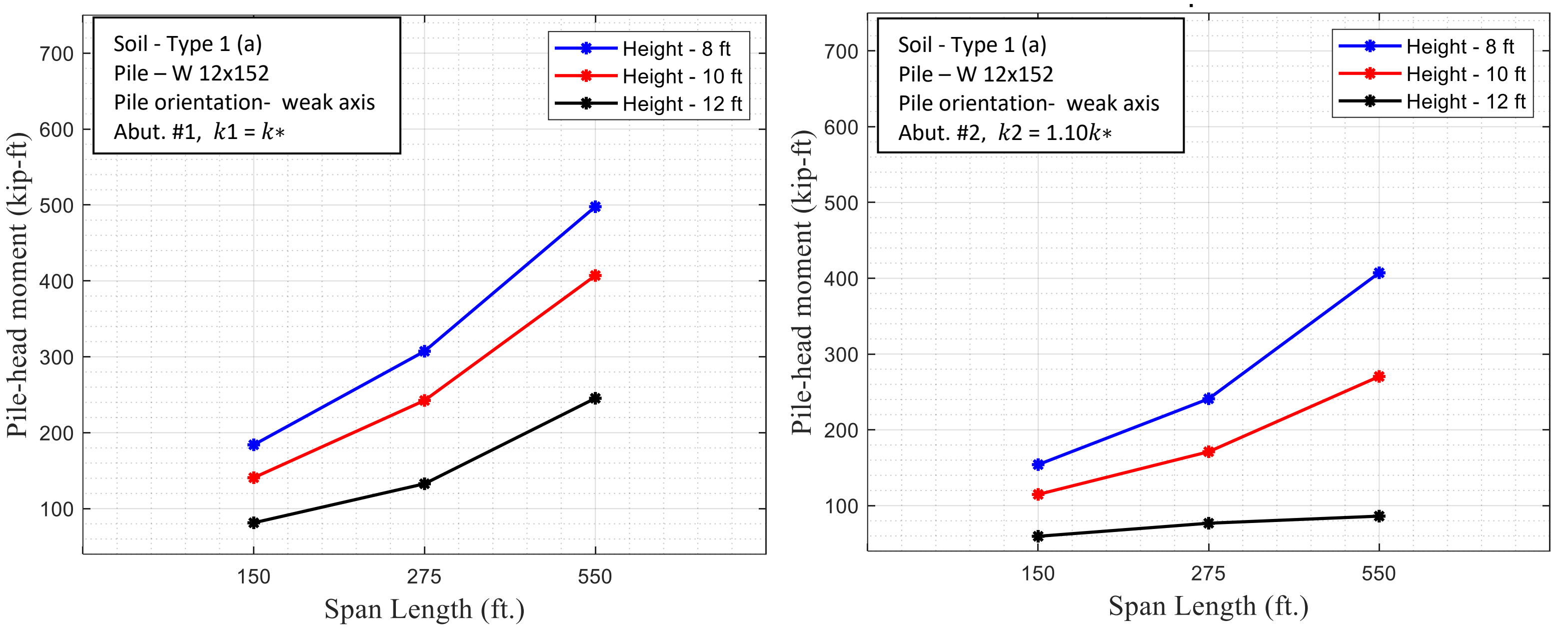

Fig. C.60 W 12x152 pile-head moment due to temp. – 8/10/12 ft - $k_2 = k_1 = k*$, $k_2 = 1.10k*$/ GTStrudl

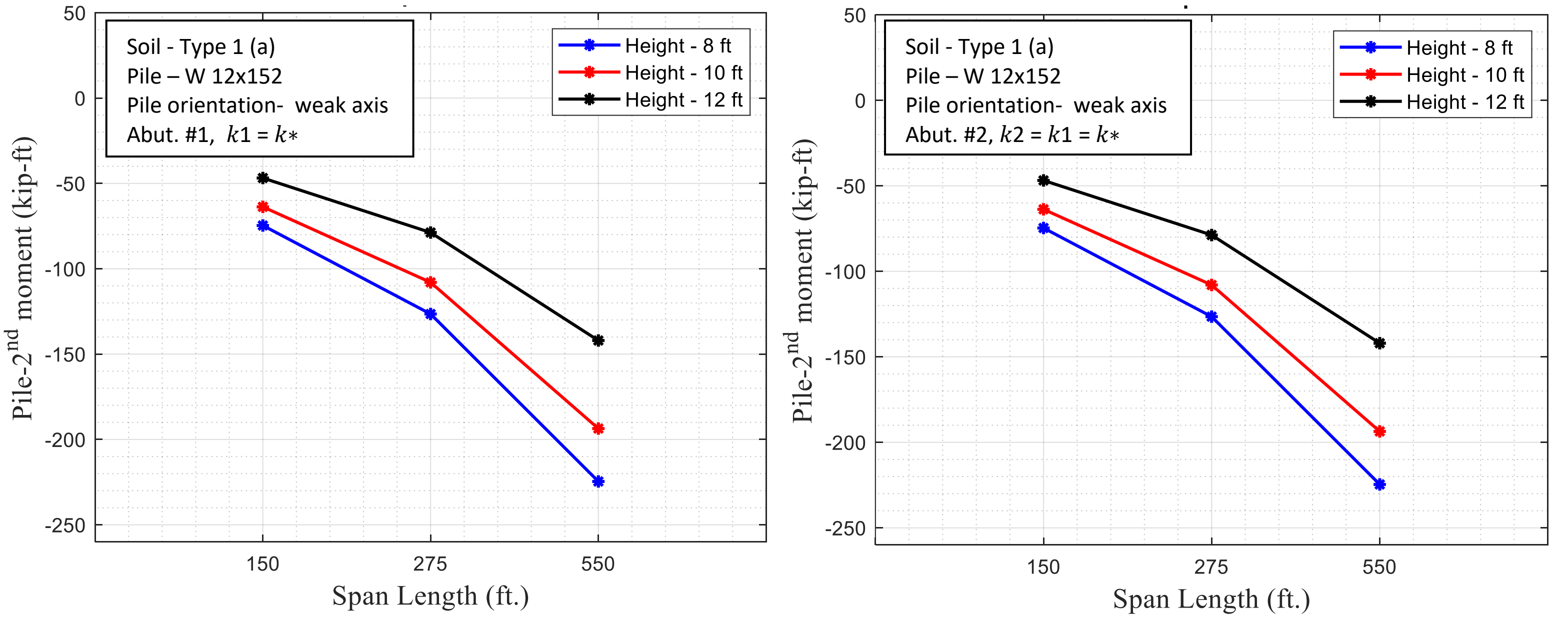

Fig. C.61 W 12x152 pile-2nd moment due to temp. – 8/10/12 ft - $k_2 = k_1 = k*$/ GTStrudl

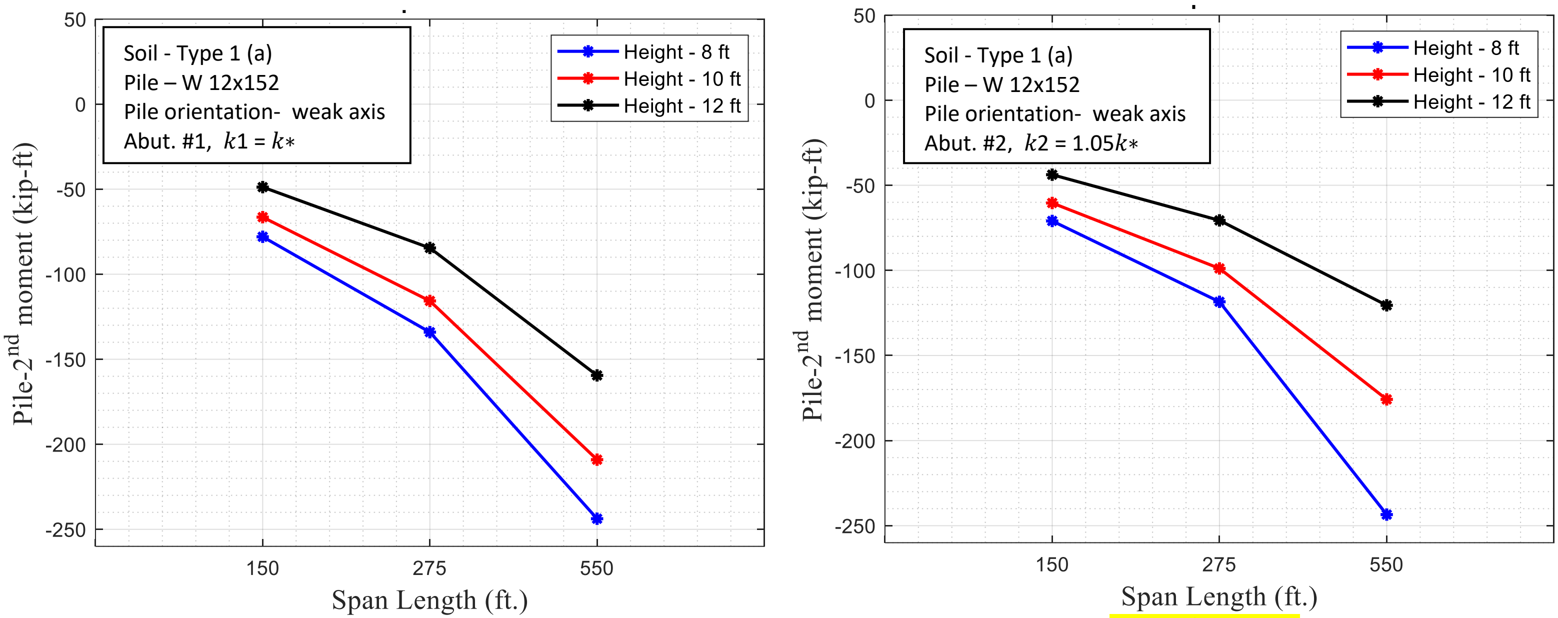

Fig. C.62 W 12x152 pile-2nd moment due to temp. – 8/10/12 ft - $k_2 = k_1 = k*$, $k_2 = 1.05k*$/ GTStrudl

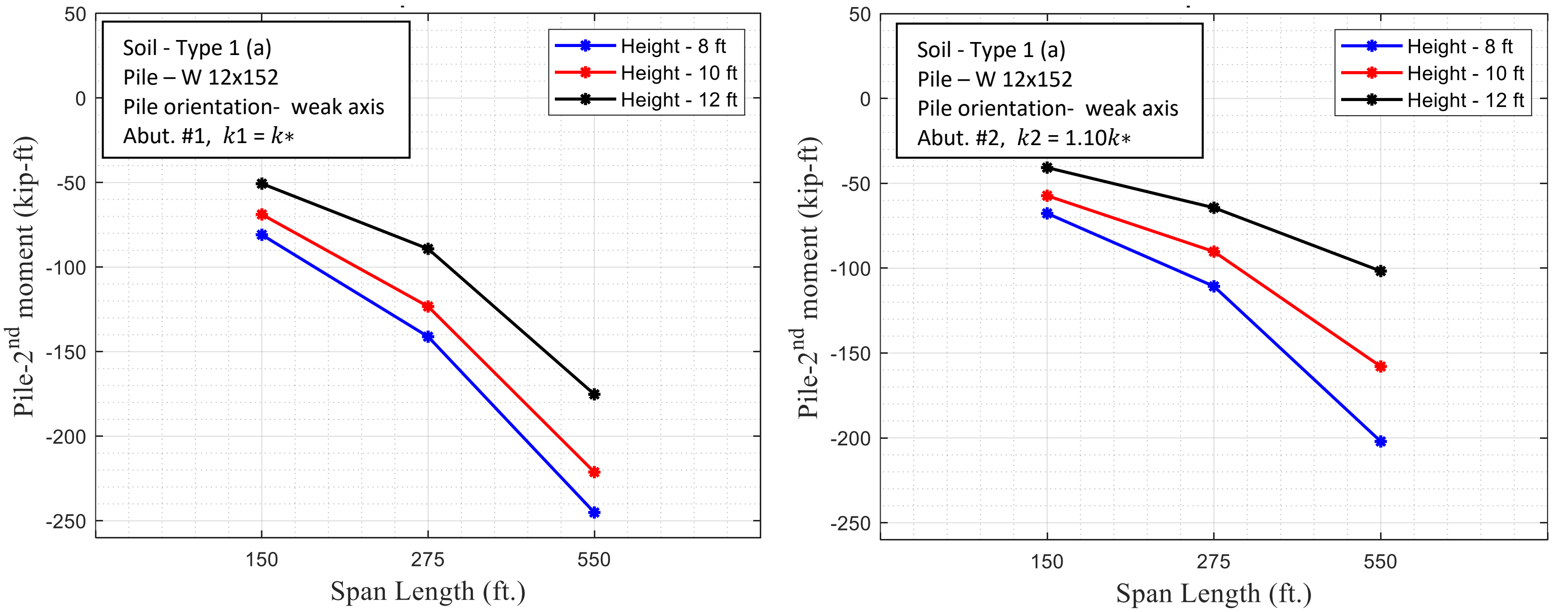

Fig. C.63 W 12x152 pile-2nd moment due to temp. – 8/10/12 ft - $k_2 = k_1 = k*$, $k_2 = 1.10k*$/ GTStrudl

Effect of Soil Stiffness at Abut. #2 – 100%, 105%, 110%

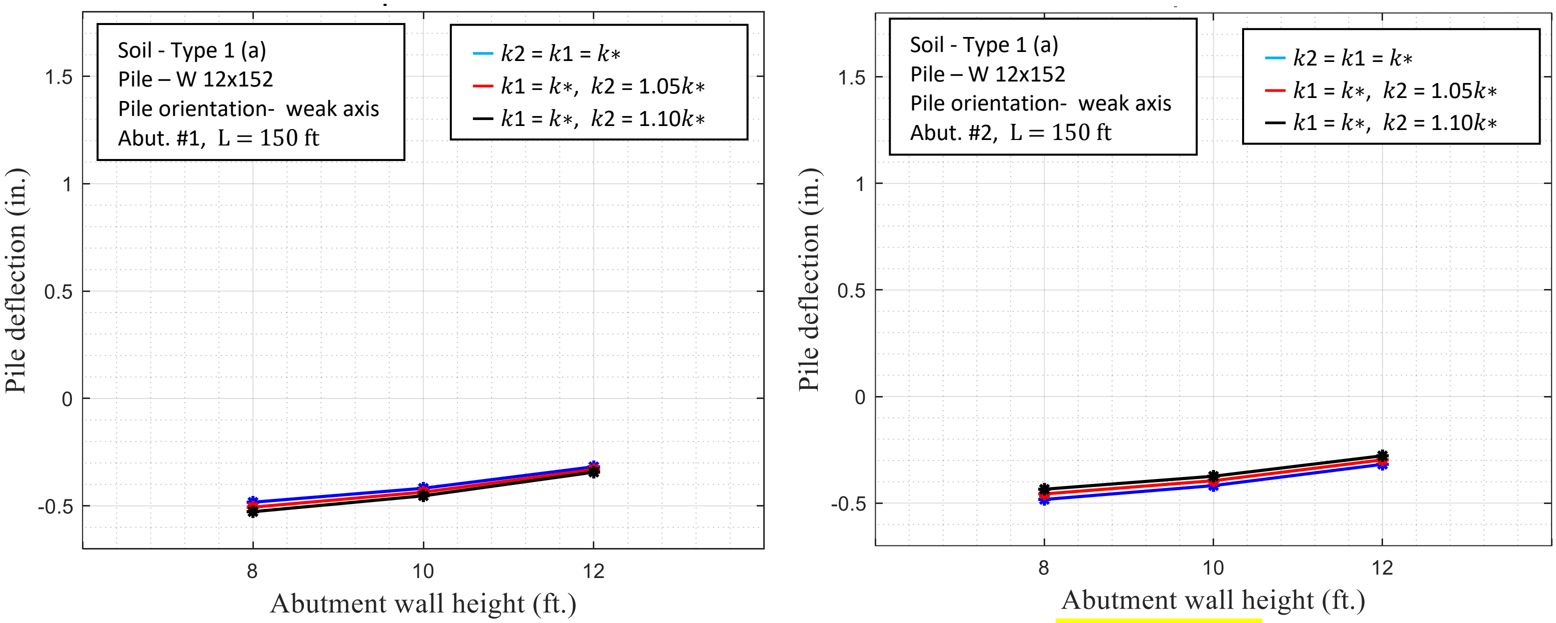

Fig. C.64 W 12x152 pile displacement due to temp. – varying backfill stiffness at abut. #2 - L=150 ft / GTStrudl

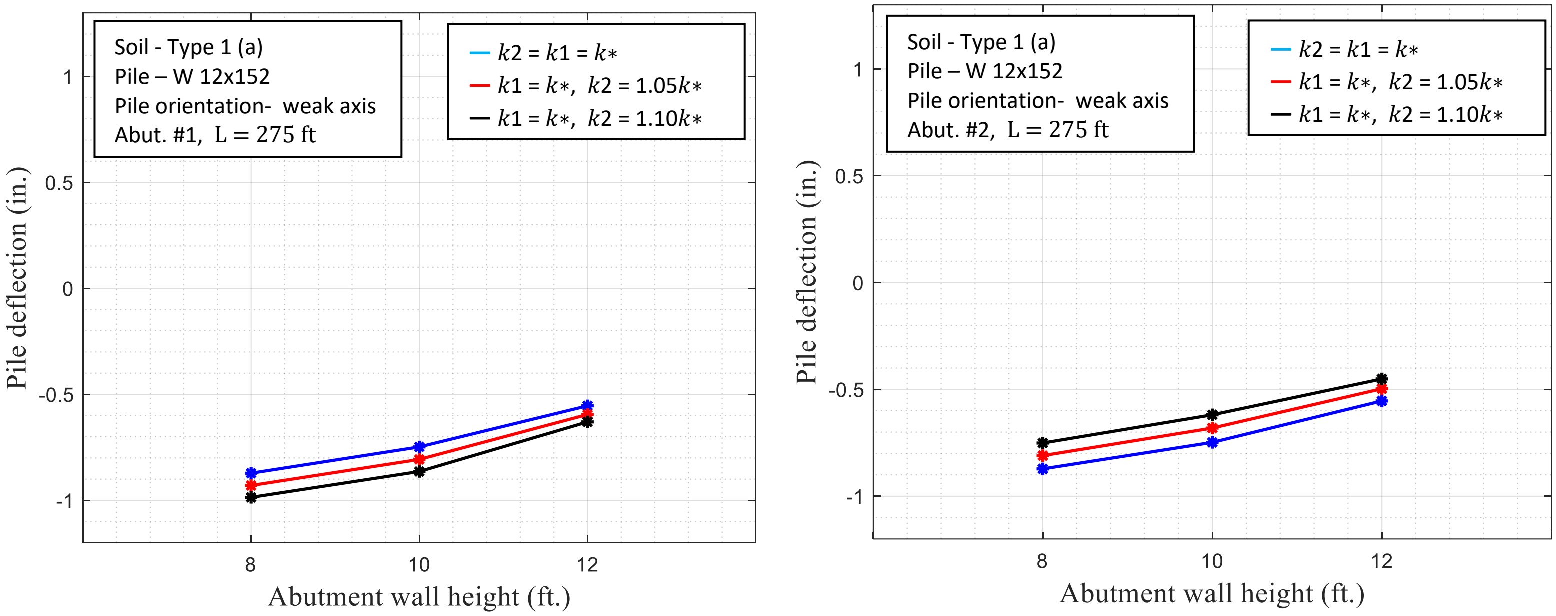

Fig. C.65 W 12x152 pile displacement due to temp. - varying backfill stiffness at abut. #2 - L=275 ft / GTStrudl

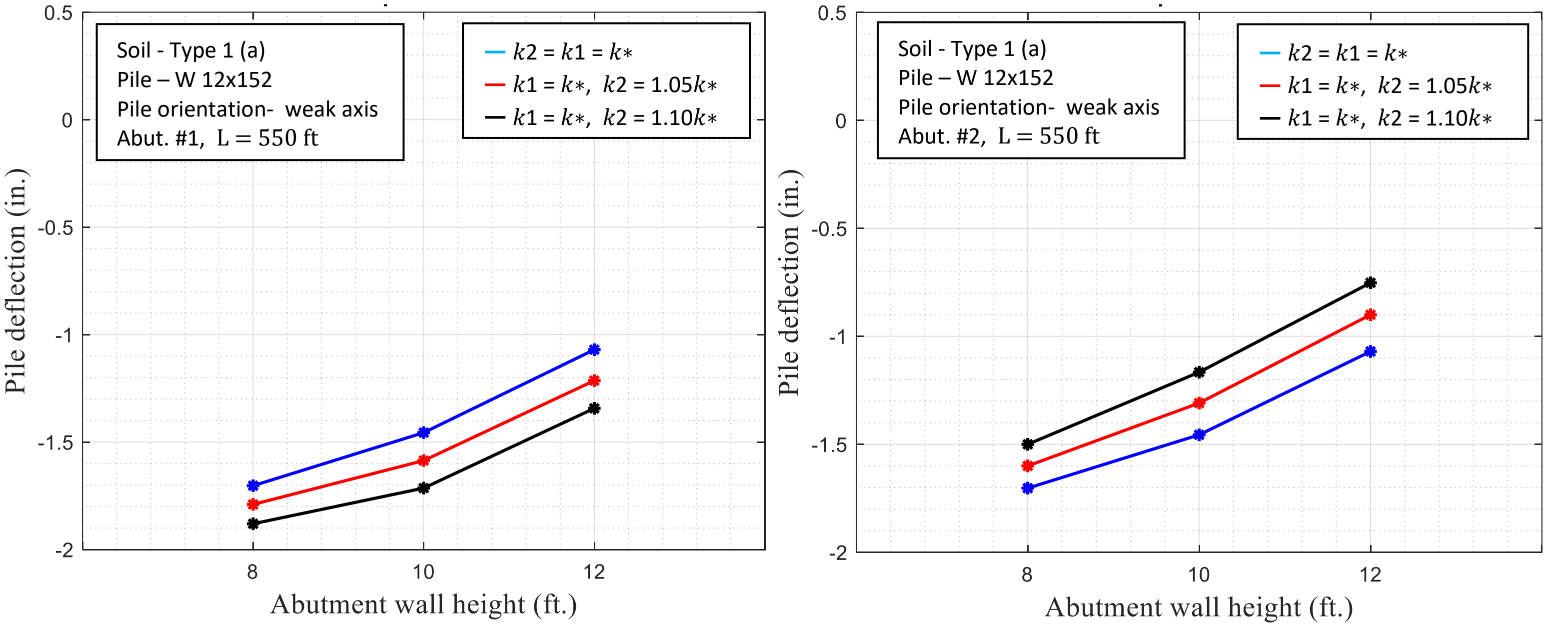

Fig. C.66 W 12x152 pile displacement due to temp. - varying backfill stiffness at abut. #2 - L=550 ft / GTStrudl

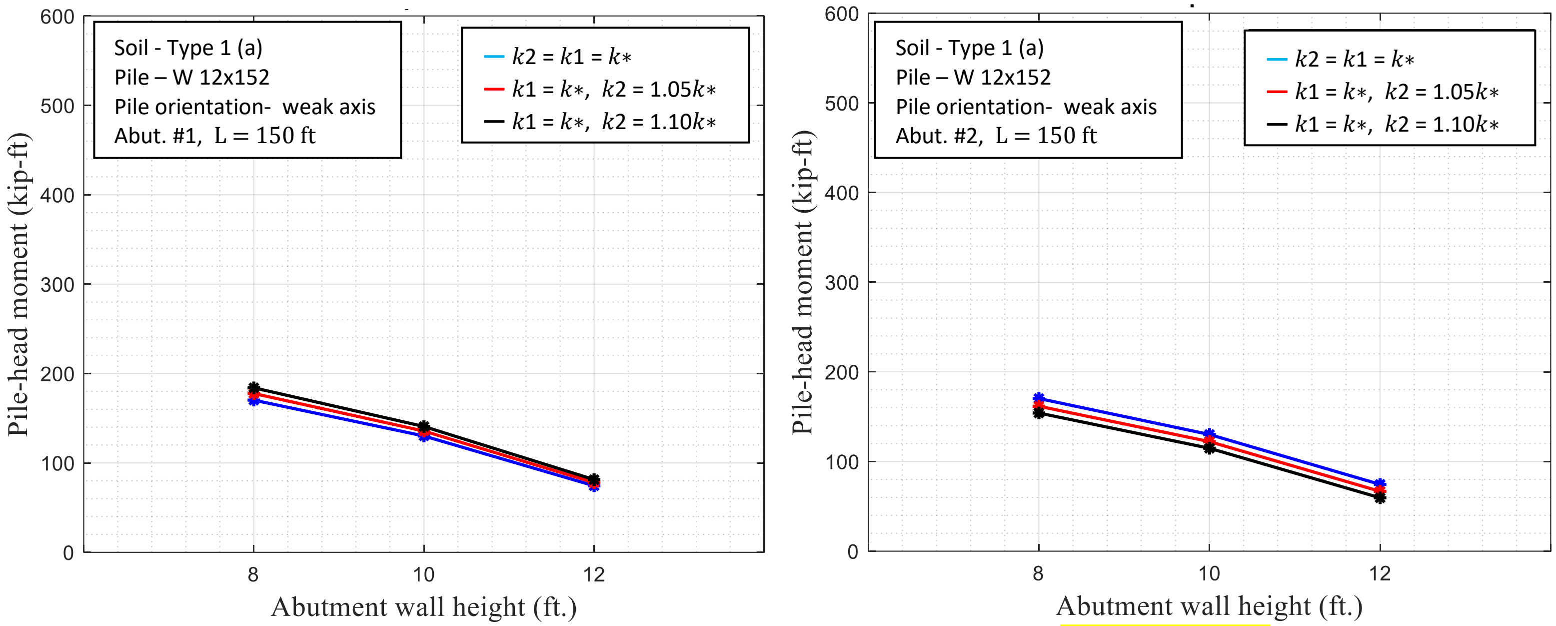

Fig. C.67 W 12x152 pile head moment due to temp. - varying backfill stiffness at abut. #2 - L=150 ft / GTStrudl

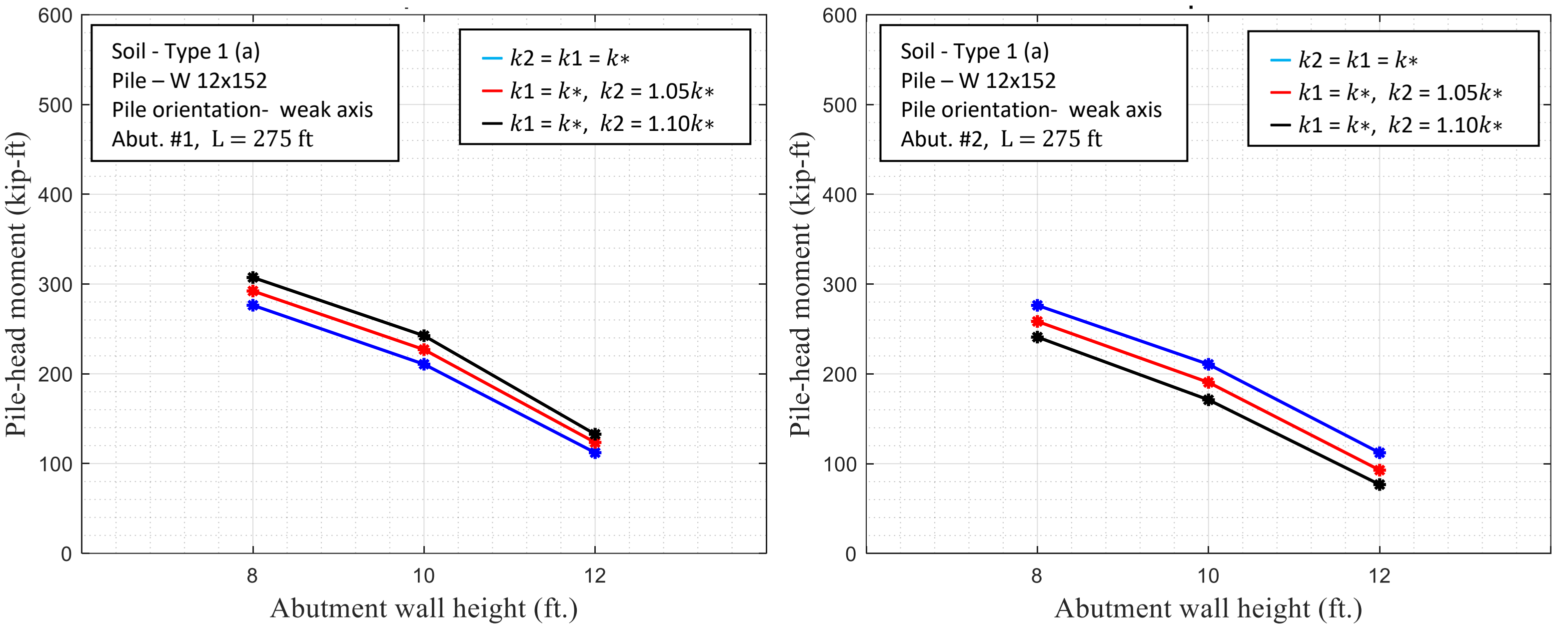

Fig. C.68 W 12x152 pile head moment due to temp. - varying backfill stiffness at abut. #2 - L=275 ft / GTStrudl

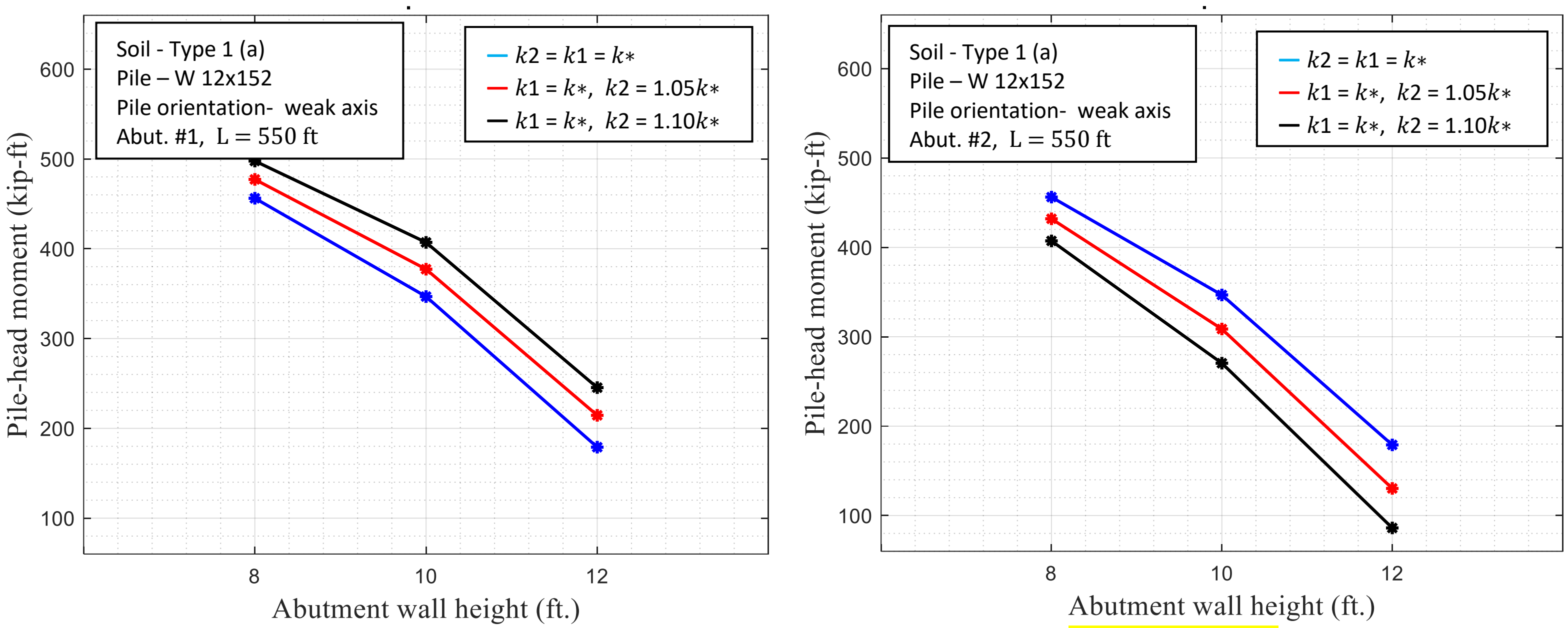

Fig. C.69 W 12x152 pile head moment due to temp. - varying backfill stiffness at abut. #2 - L=550 ft / GTStrudl

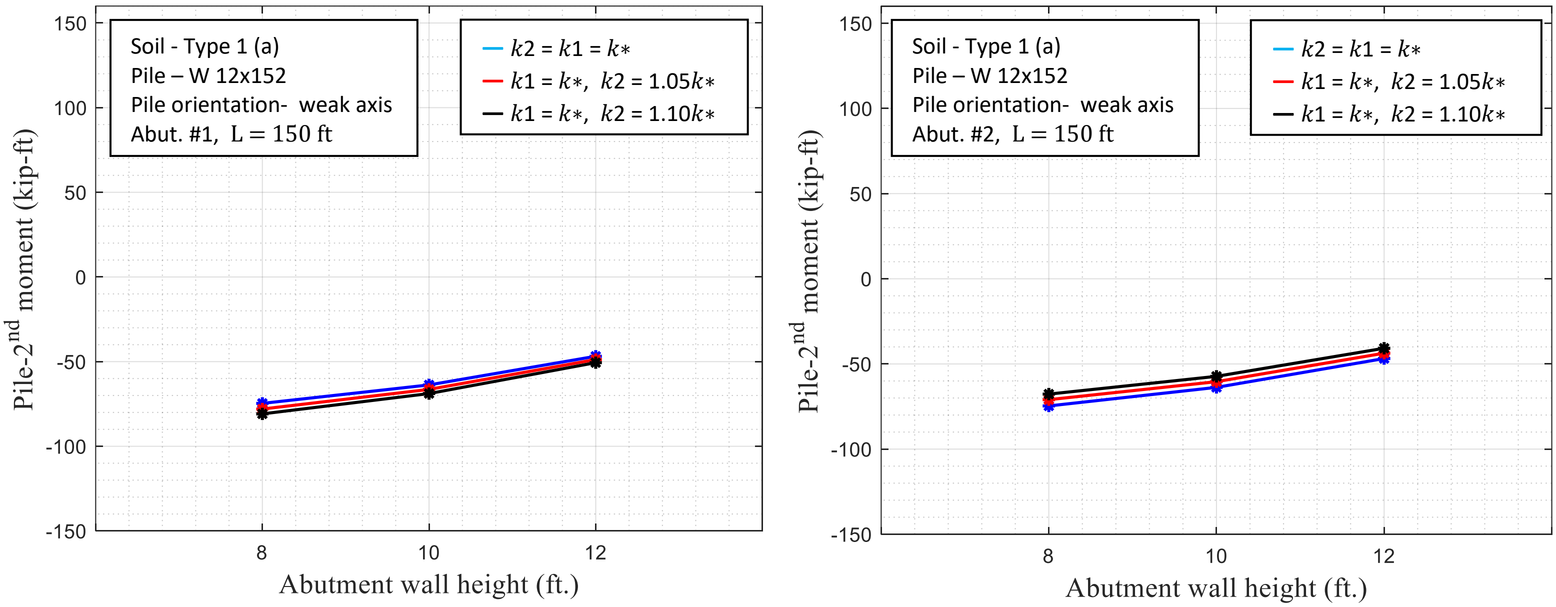

Fig. C.70 W 12x152 pile-2nd moment due to temp. - varying backfill stiffness at abut. #2 - L=150 ft / GTStrudl

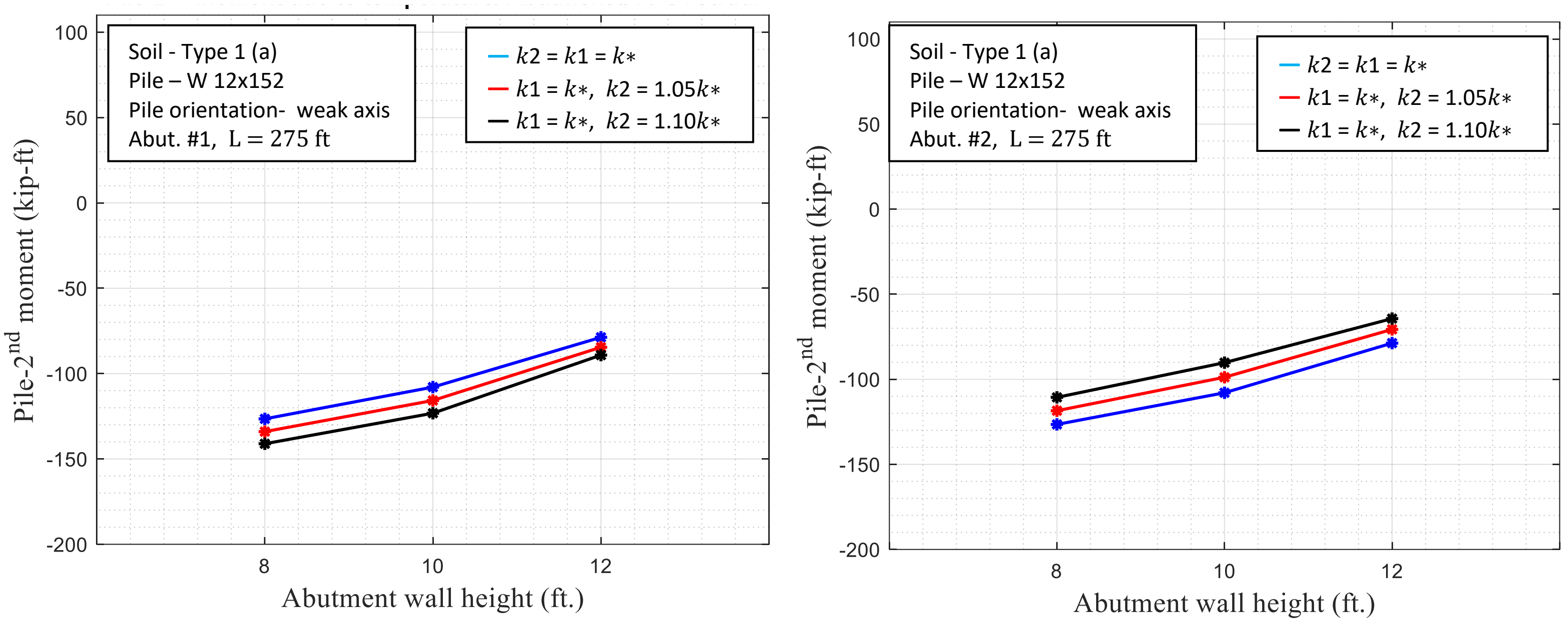

Fig. C.71 W 12x152 pile-2nd moment due to temp. - varying backfill stiffness at abut. #2 - L=275 ft / GTStrudl

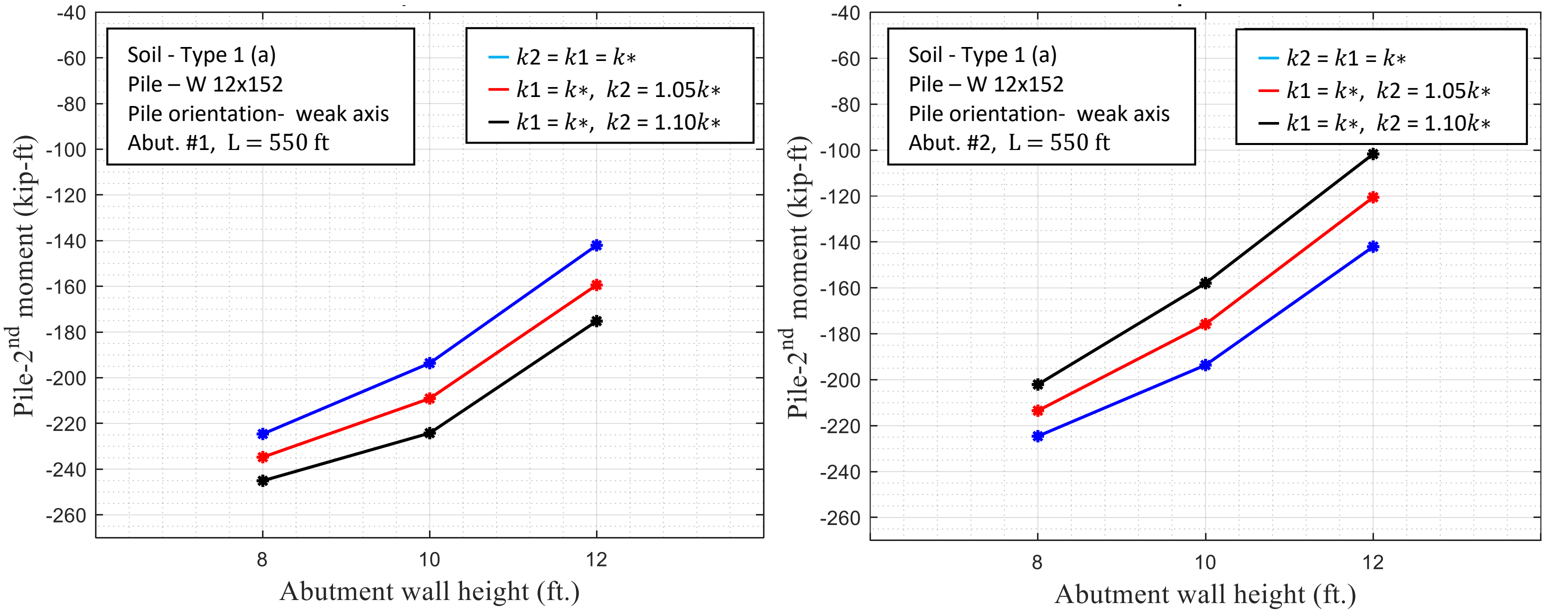

Fig. C.73 W 12x152 pile-2^{nd} moment due to temp. - varying backfill stiffness at abut. #2 - L=550 ft / GTStrudl

Chapter 4

The impact of the use of expanded polystyrene (EPS) geofoam on thermally induced stresses on the superstructure and substructure of integral abutment bridges: A parametric study

---

Abstract

Integral abutment bridges (IABs) are single-span or multi-span continuous deck-type bridges having the deck integral with the walls of the abutments and the walls supported on single rows of flexible piles. For simply supported bridges, the expansion joints accommodate the deck movement caused by daily or seasonal cycle thermal changes. But in IABs, with the elimination of the expansion joints, the expansion and contraction of the deck will cause the abutments to move into or away from the soil behind the abutments. These movements alter the soil pressure on the abutments, causing the state of soil to vary from fully passive to fully active. The thermal expansion of the deck is a major contributor to the total stress in IABs. The reason is that, with an increase in temperature, the abutment walls move into the backfill soil and the interaction with the soil (passive pressure) will greatly impact the longitudinal forces that must be carried by the bridge superstructure as well as by the substructure.

In recent decades, the use of light-weight compressible materials, such as expanded polystyrene (EPS) geofoam behind the abutment walls of IABs, has gained in popularity because of their many benefits, one being a reduction in the lateral earth pressure acting on the abutment walls.

The objective of this study is to assess the impact of the insertion of EPS geofoam between each abutment wall and the compacted backfill on the thermally induced stresses in the superstructure of IABs. To accomplish this objective, a parametric study was conducted using commercially available finite element software. Full 3-D finite element models of multi-span sample IABs were created and analyzed. In these sample IABs, the Geofoam blocks at each abutment were modeled as a brick element and the compacted backfill modeled as nonlinear springs.

The results of this parametric study show that the use of EPS geofoam between the abutment

walls and the backfill soil reduces significantly the thermally induced (i) axial forces and moments of girders at their connection to the abutment walls and (ii) stresses in the backwalls compared to using compacted backfill alone. The reduction in stress is much greater for IABs with longer spans and taller walls.

Introduction

Integral abutment bridges (IABs) are indeterminate single story framed structures with soil interaction. As in any indeterminate frame, the distribution of the forces between the frame members depends on the relative stiffness of the frame members. The biggest uncertainty in the analysis and design of IABs is the reaction of the soil behind the abutment walls and next to the foundation piles. The magnitude of these forces can become substantial during the thermal expansion of the bridge and can greatly affect the overall structural design of the abutment wall-pile system in IABs (Faraji *et al.* (2001)). In recent decades the use of comprisable material such as EPS geofoam behind the abutment walls of IABs (see Fig. 1), has gained in popularity because of its ability to reduce the lateral earth pressure acting on the walls. Many researchers have studied the impact of the use of light-weight compressible materials, such as expanded polystyrene (EPS) behind retaining walls (AbdelSalam and Azzam (2016), Khan and Meguid (2021), Ertugul and Trandafir (2011)). But there has been limited study on the impact of EPS geofoam behind the abutment walls of IABs.

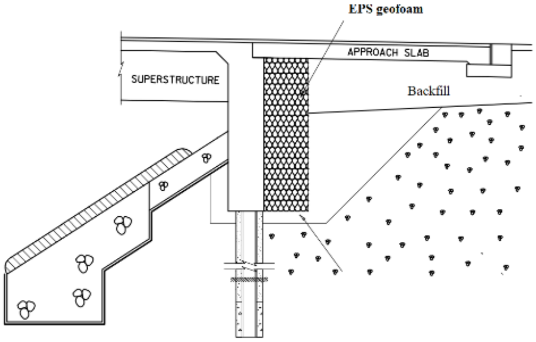

Fig. 1 Use of EPS geofoam in IABs

Methodology

The objective of this study is to assess the impact of the use of EPS geofoam inserted between abutment walls and the compacted backfill on the thermally induced stresses in the superstructure and substructure of IABs. To accomplish this objective, a parametric study was conducted using commercially available finite element software. Full 3-D finite element models of three-span sample IABs with span length ranges of 45.7-167.6 m, abutment wall heights ranges of 2.4-3.6 m were created. In these sample IABs, the geofoam blocks at each abutment were modeled as brick elements and the compacted backfill modeled as nonlinear springs.

Summary of the parametric study

The following figures 2-4 and tables 1-2 show the analysis results for a 3-span sample IAB with total span length of L=167.6 m(48.7, 70.2, 48.7), wall height of H=3.6 ft, with 7 plate girders, 7 predrilled shafts (w shape steel piles) oriented in the weak direction, and two concrete piers subjected to a thermal loading increase of $\Delta T = 37.8^{oC}$.

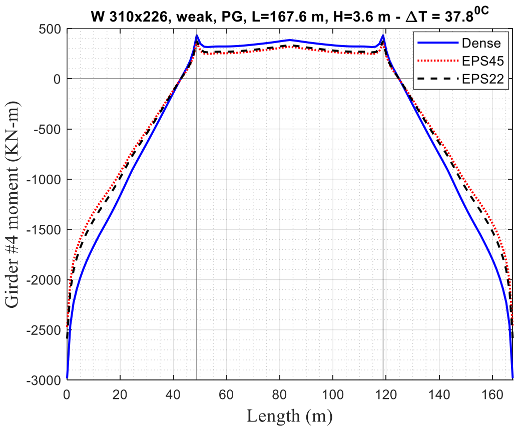

Fig. 2 Girder-bending moment profile

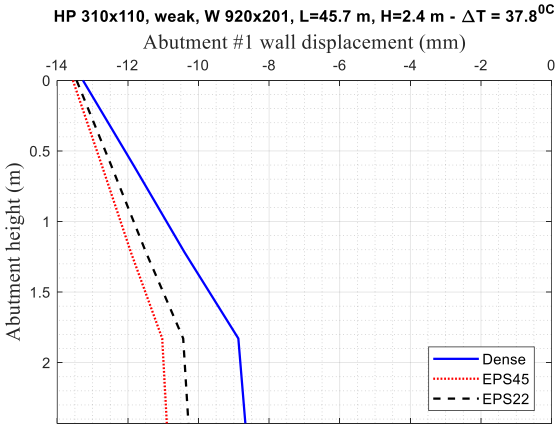

Fig. 3 Wall-vertical displacement profile

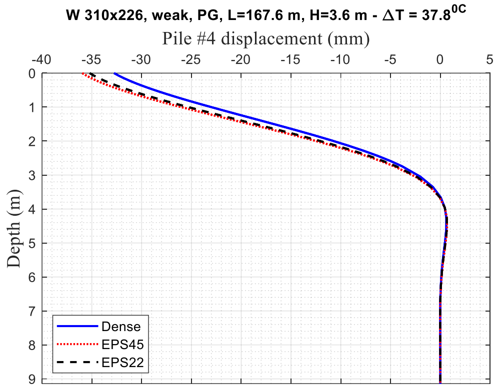

Fig.4(a) Pile displacement profile

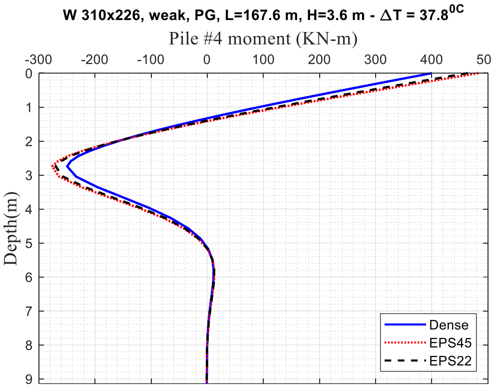

Fig.4(b) Pile moment profile

Table 1. Backfill material impact

Pile # 4		Predrilled – 2.4 m		
		EPS22	EPS45	Dense
Displacement (mm)	Δ_T^a	-47.75	-47.8	-47.5
	δ_T^b	-34.54	-35.8	-32.8
Moment^1 (KN-m)	M_T^{1c}	464.0	482.9	400.2
Moment^2 (KN-m)	M^2_T	-270.3	-276.5	-249.8
Axial (KN)	F_T^d	-636.9	-641.9	-620.1

Table 2. Predrilling impact

Pile #4 (EPS45)		Predrilled (m)			
		2.4	3.0	3.7	15.2
Displacement (mm)	Δ_T^a	-47.8	-47.8	-47.8	-47.8
	δ_T^b	-35.8	-36.1	-36.3	-36.6
Moment^1 (KN-m)	M_T^{1c}	482.9	457.4	438.5	434.1
Moment^2 (KN-m)	M^2_T	-276.5	-254.5	-226.2	-219.5
Axial (KN)	F_T^d	-641.9	-644.6	-646.4	-646.4

a: Displacement at girder level, b: displacement at pile head, c: pile head moment, d: Axial force

Conclusion

The results of this parametric study show that the use of EPS Geofoam between the abutment walls and the backfill soil reduces significantly the thermally induced (i) axial forces and moments of girders at their connection to the abutment walls and (ii) the stresses in the back walls compared to using compacted backfill alone. The reduction is much greater for IABs with longer spans and taller walls. On the other hand, the use of EPS geofoam will cause a slight decrease in the axial force and bending moment of the piles that can be reduced by increasing the predrilling length (see Tables 1 and 2).

References

AbdelSalam, S.S., Azzam, S.A. (2016). 'Reduction of lateral pressures on retaining walls using geofoam inclusion'. Geosynthetics International, 23(6), pp. 395-407.

Ertugul, O., Trandafir, A. (2011). 'Reduction of lateral forces acting on rigid nonyielding retaining walls by EPS geofoam inclusions'. Journal of Materials in Civil Engineering, 23(12), pp. 1711-1718.

Faraji, S. et al. (2001). 'Non-linear analysis of integral bridges: finite element model**.'** *Geotech and Geoenvironmental Engineering*, 127(5), pp. 454-461.

Khan, Muhammad I., Meguid, Mohamed A. (2021). 'Evaluating the role of Geofoam properties in reducing lateral loads on retaining walls: A numerical study'. Sustainability, 13(9), pp. 4754.

APPENDIX D

The impact of the use of expanded polystyrene (EPS) geofoam on thermally induced stresses on the superstructure and substructure of integral abutment bridges: A parametric study

The following Plots and Tables are created for a three-span integral abutment bridge with span length of 150 ft (45, 60, 45), with seven HP12x74 piles, seven W36 steel girders, and eight feet abutment wall height

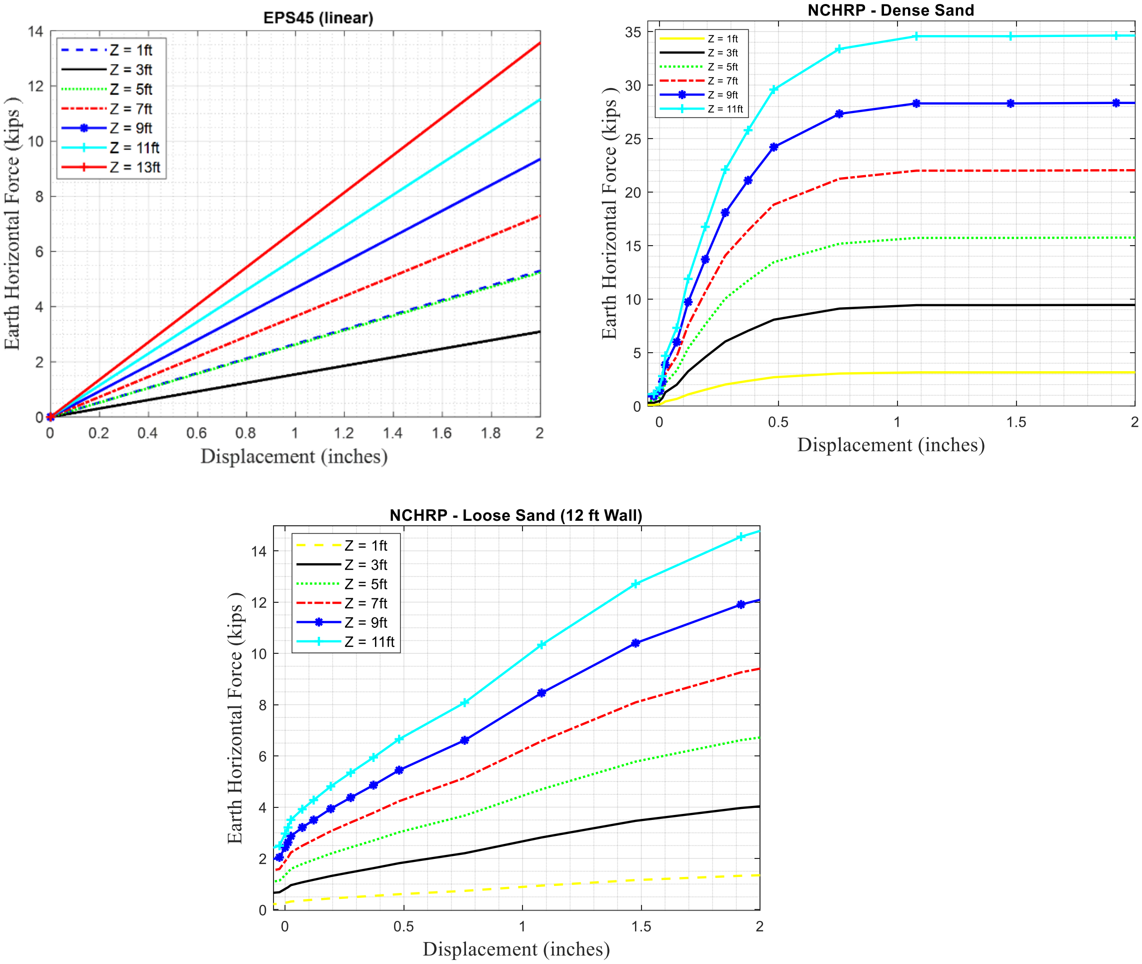

Fig. D.1 Force-deflection relations for the main typical abutment wall nodes (2ft x2ft) for different backfill materials: EPS45 (linear modeling) and NCHRP loose and dense soil

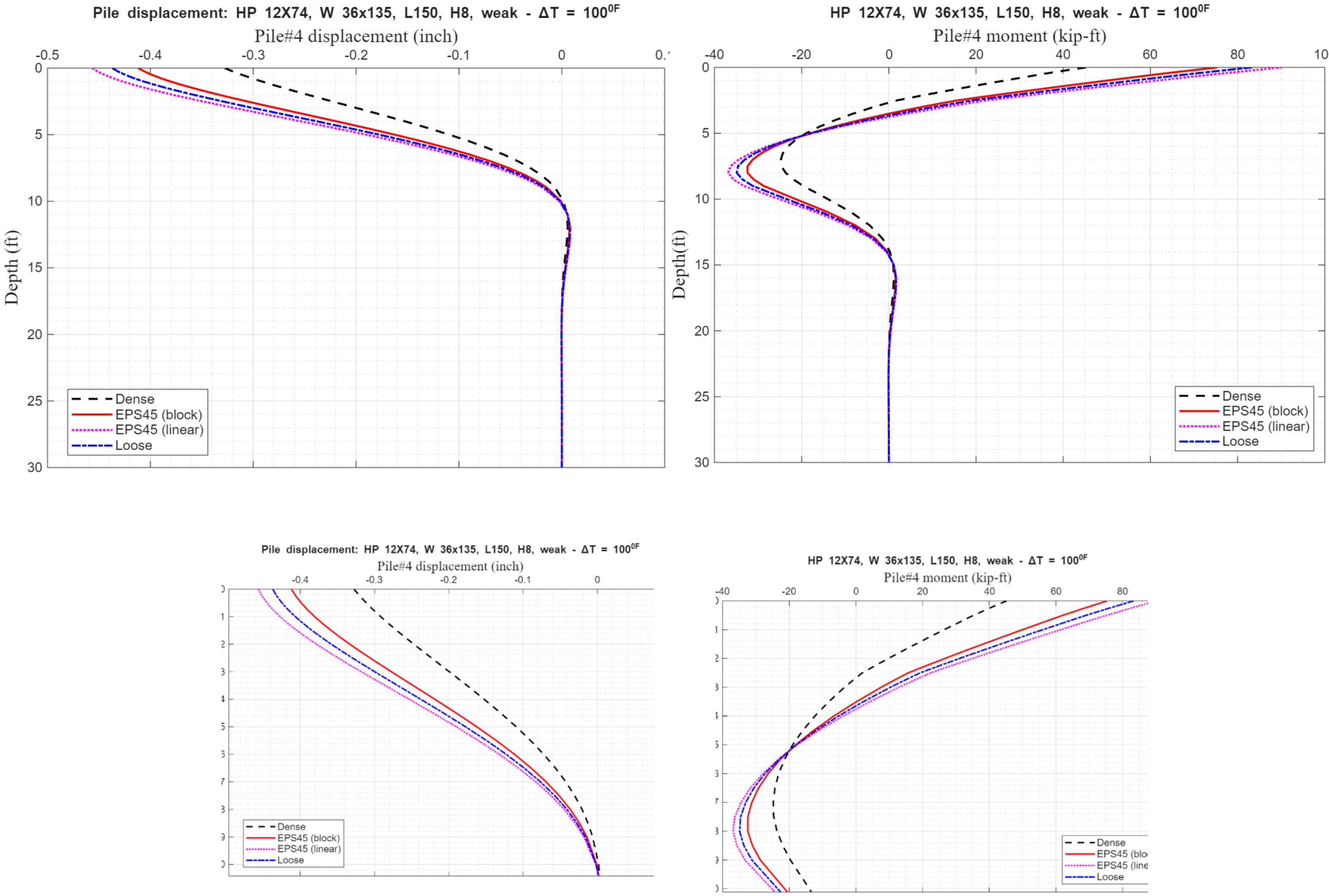

Fig. D.2 Comparison of the lateral displacement and bending moment profiles for pile #4 (HP 12x74) for the range of backfill material behind the abutment wall: dense soil, EPS45 (block), EPS45 (linear), and loose soil

Table D.1 Backfill material impact on pile #4 (HP12x74)

HP 12x74 piles- weak, W36 girder, L= 150 ft (45,60,45), $\Delta T = 100^{0F}$							
Wall Height (ft)	Backfill Soil	Δ (inch)	δ (inch)	V (kips)	M_1 (kip-ft)	M_2 (kip-ft)	F (kips)
H = 8	EPS45 (linear)	-0.50	-0.45	30.55	90.11	-36.86	-94.85
	EPS45 (block)	-0.49	-0.41	27.16	75.37	-32.44	-90.76
	Loose	-0.50	-0.43	29.00	83.29	-34.89	-92.93
	Dense	-0.48	-0.33	20.36	45.62	-24.89	-82.44

Chapter 4 Use of EPS as Backfill Material in Integral Abutment Bridges, 2025. S. Faraji-Hennessey

Table D.2 Data for pile #4 (Hp12x74) due to dead load, live load (truck), and temperature load of $\Delta T = 100^{0F}$

PILE #4		Dense	EPS45 (block)	% Difference
Displacement Δ (Inch)	Δ_T	-0.48	-0.49	2.08
	Δ_D	0.005	0.004	-20.00
	Δ_L	0.00674	0.00673	-0.15
Displacement δ (Inch)	δ_T	-0.33	-0.41	24.24
	δ_D	-0.02	-0.03	60.0
	δ_L	0.00874	0.00723	-17.28
Shear (Kips)	V_T	20.36	27.16	33.40
	V_D	5.98	7.81	30.60
	V_L	-2.41	-3.28	36.10
Moment^1 (Kip-ft)	M^1_T	45.62	75.37	65.21
	M^1_D	13.78	19.47	41.29
	M^1_L	-5.08	-6.62	30.31
Moment^2 (Kip-ft)	M^2_T	-24.89	-32.44	30.33
	M^2_D	-2.22	-3.44	54.95
	M^2_L			
Axial (Kips)	F_T	-82.44	-90.79	10.13
	F_D	71.90	71.37	-0.74
	F_L	-17.89	-17.86	-0.17

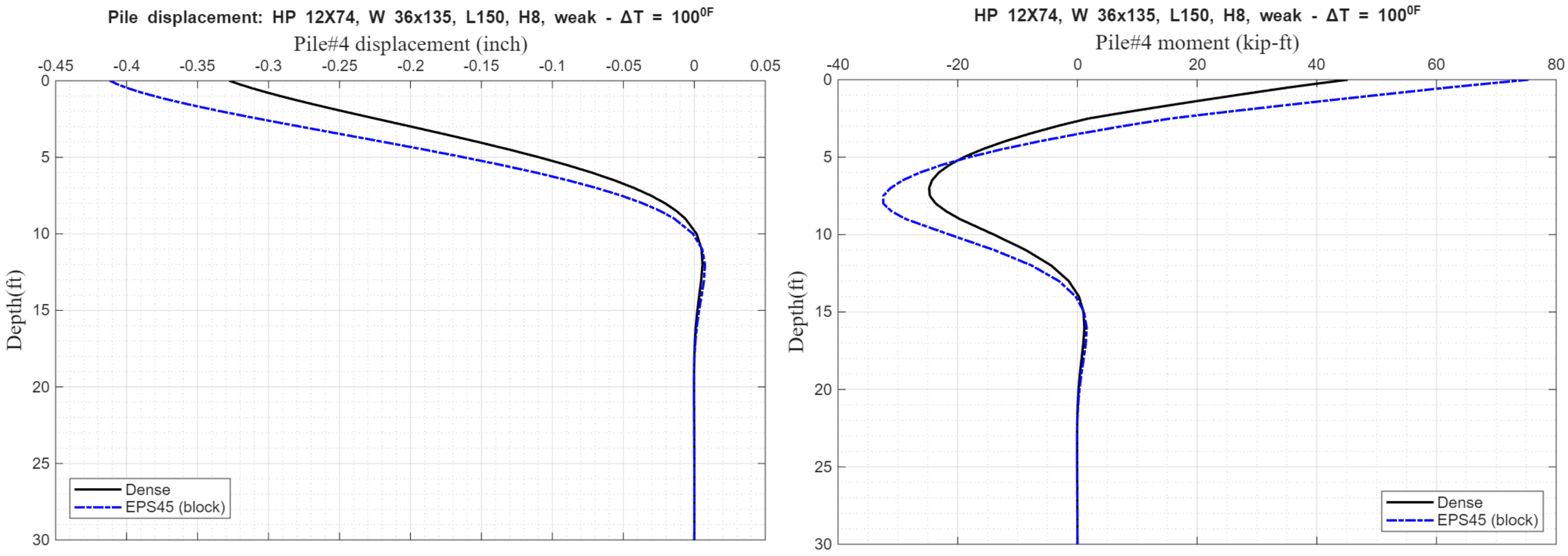

Fig. D.3 Lateral displacement and bending moment profiles for pile #4 (HP 12x74) for dense soil and EPS45 (block) backfill material behind the abutment wall

Table D.3 Data for pile #4 (HP12x74) due to due to $\Delta T = 100^{0F}$

PILE #4		EPS22 (block)	EPS45 (block)
Displacement Δ (Inch)	Δ_T	-0.49	-0.49
Displacement δ (Inch)	δ_T	-0.40	-0.41
Shear (Kips)	V_T	26.38	27.16
Moment^1 (Kip-ft)	M^1_T	71.97	75.37
Moment^2 (Kip-ft)	M^2_T	-31.55	-32.44
Axial (Kips)	F_T	-89.84	-90.79

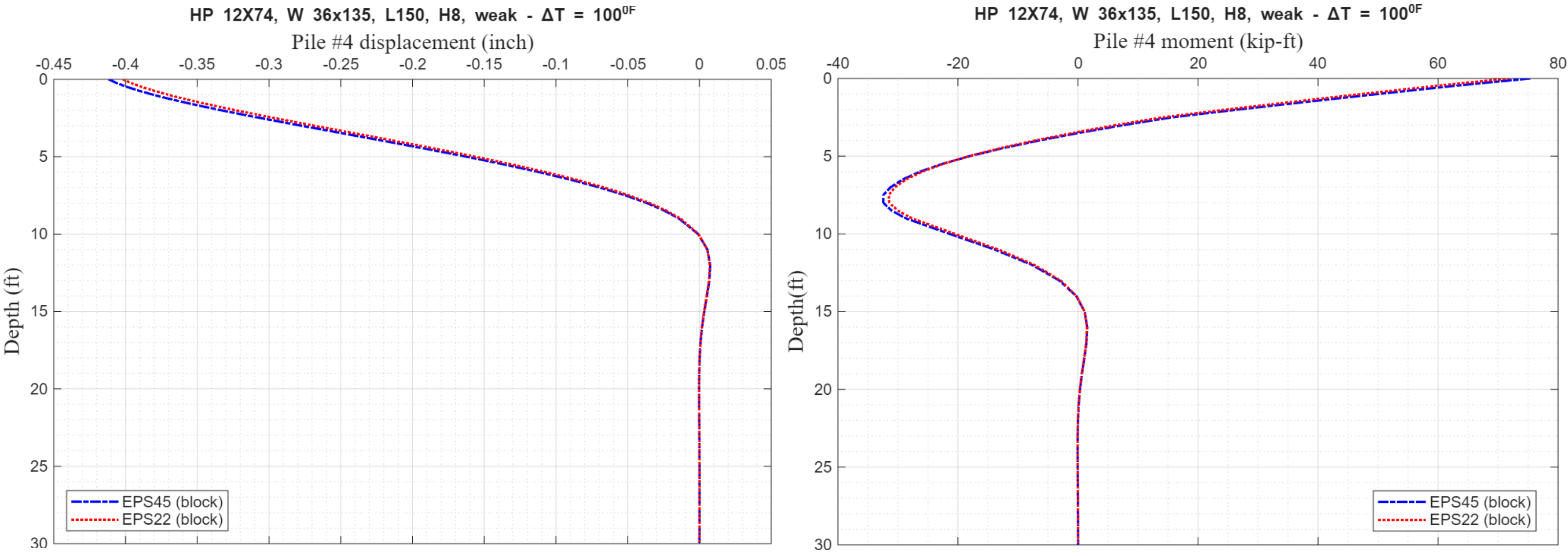

Fig. D.4 Lateral displacement and bending moment profiles for pile #4 (HP 12x74) for EPS45 (block) and EPS22 (block) backfill material behind the abutment wall due to $\Delta T = 100^{0F}$

Table D.4 Data for pile #4 (HP12x74) due to due to dead load

PILE #4		Dense	EPS45 (block)
Displacement Δ (Inch)	Δ_D	0.005	0.004
Displacement δ (Inch)	δ_D	-0.02	-0.03
Shear (Kips)	V_D	5.98	7.81
Moment[1] (Kip-ft)	M^1_D	13.78	19.47
Moment[2] (Kip-ft)	M^2_D	-2.22	-3.44
Axial (Kips)	F_D	71.90	71.37

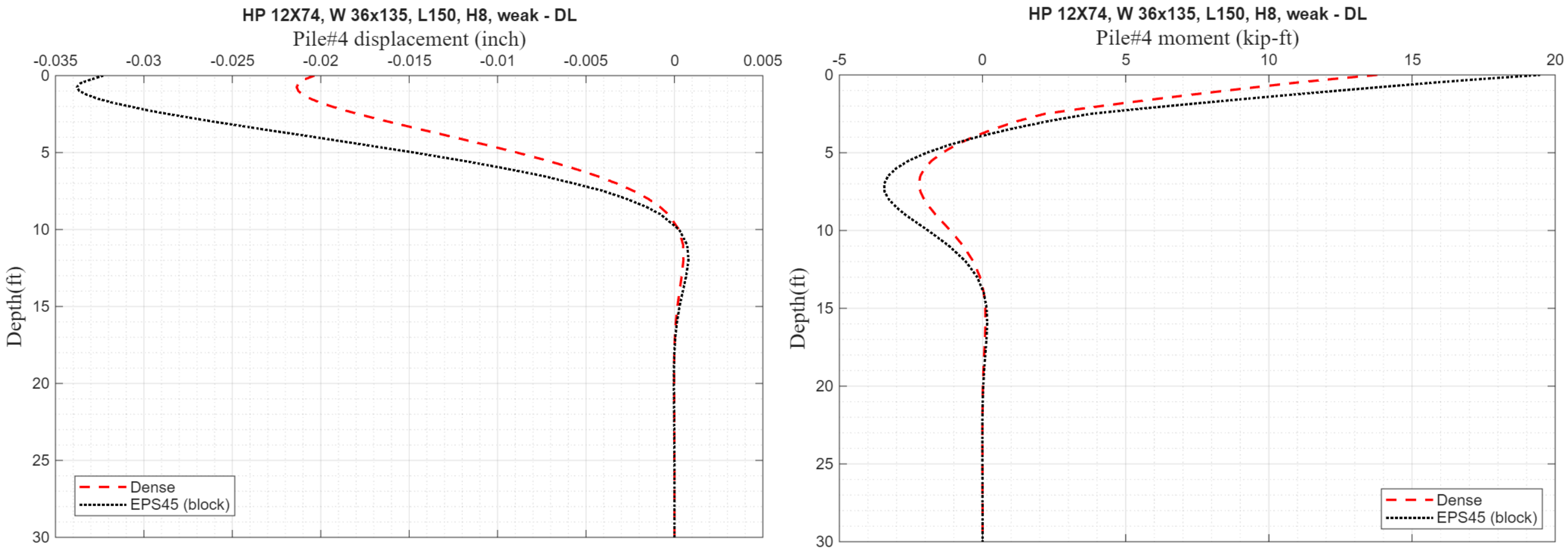

Fig. D.5 Lateral displacement and bending moment profiles for pile #4 (HP 12x74) for dense and EPS (block) backfill material behind the abutment wall due to dead load

Table D.5 Data pile #4 (HP12x74) due to due to truck load

PILE #4		Dense	EPS45 (block)
Displacement Δ (Inch)	Δ_L	0.00674	0.00673
Displacement δ (Inch)	δ_L	0.00874	0.00723
Shear (Kips)	V_L	-2.41	-3.28
Moment^1 (Kip-ft)	M^1_L	-5.08	-6.62
Moment^2 (Kip-ft)	M^2_L		
Axial (Kips)	F_L	-17.89	-17.86

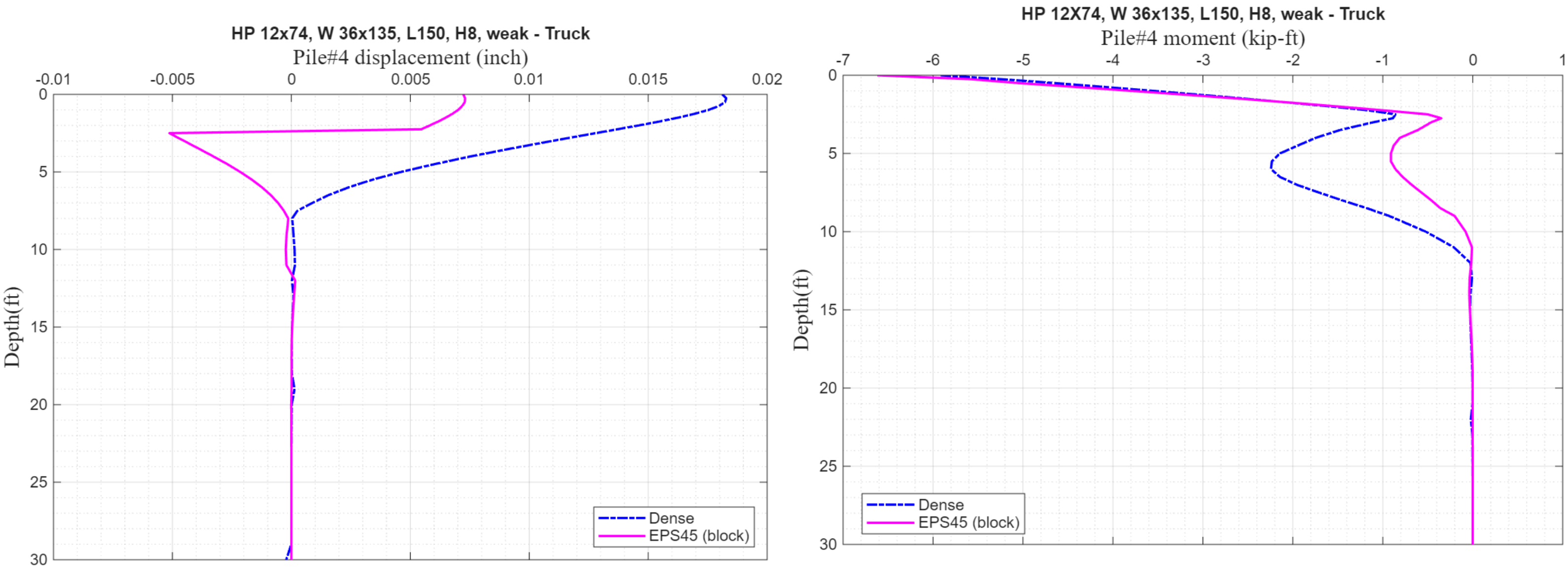

Fig. D.6 Lateral displacement and bending moment profiles for pile #4 (HP 12x74) for dense and EPS45 (block) backfill material behind the abutment wall due to truck load

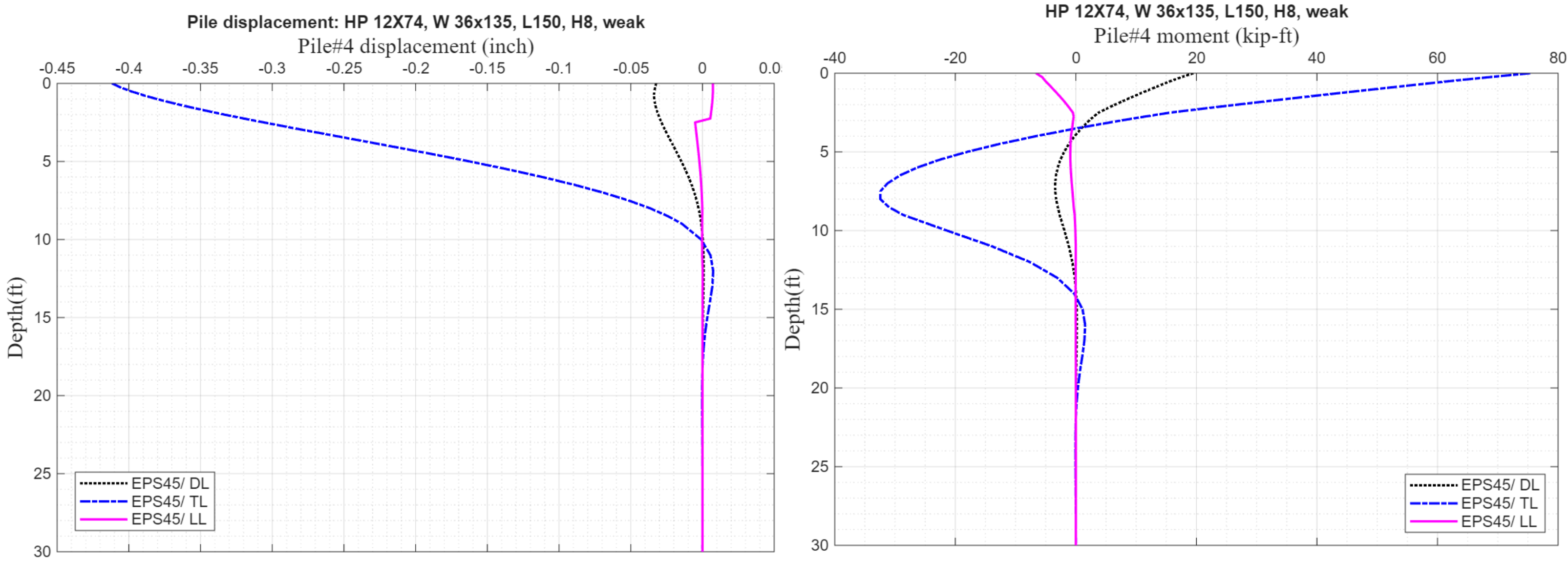

Fig. D.7 Lateral displacement and bending moment profiles for pile #4 (HP 12x74) for EPS45 (block) backfill material behind the abutment wall due to dead load, temperature ($\Delta T = 100^{0F}$) and truck load

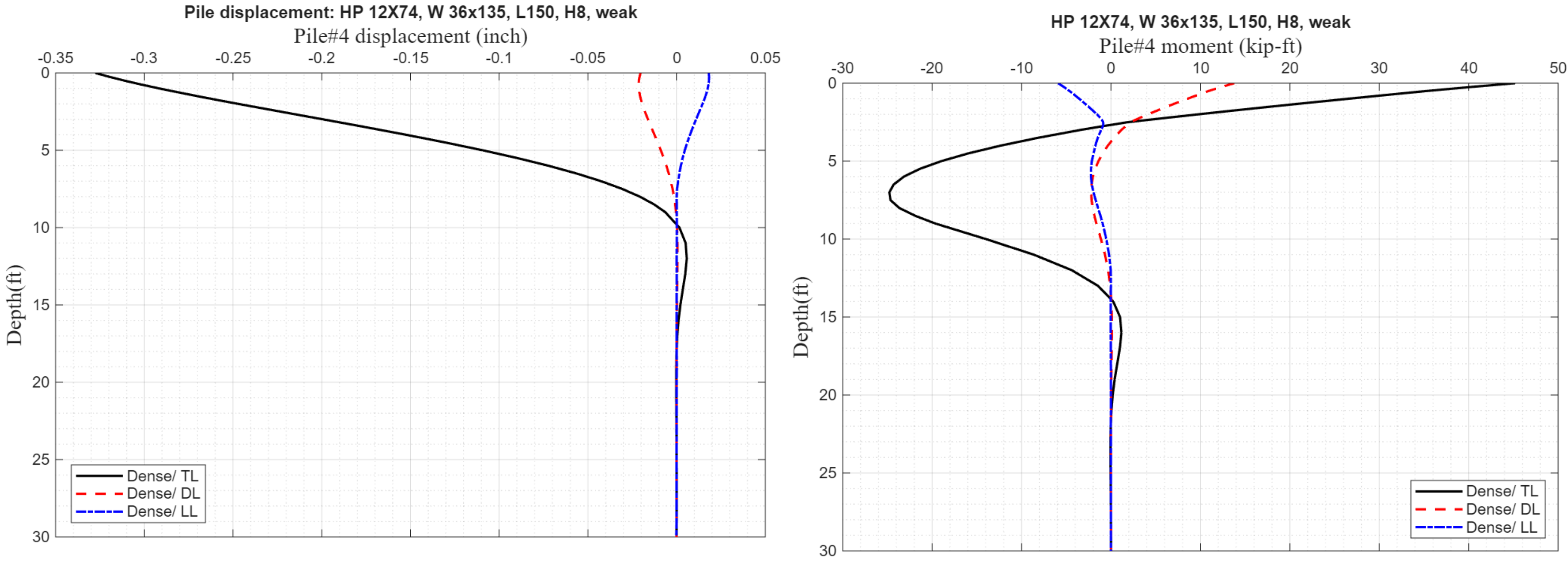

Fig. D.8 Lateral displacement and bending moment profiles for pile #4 (HP 12x74) for dense backfill material behind the abutment wall due to dead load, temperature ($\Delta T = 100^{0F}$), and truck load

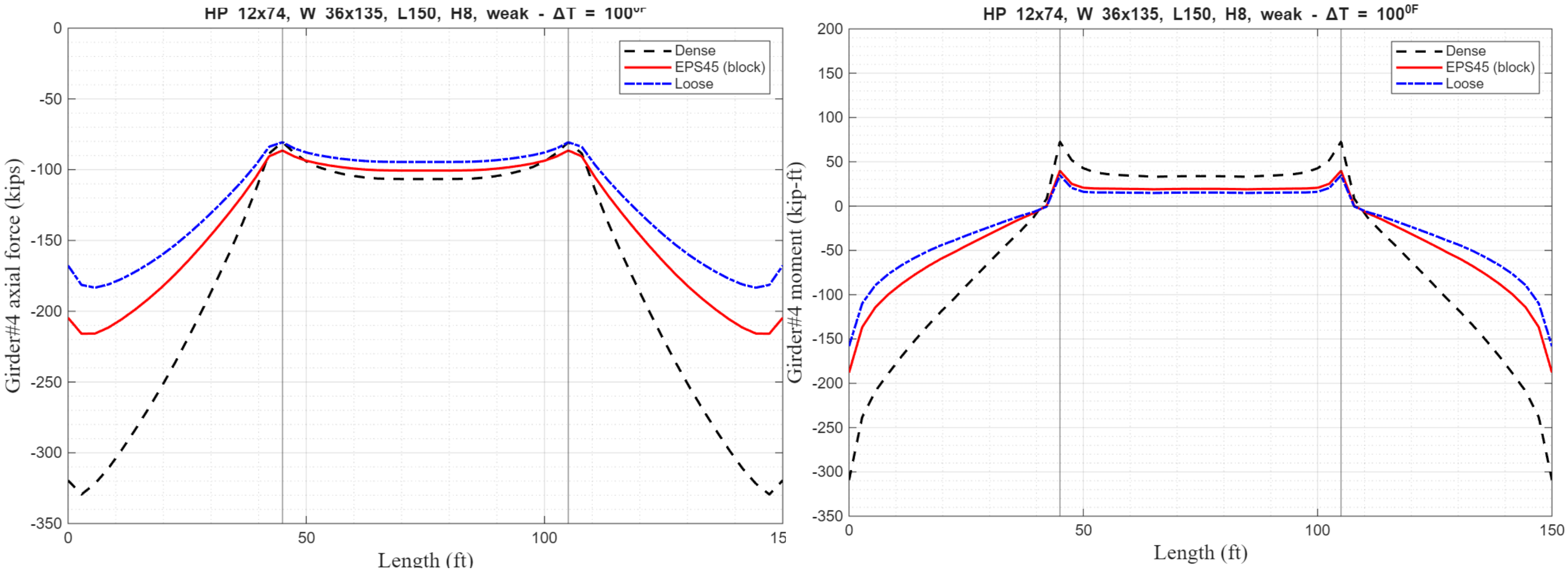

Fig. D.9 Comparison of the axial force and bending moment profiles for Girder #4 for the range of backfill material behind the abutment wall: dense, EPS45 (block), and loose due to $\Delta T = 100^{0F}$

Table D.6 Data Comparison for Girder #4 due to $\Delta T = 100^{0F}$

GIRDER #4		At the abutment		Mid-1st span		At the bent		Mid-2nd span	
		Dense	EPS45 (block)	Dense	EPS45 (block)	Dense	EPS45 (block)	Dense	EPS45 (block)
Axial (Kips)	F_T	-319.5	-204.6	-236.0	-173.9	-80.5	-86.4	-106.6	-100.6
Moment (Kip-ft)	M_T	-309.2	-187.9	-9.1	-51.8	72.6	39.8	33.8	19.5
Shear (Kips)	V_T	-17.2	-11.5	-16.0	-9.1	13.6	8.8	0.018	0.028

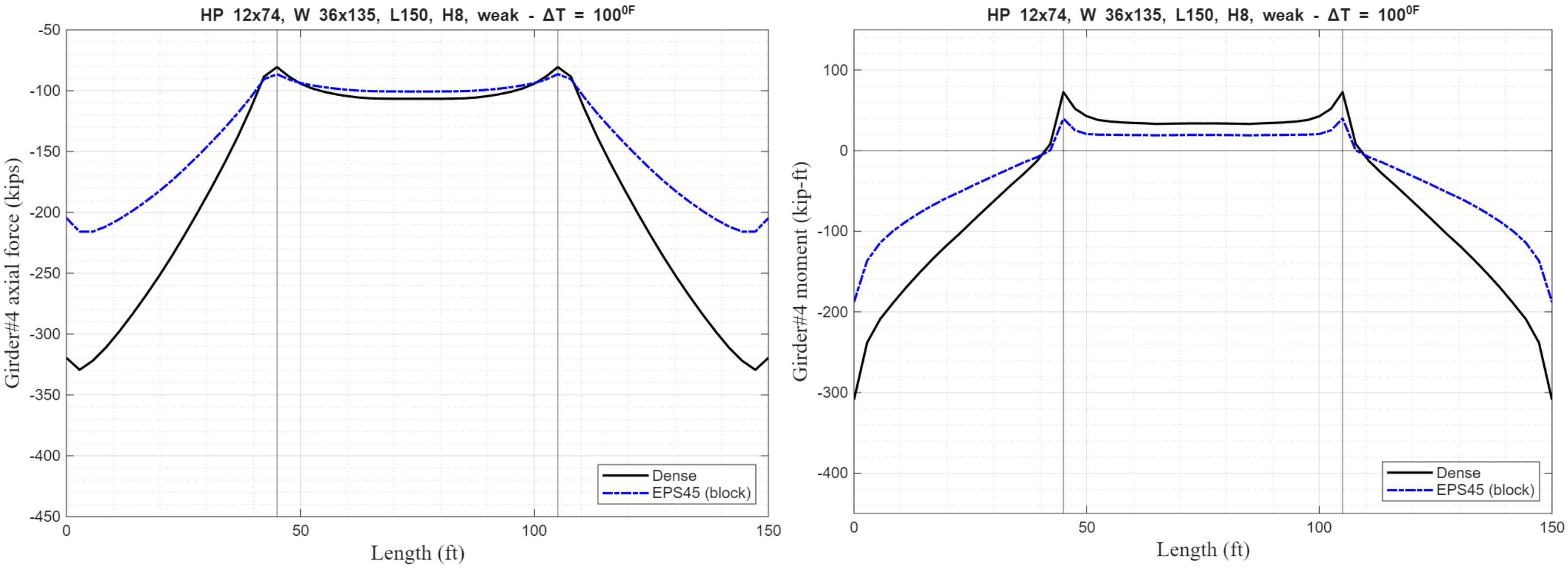

Fig. D.10 Comparison of the axial force and bending moment profiles for Girder #4 for the backfill material behind the abutment wall, dense vs. EPS45 (block) due to $\Delta T = 100^{0F}$

Table D.7 Data Comparison for Girder #4 due to $\Delta T = 100^{0F}$

GIRDER #4		At the abutment		Mid-1st span		At the bent		Mid-2nd span	
		EPS22 (block)	EPS45 (block)	EPS22 (block)	EPS45 (block)	EPS22 (block)	EPS45 (block)	EPS22 (block)	EPS45 (block)
Axial (Kips)	F_T	-218.0	-204.6	-181.1	-173.9	-87.2	-86.4	-101.5	-100.6
Moment (Kip-ft)	M_T	-202.6	-187.9	-57.6	-51.8	42.0	39.8	21.4	19.5
Shear (Kips)	V_T	-12.7	-11.5	-10	-9.1	8.9	8.8	0.012	0.028

.

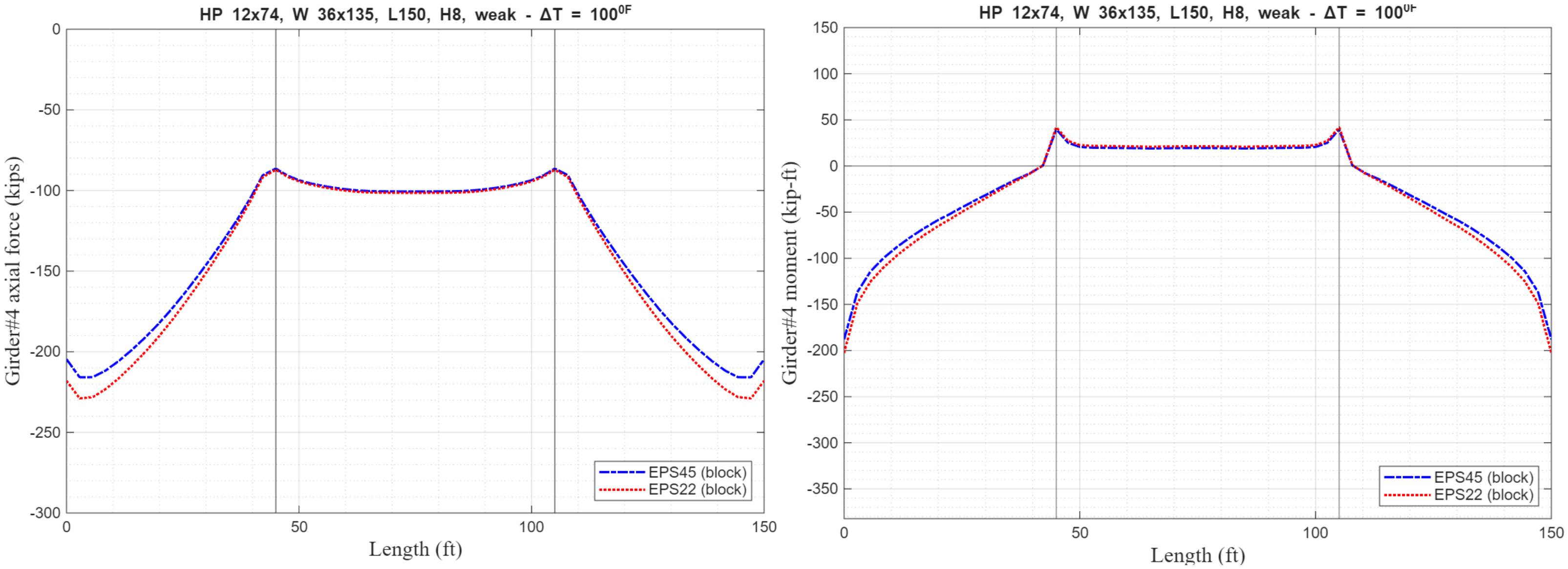

Fig. D.11 Comparison of the axial force and bending moment profiles for Girder #4 for EPS45 (block) and EPS22 (block) as backfill material behind the abutment wall, due to $\Delta T = 100^{0F}$

Table D.8 Data Comparison for Girder #4 due to dead load

GIRDER #4		At the abutment		Mid-1st span		At the bent		Mid-2nd span	
		Dense	EPS45 (block)	Dense	EPS45 (block)	Dense	EPS45 (block)	Dense	EPS45 (block)
Axial (Kips)	F_D	-34.3	-18.0	51.6	59.9	-185.6	-184.4	126.4	127.1
Moment (Kip-ft)	M_D	-88.6	-73.7	77.7	86.5	-278.2	-285.9	138.3	136.8
Shear (Kips)	V_D	-33.2	-34.5	11.7	13.7	-62.9	-65.7	-7.4	-7.8

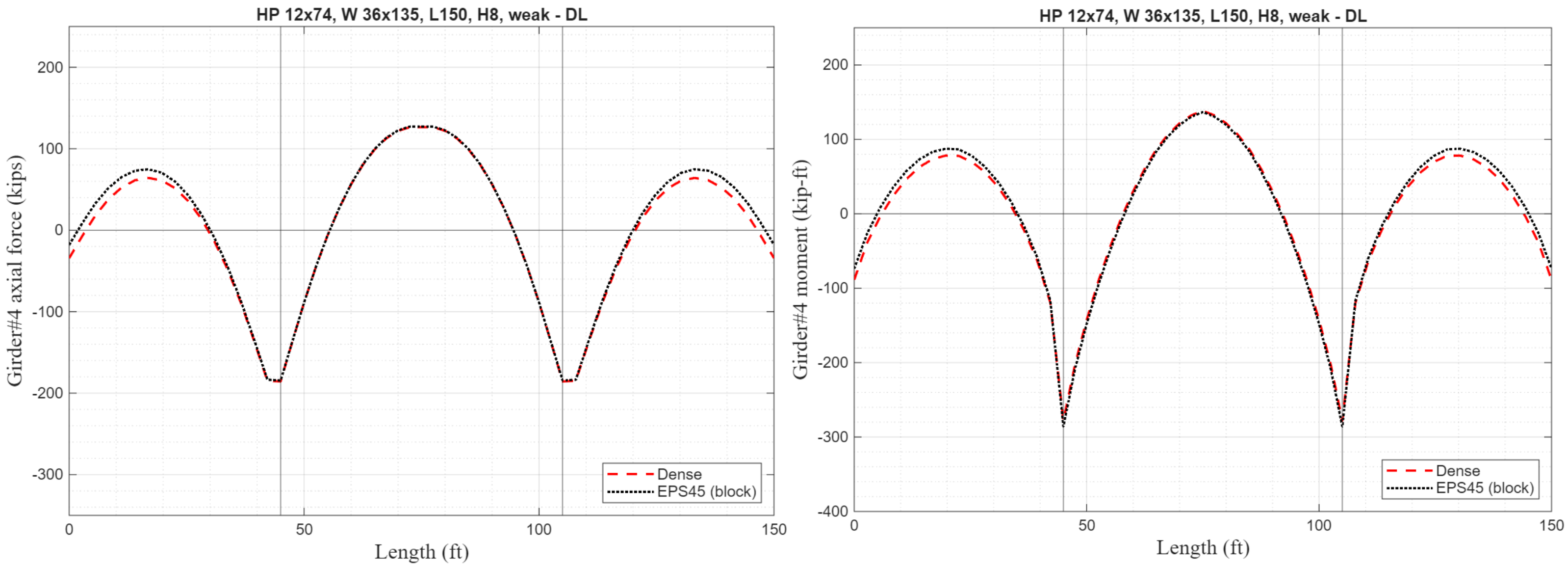

Fig. D.12 Comparison of the axial force and bending moment profiles for Girder #4, dense soil vs. EPS45 (block) as backfill material behind the abutment wall, due to live load (truck)

Table D.9 Data for Girder #4 due to live load(truck)

GIRDER #4		At the abutment		Mid-1st span		At the bent		Mid-2nd span	
		Dense	EPS45 (block)	Dense	EPS45 (block)	Dense	EPS45 (block)	Dense	EPS45 (block)
Axial (Kips)	F_L	-46.8	-43.2	-16.3	-16.0	-55.6	-55.2	-7.1	-7.4
Moment (Kip-ft)	M_L	-106.6	-108.4	-10.7	-9.9	-97.3	-100.4	-4.5	-5.2
Shear (Kips)	V_L	-48.2	-49.3	-24.1	-23.7	-45.6	-47.0	-19.4	-19.3

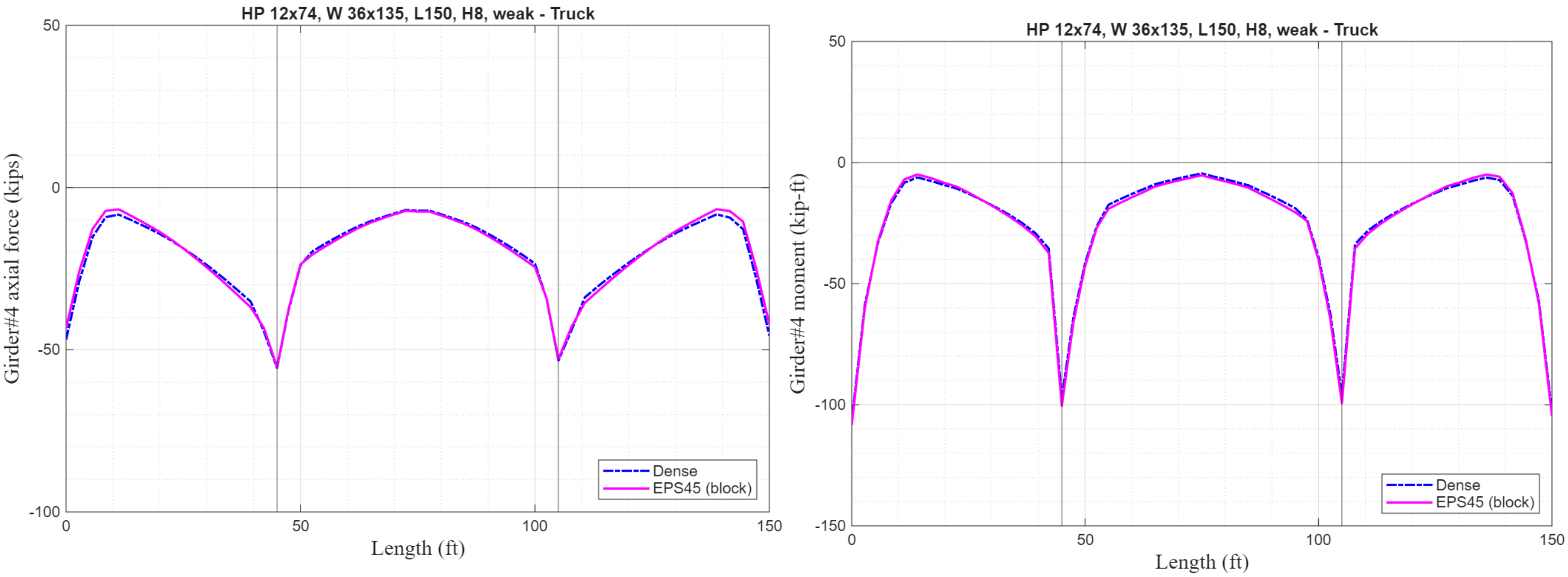

Fig. D.13 Comparison of the axial force and bending moment profiles for Girder #4, dense soil vs. EPS45 (block) as backfill material behind the abutment wall, due to live load (truck)

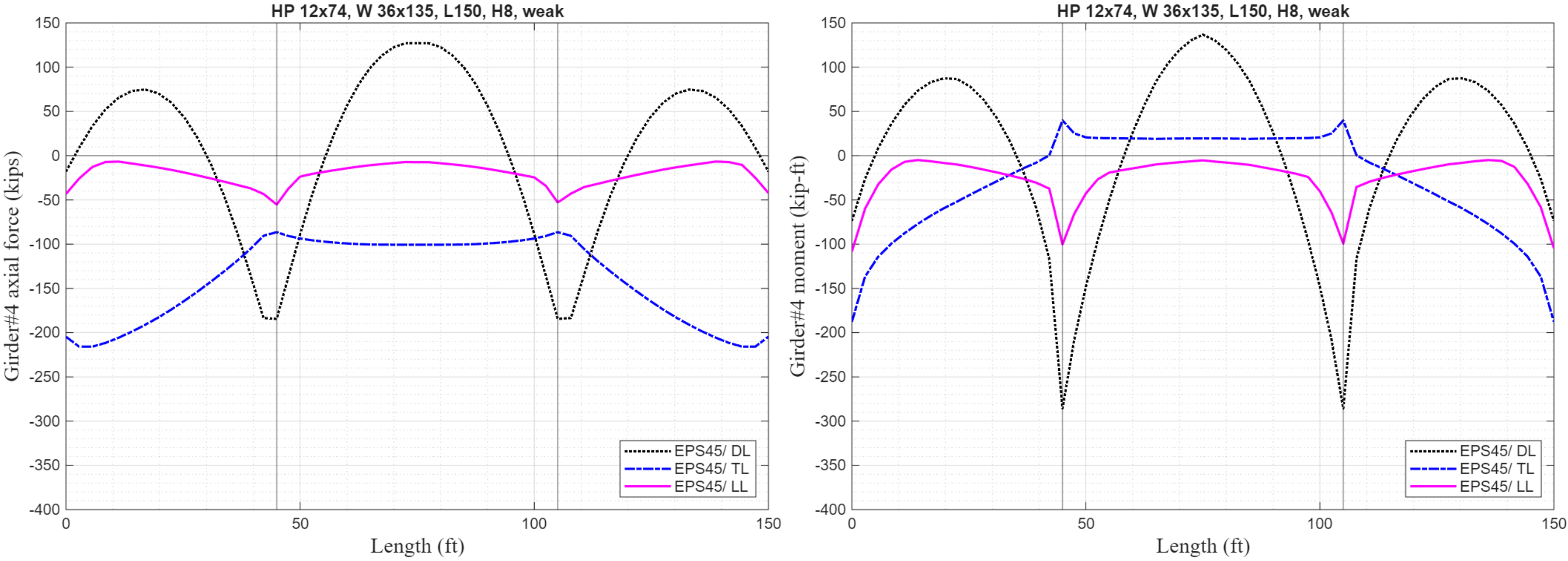

Fig. D.14 Axial force and bending moment profiles for Girder #4, EPS45 (block) as backfill material behind the abutment wall, due to dead load, live load (truck), and temperature load, $\Delta T = 100^{0F}$

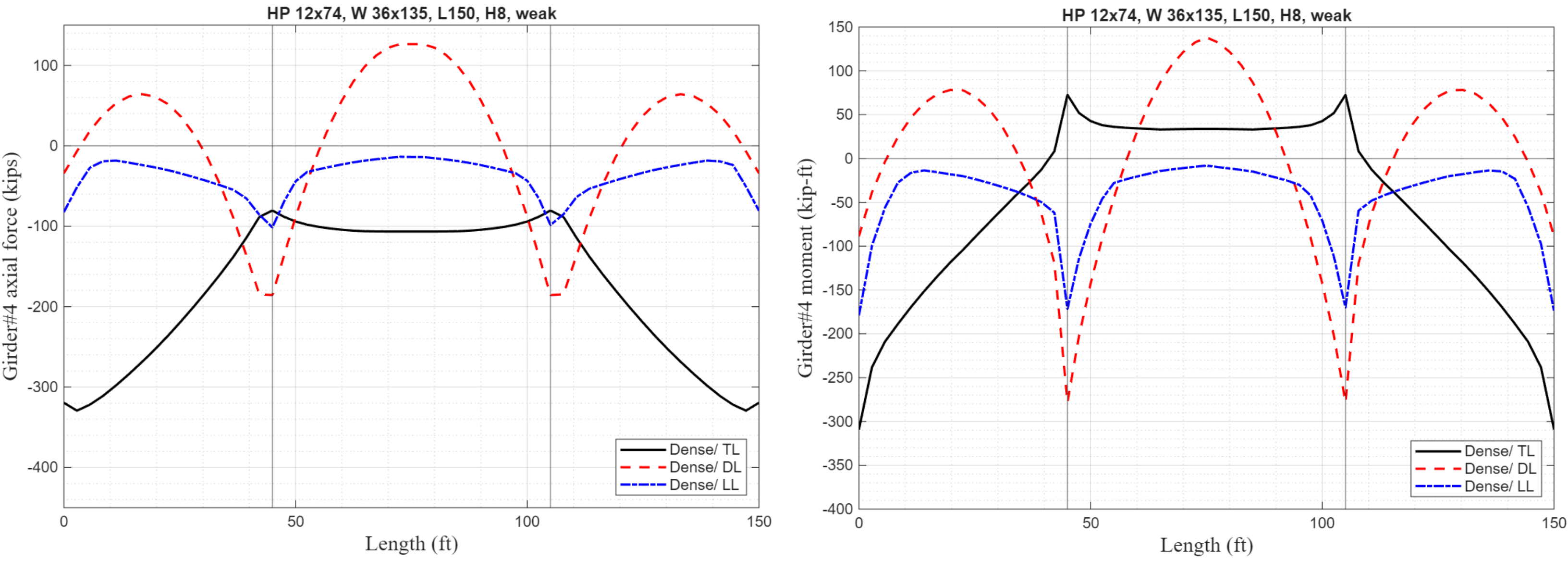

Fig. D.15 Axial force and bending moment profiles for Girder #4, dense soil as backfill material behind abutment wall, due to dead load, live load (truck), and temperature load, $\Delta T = 100^{0F}$

Table D.10 Data for Girder #4 due to due to dead load, live load (truck), and temperature, $\Delta T = 100^{0F}$

GIRDER #4		At the abutment			Mid-1st span			At the bent			Mid-2nd span		
		Dense	EPS45 (block)	% Difference	Dense	EPS45 (block)	% Difference	Dense	EPS45 (block)	% Difference	Dense	EPS45 (block)	% Difference
Axial (Kips)	F_T	-319.5	-204.6	-35.9	-236.0	-173.9	-26.3	-80.5	-86.4	7.3	-106.6	-100.6	-5.5
	F_D	-34.3	-18.0	-47.6	51.6	59.9	15.9	-185.6	-184.4	-0.6	126.4	127.1	0.5
	F_L	-46.8	-43.2	-7.6	-16.3	-16.0	-1.8	-55.6	-55.2	-0.7	-7.1	-7.4	3.9
Moment (Kip-ft)	M_T	-309.2	-187.9	-39.2	-9.1	-51.8	-50.1	72.6	39.8	-45	33.8	19.5	-42.6
	M_D	-88.6	-73.7	-16.8	77.7	86.5	11.3	-278.2	-285.9	2.7	138.3	136.8	-1.1
	M_L	-106.6	-108.4	1.6	-10.7	-9.9	-7.4	-97.3	-100.4	3.1	-4.5	-5.2	17.3
Shear (Kips)	V_T	-17.2	-11.5	-33.1	-16.0	-9.1	-43.1	13.6	8.8	-35	0.018	0.028	55.6
	V_D	-33.2	-34.5	3.9	11.7	13.7	17.3	-62.9	-65.7	4.5	-7.4	-7.8	4.8
	V_L	-48.2	-49.3	2.4	-24.1	-23.7	-1.6	-45.6	-47.0	3.07	-19.4	-19.3	-0.7

APPENDIX E

The impact of the use of expanded polystyrene (EPS) geofoam on thermally induced stresses on the superstructure and substructure of integral abutment bridges: A parametric study

The following plots and Tables are created for a three span integral abutment bridge with span length of 550 ft (160,230,160), with seven W12x152 piles, seven steel plate girders, 12 feet abutment wall height

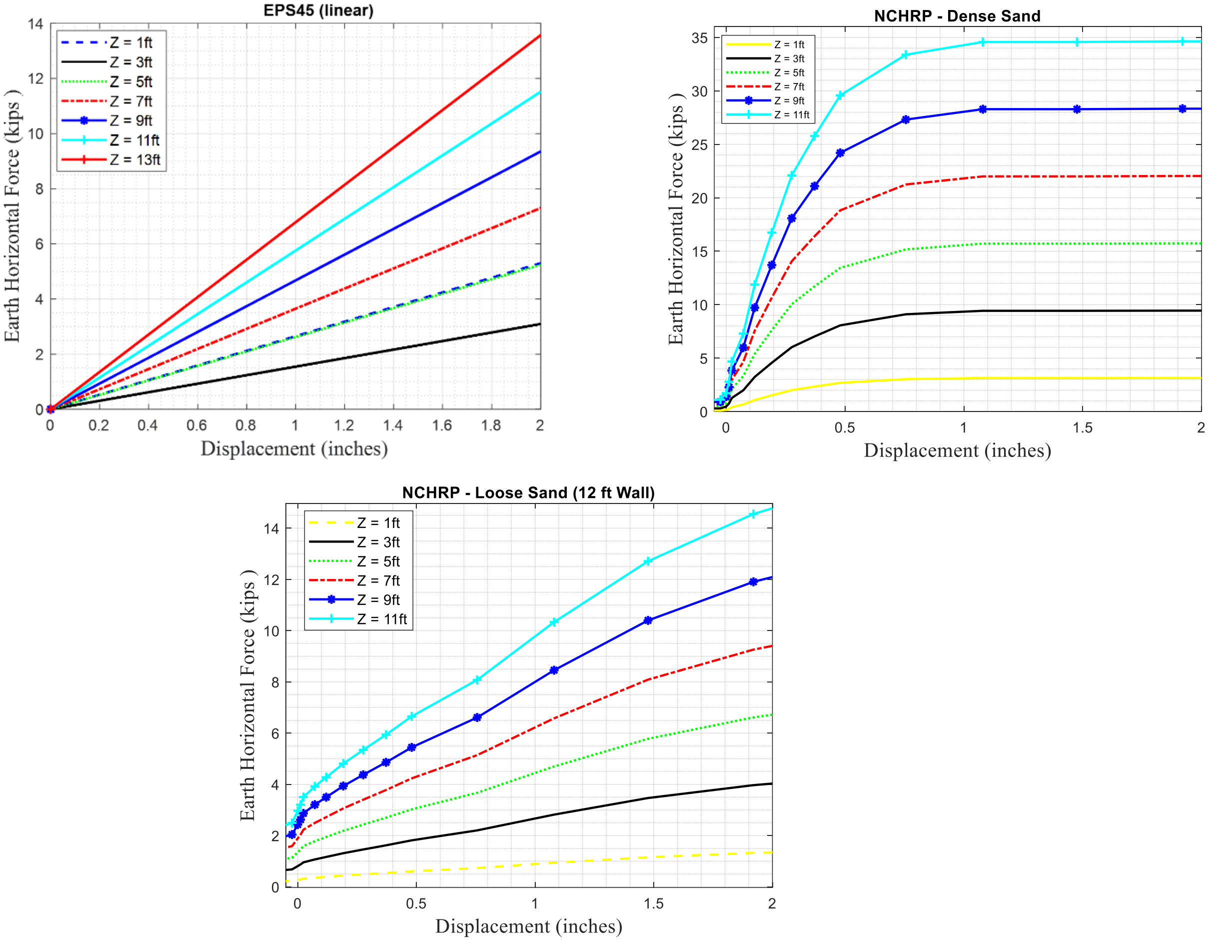

Fig. E.1 Force-deflection relations for the main typical abutment wall nodes (2ft x2ft) for different backfill materials: EPS45 (linear modeling) and NCHRP dense and loose soil

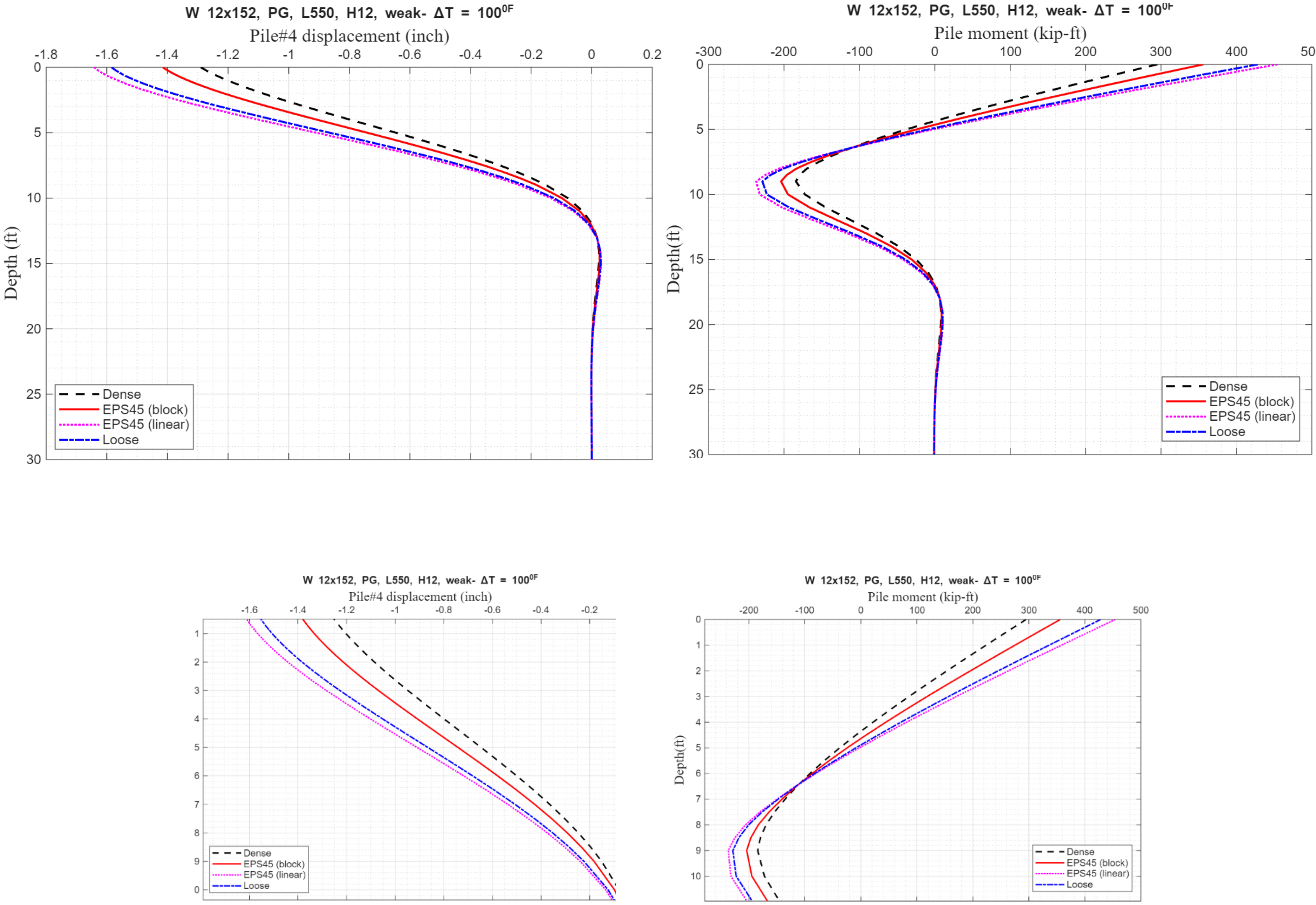

Fig. E.2 Comparison of the lateral displacement and bending moment profiles for pile #4 (W12x152) for the range of backfill material behind the abutment wall: dense soil, EPS45 (block), EPS45 (linear), and loose soil

Table E.1 Backfill material impact on pile #4 (W12x152)

W 12x152 pile- weak, Plate girder, L= 550 ft (160,230,160), $\Delta T = 100^{0F}$							
Wall Height (ft)	Backfill Soil	Δ (inch)	δ (inch)	V (kips)	M_1 (kip-ft)	M_2 (kip-ft)	F (kips)
H = 12	EPS45 (linear)	-1.95	-1.64	96.38	454.54	-236.79	-152.35
	EPS45 (block)	-1.88	-1.41	81.09	356.19	-203.89	-144.35
	Loose	-1.94	-1.58	92.40	428.41	-228.56	-150.12
	Dense	-1.87	-1.29	71.55	295.11	-184.18	-139.40

Table E.2 Data for pile #4 (W12x152) due to $\Delta T = 100^{0F}$

		Dense	EPS45 (block)
Displacement Δ (Inch)	**Δ_T**	-1.87	-1.88
Displacement δ (Inch)	**δ_T**	-1.29	-1.41
Shear (Kips)	**V_T**	71.55	81.09
Moment[1] (Kip-ft)	**M^1_T**	295.16	356.19
Moment[2] (Kip-ft)	**M^2_T**	-184.18	-203.89
Axial (Kips)	**F_T**	-139.35	-144.35

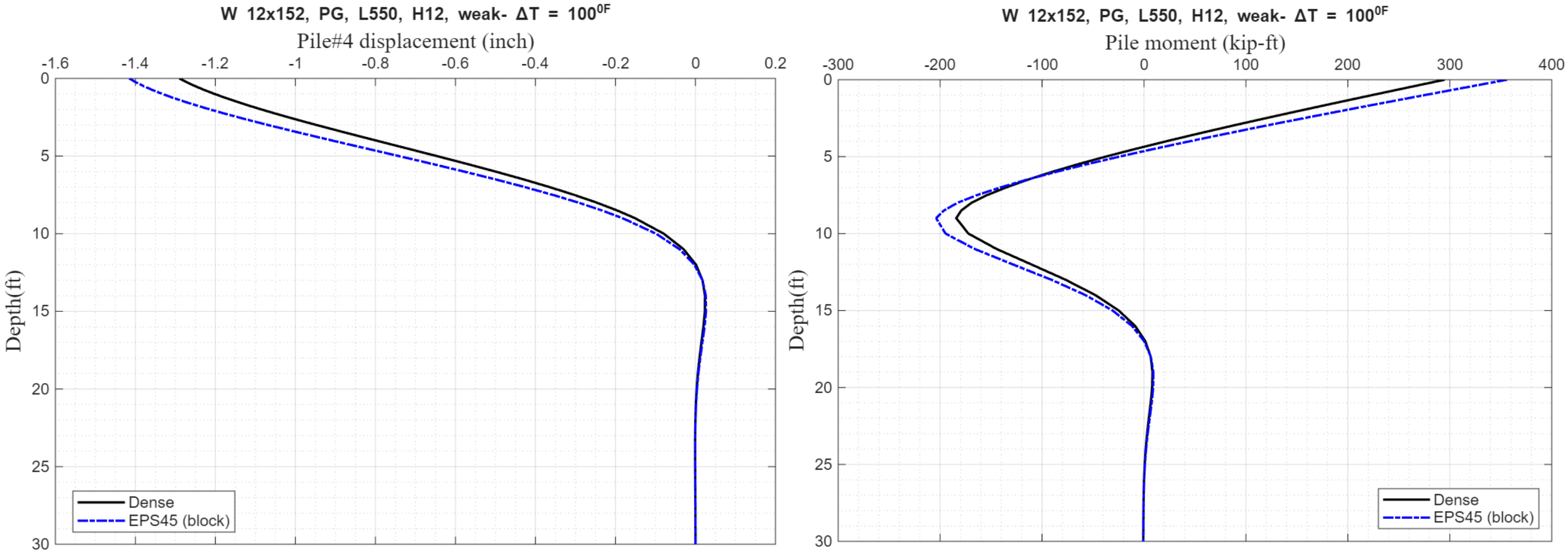

Fig. E.3 Lateral displacement and bending moment profiles for pile #4 (W12 x152) for dense soil and EPS45 (block) backfill material behind the abutment wall due to $\Delta T = 100^{0F}$

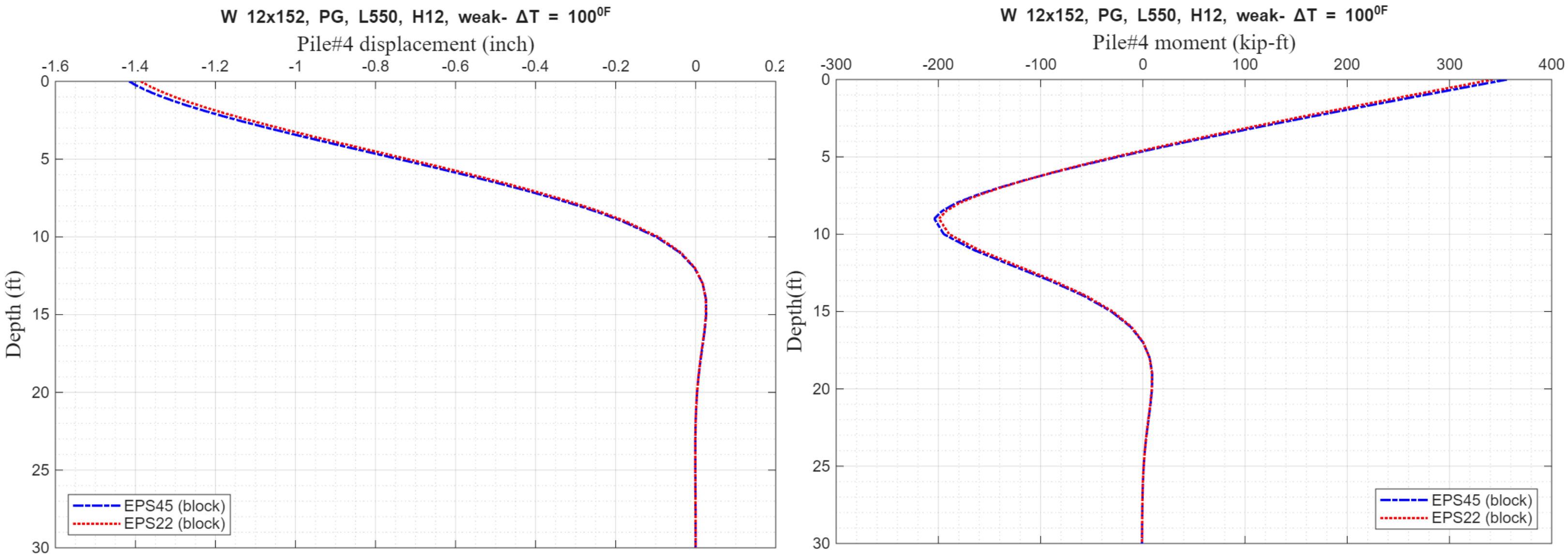

Fig. E.4 Lateral displacement and bending moment profiles for pile #4 (W12x152) for EPS45 (block) and EPS22 (block) backfill material behind the abutment wall due to $\Delta T = 100^{0F}$

Table E.3 Data for pile #4 (W12x152-weak) due to due to dead load

PILE #4		Dense	EPS45 (block)
Displacement Δ (Inch)	Δ_D	0.103	0.086
Displacement δ (Inch)	δ_D	-0.199	-0.312
Shear (Kips)	V_D	32.06	42.68
Moment¹ (Kip-ft)	M^1_D	156.62	215.75
Moment² (Kip-ft)	M^2_D	-42.67	-63.03
Axial (Kips)	F_D	215.96	212.46

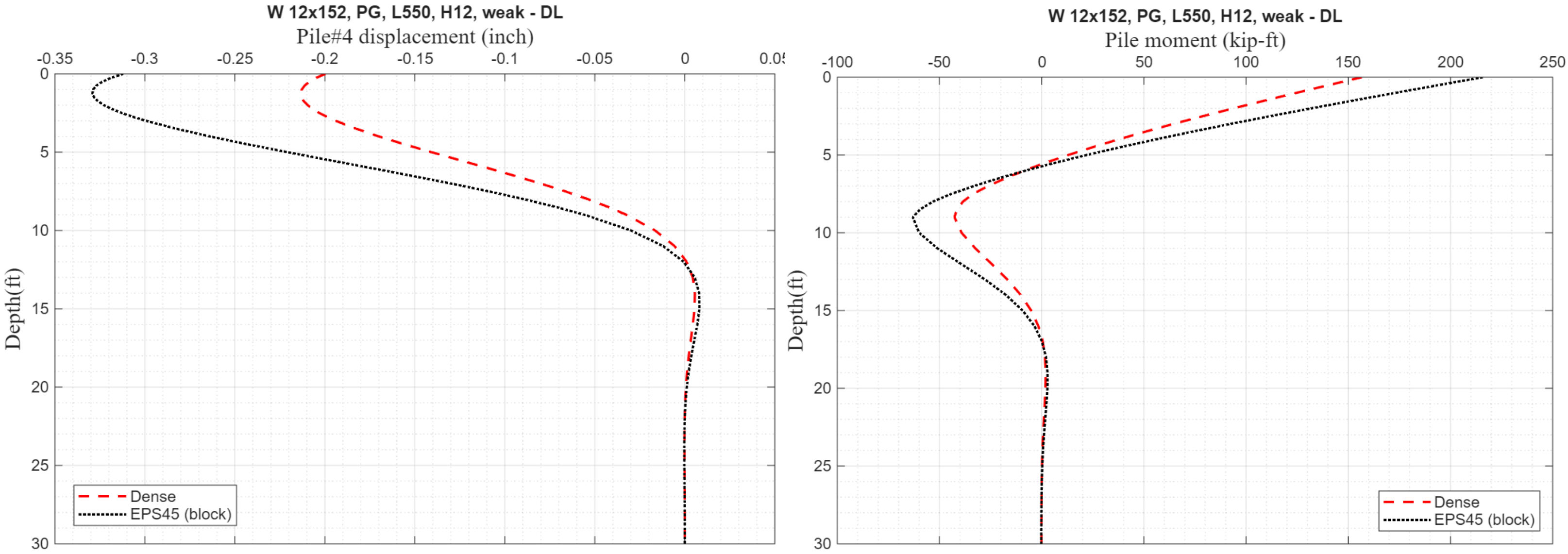

Fig. E.5 Lateral displacement and bending moment profiles for pile #4 (W12x152) for dense and EPS (block) backfill material behind the abutment wall due to dead load

Table D.4 Data pile #4 (W12x152) due to due to truck load

PILE #4		Dense	EPS45 (block)
Displacement Δ (Inch)	Δ_L	0.0190	0.021
Displacement δ (Inch)	δ_L	0.0199	0.0169
Shear (Kips)	V_L	-2.39	-3.64
Moment^1 (Kip-ft)	M^1_L	-8.91	-13.63
Moment^2 (Kip-ft)	M^2_L		
Axial (Kips)	F_L	-17.13	-16.93

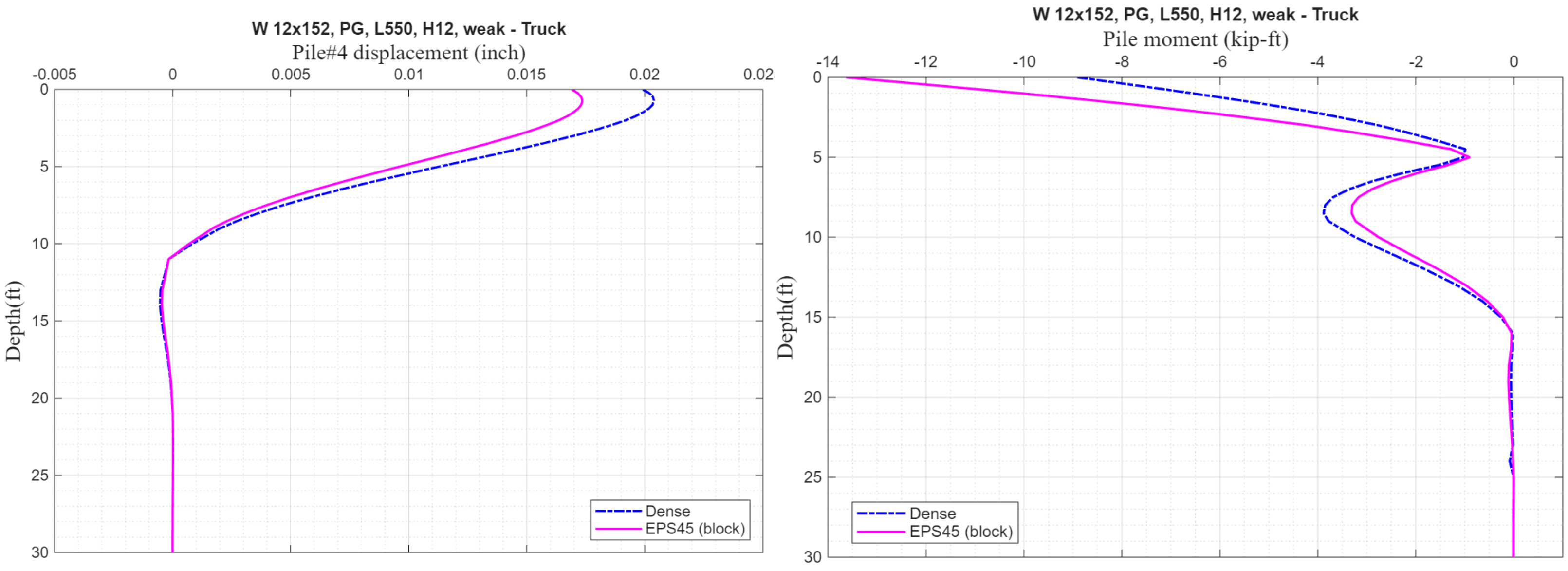

Fig. E.6 Lateral displacement and bending moment profiles for pile #4 (W12x152) for dense and EPS45 (block) backfill material behind the abutment wall due to truck load

Table E.5 Data for pile #4 (W12x152) due to dead load, live load (truck), and temperature of $\Delta T = 100^{0F}$

PILE #4		EPS45 Block (Temp.)	EPS45 Block (DL)	EPS45 Block (Truck)
Displacement Δ (Inch)	Δ_L	-1.88	0.086	0.021
Displacement δ (Inch)	δ_L	-1.41	-0.312	0.0169
Shear (Kips)	V_L	81.09	42.68	-3.64
Moment^1 (Kip-ft)	M^1_L	356.19	215.75	-13.63
Moment^2 (Kip-ft)	M^2_L	-203.89	-63.03	
Axial (Kips)	F_L	-144.35	212.46	-16.93

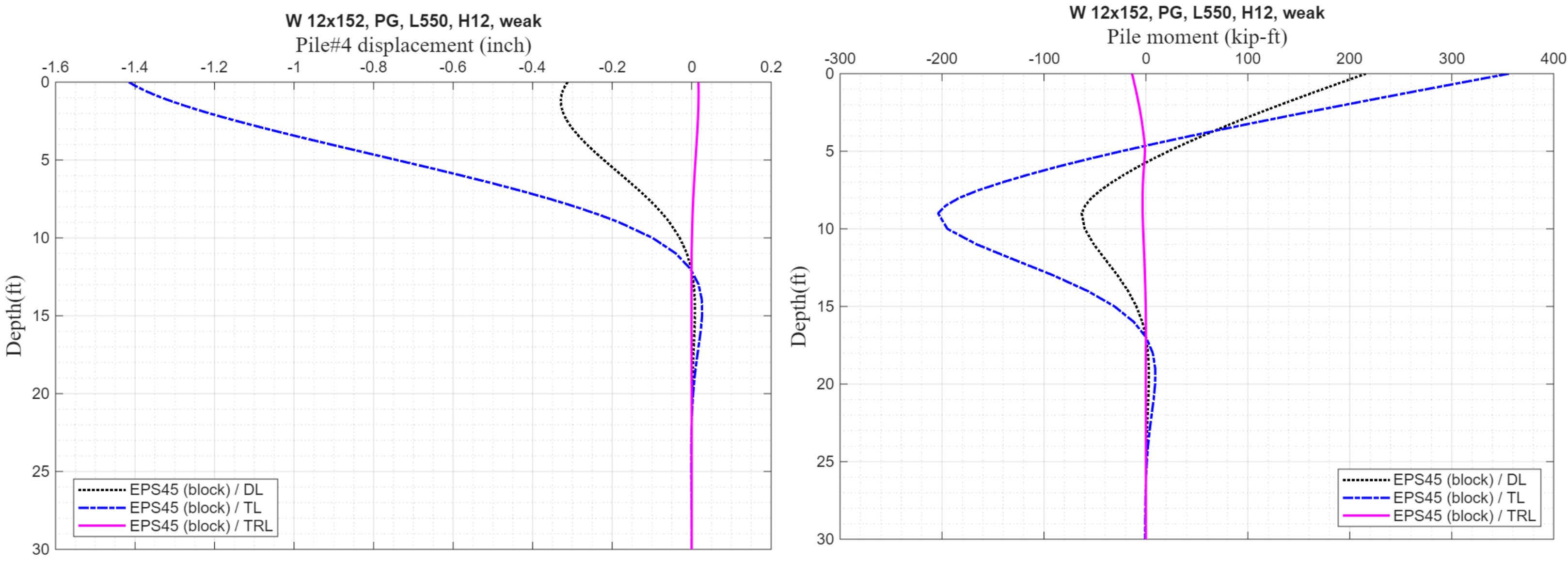

Fig. E.7 Lateral displacement and bending moment profiles for pile #4 (W12x152) for EPS45 (block) backfill material behind the abutment wall due to dead load, temperature ($\Delta T = 100^{0F}$) and truck load

Table E.6 Data for pile #4 (W12x152) due to dead load, live load (truck), and temperature of $\Delta T = 100^{0F}$

PILE #4		Dense (Temp.)	Dense (DL)	Dense (Truck)
Displacement Δ (Inch)	Δ_L	-1.87	0.103	0.0190
Displacement δ (Inch)	δ_L	-1.29	-0.199	0.0199
Shear (Kips)	V_L	71.55	32.06	-2.39
Moment^1 (Kip-ft)	M^1_L	295.16	156.62	-8.91
Moment^2 (Kip-ft)	M^2_L	-184.18	-42.67	
Axial (Kips)	F_L	-139.35	215.96	-17.13

.

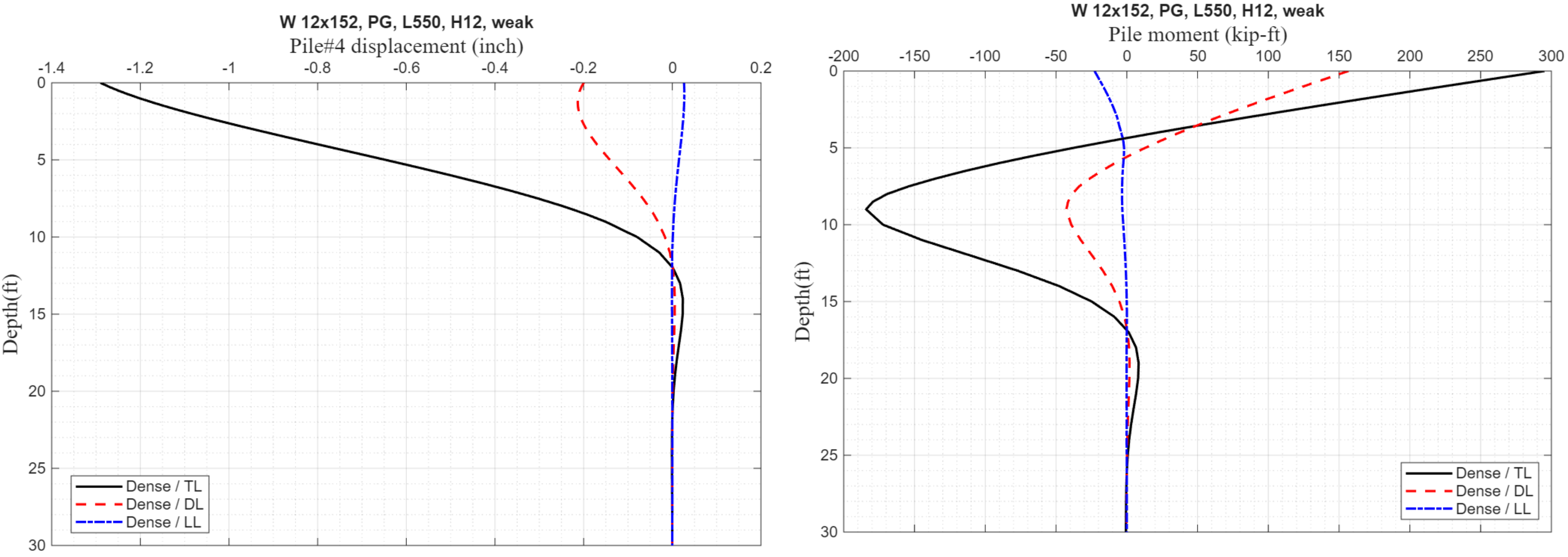

Fig. E.8 Lateral displacement and bending moment profiles for pile #4 (W12x152) for dense backfill material behind the abutment wall due to dead load, temperature ($\Delta T = 100^{0F}$) and truck load

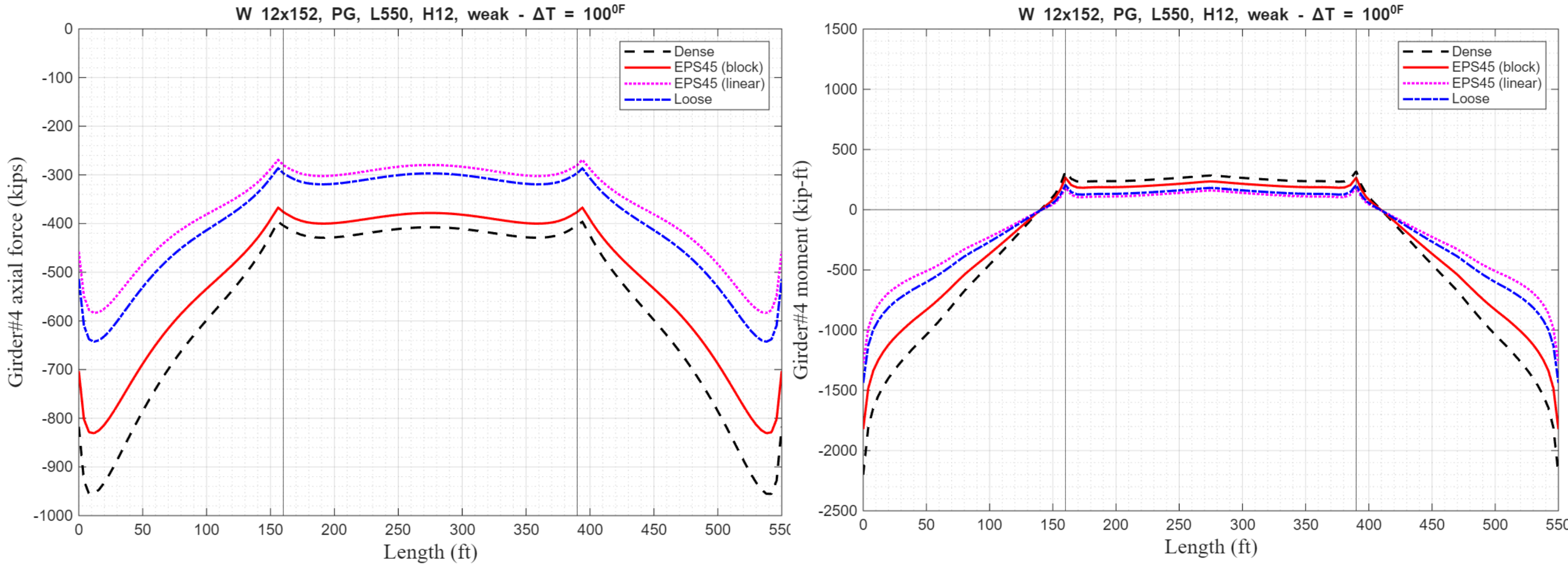

Fig. E.9 Comparison of the axial force and bending moment profiles for Girder #4 for the range of backfill material behind the abutment wall: dense, EPS45 (block), and loose due to $\Delta T = 100^{0F}$

Table E.7 Data Comparison for PG4 (Plate Girder #4) due to $\Delta T = 100^{0F}$

Chapter 4 Use of EPS as Backfill Material in Integral Abutment Bridges, 2025. S. Faraji-Hennessey

Plate Girder #4		At the abutment		Mid-1st span		At the bent		Mid-2nd span	
		Dense	EPS45 (block)	Dense	EPS45 (block)	Dense	EPS45 (block)	Dense	EPS45 (block)
Axial (Kips)	F_T	-817.4	-703.0	-662.2	-585.5	-405.8	-265.4	-408.5	-235.2
Moment (Kip-ft)	M_T	-2200.3	-1822.2	-673.1	-538.8	317.6	376.3	283.6	378.4
Shear (Kips)	V_T	-24.1	-19.1	-20.3	-16.3	18.0	17.6	0.59	0.58

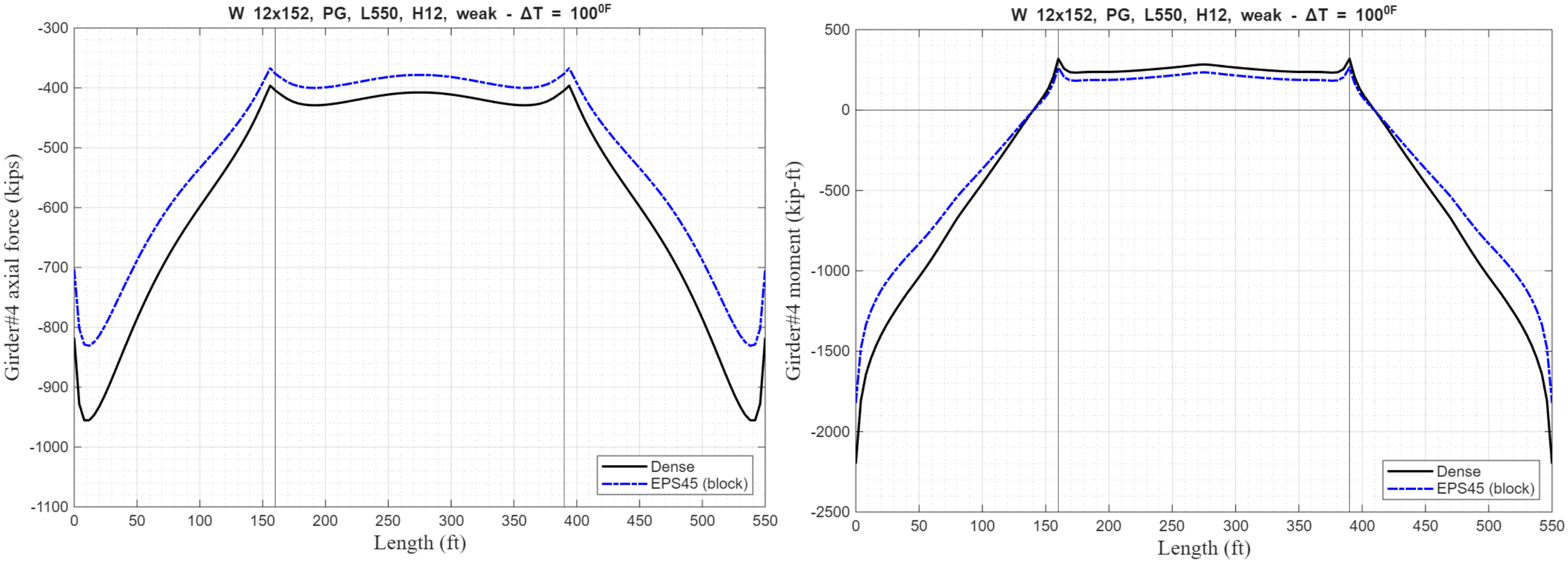

Fig. E.10 Comparison of the axial force and bending moment profiles for PG4 (Plate Girder #4)for the range of backfill material behind the abutment wall: dense, EPS45 (block), and loose due to $\Delta T = 100^{0F}$

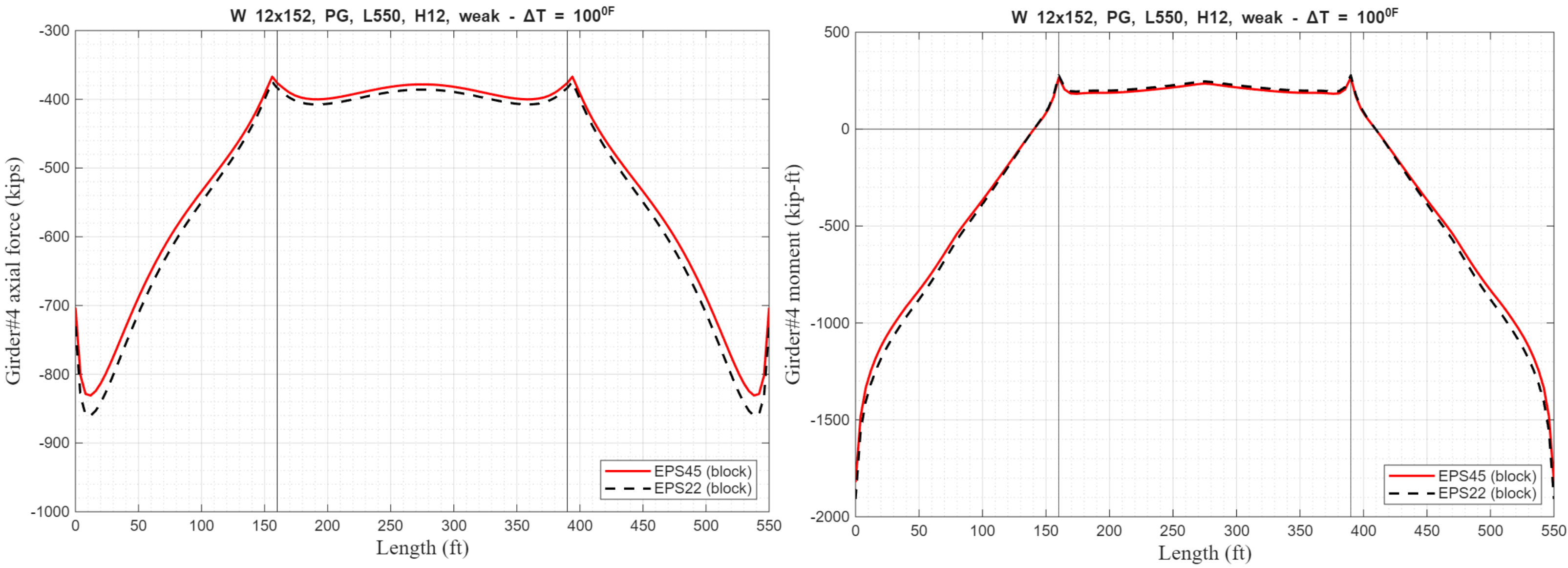

Fig. E.10 Comparison of the axial force and bending moment profiles for PG4 for the backfill material behind the abutment wall, dense vs. EPS45 (block) due to $\Delta T = 100^{0F}$

Table E.7 Data Comparison for PG4 due to dead load

Plate Girder #4		At the abutment		Mid-1st span		At the bent		Mid-2nd span	
		Dense	EPS45 (block)	Dense	EPS45 (block)	Dense	EPS45 (block)	Dense	EPS45 (block)
Axial (Kips)	F_D	-244.2	-136.7	277.3	349.3	-1571.2	-1542.0	941.4	972.0
Moment (Kip-ft)	M_D	-1144.0	-814.3	1465.0	1583.3	-6316.2	-6363.5	3826.7	3784.1
Shear (Kips)	V_D	-149.0	-144.4	55.1	58.7	319.8	322.7	3.2	3.2

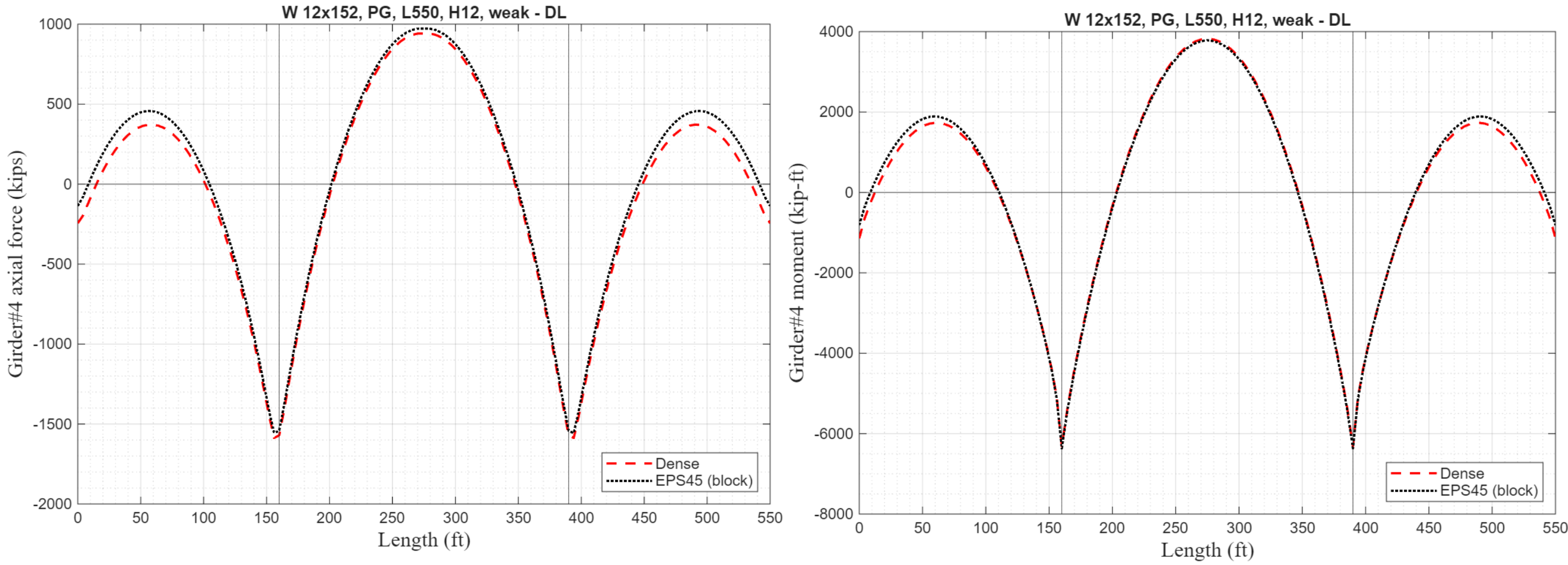

Fig. E.11 Comparison of the axial force and bending moment profiles for PG4 vs. EPS45 (block) as backfill material behind the abutment wall, due to live load (truck)

Table E.9 Data for PG4 due to live load (truck)

Plate Girder #4 (PG4)		At the abutment		Mid-1st span		At the bent		Mid-2nd span	
		Dense	EPS45 (block)	Dense	EPS45 (block)	Dense	EPS45 (block)	Dense	EPS45 (block)
Axial (Kips)	F_L	-63.7	-56.73	-25.8	-23.3	-43.0	-41.1	-13.8	-19.7
Moment (Kip-ft)	M_L	-286.4	-270.3	-48.96	-46.64	-76.1	-79.0	-17.1	-12.2
Shear (Kips)	V_L	-58.94	-58.73	-30.5	-30.0	-32.7	-32.7	-29.9	-29.9

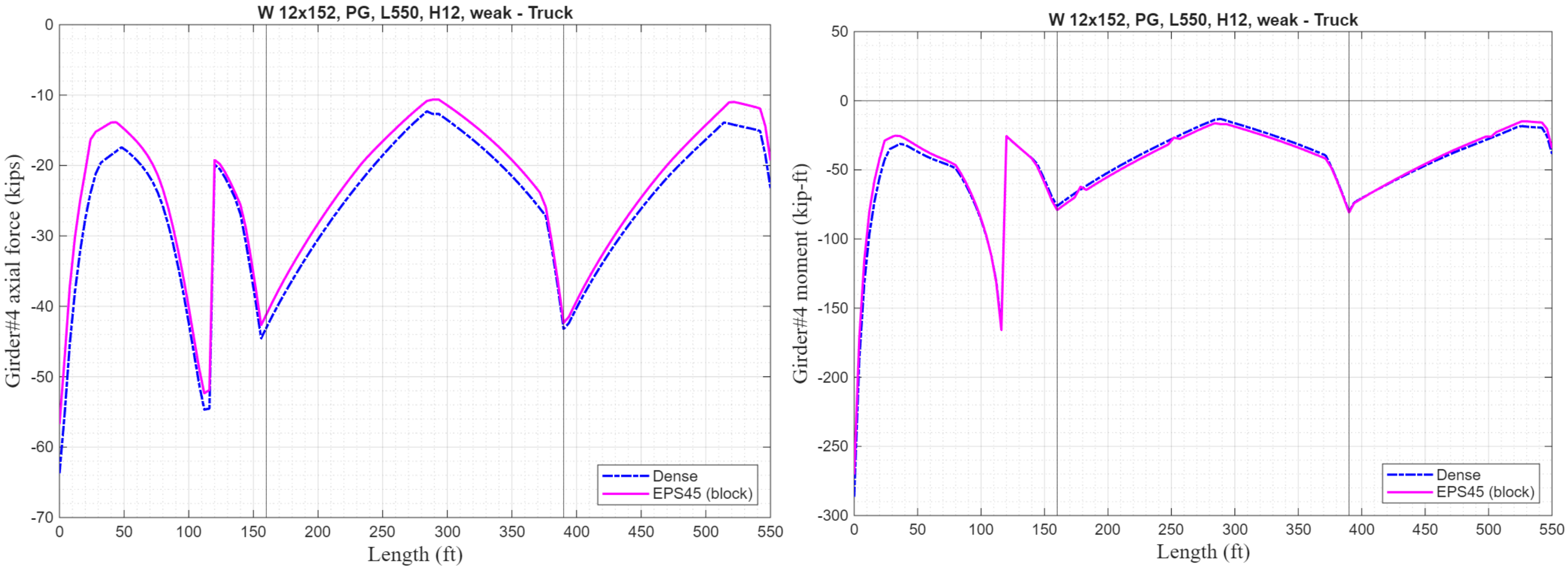

Fig. E.12 Comparison of the axial force and bending moment profiles PG4, dense soil vs. EPS45 (block) as backfill material behind the abutment wall, due to live load (truck)

Table E.10 Data for Plate Girder #4 due to $\Delta T = 100^{0F}$

GIRDER #4		At the abutment			Mid-1st span			At the bent			Mid-2nd span		
		EPS45 block (Temp)	EPS45 block (DL)	EPS45 block (Truck)	EPS45 block (Temp)	EPS45 block (DL)	EPS45 block (Truck)	EPS45 block (Temp)	EPS45 block (DL)	EPS45 block (Truck)	EPS45 block (Temp)	EPS45 block (DL)	EPS45 block (Truck)
Axial (Kips)	F_T	-703.0	-136.7	-56.73	-585.5	-136.7	-56.73	-265.4	-1542	-56.73	-235.2	972.0	-56.73
Moment (Kip-ft)	M_T	-1822.2	-814.3	-270.3	-538.8	-814.3	-270.3	376.3	-6363	-270.3	378.4	3784.1	-270.3
Shear (Kips)	V_T	-19.1	-144.4	-58.73	-16.3	-144.4	-58.73	17.6	322.7	-58.73	0.58	3.2	-58.73

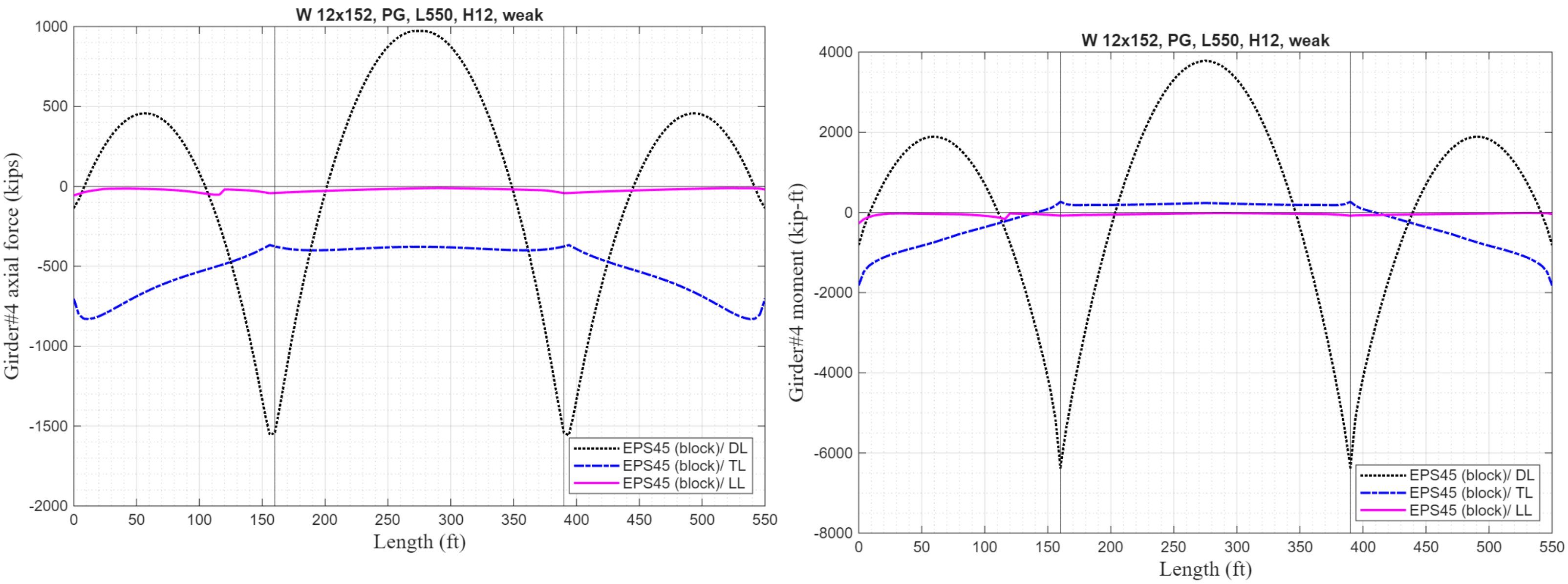

Fig. E.13 Axial force and bending moment profiles for Plate Girder #4, EPS45 (block) as backfill material behind the abutment wall, due to dead load, live load (truck), and temperature load, $\Delta T = 100^{0F}$

Table E.10 Data for Plate Girder #4 due to $\Delta T = 100^{0F}$

GIRDER #4		At the abutment			Mid-1st span			At the bent			Mid-2nd span		
		EPS45 block (Temp)	EPS45 block (DL)	EPS45 block (Truck)	EPS45 block (Temp)	EPS45 block (DL)	EPS45 block (Truck)	EPS45 block (Temp)	EPS45 block (DL)	EPS45 block (Truck)	EPS45 block (Temp)	EPS45 block (DL)	EPS45 block (Truck)
Axial (Kips)	F_T	-817.4	-244.2	-63.7	-662.2	277.3	-25.8	-405.8	-1571	-43.0	-408.5	941.4	-13.8
Moment (Kip-ft)	M_T	-2200.3	-1144	-286.4	-673.1	1465.0	-48.96	317.6	-6316	-76.1	283.6	3826	-17.1
Shear (Kips)	V_T	-24.1	-149.0	-58.94	-20.3	55.1	-30.5	18.0	319.8	-32.7	0.59	3.2	-29.9

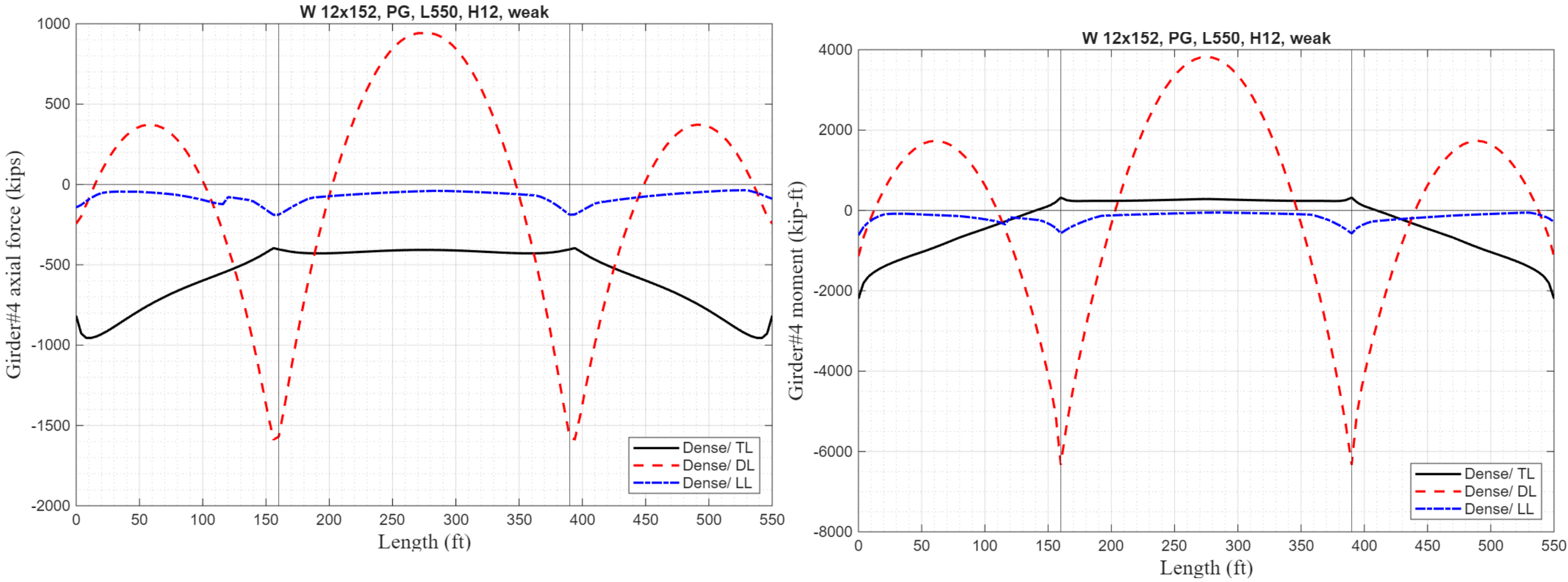

Fig. E.14 Axial force and bending moment profiles for Plate Girder #4, EPS45 dense soil as backfill material behind the abutment wall, due to dead load, live load (truck), and temperature load, $\Delta T = 100^{0F}$

Table E.10 Data for Plate Girder #4 due to due to dead load, live load (truck), and temperature, $\Delta T = 100^{0F}$

GIRDER #4		At the abutment			Mid-1st span			At the bent			Mid-2nd span		
		Dense	EPS45 (block)	% Difference	Dense	EPS45 (block)	% Difference	Dense	EPS45 (block)	% Difference	Dense	EPS45 (block)	% Difference
Axial (Kips)	F_T	-817.4	-703.0	-14.0	-662.2	-585.5	-11.6	-405.8	-265.4	-34.3	-408.5	-235.2	-42.31
	F_D	-244.2	-136.7	-44.0	277.3	349.3	25.9	-1571.2	-1542.0	-1.8	941.4	972.0	3.25
	F_L	-63.7	-56.73	-11.0	-25.8	-23.3	-9.3	-43.0	-41.1	-4.3	-13.8	-19.7	42.9
Moment (Kip-ft)	M_T	-2200.3	-1822.2	-17.1	-673.1	-538.8	-20.0	317.6	376.3	17.9	283.6	378.4	33.1
	M_D	-1144.0	-814.3	-28.8	1465.0	1583.3	8.0	-6316.2	-6363.5	0.7	3826.7	3784.1	-1.1
	M_L	-286.4	-270.3	-5.6	-48.96	-46.64	-4.7	-76.1	-79.0	3.8	-17.1	-12.2	-28.7
Shear (Kips)	V_T	-24.1	-19.1	-20.7	-20.3	-16.3	-20.1	18.0	17.6	-3.3	0.59	0.58	-1.6
	V_D	-149.0	-144.4	-3.0	55.1	58.7	6.5	319.8	322.7	0.9	3.2	3.2	0
	V_L	-58.94	-58.73	-0.36	-30.5	-30.0	-1.5	-32.7	-32.7	0	-29.9	-29.9	0